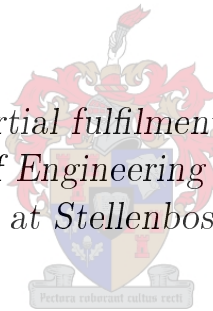


# The Influence of Dust Soiling on the Performance of Photovoltaic Modules in the Semi-Arid Areas of South Africa

by

Armand A. du Plessis

*Thesis presented in partial fulfilment of the requirements for the degree of Master of Engineering (E&E) in the Faculty of Engineering at Stellenbosch University*



Department of Electrical and Electronic Engineering,  
University of Stellenbosch,  
Private Bag X1, Matieland 7602, South Africa.

Supervisor: Dr. Johann M. Strauss

March 2017

# Declaration

By submitting this thesis electronically, I declare that the entirety of the work contained therein is my own, original work, that I am the sole author thereof (save to the extent explicitly otherwise stated), that reproduction and publication thereof by Stellenbosch University will not infringe any third party rights and that I have not previously in its entirety or in part submitted it for obtaining any qualification.

Date: ..... March 2017 .....

Copyright © 2017 Stellenbosch University  
All rights reserved

# Abstract

## The Influence of Dust Soiling on the Performance of Photovoltaic Modules in the Semi-Arid Areas of South Africa

A. A. du Plessis

*Department of Electrical and Electronic Engineering,  
University of Stellenbosch,  
Private Bag X1, Matieland 7602, South Africa.*

Thesis: MEng (E&E)

December 2016

With various commercial photovoltaic (PV) power plants in South Africa located in the semi-arid areas of the Northern Cape, this thesis provides field generated data for PV modules subjected to this environment. The effects of dust soiling, concerning the performance of PV modules, are analysed and the results obtained serve as a quantitative and mechanistic understanding for PV system engineers and investors.

In attempt to determine whether cleaning PV modules is a relevant option, experimental dust mitigation methods are investigated. These methods include the application of a hydrophobic anti-soiling coating, as well as the execution of biweekly and long term (six months) cleaning routines, consisting of water based (wet) and dry cleaning methods. Results of these mitigation methods are compared to that of modules exposed indefinitely.

The research objectives are successfully investigated by means of the design and commissioning of a PV research facility. The facility consists of 16 stationary mounted polycrystalline (pc-Si) modules, analysed for the six month period of May to October 2016. A single axis tracker (SAT) system, is also designed and implemented. This provides the required experimental platform for the investigation of dust soiling on four tracking pc-Si modules, during a three month period of mid-August to November 2016. Raw data validation is established with comprehensive weather monitoring (ambient temperature, wind speed, wind direction, rainfall, pressure, and humidity), plane of array irradiance ( $G_{POA}$ ) and PV module back sheet temperatures recorded, in accordance with the IEC 61724 standard. A MasterController, an intelligent data logging and communications device, is also designed and implemented, which is responsible for the gathering of the meteorological on-site data, measured at one minute log intervals. Also, as specified by the IEC 61724 standard, an intelligent device capable of extracting I-V curves, from individual PV modules at a 10 minute interval is utilised.

PV module power output is derived from the measured I-V curves, validated with a single-diode curve fitting routine. A comparative study between various modules is analysed with a performance ratio (PR), defined as the temperature and irradiance corrected performance factor of a PV module. A clearness ratio (CR) is also used to further quantify dust soiling

for the stationary modules, which compares the PR of modules to that of two reference modules, cleaned biweekly.

For the six month stationary module analysis, results conclude a maximum recorded reduction in CR of 2.7 %. A maximum ideal PR difference of  $\sim 1.9$  % is recorded for both the coated and uncoated sets of long term exposed modules, compared to the short term cleaned modules. This maximum deviation in performance is recorded after a 75 day absence of rainfall. The analysis does suggest that a rainfall of about 6 mm, every four to six weeks, is substantial to maintain the CR of unclean stationary modules, within 1 % of the cleaned reference modules. Results further indicate little to no deviation in performance between dry cleaned stationary modules and a set of water (distilled) cleaned modules. Regarding the SAT modules, a maximum ideal PR difference of 5.5 % is recorded for a coated, as compared to an uncoated module. The applied self-cleaning capability of the SAT system did not yield any conclusive remarks regarding this dust mitigation method. It is concluded that the hydrophobic coating for both topologies, stationary and tracking, promoted dust soiling. Finally, the research also suggests that SAT modules, which adopt a horizontal resting position during night time, are more vulnerable to dust soiling than stationary modules.

# Uittreksel

## Die Invloed van Stofbesoedeling op Fotovoltaïese Sonpanele in die semi-droë dele van Suid-Afrika

*(“The Influence of Dust Soiling on the Performance of Photovoltaic Modules in the Semi-Arid Areas of South Africa”)*

A. A. du Plessis

*Departement Eletriëse en Elektroniese Ingenieurswese,  
Universiteit van Stellenbosch,  
Privaatsak X1, Matieland 7602, Suid Afrika.*

Tesis: MIng (E&E)

Desember 2016

Met verskeie kommersiële fotovoltaïese (FV) kragstasies in Suid Afrika, geleë in die semi-droë areas van die Noord-Kaap, voorsien hierdie tesis veld gegenereerde data vir FV panele, blootgestel aan hierdie omgewing. Die effek van stofbesoedeling aangaande die prestasie van FV panele word geanaliseer en die resultate verkry dien as 'n kwantitatiewe en meganistiese aanduiding vir FV stelselgenieurs en beleggers.

In 'n poging om te bepaal of die skoonmaak van FV panele werklik van waarde is, word eksperimentele stofneerslagverminderingmetodes ondersoek. Onder andere word die toepassing van 'n hidrofobiese-teenmiddel vir stofbesoedeling ondersoek, asook die uitvoer van tweeweklikse en langtermyn (ses maande) skoonmaak roetines, wat water gebasseerde (nat) en droogskoonmaak metodes behels. Die resultate van hierdie stofneerslagverminderingmetodes word vergelyk met FV panele wat onbepaald (lang termyn) blootgestel is aan die omgewing.

Die navorsingsdoelwitte word suksesvol ondersoek deur middel van die ontwerp en ingebruikneming van 'n fotovoltaïesenavorsingsfasiliteit. Hierdie fasiliteit bestaan uit 16 stasionêre polikristallyne (pk-Si) panele, geanaliseer oor 'n ses maande tydperk vanaf Mei tot Oktober 2016. 'n Enkelasvolgerstelsel (EAV-stelsel) is ook ontwerp en geïmplementeer. Hierdie stelsel voorsien die nodige eksperimentele paltform om te bepaal wat die effek van stofbesoedeling op vier EAV, pk-Si panele is oor 'n drie maande tydperk vanaf middel Augustus tot en met November 2016. Die validasie van die proses van rou dataopname word bevestig met die meet van omvattende weermonitering (omgewingstemperatuur, windspoed, windrigting, reënval, lugdruk en humiditeit), fotovoltaïese-paneelvlak-uitstralings-intensiteit en die meet van FV paneel temperatuur, soos vereis deur die IEC 61724 standaard. 'n Intelligente data-insamelings-en-kommunikasietoestel, naamlik 'n MeesterBeheerder, is ook ontwerp en geïmplementeer, wat verantwoordelik is vir die opname van die meteorologiese data, gemeet in intervale van een minuut. Verder, soos vereis deur die IEC 61724 standaard, is 'n intelli-

gente toestel gebruik om die stroom en spanning (I-V) kurwes te onttrek vanaf individuele panele, teen 'n 10 minute interval.

Die drywing gelewer deur die FV panele word afgelei vanaf die gemete I-V kurwes, deur middel van 'n toegepaste krommepassing, gebasseer op die enkeldiodemodel. 'n Vergelykende studie tussen verskeie panele is bewerkstellig deur middel van 'n prestasieverhouding (PV), wat gedefinieër word as die reggestelde prestasiefaktor van 'n paneel met betrekking tot die temperatuur en uitstralingsintensiteit waaraan 'n paneel blootgestel is. 'n Skoonheidsverhouding (SV) word ook toegepas om verder stofbesoedeling te kwantifiseer vir stasionêre panele, waar die PV van modules gemeet word, met betrekking tot die PV van twee verwysingsmodules, elk tweeweekliks skoongemaak.

Vir die ses maande analise van die stasionêre panele, dui die resultate 'n maksimum afname vir die SV aan as 2.7 %. 'n Maksimum ideale PV verskil van 1.9 % is opgeteken vir beide van die behandelde en onbehandelde langtermyn blootgestelde panele, soos gemeet teenoor die ekwivalente korttermyn panele. Die maksimum prestasie afname van die panele is gemeet tydens die periode wat gekenmerk word deur 'n 75 dae tekort aan reënval. Die resultate dui egter daarop aan dat 'n reënval lesing van meer as 6 mm, elke vier tot ses weke, genoegsaam is om die SV van nie skoongemaakte panele, binne 1 % te onderhou met betrekking tot die skoongemaakte verwysingspanele. Die navorsing het verder aangedui dat daar geen noemenswaardige verskil in prestasie is tussen tweeweeklikse droogskoongemaakte panele en water skoongemaakte panele nie. Aangaande die EAV analise, is 'n maksimum verskil in die ideale PV van 5.5 % gemeet vir 'n behandelde paneel teenoor 'n onbehandelde paneel. Die toegepaste selfskoonmaak roetine van die EAV stelsel het egter geen beduidende resultate gelewer nie. Daarom, kan daar nie 'n gevolgtrekking gemaak word oor die toepaslikheid van so 'n stofneerslagverminderingsmetode nie. Die gevolgtrekking word gemaak dat 'n hidrofobiesebedekking intendeel 'n verhoogde stoftoename tot gevolg gehad het. Uiteindelik dui die navorsing daarop dat die panele van 'n EAV stelsel, wat 'n horisontale rusposisie aanneem gedurende die aand, meer vatbaar is vir stofbesoedeling as stasionêre panele.

# Acknowledgements

God, for Your unwavering guidance and for helping me make a success of this thesis. You blessed me with all the work I have done and enabled me to achieve so much more than I thought possible.

**I would like to express my sincere gratitude to the following people...**

Dr Johann M. Strauss, for being an exceptional study leader and for believing in me and providing me with this fantastic opportunity to have been part of this research project. I am forever grateful to you and feel privileged to have had a mentor like you.

My parents, André and Henriette du Plessis who supported me until the end and gave me an unfair advantage in life by being such wonderful parents. Thank you for giving me the chance to continue with my studies. Without you I would not be where I am today.

Kurt and Enid Krog, whom I can call my dearest friends. You have given me some of the best memories and every day spent with you was amazing. Thank you for all the meals and laughter we shared.

Charl Kraphol and Johan Badenhorst. Thank you for the friendship that we have and for always being accommodating and ready to help throughout this project. You contributed greatly to making a success of this project.

André Swart, Murray Jumat, Pietro Petzer, Howard and Jenny Martin. Without your help we would not have had a research facility. I am forever grateful for the hard work that you did.

Malem Heymans, who has been a friend and mentor to me and who shared many late nights with me. Thank you for always being willing to help and give advice. I am truly grateful for the times we spent together.

Louis Joubert, for your friendship and for all of the many hours that we spent together in the field. The journeys with you to Kalkbult were most interesting and I had great times with you. Thank you for your contribution to this project.

The entire lab, which includes Tashriq Pandy, Jason Samuels, Carmen Lewis, Tafara Mahachi, Brian De Beer, Tafadzwa Gurupira. It was great sharing a lab with you and the occasional laughter. The positive spirit we shared made it an absolute pleasure to work with you all. We truly have become brothers and sisters.

Terusa de Ridder, for standing with me every single day and sharing this journey with me. Thank you for your never ending support and for sitting with me all those nights in the lab. Without you it would not have been the amazing journey that it was. I am forever grateful to you.

# Dedications

*This thesis is dedicated to Terusa...*



# Contents

<b>Declaration</b>	<b>i</b>
<b>Abstract</b>	<b>ii</b>
<b>Uittreksel</b>	<b>iv</b>
<b>Acknowledgements</b>	<b>vi</b>
<b>Dedications</b>	<b>vii</b>
<b>Contents</b>	<b>viii</b>
<b>List of Figures</b>	<b>xii</b>
<b>List of Tables</b>	<b>xvii</b>
<b>Nomenclature</b>	<b>xix</b>
<b>1 Introduction</b>	<b>1</b>
1.1 Background . . . . .	1
1.2 Research motivation and problem statement . . . . .	2
1.2.1 Research questions . . . . .	3
1.2.2 Research objectives . . . . .	3
1.2.3 Research tasks . . . . .	3
1.2.4 Research hypothesis . . . . .	4
1.3 Scope And Limitations . . . . .	4
1.4 Thesis Overview . . . . .	5
<b>2 Literature review and background study</b>	<b>7</b>
2.1 Chapter overview . . . . .	7
2.2 Previous research . . . . .	7
2.2.1 The origins of dust deposition . . . . .	7
2.2.2 Effects of soiling on different PV systems around the world . . . . .	7
2.2.3 Dust mitigation methods . . . . .	10
2.2.4 Field generated data of anti-soiling coatings on different PV system topologies . . . . .	13
2.3 Movement of the Sun . . . . .	15
2.3.1 Position of the Sun relative to the Earth . . . . .	15
<b>3 Photovoltaic research facility</b>	<b>19</b>
3.1 Overview . . . . .	19
3.2 Research facility objective . . . . .	19

3.3	Location of the research station . . . . .	20
3.4	Design and construction of the research facility . . . . .	21
3.4.1	General layout . . . . .	21
3.4.2	Photovoltaic modules . . . . .	22
3.4.3	Design and implementation of stationary PV module rows . . . . .	22
3.4.4	Battery storage . . . . .	27
3.4.5	Communication . . . . .	28
3.4.6	Meteorology instrumentation . . . . .	29
3.5	PV measurement stations . . . . .	30
3.5.1	Description . . . . .	30
3.6	Construction of the PV research facility . . . . .	32
3.7	Installation problems and solutions . . . . .	34
<b>4</b>	<b>MasterController and weather station data acquisition</b>	<b>36</b>
4.1	Overview . . . . .	36
4.2	Function of the MasterController . . . . .	36
4.3	Conceptual hardware design . . . . .	37
4.3.1	General system overview . . . . .	37
4.3.2	Microcontroller . . . . .	37
4.3.3	Power supply and voltage sources . . . . .	38
4.3.4	USART communication and RS485 circuit . . . . .	39
4.3.5	SD card . . . . .	42
4.3.6	Real time clock . . . . .	44
4.4	Printed circuit board design . . . . .	44
4.5	MasterController set up and connection . . . . .	45
4.6	Detailed Software Design . . . . .	47
4.6.1	Programming the MCU . . . . .	47
4.6.2	Overview of data retrieval . . . . .	47
4.6.3	USART communication . . . . .	47
4.6.4	MC slave device data acquisition and processing . . . . .	49
4.6.5	MasterController user interface commands . . . . .	54
<b>5</b>	<b>Single axis tracking</b>	<b>60</b>
5.1	Introduction and chapter overview . . . . .	60
5.2	Sun tracking fundamentals of the SAT system . . . . .	60
5.2.1	Backtracking fundamentals . . . . .	62
5.3	Hardware design . . . . .	65
5.3.1	Conceptual hardware design . . . . .	65
5.3.2	Microcontroller . . . . .	65
5.3.3	Power supply . . . . .	66
5.3.4	USART communication . . . . .	66
5.3.5	Real time clock . . . . .	67
5.3.6	Full H-bridge driver circuit . . . . .	67
5.3.7	Heat sink design . . . . .	69
5.3.8	Analogue measurement circuitry and over current detection . . . . .	71
5.3.9	Position sensor and isolated SPI design . . . . .	73
5.3.10	Proximity sensors . . . . .	75
5.3.11	LCL filter and input bus capacitor design . . . . .	75
5.4	PCB design . . . . .	77
5.4.1	SAT PCB board . . . . .	77

5.4.2	Position sensor . . . . .	77
5.4.3	SAT circuit problems encountered . . . . .	77
5.4.4	Electronic installation of the SAT system . . . . .	78
5.4.5	SAT Mechanical and structural assembly . . . . .	78
5.5	Software design . . . . .	79
5.5.1	SAT software design overview . . . . .	79
5.5.2	Software application of the tracking algorithm . . . . .	80
5.5.3	SAT operation modes . . . . .	86
5.5.4	Motor control and SAT positioning . . . . .	88
5.5.5	ADC set up . . . . .	89
5.5.6	Reading the position sensor . . . . .	89
5.5.7	SAT communication and software commands . . . . .	92
<b>6</b>	<b>Experimental set up and methodology</b>	<b>98</b>
6.1	Overview . . . . .	98
6.2	Dust mitigation strategy applied . . . . .	98
6.2.1	Stationary PV modules . . . . .	98
6.2.2	Dust mitigation method applied to SAT system . . . . .	100
6.3	Application of the module coating . . . . .	102
6.3.1	Coating product specifications . . . . .	102
6.3.2	Applying the hydrophobic coating . . . . .	103
6.3.3	Execution of the cleaning routines . . . . .	105
<b>7</b>	<b>Results and Analysis</b>	<b>107</b>
7.1	Overview . . . . .	107
7.2	Performance ratio defined . . . . .	107
7.3	Raw data validation . . . . .	108
7.3.1	Overview . . . . .	108
7.3.2	PV module data . . . . .	108
7.3.3	ActiveLoads . . . . .	109
7.3.4	Weather station and irradiance measurements . . . . .	109
7.4	Data alignment, storage and monitoring . . . . .	110
7.5	Data related documentation . . . . .	111
7.6	Problems encountered during the process of data acquisition . . . . .	112
7.7	Process of data extraction and filtering . . . . .	114
7.7.1	Data extraction . . . . .	114
7.7.2	Data filtering . . . . .	114
7.8	Curve fitting . . . . .	116
7.8.1	Introduction . . . . .	116
7.8.2	Single-diode curve fitting model . . . . .	116
7.8.3	Parameter extraction . . . . .	118
7.8.4	Software implementation of PV module parameter extraction . . . . .	120
7.9	Results and discussion . . . . .	123
7.9.1	Overview . . . . .	123
7.9.2	Holistic data representation for stationary modules . . . . .	123
7.9.3	Performance ratio characterisation . . . . .	125
7.9.4	Quantifying the effect of dust soiling . . . . .	127
7.9.5	Analysis of dust mitigation methods . . . . .	129
7.9.6	Long term vs. short term . . . . .	132
7.9.7	Short term PV module analysis . . . . .	136

7.9.8	Long term PV module analysis . . . . .	140
7.9.9	Defining the single axis tracker performance ratio . . . . .	142
7.10	Performance ratio results of SAT modules . . . . .	143
7.10.1	Overview . . . . .	143
7.10.2	Comparison of all four tracker module performance ratios . . . . .	144
7.10.3	Coated vs. uncoated tracking modules . . . . .	145
7.10.4	Self cleaning vs. normal tracking operation . . . . .	146
7.11	In field visual observations made . . . . .	148
7.11.1	Overview . . . . .	148
7.11.2	Stationary PV module observations . . . . .	148
7.11.3	Single axis tracker PV module behaviour . . . . .	150
7.11.4	Cleaning routine observations . . . . .	151
<b>8</b>	<b>Conclusions and Recommendations</b>	<b>152</b>
8.1	Stationary modules . . . . .	152
8.1.1	Single axis tracking modules . . . . .	153
8.1.2	Conclusive remarks . . . . .	155
8.2	Recommendations and future research . . . . .	156
	<b>Appendices</b>	<b>157</b>
<b>A</b>	<b>Research facility</b>	<b>158</b>
A.1	Phase 1: Basic infrastructure . . . . .	158
A.2	Items installed at Kalkbult PVRF . . . . .	162
A.2.1	Photos of PVRF . . . . .	162
<b>B</b>	<b>Master Controller PCB design</b>	<b>164</b>
B.1	Relevant datasheet information . . . . .	164
B.2	MC PCB design documents . . . . .	164
<b>C</b>	<b>Single Axis Tracker related</b>	<b>171</b>
C.1	Angular position of SAT and the sun . . . . .	171
C.2	Hardware design related . . . . .	172
C.2.1	LM311D comparator . . . . .	172
C.3	SAT and position sensor PCB design schematics . . . . .	173
C.4	Software design related . . . . .	181
C.4.1	PWM software set up . . . . .	181
C.4.2	ADC set up . . . . .	182
<b>D</b>	<b>Data-Analysis</b>	<b>183</b>
D.1	Rated PV module values of stationary modules . . . . .	183
D.2	Rated PV module values of SAT modules . . . . .	183
D.3	Shading analysis of the PVRF . . . . .	183
D.4	Meteorological data . . . . .	187
	<b>List of References</b>	<b>189</b>

# List of Figures

1.1	Dust soiling on a field exposed PV module. . . . .	2
2.1	Factors that influence dust accumulation on PV modules . . . . .	8
2.2	Effects of hard and soft shading on PV module I-V curves . . . . .	8
2.3	Illustration of the formation of water droplets on untreated, hydrophobic, hydrophilic and cleaned glass. . . . .	11
2.4	Schematic illustrations of the self-cleaning processes on a hydrophilic surface and a hydrophobic surface. . . . .	12
2.5	Illustration of the super-hydrophobic (water repellent) properties of a lotus leaf. . . . .	13
2.6	Tilt angle of the Earth and ecliptic movement around the Sun. . . . .	16
2.7	Declination angle as a result of the Earth and Sun movement. . . . .	16
2.8	Illustration of the position of the Sun, determined by altitude angle $\beta$ and azimuth angle $\Phi_S$ . . . . .	17
3.1	Kalkbult location as indicated on DNI map of South African . . . . .	20
3.2	Aerial view of the surrounding environment of the research facility at Kalkbult. . . . .	21
3.3	Layout of the PVRF. . . . .	23
3.4	Illustration of how PV module placement determines the exposed module surface area. . . . .	24
3.5	Image of PVRF and the three stationary north facing PV module rows, with thin-film modules in front and the polycrystalline modules behind. . . . .	25
3.6	PV module layout and structure details of a stationary row. . . . .	26
3.7	Illustrative description of the SAT layout. . . . .	27
3.8	Standalone battery bank and wifi-communications box. . . . .	28
3.9	Pyranometer mounted at a 30° tilt angle. . . . .	30
3.10	Active Load with main PCB board features. . . . .	31
3.11	Installation of the research facility . . . . .	33
3.12	Installation of the measurement stations. . . . .	34
4.1	Conceptual hardware layout of the MC. . . . .	37
4.2	Schematic pin allocation of MCU and externally connected 20 MHz crystal. . . . .	38
4.3	Power supply circuit layout of MC . . . . .	39
4.4	Fig: Illustration of the dedicated USART lines of the MCU. . . . .	39
4.5	PCB schematic of the communications circuit design, which provides isolated USART signals to the RS485 transceiver. . . . .	40
4.6	Data sheet information of the HCPL0501 optocoupler. . . . .	40
4.7	Schematic layout of the optocoupler and the SP485EEN chip. . . . .	42
4.8	Circuit design of separating the USART1 channel into two separate channels Comms1 (UART1a) and Comms2 (UART1b). . . . .	42
4.9	Circuit design of the micro SD-card adaptor. . . . .	43
4.10	Circuit design of the RTC with SPI connections indicated. . . . .	44

4.11	PCB circuit design of the MC circuit board. . . . .	44
4.12	Cable connection diagram of the MSO weather sensor, the MC and the 372C rain gauge. . . . .	45
4.13	Cable connection diagram of the SMP10 pyranometer and the SHP1 Pyrheliometer. . . . .	46
4.14	Physical connection of the MC and the single axis trackers. . . . .	46
4.15	Communication between the Master device, MC and user. . . . .	46
4.16	MODBUS information exchange structure, with delays between data packets. . . . .	48
4.17	USART 0 transmit and receive program flow, with MC operating as a slave device. . . . .	48
4.18	USART 1 transmit and receive program flow, with MC operating as a master device. . . . .	49
4.19	Overview of the slave data acquisition process applied by the MC. . . . .	50
4.20	Illustration of how wind direction is recorded by means of a bin counter, where several sample measurements are made during a log interval. . . . .	52
4.21	Format of the data sent to the pyrheliometer and pyranometer, which requests the processed (not raw) irradiance data from the irradiance device. . . . .	52
4.22	MODBUS data packet format as sent from the MC to a SAT. . . . .	53
4.23	Communication interaction between the user and a SAT. . . . .	53
4.24	Data packet format where data is sent from the RPi to the MC. . . . .	54
4.25	Data packet format where the MC replies to the RPi. . . . .	54
4.26	Basic software process for executing master device commands received. . . . .	55
4.27	Graphic user interface to communicate with the MC, as well as ALs. . . . .	55
4.28	Data packet format applied when data is sent by the user, via the RPi, to a SAT through the interface provided by the MC. . . . .	58
5.1	Trigonometric relationship of the relative position of the sun to the angle of tilt for the SAT. . . . .	62
5.2	Results comparing the SAT implemented TA to that of the NOAA Earth System Research Laboratory solar position calculator. . . . .	63
5.3	Backtracking in progress, where modules avoid table-on-table shading with a determined tilt angle of $\varepsilon^\circ$ . . . . .	63
5.4	Shading distance as a result of the position of the sun. . . . .	64
5.5	Illustration of the applied control system used to ensure the modules are tilted towards the desired tilt angle. . . . .	65
5.6	Illustration of the ATmega 1284P-AU MCU pin connections for the SAT. . . . .	66
5.7	Illustration of the resulting H-bridge circuit behaviour for various activated transistor combinations. . . . .	67
5.8	Schematic design of the HIP4082 driver circuitry. . . . .	68
5.9	Schematic design of the MOSFET H-bridge topology. . . . .	68
5.10	Equivalent electrical model for the applied heat sink design. . . . .	69
5.11	Analogue measurement circuits to read battery supplied voltage and current supplied to the DC motor. . . . .	71
5.12	Illustration of how the LM311D comparator circuit is connected to the MCU and H-bridge, to enable a second stage hardware reset. . . . .	72
5.13	Signal input from MCU and comparator to disable H-bridge. . . . .	73
5.14	Illustration of the application of the AS5048A magnetic position sensor. . . . .	73
5.15	Recommended layout for a single-transformer isolation set up. . . . .	74
5.16	Circuit design of the master and slave side implementation of the LTC6820 (isoSPI) and the AMS5048A position sensor. . . . .	74
5.17	Circuit design of the proximity sensor circuit which generates an interrupt when over tilt occurs. . . . .	75

5.18	Illustration of the completed SAT PCB design . . . . .	77
5.19	Illustration of the SAT position sensor PCB board. . . . .	77
5.20	Electronic installation of one of the SAT systems systems. . . . .	78
5.21	Mechanical assembly and installation of the SATs. . . . .	79
5.22	Illustration of the SAT defined tilt angles. . . . .	80
5.23	Illustration of the SAT defined tilt angles. . . . .	81
5.24	Flow diagram of the tracking algorithm which determines the ideal SAT tilt angle $\varepsilon^\circ$ . . . . .	81
5.25	Normal tracking illustrated. Illustration a, b and c represents tracker positions as the sun progresses during hours associated with normal tracking. . . . .	82
5.26	Overview of the software routine used to apply the normal tracking procedure. . . . .	83
5.27	Backtracking during sunrise, with the difference in projected shadows for the three different tilt angles. . . . .	84
5.28	Backtracking during sunset, with the shadow position indicated for the three different tilt angles $\varepsilon_{ideal}^\circ$ , $\varepsilon_{now}^\circ$ and $\varepsilon_{bt}^\circ$ . . . . .	85
5.29	Backtracking algorithm flow diagram for sunset and sunrise. . . . .	85
5.30	Emergency $0^\circ$ tilt initiated during high wind speeds. . . . .	87
5.31	SAT tilt angles adopted for self-cleaning mode. . . . .	88
5.32	Overview of the software routine applied to collect angular data from the position sensor (AS5048A) via the isoSPI (LTC6820) chip. . . . .	90
5.33	Illustration of the reference angles of the SAT system and the position sensor. . . . .	91
5.34	Software routines of angular translation between position sensor and SAT. . . . .	91
5.35	MODBUS reply message of SAT after address and baud-rate are set. . . . .	93
5.36	User defined tracker lengths of SAT set up. . . . .	94
6.1	Framework of the DMS, consisting of various dust mitigation methods applied to the allocated stationary PV modules. . . . .	99
6.2	Layout of the applied dust mitigation methods to allocated stationary modules. . . . .	99
6.3	Formulated DMS for the single axis tracking PV modules as indicated. . . . .	101
6.4	Illustration of the dust mitigation methods applied to the single axis tracking PV modules as indicated. . . . .	102
6.5	PV modules to which the coating is applied . . . . .	103
6.6	Illustrations of the process for applying the hydrophobic coating. . . . .	105
7.1	Monitoring website, which displays the status and most recent measurement entries from all devices. . . . .	111
7.2	Illustration of the power curve limitation, imposed by the condition of a maximum GHI deviation. . . . .	115
7.3	Equivalent circuit of a solar cell. . . . .	117
7.4	Illustration of the curve fitting routine. . . . .	119
7.5	Demonstration of how the shunt, $R_{SH}$ , and series, $R_S$ , resistances are approximated for an initial value guess, used by the optimisation algorithm. . . . .	120
7.6	Illustration of a curve fitted routine applied by the Spline, Savgol (3rd order) and Single-diode curve fitting routines, onto a regular set of measured data points. . . . .	121
7.7	Illustration of a curve fitted routine applied by the Spline, Savgol (3rd order) and Single-diode curve fitting routines, onto a shaded module. . . . .	121
7.8	Software flow diagram illustrating the process of parameter extraction for the Single-diode curve fitting algorithm. . . . .	122
7.9	Extracted PR values of all the stationary PV modules, with rainfall and cleaning sessions indicated. . . . .	124
7.10	Amplified view of the extracted PR values. . . . .	124

7.11	Chronologically spaced representation of the measured PR. . . . .	125
7.12	Relationship between the measured plane of array irradiance ( $G_{POA}$ ) and the measured PR values. . . . .	126
7.13	Clearness ratio represented for each module over a six month period, with PV modules P6 and P11 as reference modules. . . . .	127
7.14	CR represented for two groups of regularly cleaned and non-cleaned modules. . .	128
7.15	Illustration of the adjusted DMS for the analysis. . . . .	130
7.16	Illustration of how unavailable PR data points are added to the measured PR data set. . . . .	131
7.17	Illustration of two measured PR data sets. . . . .	131
7.18	Coated module PR comparison of set A-1. . . . .	133
7.19	Coated module PR comparison of set A-2. . . . .	133
7.20	Histogram summary of set A-1 and A-2 for the coated modules. . . . .	133
7.21	Comparison of uncoated module set B-1. . . . .	135
7.22	Comparison of uncoated module set B-2 . . . . .	135
7.23	Histogram summary of set B-1 and B-2 for the uncoated modules. . . . .	135
7.24	PR of comparison set C-1. . . . .	137
7.25	PR of comparison set C-2. . . . .	137
7.26	PR distribution of short term coated modules displayed w.r.t. non-coated modules.	137
7.27	PR of comparison set D-1. . . . .	139
7.28	PR of comparison set D-2 . . . . .	139
7.29	PR distributions of short term dry cleaned modules w.r.t. water cleaned modules.	139
7.30	PR of comparison set E-1. . . . .	141
7.31	Histogram distribution of coated and uncoated long term exposed modules. . . .	141
7.32	Illustration of the various angle positions required for the process of finding the angle of incidence. . . . .	142
7.33	Layout of the SAT system and the modules with applied anti-soiling coatings. . .	144
7.34	Overview of all the measured performance ratios for the four SAT modules. . . .	144
7.35	PR and histogram distribution of comparison set F-1. . . . .	145
7.36	PR and histogram distribution of comparison set F-2. . . . .	146
7.37	PR and histogram distribution of comparison set G-1. . . . .	147
7.38	PR and histogram distribution of comparison set G-2. . . . .	147
7.39	Illustration of the PV module surfaces shortly after rainfall is received. . . . .	148
7.40	Illustration of the PV modules surfaces, two weeks after rainfall is received. . . .	149
7.41	Illustration of the PV modules surfaces, two months after rainfall is received. . .	149
7.42	Illustration of the single axis tracker PV modules surfaces, after a two month absence of rainfall. . . . .	150
A.1	Images of the PVRF after the completion of Phase 1 construction. . . . .	159
A.2	Communication and meteorological device set-up. . . . .	162
A.3	Images of the stationary rows, one of the SATs and an example of a wired orange enclosure box. . . . .	163
A.4	Images of the battery bank and an AL inside the electronic housings. . . . .	163
B.1	Value of drain-source on resistance for P-channel BSS84P MOSFET. . . . .	164
B.2	Schematic design of the MCU circuitry. . . . .	165
B.3	Schematic design of the power supply circuitry. . . . .	166
B.4	Schematic design of the RS485 UART0 communication circuitry. . . . .	167
B.5	Schematic design of the RS485 UART1A communication circuitry. . . . .	168
B.6	Schematic design of the RS485 UART1B communication circuitry. . . . .	169
B.7	PCB design of the MC circuit board. . . . .	170



C.1	Illustration of the derivation which presents the angles present of the sun relative to the SAT surface. . . . .	171
C.2	Trigonometric relationship of the position of the sun relative to the angle of tilt for the SAT. . . . .	172
C.3	Timing diagram of the LM311D comparator. . . . .	172
C.4	Schematic design of the MCU circuitry for the SAT PCB board. . . . .	174
C.5	Schematic design of the H-bridge circuitry. . . . .	175
C.6	Schematic design of the SAT power supply and proximity sensor circuitry. . . .	176
C.7	Schematic design of the RS485 communication circuitry. . . . .	177
C.8	PCB design of the SAT circuit board. . . . .	178
C.9	Schematic design of the SAT position sensor board. . . . .	179
C.10	PCB design of the SAT position sensor circuit board. . . . .	180
C.11	Fast PWM timing diagram. . . . .	181
C.12	Fast PWM timing register set up. . . . .	181
D.1	Facility layout indicating positions from where the shading analysis is conducted. .	184
D.2	Substation and lightning rods which cast a shadow. . . . .	185
D.3	Shading diagram of location 1. . . . .	185
D.4	Shading diagram of location 2. . . . .	186
D.5	Shading diagram of location 3. . . . .	186
D.6	Average ambient temperature compared to stationary PV module performance ratios. . . . .	187
D.7	Average humidity compared to stationary PV module performance ratios. . . .	187
D.8	Average irradiance, compared to stationary PV module performance ratios. . . .	188
D.9	Average barometric pressure compared to PR. . . . .	188
D.10	Average wind speed compared to PR. . . . .	188

# List of Tables

2.1	Results for soiling losses as determined by Mallineni et al. for various PV system types, based in different locations in Arizona. . . . .	9
2.2	Arabian Gulf results after ten days of exposure as determined by A. Dowsari et al.	10
3.1	Electrical characteristics of the pc-Si JC255M modules as rated at STC conditions (AM 1.5, Irradiance 1000W/m <sup>2</sup> , Cell temp. 25°C). . . . .	22
3.2	Temperature coefficients of the pc-Si JC255M modules. . . . .	22
3.3	MSO weather sensor outputs . . . . .	29
3.4	ActiveLoad design parameters . . . . .	31
3.5	ActiveLoad assignments. . . . .	32
4.1	Short summary of the microcontroller specifications . . . . .	38
4.2	Logic truth table of the UART1 Comms1 (UART1a) channel. . . . .	42
4.3	Reserved addresses for specific devices and functionality. . . . .	49
4.4	Weather station data recorded after each log interval. . . . .	51
4.5	List of the data collected from the pyranometer and the pyrhelimeter. . . . .	52
4.6	MC's user commands available to exchange information with the SAT. . . . .	53
4.7	List of the available python HEX-41 and HEX-42 MC commands. . . . .	56
4.8	List of items that define the set up of the MC. . . . .	57
4.9	List of the available HEX-43 special commands list, for the MC. . . . .	58
4.10	Functions that allow a user to send and request data to and from a SAT. . . . .	59
5.1	Truth table of the applied H-bridge MOSFET signals. . . . .	68
5.2	Truth table logic for H-bridge disable pin . . . . .	73
5.3	DC motor rated values. . . . .	78
5.4	SAT direction of rotation for applied duty cycle ( <i>D</i> ) . . . . .	88
5.5	HEX-41 and HEX-42 commands . . . . .	92
5.6	Different SAT modes of operation . . . . .	94
5.7	HEX-43 user commands list. . . . .	95
5.8	Tracking data provided by the SAT. . . . .	96
5.9	Active backtracking details. . . . .	96
6.1	Applied dust mitigation methods to individual stationary PV modules . . . . .	100
6.2	Applied dust mitigation methods to individual SAT PV modules . . . . .	102
7.1	Instrument measurement accuracy and IEC 61724 standards. . . . .	110
7.2	Bird-dropping size definition . . . . .	112
7.3	Renesola VirtusII PV module datasheet specifics for irradiance and efficiency . .	114
7.4	Maximum decrease in clearness ratio for unclean modules, as extracted from Figure 7.13. . . . .	129
7.5	Long term allocated modules compared to short term PV modules. . . . .	132
7.6	Summary of most significant data points for data set A-1 and A-2. . . . .	134

7.7	Details of the uncoated long term allocated PV modules compared to short term PV modules. . . . .	134
7.8	Summary of results for the maximum difference in PR values recorded. . . . .	136
7.9	Description of the PV module comparison group C. . . . .	136
7.10	Summary of PR and histogram distribution results for sets C-1 and C-2. . . . .	138
7.11	Comparison group D module comparison details. . . . .	138
7.12	Summary of PR and histogram distribution results for sets D-1 and D-2 . . . . .	140
7.13	Details of the PV module comparison group E. . . . .	140
7.14	Summary of the PR results and histogram distribution for set E-1. . . . .	141
7.15	Module analysis for SAT-1 and SAT-2, comparing coated and uncoated modules. . . . .	145
7.16	Summary of the results obtained for comparison sets F-1 and F-2. . . . .	146
7.17	Details regarding comparison group G . . . . .	147
7.18	Summary of the results obtained for the modules compared of Set G-1 and G-2. . . . .	148
A.1	Active-Load assignments. . . . .	158
A.2	List of items required for the successful installation of the PVRF. . . . .	162
D.1	Rated power of individual PV modules number 1-16, as determined by measurement. . . . .	183
D.2	Rated power of individual PV modules number 21-24, as determined by measurement. . . . .	183

# Nomenclature

## Constants

$$k = 1.38064852 \times 10^{-23} \text{ m}^2 \cdot \text{kg} \cdot \text{s}^{-2} \cdot \text{K}^{-1}$$

$$q = 1.60217662 \times 10^{-19} \text{ C}$$

## Symbols and Variables

$\beta$	Sun Altitude Angle . . . . .	[°]
$\phi_S$	Sun Azimuth Angle . . . . .	[°]
$G_{POA}$	Plane Of Array Irradiance . . . . .	[W/m <sup>2</sup> ]
$G_{POA-SAT}$	Single Axis Tracker Plane Of Array Irradiance . . . . .	[W/m <sup>2</sup> ]
$G_{POA-fixed}$	Plane Of Array Fixed Tilt Angle . . . . .	[W/m <sup>2</sup> ]
$G_{incident}$	Incident Irradiance . . . . .	[W/m <sup>2</sup> ]
$G_{STC}$	Irradiance at rated Standard Test Conditions . . . . .	[W/m <sup>2</sup> ]
$D$	Duty Cycle . . . . .	[%]
$\varepsilon_{ideal}$	Single Axis Tracker Ideal Tilt Angle . . . . .	[°]
$\varepsilon_{now}$	Current Single Axis Tracker Tilt Angle . . . . .	[°]
$\varepsilon_{bt}$	Single Axis Tracker Tilt Angle . . . . .	[°]
$E_{real}$	Daily energy produced . . . . .	[kWh]
$E_{ideal}$	Theoretical expected daily energy . . . . .	[kWh]
$T_{cell}$	Cell Temperature . . . . .	[C°]
$T_{STC}$	temperature at Standard Test Conditions . . . . .	[C°]
$\delta$	Declination Angle . . . . .	[C]
$n$	Day of the year . . . . .	[day]
$\Phi_S$	Azimuth angle of the sun . . . . .	[°]
$\beta$	Altitude angle of the sun . . . . .	[°]
$L$	Latitude angle . . . . .	[°]
$H$	Hour angle . . . . .	[°]

$ST$	Solar Time . . . . .	[min]
$CT$	Clock Time . . . . .	[min]
$EOT$	Equation Of Time . . . . .	[min]
$B$	Earth day angle . . . . .	[°]
$P_{MPP}$	Power at Maximum Power Point . . . . .	[W]
$MPP$	Maximum Power Point . . . . .	[W]
$I_{SC}$	Short Circuit Current . . . . .	[A]
$V_{OC}$	Open Circuit Voltage . . . . .	[V]
$V_{MPP}$	Voltage at Maximum Power Point . . . . .	[V]
$I_{MPP}$	Current at Maximum Power Point . . . . .	[A]
$\varepsilon$	Module tilt angle . . . . .	[°]
$\varepsilon_{SAT}$	Single axis tracker tilt angle . . . . .	[°]
$\lambda$	Angle between normal and incident irradiance . . . . .	[°]
$\beta_N$	Altitude angle of the sun at solar noon . . . . .	[°]
$L_S$	True Shadow Length . . . . .	[m]
$V_{OUT}$	Output voltage . . . . .	[V]
$V_A$	RS485 A line voltage . . . . .	[V]
$V_B$	RS485 B line voltage . . . . .	[V]
$f_{OSC}$	clock source oscilating frequency . . . . .	[Hz]
$d_{row}$	Distance between single axis tracker modules . . . . .	[m]
$d_{axis}$	Distance between single axis tracker axes . . . . .	[m]
$d_S$	Inter row shado distance . . . . .	[m]
$\theta_{sa}$	Sink to ambient thermal resistance . . . . .	[W/C°]
$\theta_{cs}$	Case to sink thermal resistance . . . . .	[W/C°]
$\theta_{dc}$	Device to case thermal resistance . . . . .	[W/C°]
$T_{amb}$	Ambient temperature . . . . .	[C°]
$T_{dev}$	Device temperature . . . . .	[C°]
$T_{case}$	Case temperature . . . . .	[C°]
$T_{snk}$	Sink temperature . . . . .	[C°]
$P_D$	Power dissipated . . . . .	[W]
$I_{SW}$	Switching current . . . . .	[A]
$f_S$	Switching frequency . . . . .	[Hz]

$P_{cond}$	Conduction power losses . . . . .	[W]
$P_{sw}$	Switching power losses . . . . .	[W]
$t_{rise}$	rise time . . . . .	[s]
$t_{fall}$	fall time . . . . .	[s]
$V_{BAT}$	Battery supply voltage . . . . .	[V]
$\omega$	Allowed deviation from ideal tracker tilt angle . . . . .	[°]
$D_{max}$	Maximum duty cycle . . . . .	[%]
$D_{min}$	Minimum duty cycle . . . . .	[%]
$D_{rated}$	Rated duty cycle . . . . .	[%]
$\Phi_{POS}$	Position sensor tilt angle . . . . .	[°]
$\Phi_C$	Collector azimuth angle . . . . .	[°]
$I_T$	Terminal current . . . . .	[A]
$V_T$	Terminal voltage . . . . .	[V]
$R_S$	Series resistance . . . . .	[Ω]
$R_{SH}$	Shunt resistance . . . . .	[Ω]
$PR_{Tcell-G-corrected}$	Temperature and irradiance corrected PR . . . . .	[W/m <sup>2</sup> ]
$PR_{Tcell-G-corrected-clean}$	Temp. and irradiance corrected PR of clean module . . . . .	[W/m <sup>2</sup> ]
$\theta_{AOI-SAT}$	Angle of incidence for single axis tracker . . . . .	[°]

### Subscripts

$N$	Number of items
$i$	i-th data point

### Abbreviations

AOI	Angle Of Incidence
BTA	Back Tracking Algorithm
PCB	Printed Circuit Board
MCU	Microcontroller Unit
Cd-Te	Cadmium-Telluride
CR	Cleanness Ratio
IC	Integrated Circuit
PR	Performance Ratio

WS	Weather Sensor
USART	Universal Synchronous and Asynchronous serial Receiver and Transmitter
TVS	Transient Voltage Suppression
pc-Si	Polycrystalline
STC	Standard Test Conditions (1000 W/m <sup>2</sup> , 25 C°, 1.5 AM)
DMS	Dust Mitigation Strategy
PR	Performance Ratio
mc-Si	Multi Crystalline Silicon
SAT	Single Axis Tracker
CI	Clearness Index
MISO	Master In Slave Out
MOSI	Master Out Slave In
RPi	Raspberry Pi
SPI	Serial Peripheral Interface
SCK	Serial Clock
TA	Tracking Algorithm
GND	Ground
DAT	Double Axis Tracker
CSV	Comma Separated Value
HEX	Hexadecimal
PV	Photovoltaic
PPI	Power Performance Index
DNI	Direct Normal Irradiance
PVRF	Photovoltaic Research Facility
MPPT	Maximum Power Point Tracking
MC	MasterController
AL	ActiveLoad
WS	Weather Sensor
PVMS	Photovoltaic Measurement Station
DC	Direct Current
ADC	Analogue To Digital
RTC	Real Time Clock

SD	Secure Digital
I-V	Current Voltage
TX	Transmit
RX	Receive
TXE	Transmit Enable
DE	Data Enable
GHI	Global Horizontal Irradiance
RSS	Remote Supply Switch



# Chapter 1

## Introduction

### 1.1 Background

Unlike fossil fuels, solar power is an energy revolution driven by technology [1]. There is a term known as *solar's learning rate*, which refers to the fact that PV module costs are falling 26 % every year as the technology becomes cheaper [1]. This cost reduction has allowed more entrepreneurs to gain access to the renewable energy (RE) market, which has set the stage for fierce competition amongst bidders. Evidence of this highly ambitious environment is also evident in the renewable energy sector of South Africa.

Motivated to alleviate the energy constraints of the public electricity provider, ESKOM, the South African Department of Energy (DoE) established the well known public-private partnership model, known as the Renewable Energy Independent Power Producer Procurement Programme (REIPPPP) [2]. With five successful rounds of bidding, the cost competitiveness of RE suppliers has increased substantially. Averaged bid prices for wind power dropped from R1.15/kWh(round one bids, 2011) to as low as R0.62/kWh (round five bids, 2014). On the other hand, averaged tariffs for solar PV also reduced from R2.76/kWh to R0.79/kWh [2, 3]. Financially speaking, with these competitive prices, any externalities that influence the operational efficiency of PV modules, will influence the over all investment. This is why the RE sector is now, more than ever, striving for higher levels of PV module and operational efficiency.

It is well known that locations ideal in terms of the high levels of available irradiance, are also prone to high soiling rates, due to the airborne dust, wind and also high levels of humidity, associated with some of these regions [4–8]. Soiling, in essence, refers to the accumulation of dust and dirt on solar panels, which reduces the exposure of solar cells to sunlight [5]. After irradiance and module temperature, dust soiling is regarded by some researchers as the most influential environmental factor, in terms of affecting PV output power[9].

This thesis aims to investigate the external factors that could lead to a significant decrease in PV module energy yield. In particular, the effects of dust deposition on PV module surfaces are to be investigated. Although there is nothing PV system operators can do with regards to the received irradiance and ambient temperature, dust deposition is however a tangible component, which does permit human intervention. In other words, the ability to potentially control the effect that dust soiling has on module performance, serves as the source of interest for this research. Thus, the question to ask is whether or not an attempt to reduce the accumulation of dust on PV module surfaces, will prove to be beneficial in terms of PV module performance?

## 1.2 Research motivation and problem statement

Utility scale PV system designers and operators, are constantly seeking to quantify PV soiling losses, so that PV module cleaning can be motivated and performance modelling can be optimised. This is all in an attempt to avoid deviation from the projected energy output. After various conversations with different PV system operators in South Africa, it is evident that dust mitigation (removal) is a highly speculative subject, with no real data available to quantify the effects of dust or provide guidelines regarding when PV modules should be cleaned. An example of dust soiling on an actual field exposed PV module is illustrated in Figure 1.1.

In terms of PV module cleaning, there are also questions regarding the implementation of different dust mitigation methods. Examples are water based cleaning, dry cleaning or the application of an anti-soiling surface coating, or a combination of these.

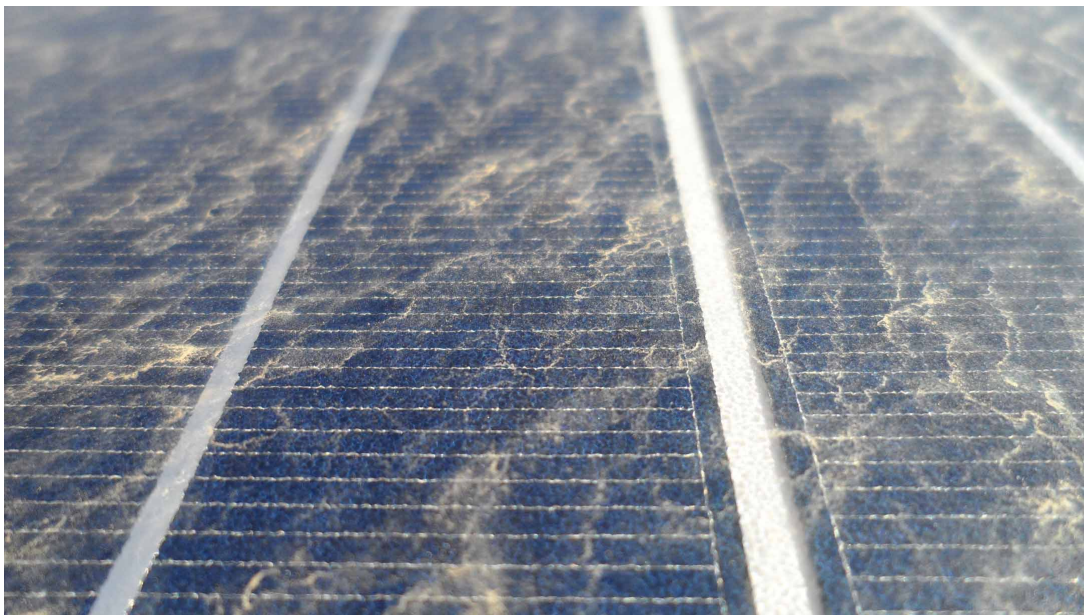


Figure 1.1: Dust soiling on a field exposed PV module.

When considering the number of international studies conducted, as summarised by S. Costa et al. [10], there is evidently world wide interest regarding dust soiling. Thus, data availability for various locations on the effects of PV module dust soiling is becoming a global effort. Concerning research studies performed in South Africa, with actual field generated data, there is however a limit. In fact, to the best knowledge of the author, no formal research with regards to the influence of dust on PV module output power, has been conducted for South Africa. This research therefore makes an important contribution to assist in establishing an encyclopaedia of global PV soiling trends.

Also, because of this lack of available PV soiling data for South Africa, up until now it has only been assumed that PV module soiling leads to significant efficiency losses, should the dust not be removed. This is particularly true for the dry and arid Northern Cape region of South Africa, which is where this research study is conducted. With more than 30 of the 45 PV power plants in South Africa either operating or scheduled for operation in the Northern Cape, it is evident that this region is well situated for PV power plants [11]. As concluded by most researchers, if not all, the availability of site specific data is essential for quantifying the effects of dust soiling and formulating a dust mitigation strategy (DMS), if required.

Therefore, this thesis, for the first time, presents data on the effect of dust on PV module performance in the semi-arid regions of the Northern Cape, South Africa. The results obtained, aim to quantify and determine the effects of dust soiling on PV module output. Ultimately, this research aims to assist PV system engineers and operators to formulate more accurate performance prediction models, as well as dust mitigation strategies.

### 1.2.1 Research questions

The project motivation serves as an incubator for the following questions:

- What is the effect of dust soiling on the energy yield of a PV module?
  - How does a PV module left over time, compare to a regularly cleaned PV module?
  - How does dust soiling of single axis tracker mounted modules, compare to stationary modules?
- Will a dust mitigation strategy result in higher PV module output?
  - How does a water-based cleaning routine compare to a dry-cleaning routine?
  - How effective are anti-soiling coatings?
  - To what extent does rainfall recover the performance of a dirty (due to dust) module?
  - How do different cleaning intervals (weekly, monthly, yearly) compare to one another?

### 1.2.2 Research objectives

The following objectives are set to successfully execute this research:

- Acquire data from actual field exposed PV modules, which are subjected to the Northern Cape environment.
- Extract I-V curve and back-plate temperature data from individual PV modules.
- Collect weather and irradiance data.
- Analyse the effect of dust soiling on stationary polycrystalline (pc-Si) modules.
- Analyse the effect of dust soiling on single-axis-tracking modules.
- Compare different dust mitigation methods.

### 1.2.3 Research tasks

To accomplish the set objectives, the following tasks have to be executed:

- Design and construct the necessary infrastructure to allow stationary and single-axis-tracking PV modules to be exposed to actual field conditions.
- Make use of an intelligent device capable of extracting IV-curve and back-plate temperature data from PV modules.

- Install an on-site weather station and Pyranometer, which provides weather and irradiance [ $\text{W}/\text{m}^2$ ] data, representative of that to which the PV modules are exposed to (IEC61724 standard).
- Design and build a data logger which extracts the weather and irradiance data from the on-site weather station and pyranometer.
- Install the required communications infrastructure, which allows the transfer of all data acquired from on-site devices, onto an online database.
- Design and build a PV powered battery bank which provides power to all of the active electronic measurement devices.
- Develop a dust-mitigation-strategy (DMS) which allows different mitigation methods to be applied to selected PV modules.
- Develop the required software set-up to conduct a full data analysis, which compares the performance of the PV modules to one another.

A fully operational Photo-Voltaic Research Facility (PVRF) has to be constructed, which will provide the means to execute the listed tasks. In turn, such a research facility will allow all of the research objectives to be completed. The PVRF must preferably be located in the Northern Cape, since this is evidently where the majority of South African commercial PV power plants are constructed and will therefore be the most beneficial to the South African PV energy sector.

### 1.2.4 Research hypothesis

The following hypotheses are made with regards to the influence of dust soiling:

- PV modules with an applied anti-soiling coating, perform better than non-coated modules.
- Single-axis-tracking modules are less prone to an accumulated dust deposit on the module surfaces, than stationary modules. Reason being because of the increased tilt angle position, which is larger than that of the stationary modules ( $30^\circ$ ), gravity and wind are employed to the advantage of the module's dust removal.
- When subjected to enough rainfall ( $> 5\text{mm}$ ), PV modules output power is restored.
- PV modules cleaned regularly (once every week or two weeks), perform better than modules that are cleaned over longer time intervals (once every few months).

## 1.3 Scope And Limitations

It is not within the scope of this thesis to provide a complex financial model, which provides guidelines on projected PV module output, due to the effect of dust soiling.

Only a selected number of PV modules are installed, which is enough to effectively execute the thesis objectives. The installed research facility consists of:

- 16x Stationary pc-Si PV modules

- 4x Tracking pc-Si PV modules
- 8x Cd-Te Thin Film modules

However, this research does not include the analysis of the Thin-Film modules.

It is not the aim of this thesis to provide an in depth study with regards to the influences of weather, but rather to produce a holistic perspective on the influence of weather factors, if identified. Thus, it is primarily the interest of this thesis to solely look at the influence dust deposition. Where necessary, weather influences will be referred to.

In terms of the applied dust mitigation methods, there is a limit with regards to the number of periodic routines that are executed. Only two periodic sets of mitigation routines are applied, which are short term (two weeks) and long term (six months). This is done, since it is in the opinion of the author, that a difference in PV module output due to dust deposition will be more evident for this scenario as opposed to a short-to-medium (monthly) term comparison. A set of PV modules are however allocated to an indefinite exposure period, which involves no cleaning routines.

It is beyond the scope of the research to compare different anti-soiling coatings to one another. Only one anti-soiling coating is applied to specific PV modules.

A pyranometer is used to measure the received global plane of array irradiance ( $G_{POA}$ ) of the stationary modules. However, for the single-axis-tracker modules, there is not a dedicated pyranometer. A mathematical conversion is used to translate the received plane of array irradiance to that of the irradiance received by the tracking modules ( $G_{POA-SAT}$ ).

Only two single axis trackers are installed, each with two pc-Si modules. The SAT system only compares long term, coated and non-coated modules to one another. Double axis tracking is not considered, due to time constraints of this project.

All module performance comparisons are done based on a defined performance ratio (PR). It is not within the interest of this thesis to compare the energy yield of different PV module topologies. It is however within the objective of the thesis to compare module behaviour with regards to dust soiling on different topologies.

## 1.4 Thesis Overview

The thesis is structured as follows:

- Chapter 2: Firstly, a literature review is presented, which introduces research conducted by authors who have also studied the effects regarding dust soiling. This is followed by an investigation into the operation of various dust mitigation methods, with a focus on anti-soiling coatings. The conclusions made by other researchers regarding the application of anti-soiling coatings are also presented. The final section of this chapter is dedicated to the relevant theory regarding Earth and Sun movement. It is necessary for the reader to have a thorough understanding of this basic theory, to follow the design of the single axis tracking system, as well as other relevant sections in this thesis, which require this basic knowledge.
- Chapter 3: To accomplish the objectives set in Chapter 1, it is necessary to design and implement a research facility. This chapter presents the design and construction of this facility. All of the measurement instrumentation installed are discussed, which

also includes the ActiveLoad devices, responsible for extracting operational PV module data.

- Chapter 4: This chapter is dedicated to the design of the intelligent device known as the MasterController. Amongst other things, this device is responsible for capturing all meteorological data. A complete hardware and software design is provided regarding this device.
- Chapter 5: The design section of this thesis is continued by this chapter, with the complete hardware design and software development of the tracking system presented. The relevant theory and application of the tracking algorithms are thoroughly presented as well. Since this is a fully functional system on its own, the installation and complete user functionality is presented.
- Chapter 6: With all of the necessary infrastructure installed, the experimental analysis can finally commence. This chapter presents the experimental set up and methodology applied to ensure that all research objectives are achieved as desired.
- Chapter 7: In this chapter, all of the acquired data is presented. However, before the results are discussed, a complete step-by-step process of raw data validation and filtering is provided. After this section the reader should have full confidence in the process of data extraction. Results are presented for both the stationary and single axis tracking modules, regarding the effect of dust soiling on module performance.
- Chapter 8: With the results presented in Chapter 7, conclusions are drawn regarding the effect of dust soiling and how the different dust mitigation methods reacted. Based on the results, guidelines are also provided to PV system operators for the effective monitoring of PV system behaviour.

# Chapter 2

## Literature review and background study

### 2.1 Chapter overview

This chapter reviews studies that have been conducted by other researchers, who have contributed noteworthy information to this particular field of study. Different anti-soiling technologies are also presented and the results of researchers who applied such anti-soiling methods. The chapter then progresses towards the fundamentals of Earth-Sun movement. All other relevant theory, which may aid the reader's understanding is provided accordingly.

### 2.2 Previous research

#### 2.2.1 The origins of dust deposition

Numerous authors have devoted their research to the adverse effects of atmospheric variables on PV plant performance. In general, as noted by A. Dowsari et al. [4] and M. Maghami et al. [12], factors that can affect PV performance include organic and inorganic contaminants. These include: dust, snow, irradiance, module temperature, salt, bird droppings, humidity, aerosols and the angle of tilt, to name a few. As mentioned, soiling in the form of dust deposition, is however identified by this dissertation as the primary objective of interest.

Factors, which specifically influence dust particle deposition, are characterised by several authors [13–15] as illustrated in Figure 2.1. As seen from this illustrative summary, dust is a complex phenomenon, influenced by various factors which instigate the settlement of dust. Ultimately, it suggests that dust soiling is primarily a site specific issue, which most authors, if not all, are in agreement with.

#### 2.2.2 Effects of soiling on different PV systems around the world

Soiling ultimately leads to some degree of shading, which can be classified as either hard-shading or soft-shading, as described by M. Maghami et al. [5]. Soft shading refers to both the presence of airborne atmospheric particles and a thin uniform layer of dust, on the surface of a PV module. The overall intensity of the irradiance received by the PV module is reduced by soft shading, without resulting in any distinguishable difference of shaded and unshaded regions. Hard shading refers to a solid compound that stops sunlight from passing through, casting a definite shadow on the surface underneath. As further observed by M. Maghami et al., soft-shading results in a decrease in current, but has no noteworthy effect on voltage. Hard shading however, reduces both current and voltage, resulting in less available power as shown in Figure 2.2. From this research, it is concluded that, when investigating

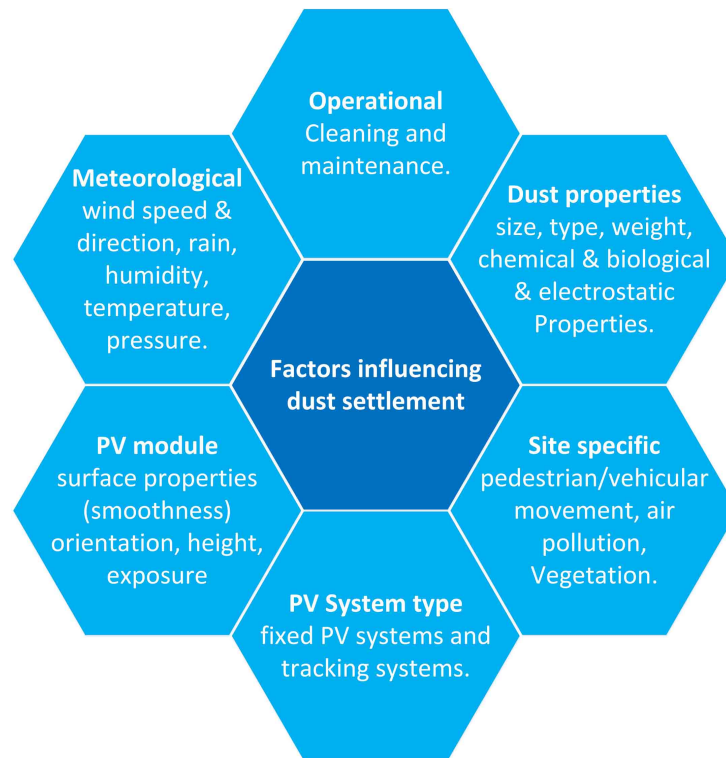


Figure 2.1: Factors that influence dust accumulation on PV modules [14, 15]

the influence of dust, it is important not to distinguish between hard and soft shading, but to embrace all factors concerning dust soiling, since this is what PV modules will be exposed to in the field.

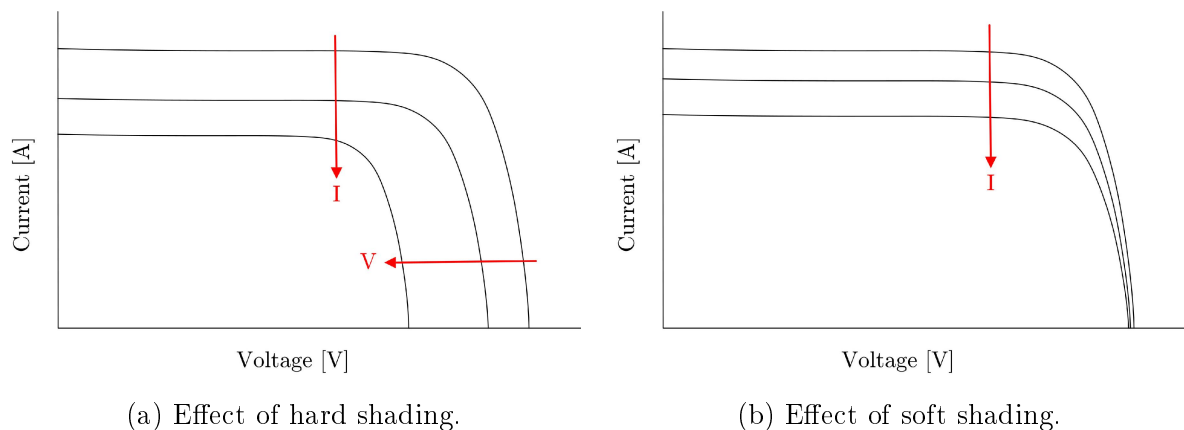


Figure 2.2: Effects of Hard and Soft shading on PV module I-V curves as described by M. Maghami et al. [5]

Studies with a focus on PV soiling have been performed in various regions around the world, most notably in Europe (Spain), North America and the Middle-East [10]. J. Mallineni et al. [16] conducted research on the effects of PV soiling in the hot-dry climate of Arizona, USA, in various regions. Soiling losses of four PV systems were quantified, with three different installations that included single-axis-tracking, fixed rooftop and fixed floor/ground level topologies. These systems were also situated in both urban and rural areas. A summary of the results published by Mallineni et al. are provided in Table 2.1:



Table 2.1: Results for soiling losses as determined by Mallineni et al. for various PV system types, based in different locations in Arizona.

Topology	Exposure (years)	Location (type)	Soiling losses (%)
SAT	12	Glendale (rural)	6.9%
SAT	4	Mesa (urban)	5.5%
Ground mount	16	Mesa (urban)	11.1%
Rooftop	8	Tempe (urban)	3.8%

It is concluded that the fixed PV modules had a higher soiling rate, compared to the single-axis-trackers. Interestingly, the research indicated that the rooftop mounted modules, even with an almost horizontal tilt angle, still displayed a lower soiling loss than the ground mounted modules.

The conclusion made by M. Mallineni, with regards to the almost horizontal rooftop PV modules, can most probably be ascribed to an advantage in height. Reason being that this is in contrast to a study presented by J. Cano [17], who indicated just the opposite with reference to the effects of PV module tilt angles. Cano's study is performed during Jan. to Mar. 2011, in Mesa Arizona, where the relationship between tilt angle and power loss, due to soiling, is quantified. Cano performed a dust analysis on nine different frameless pc-Si modules, each at a different tilt angle ( $0^\circ$ ,  $5^\circ$ ,  $10^\circ$ ,  $15^\circ$ ,  $20^\circ$ ,  $23^\circ$ ,  $30^\circ$ ,  $33^\circ$  and  $40^\circ$ ). It is concluded that, dust accumulation decreases as tilt angle increases, with average insolation losses equating to 2.02 %, 1.05 % and 0.96 % for the  $0^\circ$ ,  $23^\circ$  and  $33^\circ$  tilt angles, respectively. A maximum degradation was reported after six weeks just before the rain as 3.87 %, 2.09 % and 1.85 % for the  $0^\circ$ ,  $23^\circ$  and  $33^\circ$  tilt angles. Only these three angles are referred to, since  $23^\circ$  is the average roof tilt angle in Arizona,  $30^\circ$  is the latitude angle and  $0^\circ$  refers to a horizontal module. It was further concluded that both rain level and wind speed play significant roles on the cleaning rate depending on the tilt angle. Rainfall of less than 2 mm without wind, was found to enhance the effect of soiling, due to the formation of combined dust particles that form mud-patches.

The quantified results provided by Cano [17] are however based on frame-less modules and do not necessarily represent the potential effect that tilt angle might have on possibly even higher levels of PV soiling, representative of framed modules. As noted by a study performed in Kuwait, by H. Qasem et al. [8], it was observed that framed PV modules experience higher levels of non-uniform shading, for specific tilt angles. This is found to be due to an excess of dust accumulation, prominently found at the bottom of the framed edge. E. Lorenzo et al. [18], who performed tests in Cartagena, Spain, noted that dust can also accumulate at the sides of framed PV modules and at the top of a module, at the frame, which only further contributes to the non-uniformity of dust settlement. Due to these non-uniform dust patterns, hot-spots can further arise and rapidly reduce the lifetime of a PV module [18].

Another study by M. Maghami et al. [19] investigated the impact of dust on two fixed arrays in tropical Serdang, Malaysia, located at the University of Putra. In this work, the arrays were fixed at a tilt angle of  $15^\circ$ , consisting of twelve 95 W mono-crystalline silicon modules. Energy yield was determined for the months of 1 April 2013 to 5 December 2013, where one array was cleaned weekly and the other was left undisturbed for the research period. The research considered power output [W] and energy generation [Wh] and found that the dirty modules produced 842.8 kWh at an averaged daily rate of 3.9 kWh. The clean array however produced 854.1 kWh at an average daily rate of 3.95 kWh per day. This indicated an approximate average loss of 1.32 % for the entire period, due to dust soiling.

It is general knowledge that different climate conditions are more appropriate for certain PV module technologies than others [20, 21]. As further noted by C. Cañete et al. [21], the reason for this being that, different PV module technologies have different temperature coefficients, efficiencies and spectral response ranges. This thought inspired A. Dowsari, et al. [4] to demonstrate the effects of soiling on thin-film modules, with low temperature coefficients. The experimental set-up was established along the Arabian Gulf in Saudi Arabia. Cadmium Telluride (CdTe) Thin-Film modules, manufactured by First Solar, were used due to the low temperature coefficient (-0.25 to -0.29 %/°C) of these modules. A monitoring station was used to compare two matched modules with one another, where one was cleaned and the other left indefinitely. After exposing modules in the field for ten days, the researchers observed that PV module losses increased as the soiling level increased, with losses equating up to 3.5 % on day ten as seen in Table 2.2.

Table 2.2: Arabian Gulf results after ten days of exposure as determined by A. Dowsari et al.

Day	5	6	7	8	9	10
Loss	2.0%	2.3%	2.7%	3.0%	3.3%	3.5%

Another dust analysis was also conducted by AlDowsari [4] on a PV system situated at the King Abdullah University of Science & Technology (KAUST), Arabia. The researchers defined a Power Performance Index (PPI), which is the output power of the plant, normalised to Standard Testing Conditions (STC). The PPI decreased linearly over time by almost 20 % for this region. Another interesting observation made by A. Dowsari et al. was with regards to the effect of construction traffic on dust accumulation, where measurements indicated an output power loss of up to 35 %, after a two-month exposure to construction traffic.

The effects of construction activity were also observed by C. Chill et al. [22]. A PV test site located in the Atlantic ocean, West of Morocco, on the Gran Canary island, was examined. Accidentally located next to a construction site, the researchers had an opportunity to analyse the effects of construction and frequent vehicular movement, on the performance of PV modules. With IV-measurements taken at 10 minute intervals, it was determined that relative PV module efficiency dropped to 20 % (an 80 % decrease) after five months of exposure to a nearby construction site. An instance of low rainfall initiated partial shading on the modules, due to the accumulation of module surface dirt. This is in agreement with the observations made by J. Cano [17], who also concluded that low amounts of rainfall are not always sufficient to clean module surface, but can in fact aggravate the effect of dust. However, C. Chill et al. did observe that PV module efficiency completely recovered after enough rainfall was received.

### 2.2.3 Dust mitigation methods

Strategies to reduce dust settlement can be categorised as either an active or passive processes. Active processes refer to efforts where there is an active/moving participation in the process of cleaning modules. On the other hand, passive cleaning strategies attempt to minimise human interaction and, in general, refer to anti-soiling surface treatments, which modify a PV module's cover glass to be less adhesive [6]. It is important to note that anti-soiling coatings alone are not necessarily capable of avoiding dust accumulation, but rather aim to facilitate (enhance) the process of dust removal when rain occurs [23].

As mentioned in Chapter 1, regions with the highest irradiance levels are usually also very dry and remote locations, synonymous with water scarcity [24]. Using water from the surrounding regions is also not always practical, since specific minerals in water can result in spotted stains on the PV module surface after cleaning [25, 26]. For these reasons, dry-cleaning methods are more favoured for such dry and remote locations [4, 18]. Apart from water scarcity, the cost of labour and the overall PV system size must also be considered. These are primarily the driving factors to be considered when deciding on a dust mitigation approach [4].

### Anti-soiling technologies

There are various technologies available to consider when formulating a Dust Mitigation Strategy (DMS). Anti-soiling coatings are one of these options, which aims to remove dust passively. As mentioned by K. Midtdal and B. Jelle [27], these coatings are primarily categorised as either hydrophobic or hydrophilic. In Figure 2.3, the effect of these coatings on the shape of the water droplets, is demonstrated.

- Hydrophobic:

A hydrophobic surface coating is water repellent and has a low surface energy, which results in a high water contact angle [28]. It is due to this high water contact angle, typically greater than  $70^\circ$  or more [29], that water droplets are formed as illustrated in Figure 2.3. These water droplets attract and capture contaminants within the droplet itself, allowing surface contaminants to roll off with the droplet [27]. In Figure 2.4 this process is demonstrated.

- Hydrophilic:

Hydrophilic refers to a surface coating that attracts water and has a high surface energy, resulting in a low water contact angle (typically  $25^\circ$  -  $40^\circ$ ) [28–30]. This is also demonstrated in Figure 2.3. Thus, when water is applied to a hydrophilic surface, thin sheets of water move across the glass surface, which displaces dust and other organic matter [27].

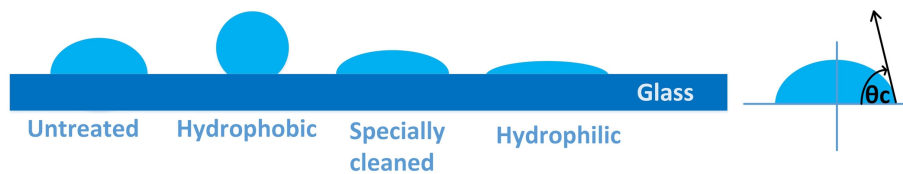


Figure 2.3: Illustration of the formation of water droplets on untreated, hydrophobic, hydrophilic and cleaned glass. On the right, the water contact angle is visualised. *Source:* Redrawn illustration as presented by K. Midtdal and B. Jelle [27].

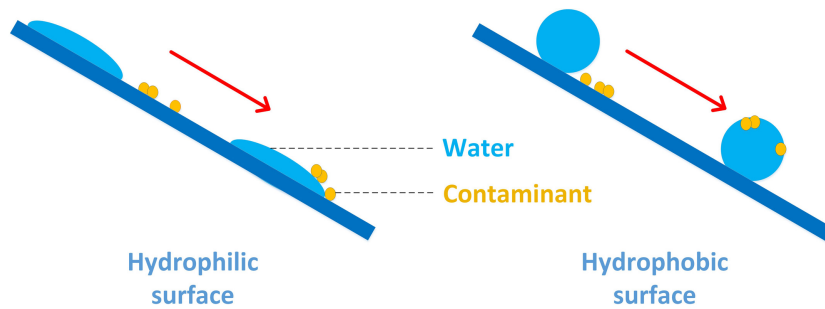


Figure 2.4: Schematic illustrations of the self-cleaning processes on a hydrophilic surface and a hydrophobic surface, as described by K. Midtdal and B. Jelle [27] and also S. Nishimoto and B. Bhushan [30].

There are also other dry-cleaning methods such as Electrostatic Discharge Screens (EDS), which consist of parallel rows of transparent electrodes, embedded within a transparent dielectric film [6]. When a phased voltage is applied, the electrodes are activated and dust particles located on the film, are then electrostatically charged and removed by a wave, formed by an applied electric field [6]. This method of using EDS was tested by A. Sayyah et al. [31] in a laboratorial set-up on a dirty module, where they confirmed a 90% restoration of the short-circuit current. However, EDS is still in development and has not been commercialised at this point in time [31].

Instead of relying on chemical coatings to enhance the self-cleaning ability of PV module surfaces, technological advances have been made in an attempt to create a self-cleaning glass that does not require any chemical coating. Researchers and engineers attempting to create nano-structured glass packaging for PV modules, attempt to imitate the same super-hydrophobic effects of a lotus plant, as illustrated in Figure 2.5, which effectively allows the formation of water beads and reduce the ability of dust to settle [32]. Such a nano-structuring process is thoroughly described by L.K. Verma et al. [32].

Research completed by J. Son et al. [33], involved the development and testing of a nano-patterned, super-hydrophilic glass-surface. After 12 weeks of outdoor exposure, this non-coated super-hydrophilic glass with anti-reflective properties, proved a solar cell efficiency drop of only 1.39 %, whereas a bare glass surface and a super-hydrophobic coated glass had a solar cell efficiency drop of 7.79 % and 2.62 %, respectively. Such nano-patterned technologies, which provide PV module glass with the ability of self-cleaning, instead of having to physically apply a chemical treatment, are definitely a viable option for future commercial implementation.

Autonomous robots are also being deployed at various large PV facilities. The focus of these robotic systems is primarily a dry-cleaning approach, such as the solutions provided by Ecoppia's E4-robot [35] and the SolarBrush [36], which effectively makes use of brushes to eliminate dust deposits. Although such robotic systems might be proven viable, it is still a highly site-specific solution, as mentioned by A. Dowsari [4], which is dependant on various operating and maintenance factors.



Figure 2.5: Illustration of the super-hydrophobic (water repellent ) properties of a lotus leaf, which cause water droplets to remain in a spherical form. *Source:* As provided by [34].

## 2.2.4 Field generated data of anti-soiling coatings on different PV system topologies

Interested in the effect of a self cleaning coating, C. Cañete et al. [37] exposed and evaluated six pc-Si modules, for one year, to the outdoor conditions of Málaga, Spain. Situated next to the Mediterranean sea, this area has a high humidity factor. All six modules were tilted at  $21^\circ$  and three of the modules were covered with an anti-soiling coating. To evaluate the effect of the coating, irradiance, weather conditions and PV-module backplate temperatures, were all acquired at a specific log-interval, together with the IV-curve measurements. With the highest losses observed during the dry, hot season, it was concluded that the coated modules produced an averaged energy loss, due to soiling, of 2.7 % and the uncoated modules indicated an energy loss of 3.6 %.

Another comparative study was conducted by Cañete et al. [38], also in Málaga Spain, where the influence of soiling losses were compared at different tilt angles for three coated and three non-coated pc-Si modules. Reference modules of each type (coated and non-coated) are also employed. The analysis was conducted over two periods of time, where the modules were tilted at  $21^\circ$  during Nov. 2010 - October 2011. For the second period, consisting of Feb. 2012 to Jan. 2013, the tilt angle was adjusted to  $40^\circ$ . Results indicated that the coated modules outperformed the uncoated modules for both periods. The first period proved a difference of 0.4 % average daily yield for the  $21^\circ$  tilt angle, in favour of the coated modules. For the second period, with the tilt angle at  $40^\circ$ , a more significant 2 % daily average gain was achieved. The research proved that the higher inclination angle reduced the rate of dust accumulation, which was further improved by the use of a coating. This also confirms the conclusions about the effects of tilt angle, that were made by J. Cano [17], mentioned in Section 2.2.2.

A hybrid self-cleaning coating for PV modules was evaluated by J. Hirose et al. [39]. PV module surface losses, due to dust accumulation, were analysed during Dec 2008 to Aug 2009, for modules exposed to the environments of Málaga in Spain (eight months), as well as the islands of Kawasaki (one year) and Miyako (five months), both in Japan. IV curves were extracted every 10 minutes and corrected to standard conditions and data was used only for clear sky days where irradiance was greater than  $800 \text{ W/m}^2$  and the wind speed was less than 2 m/s. A performance ratio (PR) was defined as:

$$PR = \frac{E_{real}}{E_{ideal}} = \frac{\text{daily energy produced}}{\text{theoretical expected daily energy}} \quad (2.1)$$

The exposure test for Spain, revealed higher transmittance losses during the rainless summer months for the uncoated modules than for the coated modules. The uncoated modules revealed an approximate 15 % irradiance loss due to soiling, whereas the two coated modules showed irradiance losses close to 13 %. The coated modules also produced roughly 3 % more energy than the uncoated modules. In Kawasaki, a 7 % difference, in favour of the coated modules, was noticed for the maximum power delivered by the uncoated and coated modules. Finally, no definitive conclusion could be drawn for the island of Miyako, due to continuous rain and wind.

In the dry subtropical desert climate of Qatar, Diego Martinez-Plaza et al. [23] studied the impact of anti-soiling coatings, different cleaning frequencies and the effect of single-and-double-axis-tracking topologies, on the performance of multi-crystalline (mc-Si) PV modules. After implementing weekly, bimonthly and biannual cleaning routines, it was concluded that the daily fall in their own defined PR ranged between 0.26 % to 0.69 %. With PV modules cleaned once a week, the PR was relatively well maintained over the entire period of testing. Modules that were left indefinitely, indicated a daily performance decrease of 1 %/day. Overall, in terms of the hydrophobic resin and anti-static anti-soiling coatings, no significant PR improvements were observed beyond that of the normal uncoated modules. The system topologies that were studied, indicated that the single-axis-tracking (SAT) system produced 10.4 % more energy than the the 22° fixed PV modules. However, the researchers found that the SAT system (orientated to follow the Azimuth angle) produced less energy during the winter months when the elevation angle of the sun was lower. The authors attribute this occurrence of less power production, due to the cosine error factor that is worse for horizontal modules than for the tilted modules. The double-axis-tracking system outperformed the SAT system and fixed topologies, with results quantified after one year of power production as 51.4 % more than the fixed modules and 37.2 % more than the SAT system.

Solar-tracking was also a point of interest for M. Garcia et al. [40], who studied the effects of soiling on both horizontally fixed and single-axis-tracking systems based in Navarra, Spain. Irradiance was measured with two horizontal pyranometers and reference modules. The field measurements of energy losses, were compiled for a period of 15 months. The research resulted in quantifying optical energy losses as a combination of soiling/dirt and losses due to angle of incidence (AOI). Annual optical energy losses were determined as 3.8 % for the tracking surfaces, of which 1 % was attributed to AOI losses and the remaining 2.8 % to soiling. For the fixed horizontal modules, optical losses accounted for a 11.9 % loss, with 6.9 % due to soiling and 5 % as a result of AOI. Rainfall of 4-5 mm was noted to effectively clean the modules, but rainfall was found to be less effective on the horizontally fixed PV modules.

Bing Guo et al. [41] also set out to quantitatively relate PV module performance degradation to dust concentration. However, they went one step further and also correlated dust deposition with meteorological effects (wind speed and direction, relative humidity, temperature, etc.), continuously recorded at one minute intervals. The analysis was performed on three arrays, consisting of eight 220 W pc-Si modules, fixed at a 22° tilt angle. Three different cleaning routines, consisting of a weekly, bimonthly and half-year (six months) period, were performed on the three different arrays. A Cleanness Index (CI) was used to quantify soiling levels and was defined as, the ratio between the PR of a module and as compared to a set of clean reference modules. The PR is defined by equation (2.2) as:

$$PR = \frac{\sum_{i=1}^n \frac{P_{DC\_i}}{(1 + \delta(T_{cell\_i} - T_{STC}))}}{\sum_{i=1}^n P_{STC} \frac{G_{POA\_i}}{G_{STC}}} \quad (2.2)$$

Where, in (2.2), the maximum power point [W] of the array in the  $i^{th}$  minute of the day is represented by  $P_{DC\_i}$ .  $P_{STC}$  and  $G_{STC}$  is the rated maximum power point of the array and the irradiance as defined at STC (Standard Testing Conditions), respectively. The measured plane of array (POA) irradiance [ $\text{kW}/\text{m}^2$ ] is represented by  $G_{POA\_i}$ . Rated cell temperature [ $^{\circ}\text{C}$ ] and actual cell temperatures of the array are represented by  $T_{STC}$  and  $T_{cell\_i}$ , respectively. Finally,  $\delta$  is the power temperature coefficient [ $\%/^{\circ}\text{C}$ ] of the array.

Thus, all PV module outputs are temperature and irradiance corrected. The average CI of PV modules cleaned every second month, was found to decrease, due to soiling alone, by 10 % - 20 % per month. Further analysis also proved that lower wind speeds, related to higher daily PV modules losses, as a result of soiling. High wind speeds on the other hand indicated the partial recovery of PV module performance. Relative humidity also proved to impact dust accumulation, with a higher relative humidity associated with a higher level of dust deposition, which results in a reduction in the CI. In terms of rainfall it is also seen that the CI of the dirty modules recovers completely. Finally, the team found that deposited dust acted like a thermal barrier, with module temperatures of heavily soiled modules less than that of clean modules.

Contrary to the temperature observations made by B. Guo et al., A. Rao et al. [42] found that dust deposition on panels increased the cell operating temperatures by 1 % - 2 %. The research team analysed the I-V characteristics of two polycrystalline PV modules, located in Bangalore, India (Latitude  $12.97^{\circ}$ , Longitude  $77.56^{\circ}$ ), which were mounted at  $13^{\circ}$  on a roof at the Indian Institute of Science. Two identical modules were compared, with one PV module cleaned and the other one left to accumulate dust. The researchers found that dust deposition lead to a 5 % - 6 % drop in power output. Open circuit voltage ( $V_{OC}$ ) was found not to be altered too much by dust accumulation, whereas the effect of dust was more prominent when a short circuit current  $I_{SC}$  drop of approximately 5 % - 6 % was observed.

## 2.3 Movement of the Sun

### 2.3.1 Position of the Sun relative to the Earth

Conceptualising the movement of the sun is the fundamental building block when considering the design of any PV system. The characteristics of the earth's orbit should be well understood, if the reader is to follow discussions with regards to the design of the Photovoltaic Research Facility (PVRF) and the Single Axis Tracking (SAT) system. Note that, for all foregoing expressions, the angles provided are measured in degrees, unless stated otherwise.

Accurately specifying the position of the sun, requires three coordinates. These are the solar altitude ( $\beta$ ) and azimuth ( $\Phi_S$ ) angles, as well as the distance between the earth and the sun [43, p.29]. As seen in Figure 2.6, the earth's orbit is elliptical. It should be mentioned that, due to what is known as Milankovitch Oscillations, this is not always the case, as the earth's orbital shape oscillates between circular and elliptical about every 100,000 years [44, pp.192-193]. However, solar applications mostly rely on the azimuth and altitude angles and the characteristics of earth's orbit and the distance from the sun are assumed to be constant.

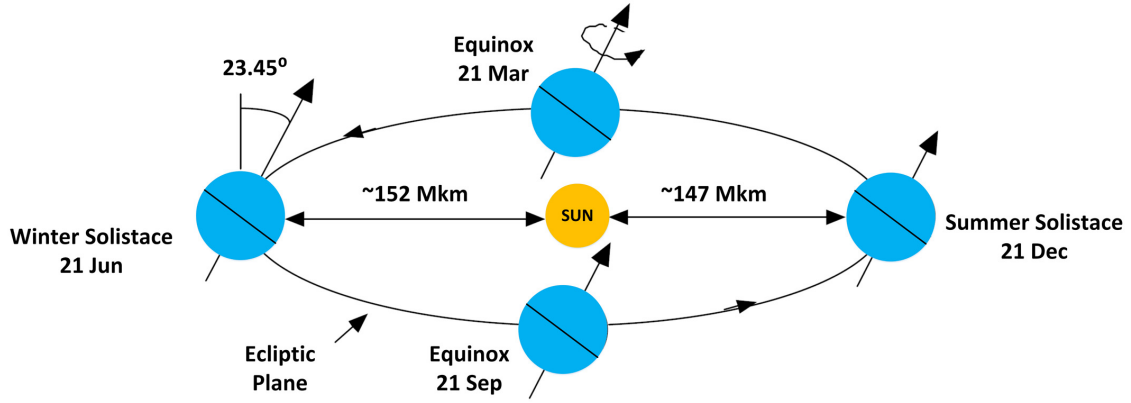


Figure 2.6: Tilt angle of the Earth and ecliptic movement around the Sun. *Source:* Redrawn illustration as presented by G. Masters [44, p.192]

Another angle of importance is the declination angle  $\delta$  [deg], which is the angle formed between the centre of the sun and the centre of the earth, as seen in Figure 2.7 [44, p.193]. Effectively,  $\delta$  represents the deviation of the sun from directly above the equator [43, p.27]. The earth's equator is tilted 23.45° relative to the plane of the orbit and equation (2.3) represents  $\delta$  at any given day ( $n$ ) of the year [44, p.194].

$$\delta = 23.45 \left[ \frac{360}{365} (n - 81) \right] \quad (2.3)$$

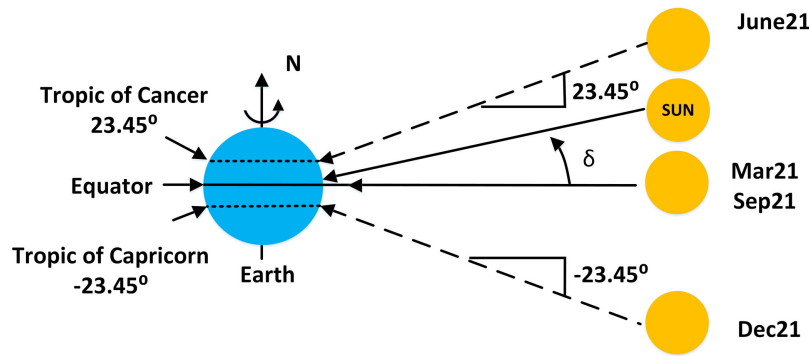


Figure 2.7: Declination angle as a result of the Earth and Sun movement. *Source:* Redrawn illustration as presented by G. Masters [44, p.193].

As displayed in Figure 2.8,  $\beta$  is the angular measure from the earth's local horizon towards the geometric center of the sun [45]. In the southern hemisphere, the  $\Phi_S$  angle represents the sun's relative position east or west of north. Following convention, the azimuth angle is positive in the morning, when  $\Phi_S$  is east of north, negative in the afternoon, when the sun is west of north and 0° at solar noon [44, p.196-197]. Solar noon refers to the time of day at which the sun's rays align perpendicular to a given line of longitude [45]. The longitude angle refers to the angular distance to the west or east of the Prime Meridian (situated at 0°). The Latitude angle refers to the angular distance north or south of the Equator. Thus, for all locations along any mutual line of longitude, solar noon occurs at the same time. Regions positioned at latitudes above the Tropic of Cancer, experience solar noon due south



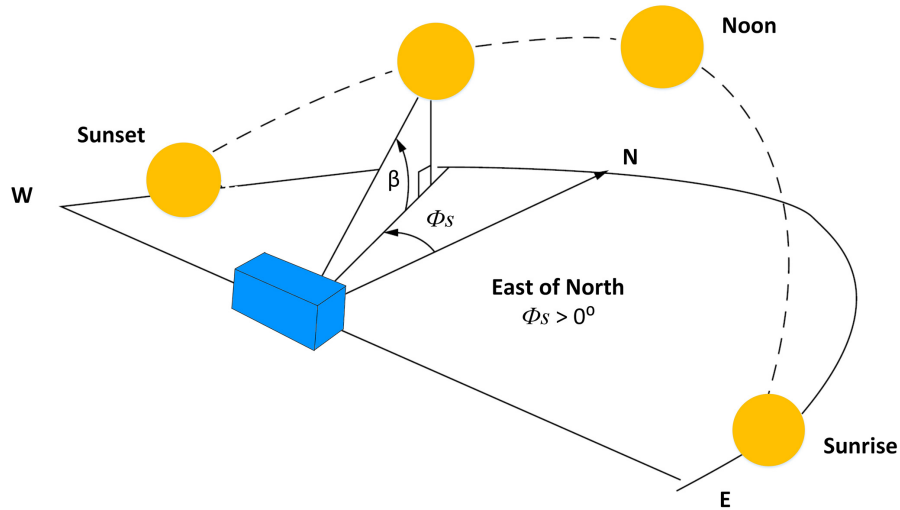


Figure 2.8: Illustration of the position of the Sun, determined by altitude angle  $\beta$  and azimuth angle  $\Phi_S$ . *Source:* Redrawn illustration as presented by G. Masters [44, p.197]

of the observer and north of the observer, for regions below the Tropic of Capricorn. Tropical regions will observe solar noon as either due North, South or directly overhead [44, p.195].

The  $\beta$  and  $\Phi_S$  angles are determined by equations 2.4 and 2.5 respectively [44, p.197]:

$$\beta = \sin^{-1}(\cos L \cos \delta \cos H + \sin L \sin \delta) \quad (2.4)$$

$$\Phi_S = \sin^{-1} \left( \frac{\cos \delta \sin H}{\cos \beta} \right) \quad (2.5)$$

It should be noted that  $\Phi_S$  can have a magnitude greater than  $90^\circ$ , should the sun's azimuth be more than  $90^\circ$  away from North [44, p.198]. Therefore, equation (2.6) [44, p.198] is used to confirm the magnitude of  $\Phi_S$ :

$$\text{if } \cos H \geq \frac{\tan \delta}{\tan L} \text{ then } |\Phi_S| \leq 90^\circ \text{ else } |\Phi_S| > 90^\circ \quad (2.6)$$

Where the variables in 2.4 - 2.6 are defined as:

Where the variables in (5.1) - (5.9) are defined as:

- $L$  = Latitude [deg]
- $H$  = Hour angle [deg]
- $\delta$  = Declination angle [deg]

The hour angle represented by  $H$  [deg], which defined by equation (2.7), is an angular representation of time, with a positive and negative value for hours before and after solar noon, respectively [44, p. 199]. With equation (2.8), the *Hours Before Solar Noon* [hours] are determined.

$$H = \left( \frac{15^\circ}{\text{Hour}} \right) \times (\text{Hours Before Solar Noon}) \quad (2.7)$$

$$\text{Hours Before Solar Noon} = 12 : 00 - ST \quad (2.8)$$

For the conversion between Solar Time (ST) [min] and Clock/Civil Time (CT) [min] the following formulas are essential, as provided by [44, p.207] :

$$ST = CT + \frac{4[\text{min}]}{1^\circ} (\text{Local Time Meridian} - \text{Local Longitude})^\circ + EOT \quad (2.9)$$

$$EOT = 9.87 \sin 2B - 7.53 \cos B - 1.5 \sin B \quad (2.10)$$

$$B = \frac{360}{364}(n - 81) \quad (2.11)$$

Where the variable  $EOT$  refers to the Equation of Time [min] and  $n$  refers to the day number. Equation (2.10) is the longitude correction between civilian clock time and solar time. Variable  $B$  [deg], as represented by equation (2.11), is the second correction that accounts for the varying length of solar days, due to the earth's elliptical orbit [44, pp.206,207].

It should be noted that, more sophisticated solar position algorithms are available with higher levels of accuracy, which make use of Julian calendar days and etc. such as presented by I. Reda and A. Andreas [46]. Although sun tracking accuracy should always be a priority in any PV system, the errors introduced by the above mentioned formulas, are negligible for flat plated modules. It is not within the scope of this document to compare tracking algorithms, but only to investigate the influence of dust accumulation on PV modules. This concludes that the position of the sun can be determined at any time of the day, by making use of equations 2.3 - 2.11 and that any introduced uncertainty/inaccuracy is negligible. The accuracy of these equations is verified in Chapter 5.2. Further, all other relevant theory concerning earth and sun movement, module placement, shading analysis and tracking algorithms will be provided in the appropriate sections.

# Chapter 3

## Photovoltaic research facility

### 3.1 Overview

This chapter describes the location, design, construction and basic operation of the research facility, which provides the necessary infrastructure for the effective monitoring of in field PV modules.

### 3.2 Research facility objective

As previously mentioned in Chapter 1, the research presented by this thesis, is executed by means of a standalone experimental photovoltaic research facility . Although, the option does exist for monitoring field exposed PV modules on large commercial PV systems, which this research is intended for, there are several reasons for rather performing the analysis on a standalone PV system.

The first and foremost advantage is the ability to exercise absolute control over the PV modules. The PVRF allows modules to be monitored individually, without the risk of interference on and from a large commercial PV system set-up. In large PV systems the modules are connected in arrays and strings, which could lead to potential mismatch losses, since the current or voltage mismatch (drop) of one module affects all the other PV modules in the array [18]. Large PV systems also handicap experimental maneuverability. For example, instead of having to execute an experiment on an entire string or array, as would be the case for a large PV system, the PVRF allows individual experiments to be executed on individual PV modules. Monitoring the effect of externalities on PV modules connected in a string, also increases uncertainty and allows less accurate quantification of the results. A study conducted by A. Brooks [47] et al. confirmed that IV measurements from individual modules, resulted in a lower measurement uncertainty of 0.4 %, as opposed to a 3 % uncertainty for a comparison of string connected PV modules.

The standalone topology also allows PV modules to be connected to the same load, with the same power requirements, which once again reduces further uncertainty. Practically speaking, extracting individual PV module I-V curve measurements and back-plate temperatures, as required by the IEC60891 standard [48], is more easily executed for a set-up where modules are isolated from one another.

### 3.3 Location of the research station.

The PVRF is situated within the fences of Scatec Solar's 75 MW commercial PV power plant, in the Northern Cape, on the farm known as Kalkbult. This Kalkbult site is located at  $30.161^\circ$  (latitude) South and  $24.132^\circ$  (longitude) east. The exact site location is displayed in Figure 3.1.

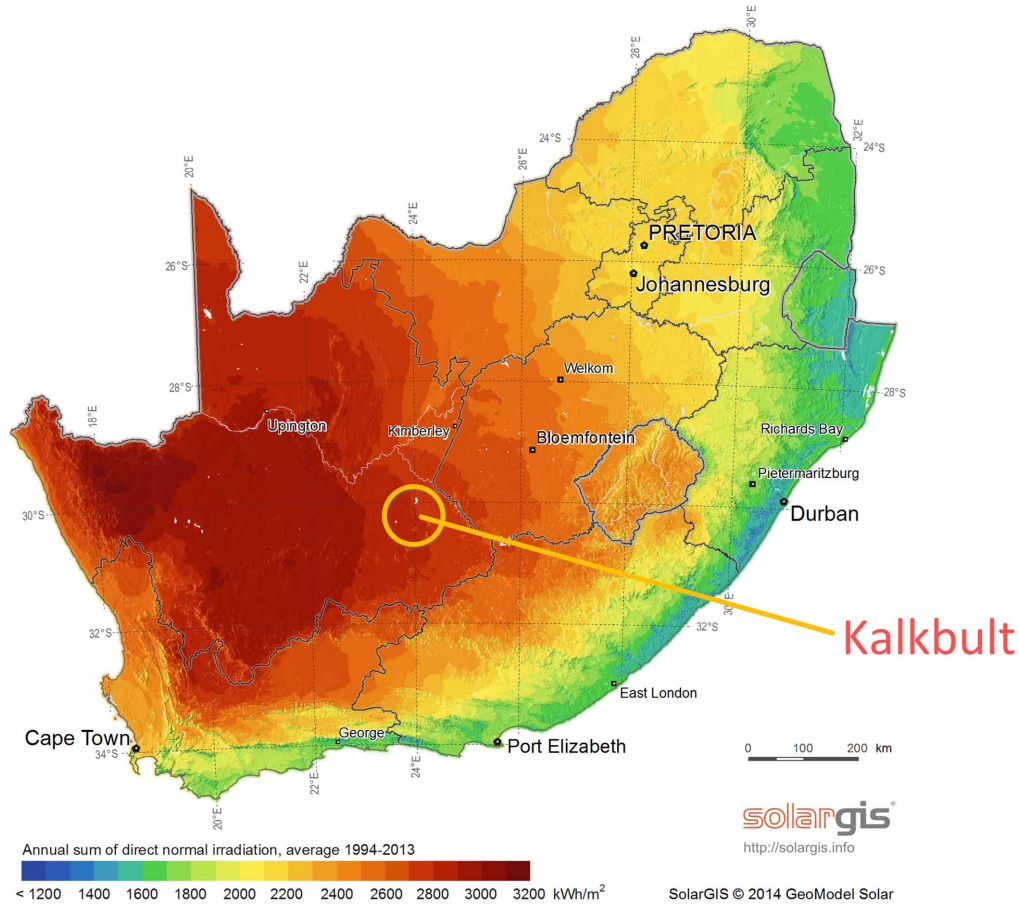


Figure 3.1: Kalkbult location as indicated on DNI map of South Africa [49].

Kalkbult is 60 km north of the town of De Aar, in the upper Karoo biome. As the recorded weather archives indicate [50], this location, has a climate of extremes, with daily summer (December to February) temperatures averaging  $32^\circ\text{C}$  and maximum temperatures of  $38^\circ\text{C}$  and higher occasionally experienced. Daily winter (June to August) averages of  $16^\circ\text{C}$  can be expected, with average night time temperatures recorded at  $2^\circ\text{C}$ , with the occasional sub-zero temperature. The average annual precipitation is 300 mm, with most rainfall occurring mainly during the summer months and autumn (March to April). Due to the flat topology and vast open spaces, wind has an almost constant presence during the day time. Average wind speeds are approximately 4 m/s during the winter months and average wind speeds of 4.5 m/s to 5.5 m/s are to be expected during the summer months (Dec. to Feb.). Humidity levels are also fairly low, ranging from 36 % to 55 %, with the highest levels of humidity during Autumn and Winter and the lowest levels during September to December. The region receives a fair amount of sunshine, with a recorded annual Direct Normal Irradiance (DNI) of approximately  $2600\text{ kWh/m}^2$  [49]. As described by the ecologist Simon Bundy, the surrounding area is generally a flat region with low hills, which consists of an underlying geology of sandstones and mud-stone, with higher elevated hills being doleritic in composition. In this Northern Cape region, calcium carbonate (also known as kalk) beds

are common, especially around the Kalkbult area. The soils are also primarily duplex, with a rocky sub surface horizon and a sandy upper horizon. For this region of the Karoo, vegetation also varies from a graminoid (grassland) habitat to a forb or shrub based habitat. The nature and structure of the habitat on site, is determined by factors such as soil depth, rainfall, grazing and even fire.

As shown in Figure 3.2 the PVRF is located within the Kalkbult 75 MW solar park. Next to this park, approximately 250 m to the west, is a gravel road as well as an active railway track. To the east and to the north, the PVRF is surrounded by the rest of the 75 MW solar park. The commercial PV modules to the east, are approximately 30 m away and the panels north, are about 100 m away. A substation is also located 40 m west of the site. The surrounding horizon is not completely flat, with small hills visible in the distance, which momentarily delay irradiance from reaching the PV modules during sunrise.

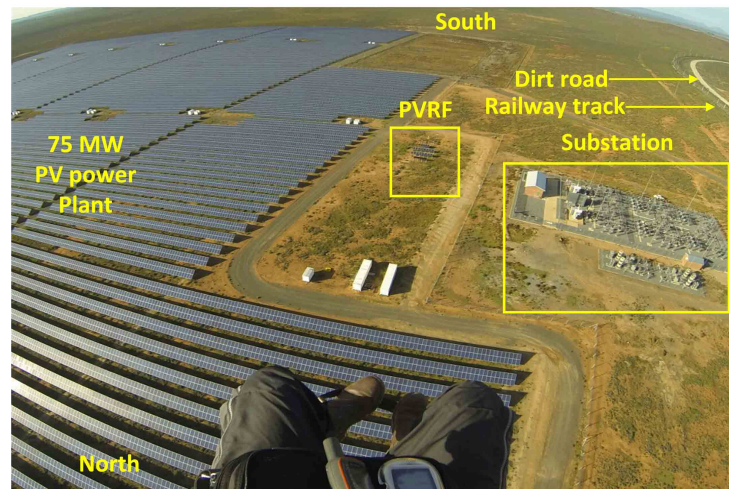


Figure 3.2: Aerial view of the surrounding environment of the research facility at Kalkbult.  
*Source:* Courtesy of Kurt Krog.

## 3.4 Design and construction of the research facility

### 3.4.1 General layout

The layout of the experimental site is displayed in Figure 3.3. The PVRF consists of the following primary features:

- 1 x Row of stationary Cadmium Telluride (Cd-Te) Thin-Film PV modules
- 2 x Rows of stationary Polycrystalline Silicon (pc-Si) PV modules
- 2 x Single-axis-trackers
- 1 x Pyranometer for irradiance measurements
- 1 x Weather station
- 1 x PV powered battery bank
- 1 x WiFi communication tower
- 24 x PV measurement stations

### 3.4.2 Photovoltaic modules

The research facility consists of both thin-film and pc-Si modules. Eight First-Solar manufactured Cd-Te Thin-Film modules are used, of which four are FS4100 models and the other four are FS4100A models [51]. The FS4100A has an anti-reflective coating, whereas the FS4100 does not. Although the thin-film modules are part of the PVRF, the analysis of these modules is not within the scope of this thesis. A total of 20 pc-Si modules are used of which each is a Renesola VirtusII JC255M-24/Bb module [52]. From observation, polycrystalline modules have thus far been the primary choice for the commercial PV sector of South Africa. Finally, four 300 W Renesola VirtusII JC300M-24/Abh pc-Si modules [53] are used to power the battery bank of the facility. These 300 W modules are however purely for charging the batteries. Tables 3.1 and 3.2 provide further details about the PV module characteristics.

Table 3.1: Electrical characteristics of the pc-Si JC255M modules as rated at STC conditions (AM 1.5, Irradiance 1000W/m<sup>2</sup>, Cell temp. 25°C).

PV module	P <sub>MPP</sub> [W]	V <sub>OC</sub> [V]	I <sub>SC</sub> [A]	V <sub>MPP</sub> [V]	I <sub>MPP</sub> [A]
JC255M-24/Bb	255 (±5 W)	37.5	8.86	30.4	8.39

Table 3.2: Temperature coefficients of the pc-Si JC255M modules.

PV module	P <sub>MPP</sub> [%/C°]	V <sub>OC</sub> [%/C°]	I <sub>SC</sub> [%/C°]
pc-Si JC255M-24/Bb	-0.4	-0.3	0.04

### 3.4.3 Design and implementation of stationary PV module rows

The PVRF consists of three north facing rows, for dust analysis of modules at fixed tilt angles. The stationary row furthest to the north, labelled as 'Thin Film Modules row 3' in Figure 3.3, is dedicated to the Cd-Te modules. However, as mentioned, the analysis of these PV modules do not fall within the scope of this thesis. The two remaining stationary rows, are dedicated for the pc-Si modules. The reason for selecting 16 of the pc-Si modules for the stationary topology, is due to the set research objectives of this thesis to be achieved.

The PV modules mounted on these structures are positioned at a tilt angle optimal for maximum energy yield. This tilt angle is determined with the theory presented by Figure 3.4. From this illustration, it is evident that the tilt angle determines the collective exposure of the module to irradiance, since the radiation component collected is dependant on the cosine of the angle ( $\lambda^\circ$ ) between the normal beam and the incident beam [43, p.35]. The exposed area of a module is determined by equation 3.1, with variable x as the PV module length,  $\lambda^\circ$  as the angle between the normal and incident irradiance components and  $\lambda^\circ$  as the module's tilt angle [43]:

$$PV \text{ Module Exposed Area} = x \cos \varepsilon \text{ [m}^2\text{]} \quad (3.1)$$

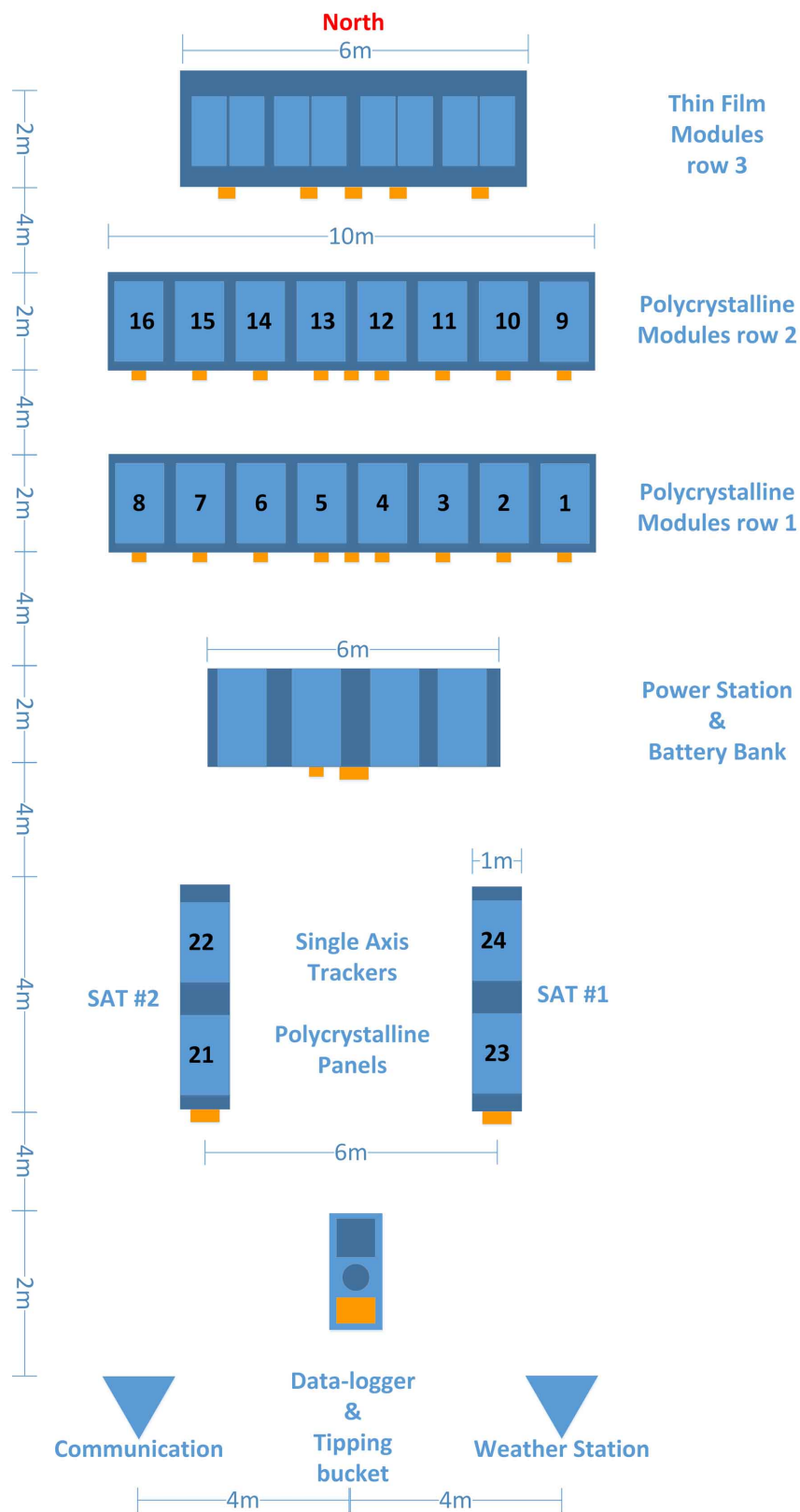


Figure 3.3: Layout of the PVRF (not to scale).

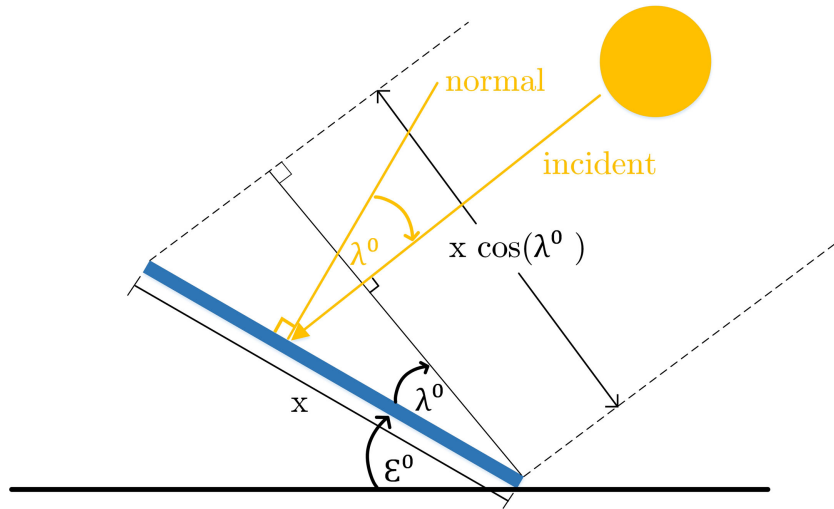


Figure 3.4: Illustration of how PV module placement determines the exposed module surface area. *Source:* Image redrawn as illustrated by R. Messenger and J. Ventre [43].

For optimal performance on any given day, a PV module should be mounted according to the relationship of equation 3.2 [44, p.196], which determines the module's tilt angle  $\varepsilon$  as indicated in Figure 3.4:

$$\varepsilon = 90^\circ - \beta_N \quad (3.2)$$

Where, in (3.2)  $\beta_N$  is determined by equation (3.3) [44, p.195]:

$$\beta_N = 90^\circ - L + \delta \quad (3.3)$$

$\beta_N$  represents the sun's altitude angle at solar noon, which is also the ideal tilt angle of a PV module, on that particular day of the year. However, for large (few hundred or more modules) PV systems it is impractical to adjust panels daily. Thus, for seasonal or yearly PV module tilt angle optimisation, a  $\delta$  average is chosen. A balance is found between the ideal module tilt angle for the summer and winter months in Kalkbult, by utilising the ideal tilt angle as on the 21st of March (day = 81) and September (day = 264). On these two days, the value of the solar declination angle  $\delta$  is calculated as:

$$\begin{aligned} \delta &= 23.45^\circ \sin \left[ \frac{360}{365}(n - 81) \right] \\ \delta &= 23.45^\circ \sin \left[ \frac{360}{365}(81 - 81) \right] = 0^\circ \\ \delta &= 23.45^\circ \sin \left[ \frac{360}{365}(264 - 81) \right] \simeq 0^\circ \end{aligned}$$

Therefore, from equation (3.3), the altitude angle of the sun at solar noon is equal to:

$$\beta_N = 90^\circ - L + \delta = 90^\circ - 30.161^\circ + 0^\circ = 59.839^\circ$$

The optimal tilt angle for the PVRF is determined with 3.2 as:



$$Tilt = \varepsilon^\circ = 90^\circ - \beta_N = 30.161^\circ$$

The three stationary rows and the PV modules of the battery bank are all tilted at an incline of  $\simeq 30^\circ$  as shown in Figure 3.5. This angle is also in agreement with the tilt angle of the 75 MW commercial PV power plant.



Figure 3.5: Image of PVRF and the three stationary north facing PV module rows, with thin-film modules in front and the polycrystalline modules behind.

It is within the aim of this research to simulate a real-world scenario, which is representative of what could be expected in a commercial PV system. Therefore, a decision is made to position the stationary module rows at a distance of 4 m from one another. This is approximately the same distance as that of the 75 MW PV power plant. At this distance, on the 21st of June, when the sunrise occurs at the latest possible morning hour, there will no longer be a risk of inter-row shading from approximately 08:00 AM. When sunset takes place, the modules will cast an inter-row shadow onto one another from about 16:45 PM. These clock times are calculated by making use of equation (3.4) to (3.12) in the same sequential order in which presented.

$$\delta = 23.45^\circ \left[ \frac{360}{365}(n - 81) \right] \quad (3.4)$$

$$B = \frac{360}{364}(n - 81) \quad (3.5)$$

$$E = 9.87 \sin 2B - 7.53 \cos B - 1.5 \sin B \quad (3.6)$$

$$ST[\text{min}] = CT[\text{min}] + \frac{4[\text{min}]}{1^\circ} (\text{Local Time Meridian} - \text{Local longitude})^\circ + E[\text{min}] \quad (3.7)$$

$$H = \left( \frac{15^\circ}{1[\text{hour}]} \right) (\text{Hours before solar noon}) \quad (3.8)$$

$$\beta = \sin^{-1}(\cos L \cos \delta \cos H + \sin L \sin \delta) \quad (3.9)$$

$$\Phi_S = \sin^{-1} \left( \frac{\cos \delta \sin H}{\cos \beta} \right) \quad (3.10)$$

$$L_s = \frac{y}{\tan(\beta)} \quad (3.11)$$

$$d = L_S \cos \Phi_S \quad (3.12)$$

From the equations listed above, the following values are known:

$n = 173$  (21 June)

*Local Time Meridian* =  $-30^\circ$

*Local longitude* =  $-24.132^\circ$

$y = (1.64 + 0.1) \sin(30.0^\circ) = 0.87$  [m], with  $y$  as the array height, calculated with the module length as 1.64 m and bird spike length of 0.1 m

The convention for the equations presented in this thesis, are that latitude angles in the Southern hemisphere are negative, and Longitude angles East of the Prime Meridian are negative.<sup>1</sup>

Triangular frames are designed and constructed from galvanised steel, so that the PV modules can be firmly mounted. These frames have a  $30^\circ$  tilt angle as illustrated in Figure 3.6 and are vertically adjustable to eliminate any horizontal offset, due to an uneven ground surface. Placed 2 m apart from one another, these frames are supported by a square concrete block at each foot of the frame, to provide a steady foundation. To ensure further stability, especially during harsh wind conditions, all of the frames are anchored to the ground with 3 mm steel cable (vineyard cable), fastened to a 1 m anchor pole, anchored in the ground. Two horizontal aluminium frames provide the necessary framework on which the PV modules are fastened to with clamps.

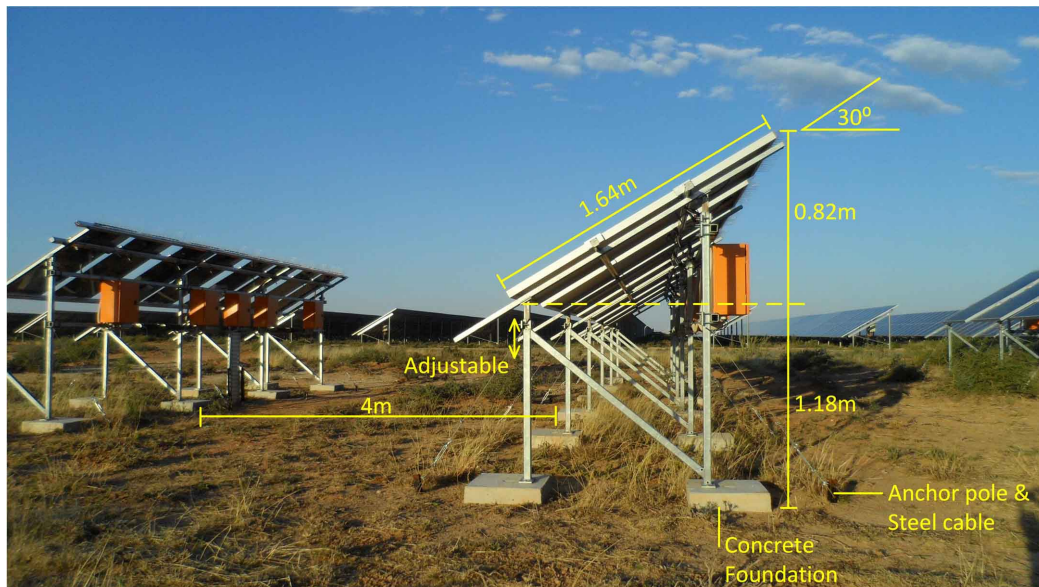


Figure 3.6: PV module layout and structure details of a stationary row.

<sup>1</sup>The internationally accepted norm is that latitudes north of the Equator and longitudes east of the Prime Meridian are regarded as positive. However, for this thesis, longitudes east of the prime meridian are regarded as negative.

### 3.4.3.1 Single Axis Tracker structural layout

The PVRF also consists of two single axis trackers, which provide an experimental platform for analysing the effects of dust deposition on tracking modules. Tracking the sun from east to west, the same 255 W Renesola PV modules [52] are used, as for the stationary rows. The trackers are also placed at a distance of 4 m south of the battery bank's stationary modules, as illustrated by Figure 3.7. The distance between the tracker axes from east to west is 6 m. This distance is selected to allow for more future experimental possibilities, such as low sun altitude experiments and etc. The SAT software design allows a user defined set-up to be made, which amongst other options, defines the theoretical distance between the PV modules. Thus, with the software set-up, the SAT system can be manipulated into thinking the inter-axis distance is only 4 m apart. However, for this research, the distance is maintained at 6 m. The primary goal, as mentioned, is to investigate the effects of dust soiling on tracker modules. By keeping the distance at 6 m, the hypothesis that SAT modules have a reduced level of dust deposition, compared to stationary modules can be tested for an exaggerated case, since the tracking modules are able to adopt a larger tilt angle, because of the 6 m inter-axis distance. If the results are in favour of the tracking system, then a proceeding experiment can determine the dust deposition at a shorter inter-module distance. However, should the trackers prove to be more prone to dust-accumulation, even for this exaggerated case where modules are allowed a higher degree of tilt, then a definitive conclusion can be made regarding such a result. Thus, no further testing would be required regarding this hypothesis/theory. All mechanical, electronic and software design and functionality is further discussed in detail in chapter 5.



Figure 3.7: Illustrative description of the SAT layout.

### 3.4.4 Battery storage

A battery bank is installed to allow the PVRF to operate at full capacity, 24 hours a day. The battery bank primarily consists of:

- 4 x VirtusII Polycrystalline 300W modules [53]
- 4 x 12V, 120AH AGM+Gel deep cycle valve-regulated lead-acid (VRLA) batteries [54]

- 1 x Victron Smart Solar Maximum Power Point (MPPT) Charge Controller [55]

Although configured to operate at 24 V, the battery array can also be set up to operate at 12 V, since all the devices are designed to be compatible with either a 12V or 24 V power supply. The battery bank is capable of supplying the PVRF with power for approximately 48 hours, without any received irradiance ( $0 \text{ W/m}^2$ ). The four 300 W pc-Si modules are connected in a parallel combination of two pairs of series connected modules. These modules are then connected to the MPPT charge controller. The charge controller is set-up to charge the 24 V battery topology at a float(resting) value of 27.6 V and an absorption (final 20% charge) setting of 28.8 V [55]. This voltage is of course translated to the battery connected devices as well, but all on-site devices are capable of receiving a 30 V or higher input. Therefore, this is not a problem.

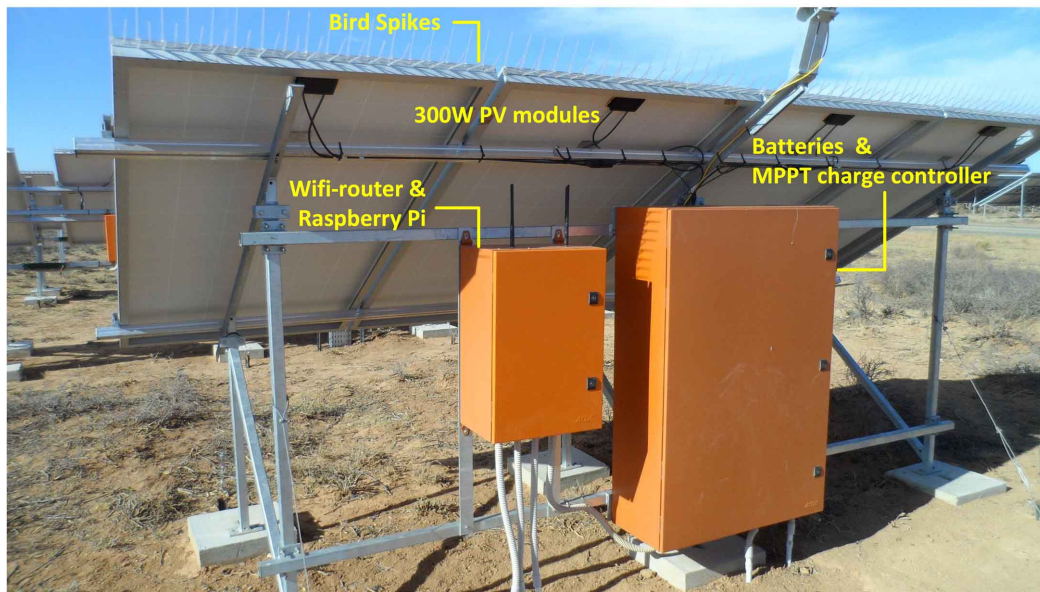


Figure 3.8: Standalone battery bank and wifi-communications box.

### 3.4.5 Communication

Effectively, the role of communication within the research facility is to allow remote system monitoring, upload data to an online database, as well provide a means for local inter-device communication.

#### Inter-device communication

A Raspberry-Pi (RPi) model B+ serves as the master device of the PVRF, responsible for handling both external and internal communications. All of the slave devices communicate through an RS-485 interface using the MODBUS protocol. The research facility's baud-rate is established at 9600 bits per second (b.p.s.). Slave device communication is performed by the master-device in either unicast (single slave communication) mode, or in broadcast mode, where data is sent to multiple slave devices simultaneously. For a more in depth description of the MODBUS protocol, please refer to any of the various online MODBUS user guides [56]. The RS-485 interface is chosen due to an effective communication distance of 1.2 km [57]. A Mylar screened cable is used to establish the physical connection between devices and is connected in a daisy chain configuration, since an open-ended star-network, with multiple end points, is not recommended as reflections within the cable may result in

data corruption [57]. Details concerning the online database data storage and acquisition are discussed in Chapter 7.4.

### On-line database and remote system monitoring

The hardware set-up that enables the effective cloud storage of the data collected on site, consists of a WiFi connection, established by a power-over-ethernet antenna, a WiFi router and an internet connection, provided by a local internet-service-provider. All of the data measured on-site is acquired by the master device and is then uploaded to an online database, where data is readily available for user interpretation. A remote system monitoring interface was developed and commands can be sent to the ActiveLoads, MasterController (MC) or the SATs by means of this interface. More details are provided in Chapter 7.4.

### 3.4.6 Meteorology instrumentation

The set-up of the instrumentation responsible for weather and irradiance measurements, has been done in accordance with the IEC61724 standard, which provides general guidelines for the procedures of electrical performance monitoring and analysis of PV systems. The calibration dates of the weather station and pyranometer are valid for the entire span of the research period presented by this thesis.

#### Weather station and rain gauge

Meteorological data is acquired with a Met-Station-One-485 (MSO-485) Weather Sensor (WS), manufactured by Met One Instruments Inc. [58], which is in accordance with the IEC61724 standards [59]. Rain fall is measured with a 372-series precipitation gauge (rain gauge) [60], also from Met One Instruments, which is essentially a tipping bucket, that tips for every 0.5 mm rainfall received. This WS provides the following data output via an RS-485 (Checksum data validation) serial communication:

Table 3.3: MSO weather sensor outputs

Measurement	Units	Measurement	Units
Wind speed	m/s	Ambient temperature	C°
Wind direction	0° – 360°	Humidity	0%-100%
Barometric pressure	500 – 1100 mbar	Rainfall	mm

The WS is orientated towards true North and is mounted at a height of 3 m. At this distance and height, influence on wind measurements from the PVRF's structures, is kept at a minimum. This location also complies with the IEC61724 standard, which requests that the WS is placed at a height and location representative of the array conditions. Wind speed is measured with a three cup anemometer and direction is determined with a lightweight vane tail.

#### Irradiance

Plane of array irradiance ( $G_{POA}$ ) [ $W/m^2$ ] is measured with a Kipp&Zonen SMP10 pyranometer [61]. The pyranometer is placed at the same 30° tilt angle as the fixed PV modules, as prescribed by the IEC61724 standard [59]. Data is provided by means of an RS-485 MOD-BUS serial output interface. Further technical detail with reference to the communication

and data collection process of the pyranometer, is provided in Chapter 4.6.4. Figure 3.9 shows how the instrument is mounted on the back of the frame of the battery bank, at a  $30^\circ$  tilt angle.



Figure 3.9: Pyranometer mounted at a  $30^\circ$  tilt angle.

## 3.5 PV measurement stations

### 3.5.1 Description

The research facility consists of individual stations, referred to as Photovoltaic Measurement Stations (PVMS). Each station operates individually and consists of a PV module, an ActiveLoad, a back-plate temperature sensor and a dumping resistor. The RPi, which serves as the master device of the entire PVRF, communicates with and collects data from each PVMS.

#### ActiveLoad

An intelligent device is employed to allow the extraction of Current-and-Voltage (I-V) measurements from a PV module. The device is known as an ActiveLoad (AL) and is developed by a previous Stellenbosch University, Master's degree student, Andreas T. Ndapuka [62]<sup>2</sup>. The AL also has addition an on-board SD-card storage functionality, to ensure the safe capture of collected data. The AL has two available modes of operation. Firstly, a Maximum Power Point (MPP) mode, which continuously extracts the available power from a PV module, whereas the I-V mode simply obtains the module's I-V curve measurements, recorded at specific time intervals. The AL does however allow for a combination of the two modes, so that the module delivers power and the I-V curve can be spontaneously recorded by the AL itself. Each AL is carefully calibrated to allow for accurate voltage and current measurements by the Analogue-to-Digital-Converters (ADC). In terms of operation, the AL's design is based on the principle of a DC-DC switch mode converter for power control [62, p.71]. The power delivered to the fixed dumping resistor  $R_{LOAD}$ , can thus be varied by controlling the duty cycle. This further allows the AL to extract an I-V curve, within two seconds,

<sup>2</sup>For more specifics regarding the design of the AL, refer to [62]. A second AL version was produced by Dr J. M. Strauss.

which ensures that irradiance and temperature measurements recorded can be regarded as instantaneous. This eliminates any uncertainty with regards to temperature and irradiance changes during the process of I-V curve extraction. The AL design parameters are displayed in Table 3.4. With a carefully conducted calibration process, it is determined with certainty that the AL device has a maximum measurement uncertainty of 0.5 %.

Table 3.4: ActiveLoad design parameters

Parameter	Value
Maximum input voltage:	100 V or 50 V
Maximum input current:	50 A/100 V or 10 A/50 V
Switching frequency:	40 kHz

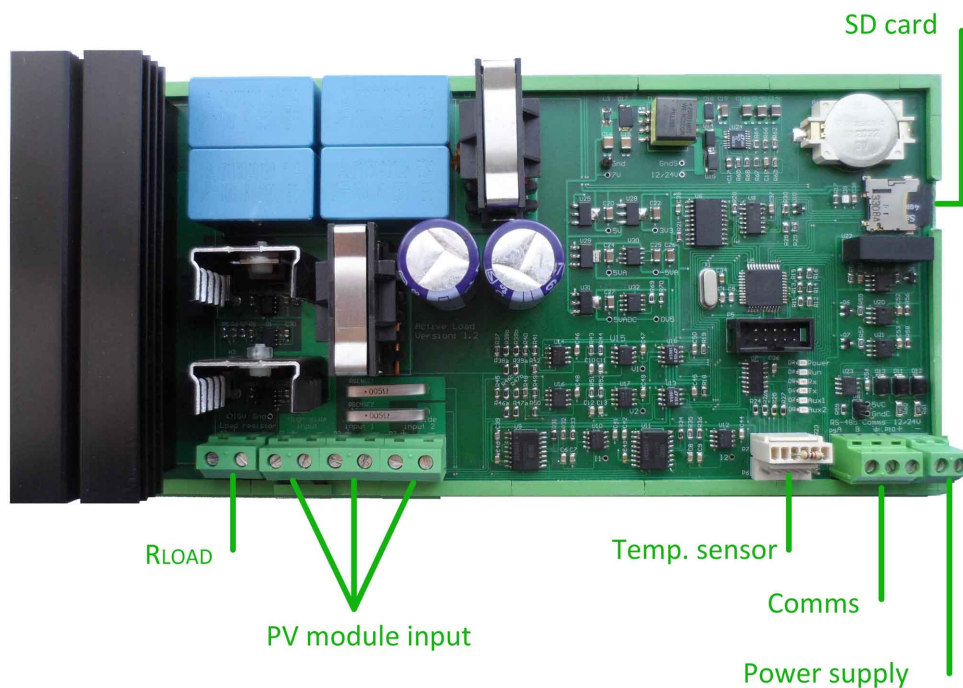


Figure 3.10: Active Load with main PCB board features.

The AL has the capability to operate in three different configurations:

- Configuration 1: Single PV module connection. Voltage and current measurements are derived for only one connected PV module.
- Configuration 2: Series connection of two PV modules. Measurement of two separate voltages and a common current.
- Configuration 3: Parallel connection of two PV modules. Measurement of two separate currents and a common voltage.

Configuration one is utilised for this thesis. The I-V curve is derived by the AL, by starting with an open-circuit (duty cycle  $D = 0\%$ ) condition and incrementing the duty cycle until a short-circuit condition ( $D = 100\%$ ) is reached. At each incremental duty cycle change,

the accompanying voltage and current is measured. A total of 20 discrete data samples are recorded for each I-V curve measurement, which is then saved onto the local SD-card. This data is also retrieved by the master device (RPi) which uploads the data to the online database. The sampling interval of the I-V-measurements can be varied from 1 min to 60 min. However, all of the ALs are configured to perform an I-V measurement every 10 minutes, as specified by the IEC61724 [59] standard. It is important to note that all I-V curve measurements are performed at the same instant by means of an on-board real-time-clock (RTC) on every AL, which keeps all of the PVMS synchronised. These clocks are also externally synchronised on a regular (every month) basis, by executing a software command on the RPi. Further, each I-V curve logged by the SD-card is provided a time stamp, to ensure that data comparisons are made for the same time instance. The AL also has a dedicated RS-485 (MODBUS) port for communication with the master-device as shown in Figure 3.10 and can communicate over a wide range of baud-rates, ranging from 2400 to 115200 b.p.s. The ALs are assigned and configured as presented by Table 3.5. As mentioned, the thin-film modules are not analysed by this thesis.

Table 3.5: ActiveLoad assignments.

ActiveLoads	PV modules	section	Configuration
#1 – 8	pc-Si	Stationary row 1	Config. mode 1
#9 – 16	pc-Si	Stationary row 2	Config. mode 1
#17 – 20	Cd-Te	Stationary row 3	Config. mode 3
#21 – 24	pc-Si	Tracker 1&2	Config. mode 1

### Dumping resistor

When the AL is set to operate in the MPP mode, or to extract an I-V curve from a module, the power is discharged into a dumping resistor. A TE750B01J high power wire wound resistor is connected to each AL, which is a  $1\ \Omega$ , 750 W resistor manufactured by TE connectivity [63]. Since each AL has a dedicated fixed resistor, all PV modules are exposed to the same load and a degree of uniformity is maintained amongst all of the PVMS, which eliminates any unwanted uncertainty regarding I-V curve measurements.

### PV module back-plate temperature sensor

As required by the IEC61724 standard, each PV module is fitted with a dedicated back-plate temperature sensor. A small temperature sensor circuit, designed by a previous student, Douw du Plessis, is used, which houses a high accuracy ADT7310 digital temp. sensor [64]. The temp. sensor operates as a 13-bit device, and digitizes the temperature to a  $0.0625^\circ$  resolution. Temperature readings are extracted by the AL via an SPI (Serial Peripheral Interface) connection and all temperatures are read simultaneously with the I-V curve measurement.

## 3.6 Construction of the PV research facility

The construction of the research facility and the installation of the electronics, is performed over the course of several installation phases. In total, several weeks are devoted to the planning of on-site activities and the procurement of equipment, building supplies and electronic components. This section provides a brief summary of the planning and the installations that are performed, to successfully implement the PVRF.



In terms of transportation, the distance from Stellenbosch to the Kalkbult site is approximately 785 km. All on-site activities are performed with the proper safety clothes and procedures, which include a hard hat, steel point shoes, reflective vest and pre-work safety inspections.

Phase one of construction is commenced during the week of 18-23 May, 2015. During this phase, the goal is to establish the basic framework for the PV module and electronic installations that will follow after this phase. This includes the installation of all PV module structures, foundations, metal enclosures, as well as underground PVC piping for the power and communication cables. Communication is also established with the WiFi network and the full battery bank installation is completed. Figure 3.11 illustrates some of these completed tasks.

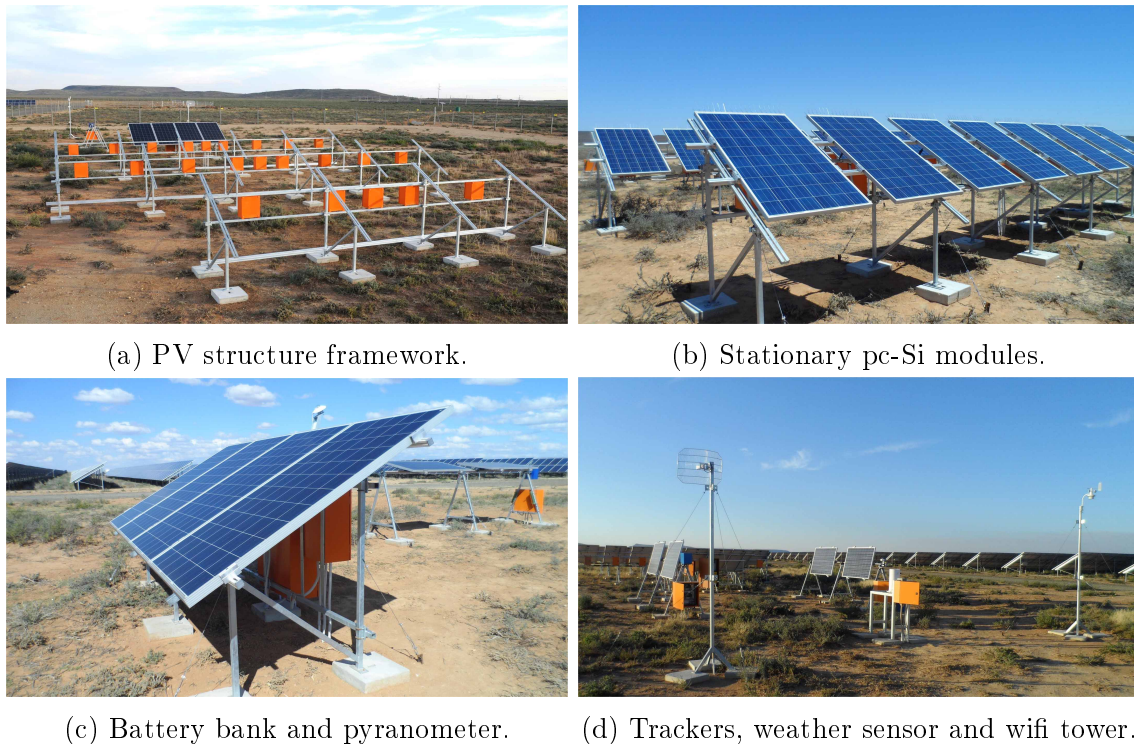


Figure 3.11: Installation of the research facility .

The objective of phase two (15-17 June 2015) is the anchoring of all structures. This is accomplished with one-meter anchor poles, steel vineyard cable and crosby clamps. In total 54 anchor poles are secured into the ground and fastened to the structure frames, as can be seen at the bottom of Figure 3.11b.

After the frames are securely anchored, phase three is executed during 28 July-1 August 2015. All stationary modules are installed, together with the 24x wire wound dumping resistors. Figure 3.11b illustrates the module installation.

With the necessary infrastructure installed, phase four (24-28 August 2015) is initiated. The main focus of this phase is the installation of all electronics, which includes the 24 AL stations, the Master-Controller (MC), pyranometer and the RPi. The orange enclosure boxes are connected with one another by means of PVC sheath, through which the power and communication cables are connected to the devices. The back-plate temp sensors, displayed by Fig. 3.12b are also installed and all wiring is completed in terms of communication and

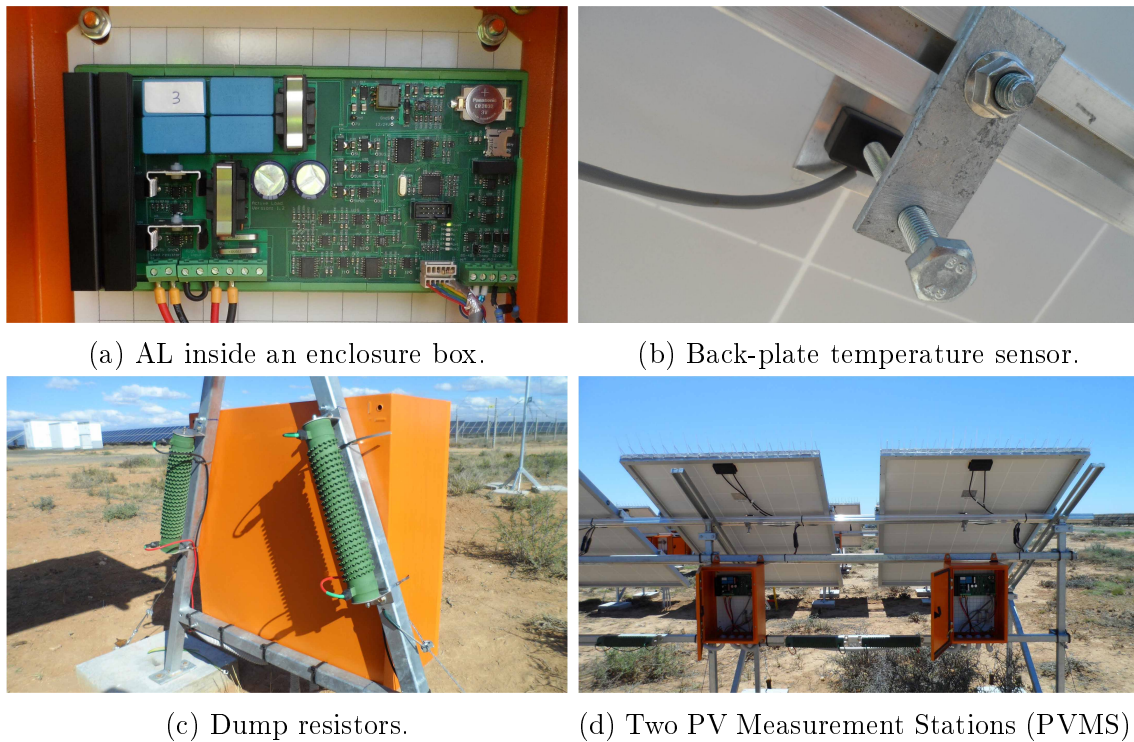


Figure 3.12: Installation of the measurement stations.

power. The dumping resistors are displayed by Fig. 3.12c and Figures 3.12d and 3.12a give show the set-up of the measurement stations.

Finally, the research facility is fully operational with the completion of phase 13 (30 May - 3 June 2016). This phase includes the final mechanical and electronic installation of the single-axis-tracking systems. There are of course several phases completed between phase four and thirteen, however these phases do not focus on the construction of the research facility, but are rather focused on operations and maintenance (O&M), PV module cleaning routines and further system integration.

A summary of the installation items is provided in Table A.2 to illustrate all of the main items required to complete the installation of the PVERF. For a full summary of phases one to fifteen, please refer to Appendix A, which also includes more photographs of the PVERF, to provide the reader with further visual insight.

### 3.7 Installation problems and solutions

As with any project, several unforeseen problems are encountered. After the installation of the electronics, the RS485 lines have several communication errors. This problem is related to grounding issues, which is solved by physically grounding the shield wire of the RS485 communication line, to the structures, which in turn are grounded via the anchor poles. Another challenge encountered is with the ALs connected to the SAT modules. As soon as power is received from the batteries, the ALs are subjected to what appears to be a voltage spike, which damages the AL power supply circuitry. To eliminate the effect of this voltage spike, a combination of two resistors and a TVS-diode is installed at each AL's terminal. This solution effectively suppresses the voltage spike and is installed at all of the AL devices for extra safety.

Another issue is with regards to the temperature sensors. Problems range from inconsistent

temp sensor readings to, measurements of consistently 0 C°. The solution is to solder on series resistors (47 ohm) onto the SPI Data-In and Data-Out lines of the temp-sensor chip. After implementation of this solution, all temperature readings are consistent.

In terms of the I-V curve measurements, it is realised that the AL current measurements clipped at 10 A. This is due to a faulty gain resistor on one of the ADC circuits. After replacement of the gain resistor to enable higher current measurements, the ALs are all recalibrated to ensure the accuracy of the I-V measurements.

The installation of the two trackers are also very challenging. The biggest challenge is to successfully mount the square PV module frames, onto the round aluminium axis. With the original clamps, the PV modules are not secure enough and new clamps are designed and installed. There is also a lot of mechanical play on the SATs due to a faulty coupling design. A new coupling is successfully implemented, so that the only play on the axis is due to the spacing between the gears. The initial step down worm-gear configuration ratio of 100:1 is also found to be inadequate, since, even with firmware adjustments to manipulate DC motor speed, it is found that the SAT speed of rotation is still too fast at 40 r.p.m. A second worm-gear is added, equating to a new step-down gear ratio of 5000:1, which proves very successful with a resulting tracking speed of 0.8 r.p.m. More about the mechanical design of the SAT is available in Chapter 5.4.5.

# Chapter 4

## MasterController and weather station data acquisition

### 4.1 Overview

This chapter starts with the conceptual hardware design of the MasterController (MC). This is followed by the actual implementation of the MC and how the corresponding slave devices are connected. Finally, the software design is presented and the details regarding the interchangeable role of the MC to either operate as a master or slave device.

### 4.2 Function of the MasterController

For the research requirements that are set for this thesis, an intelligent device is required, which collects meteorological data from on-site instruments and grants full user access to the collected data. In essence the MC serves the role of a data logger and a control board. In terms of the data logging functionality an accompanying data logger could have been bought for the weather station. However, this alternative restricts the option for customised features and does not provide maneuverability, which allows a more regulated and direct control over the active measurement devices. This is why the MC is primarily designed. The MC's on-board SD-card storage capability is also essential, since this allows data to be collected, even if an internet connection is momentarily unavailable.

The MC ultimately has the function to serve interchangeably as both a slave and a master device. As a slave device, the MC provides the RPi (master device) with acquired data from the WS, irradiance instruments and the trackers. This data is acquired when the MC operates as a master device. It is also the function of the MC to act as an intermediate device and permit a user to have communication with the single axis trackers. Also, regarding the trackers, should certain weather conditions arise such as rainfall or high wind speeds, then the MC must inform or take control of the SAT system, so that the trackers can react appropriately to these conditions.

In summary, the MC's design must enable the following functionality:

- Serve as a data-logger and routinely and at random, collect and process data from the connected slave devices.
- Provide on-board storage to avoid data loss during periods with no-internet connection.
- Serve as intermediate device for communication between the SATs and a user.

- Send collected and processed slave data to the RPi (master device).
- Inform the SATs of specific weather conditions, upon which these trackers must react.

## 4.3 Conceptual hardware design

### 4.3.1 General system overview

An illustration of the MC's conceptual hardware layout is presented Figure 4.1. As mentioned, the MC has two primary objectives, which are communication and data storage. Therefore, the focus of the hardware design is to fully utilise the two USART channels available on the microcontroller and secondly, to ensure the successful on-board storage of collected data.

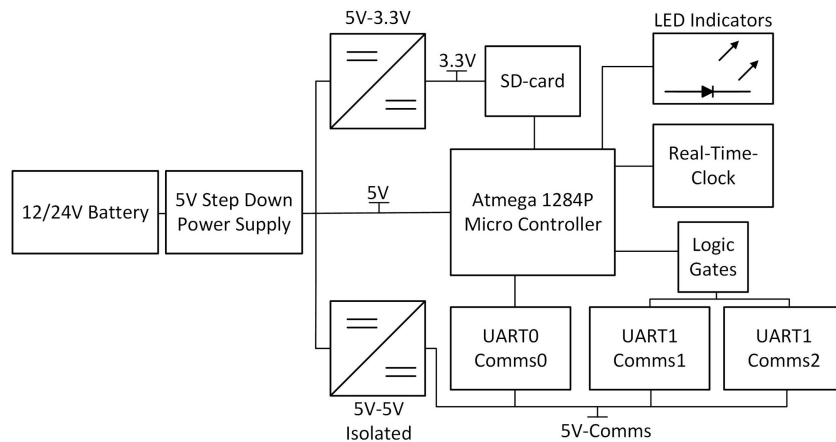


Figure 4.1: Conceptual hardware layout of the MC.

### 4.3.2 Microcontroller

The Microcontroller Unit (MCU) enables two-way communication, to allow the MC to operate as both a slave and a master device. Another goal of the MCU is to synchronise communication and data flow and to process and log all data received from slave devices. An ATmega 1284P-AU microcontroller, manufactured by Atmel, is used, which is an 8-bit AVR RISC-based microcontroller [65]. This MCU has 128 kB of ISP (In System Programmer) flash memory, 4 kB EEPROM, 16 kB SRAM and 32 general purpose I/O pins [65]. Two programmable serial USART lines are also available, which is one of the primary reasons for selecting this MCU. Figure 4.1 presents the interaction of the MCU with the other components. Communication with the SD-card, the RTC and the MCU is enabled by an SPI (Serial Peripheral Interface) communication line.

A 5V input, which is provided by the step-down power supply circuitry, supplies the MCU with power. An external clock source of 20 MHz is established by an HC49-4H quartz crystal [66], connected to pins XTAL1 and XTAL2 and two 22 pF capacitors, as displayed in Figure 4.2. A six pin header is connected to the MISO, MOSI, Reset, SCK, GND and 5V supply pins of the MCU. This provides the AVRISP mk2 in-system programmer [67] with the necessary connection on the MC's printed-circuit-board (PCB), so that code can be loaded onto the MCU. Details regarding the electrical characteristics of the ATmega 1284P are presented in Table 4.1.

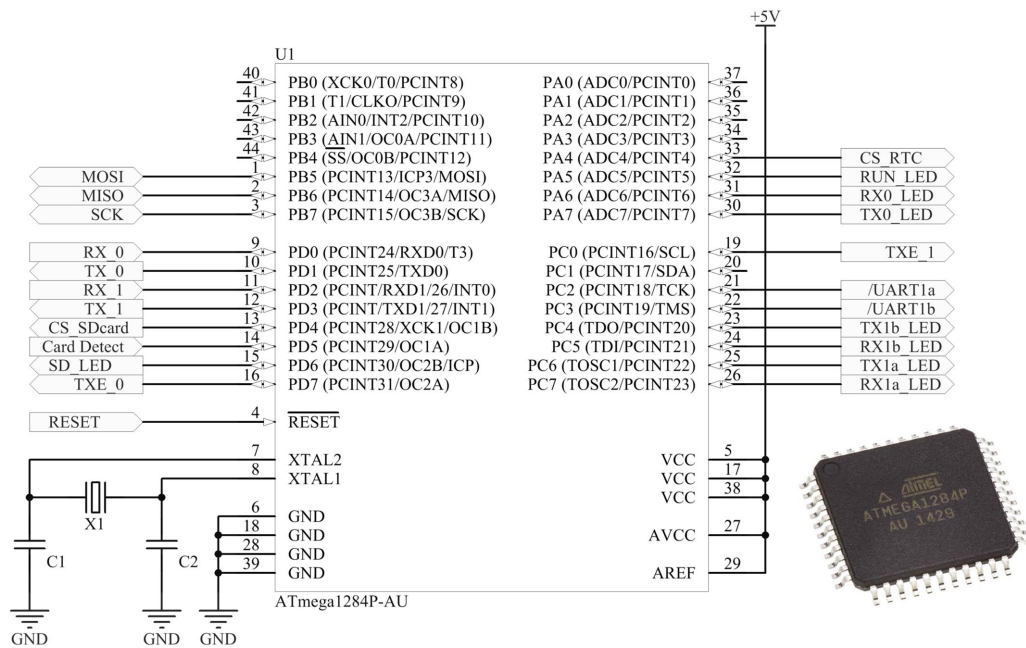


Figure 4.2: Schematic pin allocation of microcontroller and externally connected 20 MHz crystal. *Source*: MCU image as provided by [68].

Table 4.1: Short summary of the microcontroller specifications .

Microcontroller specifications			
20 MHz clock speed (max)	2 x USART channels	5 V Supply	$V_{OL} = 0.9 V(max)$
SPI channel	8 bit data bus width	10 bit ADC	$V_{OH} = 4.2 V(min)$
4 kB EEPROM	128 kB Flash memory	16 kB RAM	$V_{IL} = 1.5 V(max)$
JTAG interface	10.1 x 10.1 x 1.05mm	32 x I/O pins	$V_{IH} = 3 V(min)$

### 4.3.3 Power supply and voltage sources

As mentioned, the battery bank supplies power to all the devices. The MC's power supply is designed to allow a DC input battery configuration voltage of either 12 V or 24 V. All of the components on the MC require either a 5 V or a 3.3 V supply voltage. An MC34063A step down switching regulator [69], converts the 12/24 V battery input to a stable 5 V, 500 mA supply voltage. This power supply is found to be more than adequate to allow the successful operation of the components which make up the MC. With testing, it is also found that this switching regulator can operate successfully for input voltages ranging from approximately 7 V up to 40 V. Figure 4.3 presents the circuit layout and the desired 5 V output voltage is determined with equation (4.1). As seen from 4.1, the values of the resistors R44 and R45 are chosen as 3.6 k $\Omega$  and 1.2 k $\Omega$ . A combination of a 220  $\mu$ F [70] and 2.2  $\mu$ F inductor is added as displayed in Figure 4.3 for increased output stability, as recommended by the data sheet. The 3.3 V supply voltage is delivered by a Texas Instruments LM1117, 800 mA linear regulator [71].

$$|V_{OUT}| = 1.25 \left( 1 + \frac{R44}{R45} \right) = 1.25 \left( 1 + \frac{3.6k}{1.2k} \right) = 5 V \quad (4.1)$$

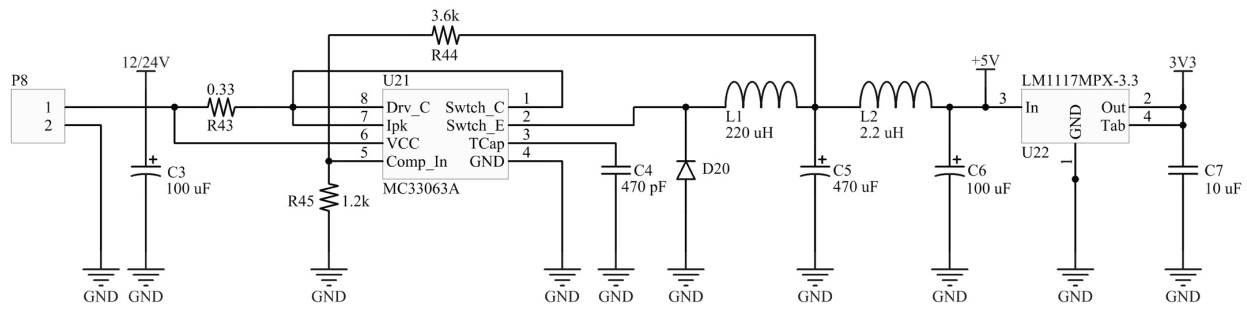


Figure 4.3: Power supply circuit layout of MC, as recommended by the data sheet[69, p.7], which delivers a 5V, 500mA output.

#### 4.3.4 USART communication and RS485 circuit

As mentioned, because the MC operates as either a slave or master device, two communication lines are established. This is achieved with the two built in USART (Universal Synchronous and Asynchronous serial Receiver and Transmitter) lines, each with a dedicated receive (RXD0, RXD1) and transmit (TXD0, TXD1) pin. This conceptual design is illustrated in Figure 4.4. USART0 is dedicated to the master device (RPI), which is thus used when the MC itself operates in slave mode. However, when communication is initiated with the slave devices, the MC is in master mode and USART1 is used. However, USART1 is further divided into two RS485 communication ports, namely Comms1 and Comms2, to allow two lines of communication for the slave devices. This is done so that the MSO-485 weather sensor, which does not follow the MODBUS protocol, is separated from the other RS485 MODBUS devices.

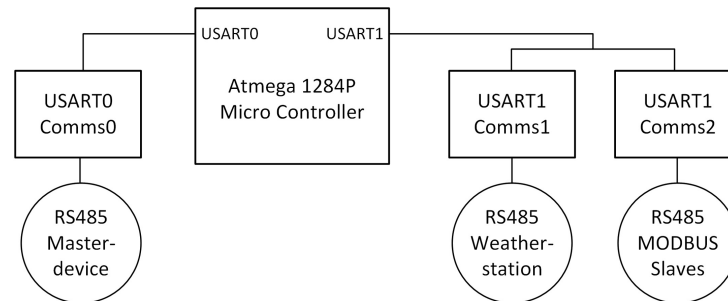


Figure 4.4: Fig: Illustration of the dedicated USART lines of the MCU.

To make the transition from the USART of the MCU to the RS485 communication standard, the circuit presented by Figure 4.5 is designed. This circuit is originally designed and tested by Dr J. M. Strauss. An Exar manufactured SP485E chip is used, which is a half duplex transceiver [72]. Thus, transmission and reception occurs alternately.

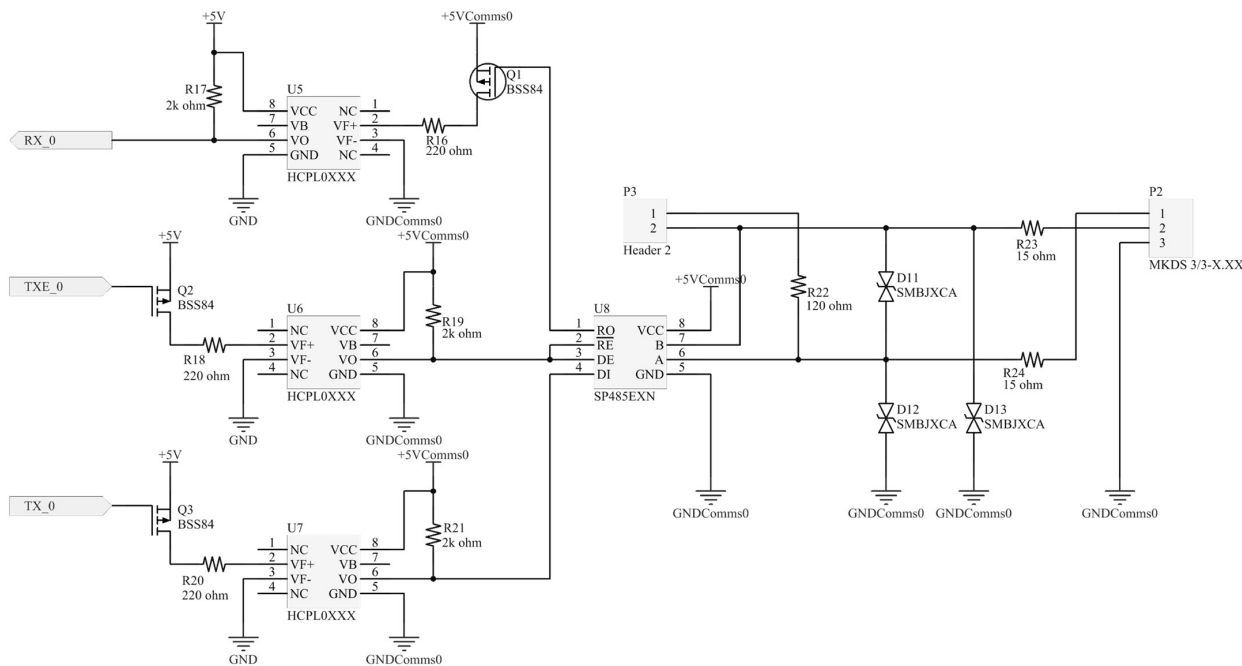


Figure 4.5: PCB schematic of the communications circuit design, which provides isolated USART signals to the RS485 transceiver.

Starting from the right hand side of the circuit, signals leave and enter the board from the three pin header P2, dedicated to the three RS485 lines A, B and Shield. To match the RS485 line’s characteristic impedance, provision is made for a 120  $\Omega$  terminating resistor, activated when a jumper is inserted at the two-pin header (P3). Three bi-directional SMBJ6.5CA TVS (Transient Voltage Suppression) diodes [73] are used for protection against voltage spikes that may be induced. With each TVS diode’s 12.3 V clamping voltage, the SP485E chip, which can withstand  $\pm 15$  V on its driver and receiver input and output, is well protected. In the event of a TVS diode activated by a voltage spike, two 15  $\Omega$  resistors are added in series (R23, R24), with the A and B lines, to assist the TVS diodes with current flow.

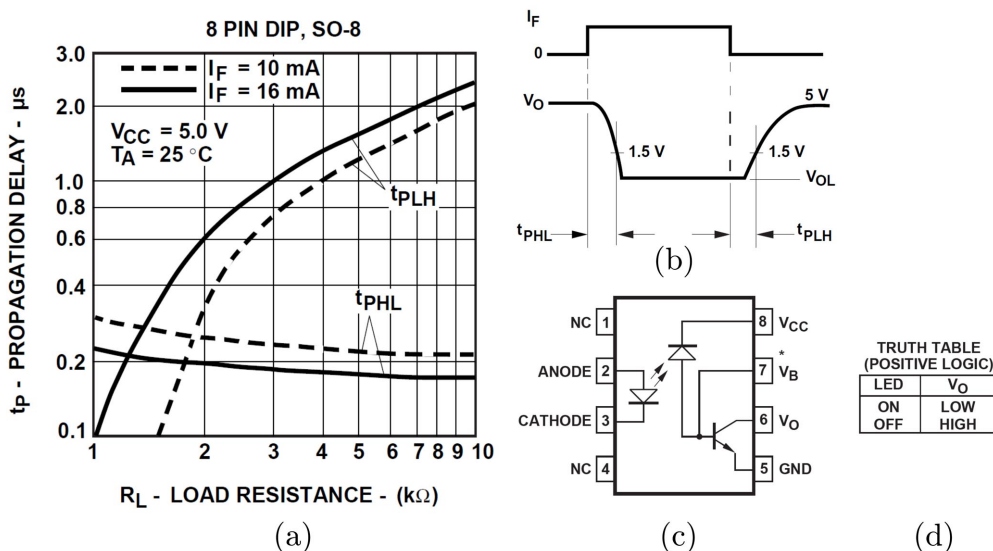


Figure 4.6: Data sheet information of the HCPL0501 optocoupler. a) Relationship between propagation delay and the load-resistance, b) Illustration of the  $t_{PLH}$  and  $t_{PHL}$  time delay, c) Circuit layout of the HCPL0501 IC, d) Optocoupler truth table logic [74, pp. 1, 14, 17].



As a precaution to eliminate noise, the RS485 communication hardware is isolated from the rest of the PCB. This is achieved with an isolated TMA0505S 5 V, DC-DC converter [75], a separate PCB ground plane and HCPL0501 diode-transistor optocouplers [74], to separate the TX, RX and TXE signals. For these optocouplers, to avoid an imbalanced propagation delay, the  $t_{PLH}$  and  $t_{PHL}$  values must be more or less the same, as displayed in Figure 4.6b. Therefore, as seen in Figure 4.6a, the goal is to choose the load resistance, so that the  $t_{PLH}$  and  $t_{PHL}$  values intersect with one another and the propagation delay is the same for the rise and fall time of the applied signal.

According to the truth table in Figure 4.6d, when a logic one is sent from the MCU to the optocoupler, a logic low will be the output and vice versa. Thus, a BSS84 P-channel MOSFET [76] is used to adapt the RX and TX signals to this logic. The circuit layout of an optocoupler (all are the same), connected to the SP485EE chip is displayed in Figure 4.7. An  $I_F$  current value of 10 mA is chosen for the design, determined from Figure 4.6a. According to the optocoupler's data sheet [74] this value results in a 1.5 V (typical) voltage drop over the diode,  $V_F$ . Also, according to the BSS84 MOSFET's data sheet (FigureB.1), the value of  $R_{DS}$  is  $\sim 6 \text{ m}\Omega$  for an  $I_D$  current of  $\sim 10 \text{ mA}$  and a  $V_{GS}$  value of -5 V. Thus, the  $V_{DS}$  value is determined as  $-0.5\text{V}$  from the MOSFET data sheet [76]. The value of  $R_1$ , in Figure 4.7 is determined with basic circuit analysis as:

$$-5V + V_{SD} + V_{R1} + V_F = 0 \quad (4.2)$$

$$-5V + V_{SD} + I_F R_1 + V_F = 0 \quad (4.3)$$

$$R_1 = \frac{5V - V_{SD} - V_F}{I_F} \quad (4.4)$$

With  $I_F$  selected as 10 mA,  $V_F$  as 1.5 V and  $V_{SD}$  as 0.5 V,  $R_1$  is determined with (4.4) as 300  $\Omega$ . However,  $R_1$  is selected as 220  $\Omega$  for the actual implementation, which did not cause any issues in terms of propagation delays.

According to the HCPL0501 datasheet (Figure 4.6a) the value of the RL resistor ( $R_2$ ) must be  $\sim 2\text{k}\Omega$ , for an  $I_F$  value of 10 mA. The optocoupler's signal output low is a max. of 0.5V, which is within the SP485EE's 0.8 V max. limit for low input voltages. The signal output high value is 5V, which is within the minimum 2 V input high of the SP485EE. The SP485EE chip allows data to be transmitted, when the DE (Data Enable) input is high. When data is received from another device, the TXE (Transmit Enable) must be low, thus enabling the  $\overline{RE}$  (Receiver Output Enable). With regards to data received from the A and B lines, logic values are defines as:

$$V_A - V_B \geq 0.2 = \text{logic high} \quad (4.5)$$

$$V_A - V_B \leq -0.2 = \text{logic low} \quad (4.6)$$

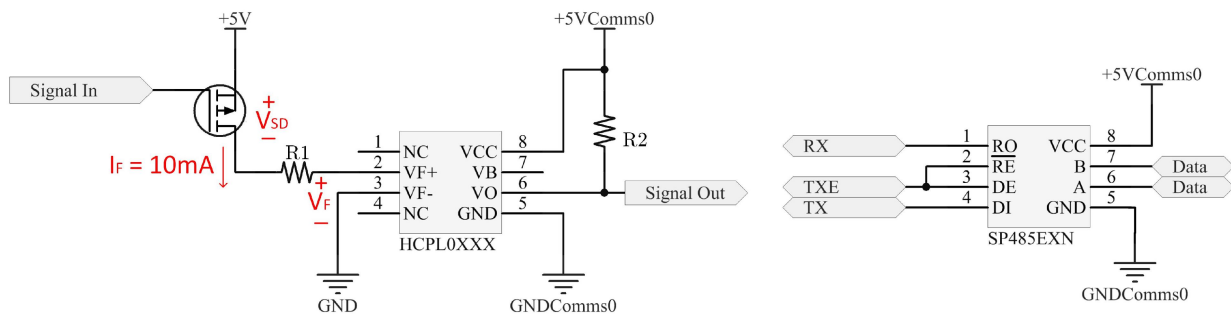


Figure 4.7: Schematic layout of the optocoupler (left) and the SP485EEN chip (right). Data flow is also indicated.

To separate data transmitted and received over USART1 Comms1 and Comms2, a combination of two 74LVC86A Quad XOR gates [77] and a 74LCX08[78] AND logic gate are used. The integration and operation of the XOR-logic gates, AND-logic gate and the USART circuit (as presented in Figure 4.5) is displayed in Figure 4.8. Table 4.2 only indicates the operation of UART1a (Comms1), but UART1b (Comms2) functions exactly the same, however when UART1b is active, the opposite logic low and high levels must be assigned to the UART1a and UART1b inputs.

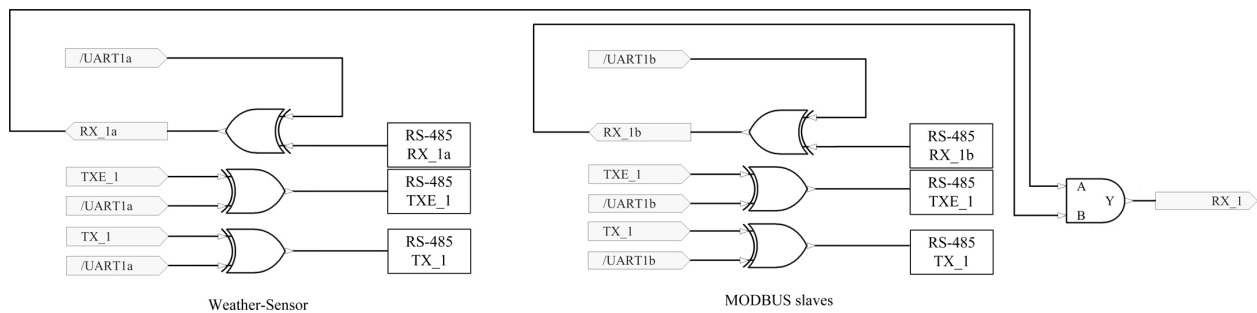


Figure 4.8: Circuit design of separating the USART1 channel into two separate channels Comms1 (UART1a) and Comms2 (UART1b).

Table 4.2: Logic truth table of the UART1 Comms1 (UART1a) channel.

UART1a	UART1b	RX_1a	TXE_1	TX_1	RS485 TXE_1	RS485 TX_1	RS485 RX_1a
Received data over UART1a from weather sensor							
0	1	Value	0	X	0	X	Value
0	1	Vlaue	0	X	0	X	Value
Transmit data over UART1a to weather sensor							
0	1	X	1	Value	1	Value	X
0	1	X	1	Value	1	Value	X

### 4.3.5 SD card

In the event of an absent internet connection, the RPi will not be able to upload the data acquired from the MC to the on-line database. The MC’s microcontroller also does not



### 4.3.6 Real time clock

As mentioned, the I-V curves are measured and logged, at an exact moment in time, together with the accompanying meteorological data at that particular moment in time. Thus, to ensure the MC is synchronised with the other devices, a DS3234 real-time-clock (RTC) [82] is used. The RTC maintains seconds, minutes, hours, days, date, month, and year information, which accounts for leap year adjustments. A 3 V external battery (V-BAT) also ensures the RTC stays active when power is removed. Access to the RTC is established with an SPI connection, which allows multiple byte transfers within one Chip Select (CS) low period. The SPI on the DS3234 interface is accessible whenever the power supply is above the V-BAT supply of 3V, which is supplied by a Panasonic CR2032 Coin Battery [82]. The RTC is selected to run in 24hr mode.

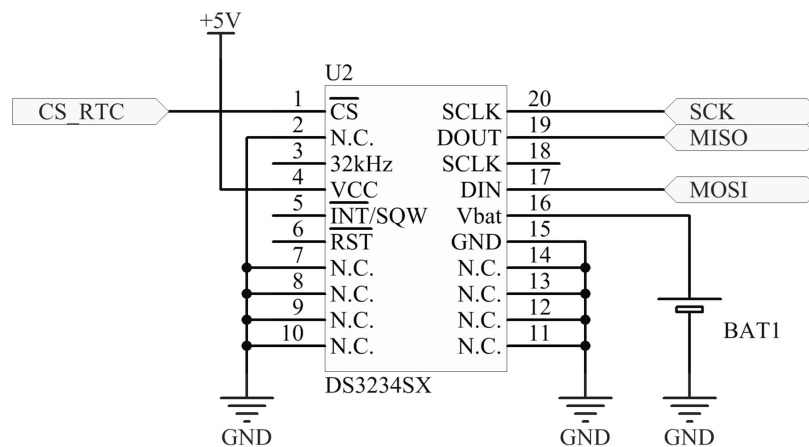


Figure 4.10: Circuit design of the RTC with SPI connections indicated.

## 4.4 Printed circuit board design

A printed PCB design is created with the Altium Designer 14.3 software package, as displayed in Figure 4.11. From the PCB design the three communication ports can be clearly seen, as well as the isolation of the RS485 circuitry from the rest of the PCB board. All of the relevant PCB design schematics are provided in Appendix B.2.

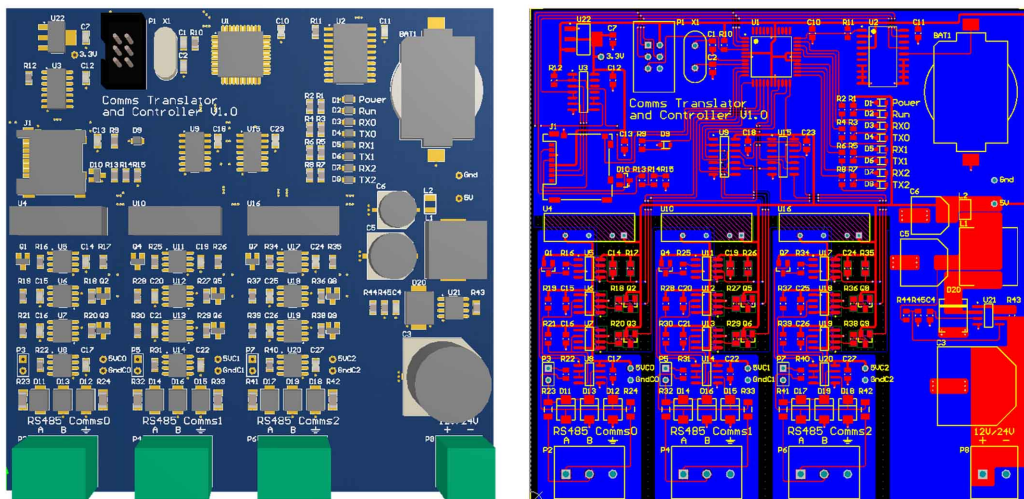


Figure 4.11: PCB circuit design of the MC circuit board.

## 4.5 MasterController set up and connection

### Weather station connection

The physical connection of the WS, MC and rain-gauge is illustrated by Figure 4.12. As seen, the weather station receives power from the battery bank, which is where the MC also receives its power from. It should be noted that the WS's RS485 MODBUS connections must be swapped so that MODBUS connection A and B connects to the MC board's RS485 Comms1, lines B and A, respectively. This is due to the SP485 [72] chip, that uses a different connection reference, which is opposite to that of the WS's RS485 line allocation.

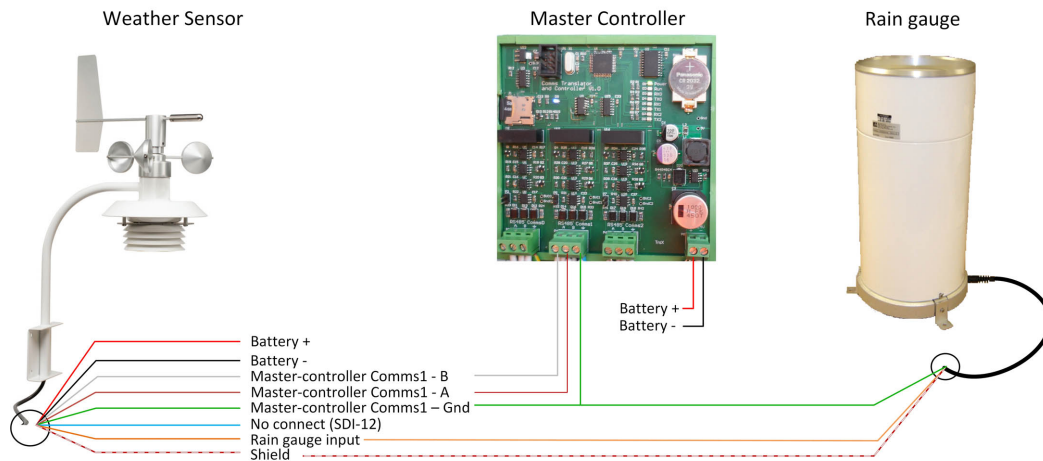


Figure 4.12: Cable connection diagram of the MSO weather sensor, the master-controller and the 372C rain gauge. *Source:* WS and rain gauge images extracted from data sheets [58, 60]

### Connection of irradiance instruments

The MC's design permits GHI and DNI to be collected from a Kipp&Zonnen SMP10 pyranometer and a SHP1 pyrliometer, respectively. These instruments are connected to the MC's RS485 Comms2 port, as indicated in Figure 4.13. It should once again be noted that, for the same reason as mentioned in section 4.5, the MODBUS A and B line connections, must be swapped. The shield-ground connection of the pyranometer is connected with the research-facility's common ground. Only one pyranometer is installed in the research facility and during the research period, a pyrliometer is not utilised.

### Communication set up with the trackers

With two SATs installed, the trackers connect with the MC's RS485 Comms2 port, as demonstrated in Figure4.14.

### Connection with the RPi and WiFi-router

User access to the MC and the SATs, is provided by the RPi, which is connected to a WiFi-router. As presented by Figure4.15, the MC's RS485 Comms0 port is dedicated to the master-device, which communicates spontaneously with the MC.

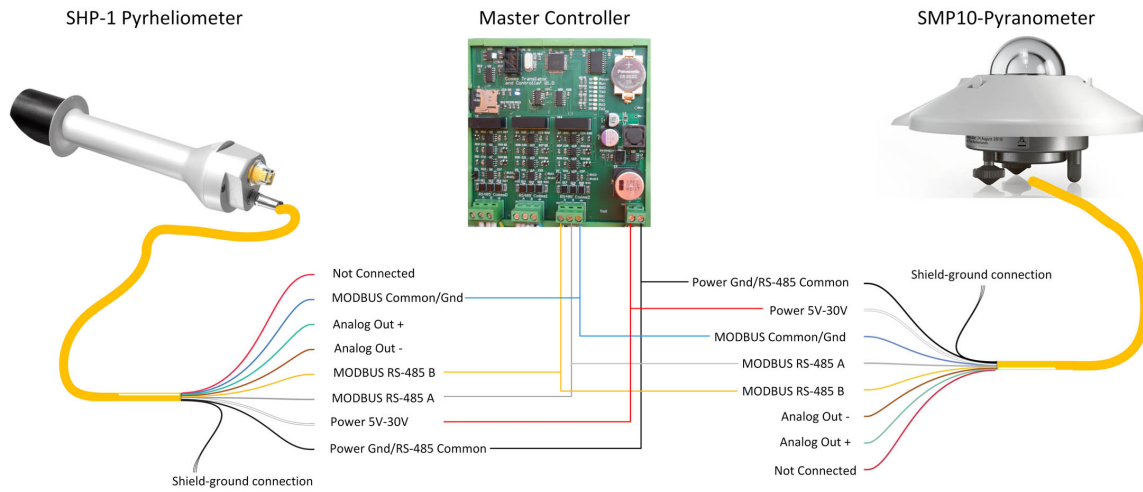


Figure 4.13: Cable connection diagram of the SMP10 pyranometer and the SHP1 Pyrheliometer. *Source:* Pictures extracted from data-sheets [61, 83].

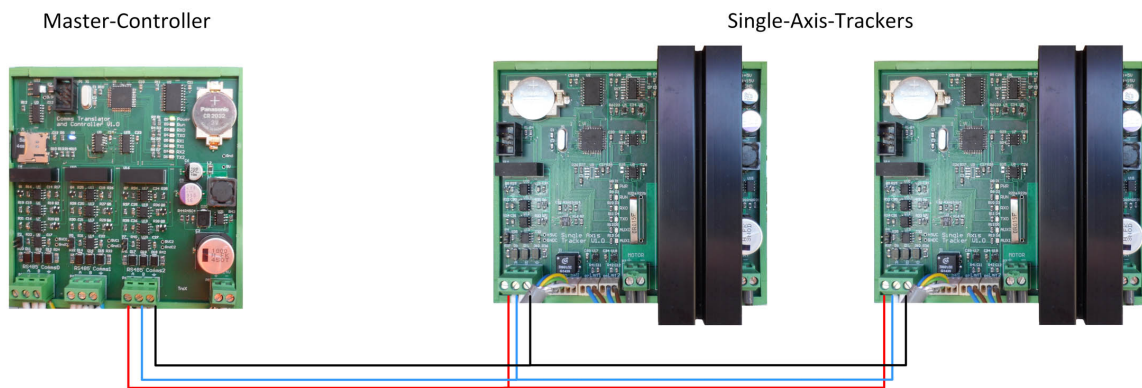


Figure 4.14: Physical connection of the MC and the single axis trackers.

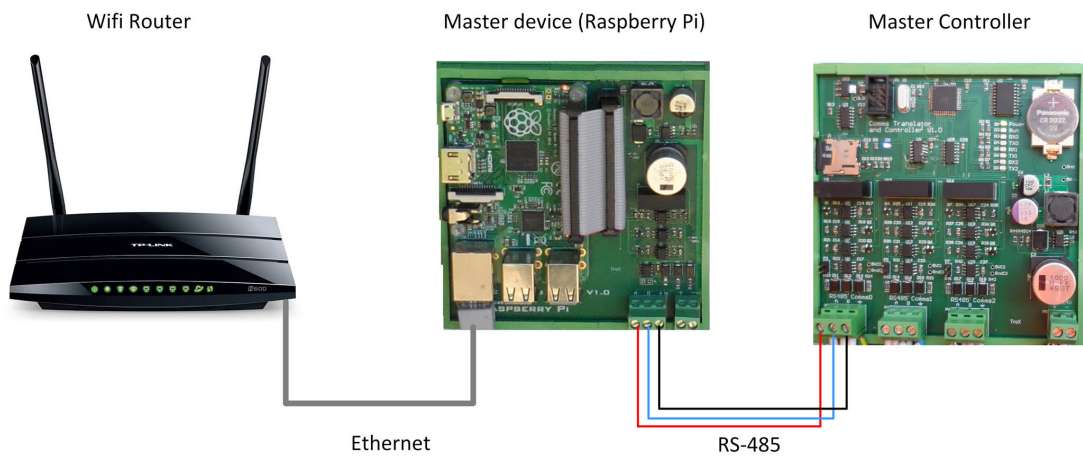


Figure 4.15: Communication between the master-device, MC and user. *Source:* WiFi-router as found at [84].

## 4.6 Detailed Software Design

### 4.6.1 Programming the MCU

Atmel-studio 6.2 is the integrated development platform, used to write, build and debug all code, which is written in the C programming language. Firmware is programmed onto the flash memory, EEPROM and fuses by means of the SPI interface, via an AVRISP mk2 in-system programmer [67].

### 4.6.2 Overview of data retrieval

The software set-up of the MC enables data to be collected from a total of nine slave devices, which consists of one WS, three pyranometers, one pyrheliometer, three SATs and one double-axis-tracker (DAT). Data is requested from the MC's active slave devices, at a sample-period of five seconds, which provides enough time for the maximum number of slaves to effectively reply to the MC. Data acquired from the slave devices is processed and at the end of a log interval, is stored onto the on-board SD-card. The log interval is user defined and simply refers to the amount of time (0 - 60 minutes) that has to pass, before the acquired data is logged as a CSV (comma separated values) file, onto the SD-card. The MC's log interval is set at one minute for this research period. The RPi then acquires the locally stored data from the MC and uploads the data onto the on-line database.

### 4.6.3 USART communication

The USART is a built in functionality of the MCU that only requires a low level set up. The initialization process consists of setting the baud rate, frame format and enabling the receiver and transmitter. The frame format is set up as: 1 start bit, 8 data bits, no parity, one stop bit and a default baud rate of 9600 b.p.s. Upon start up, the baud rate value is read from the EEPROM. Data is sent and received asynchronously, with the USART set to operate in the asynchronous-normal mode [85, p.170]. Only the USART initialisation and implementation is shortly discussed, since the theory behind the USART's operation is thoroughly discussed in [85].

#### USART0

Before the USART can be utilised, the baud rate is set in the UBRRn (USART Baud Rate Register) which is calculated with equation 4.9 [85, p.170].

$$BAUD = \frac{f_{osc}}{16(UBRRn + 1)} \quad (4.9)$$

With  $f_{osc}$  as the 20 MHz external clock frequency, UBRRn is set as 129 for a 9600 b.p.s. baud rate.

The USART communication is interrupt driven with TX and RX interrupt vectors dedicated to each USART. The USART0 receive interrupt is triggered when the master device sends a request to the MC, placing the MC in slave mode. The receive buffer (RxBuf0) is loaded with the data received from the master device, which is captured in the UDR0 register. The interrupt is triggered for each byte received. As according to the MODBUS protocol, there must always be  $3\frac{1}{2}$  characters (28 bits) worth of dead time before and after data is sent or received, as displayed in Figure 4.16. This ensures that the receiving device can distinguish between two different packets of data, as well as allow the devices to respond within enough

time. A dedicated software time-out-counter keeps track of the time elapsed, between bytes received. This process is displayed in Figure 4.17.

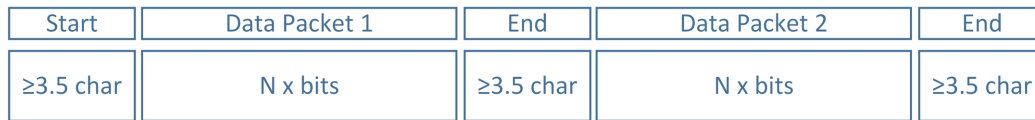
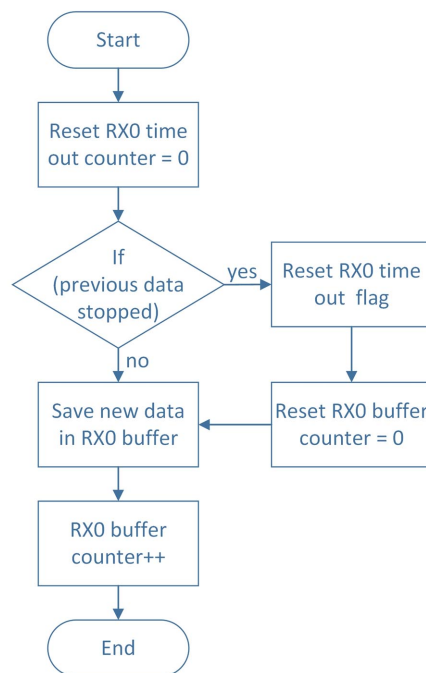


Figure 4.16: MODBUS information exchange structure, with delays between data packets.

USART0 receive interrupt, program flow.



USART0 transmit interrupt, program flow.

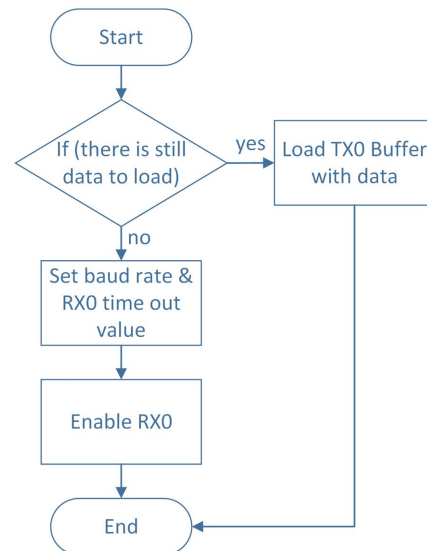


Figure 4.17: USART 0 transmit and receive program flow, with MC operating as a slave device.

## USART1

When a data request is transmitted by the MC (in master mode) to a slave device, the slave device responds and the MC's USART1 receive interrupt vector executes. While the MC is still receiving information, the receive-buffer (RxBuf1) is loaded with the new incoming data, read from the UDR1 register. A counter is used to keep track of the elapsed time between each byte that is received. When data is sent via USART1, data is loaded into the UDR1 register which executes the USART1 transmit interrupt vector. This process of data transmission and reception over USART1, is displayed in Figure 4.18. The MC only listens on the USART1 line, once it has completed the data transmission to the slaves. Should there be no reply from a slave device, the USART1 transmit-time-out-counter will exceed the predetermined value and the USART1 transmit-time-out-flag will be set, which allows the MC to abort communication with the intended device.



Transmit interrupt, program flow UART 1.

UART1 receive interrupt, program flow.

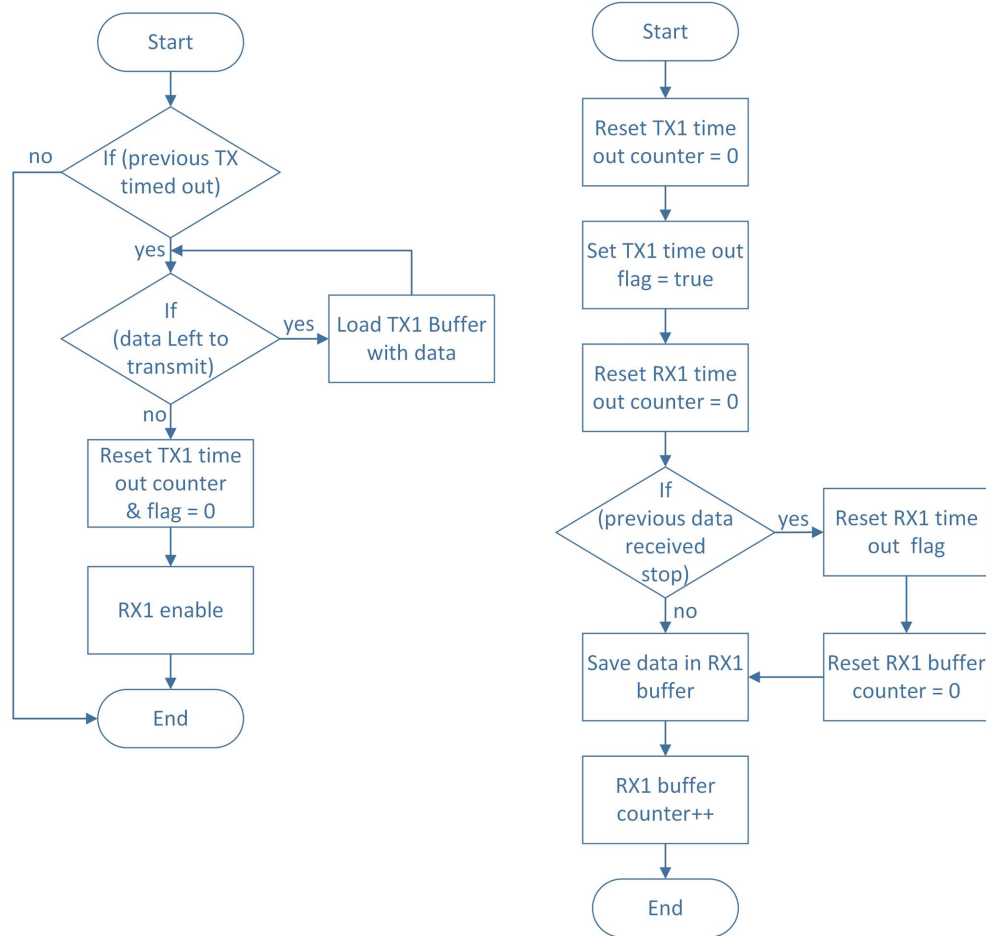


Figure 4.18: USART 1 transmit and receive program flow, with MC operating as a master device.

#### 4.6.4 MC slave device data acquisition and processing

Specific addresses are reserved for certain devices as presented by Table 4.3. When the MC operates in broadcast mode, address zero is used to communicate with all slave devices simultaneously. The universal address, 255, is used to initiate communication with the MC, only when it is removed from the system and a user has direct access to the MC device alone. This address is mainly used to configure the MC for the first time, before it is integrated with the system. Address 10 is reserved for the Remote-Supply-Switch (RSS), which is not a data-retrieval device, but simply a device which enables the remote hardware reset of the WS, if a reset is required for some reason.

Table 4.3: Reserved addresses for specific devices and functionality.

Device	WS	Pyrano.	Pyrhelio.	SAT	DAT	RSS	All Call	Universal
Address	1	2, 3, 4	5	6, 7, 8	9	10	0	255

#### USART software set up and interface

With the USART setup and software infrastructure implemented for the communication, as explained in section 4.6.3, the process of data acquisition can commence. The procedure

for collecting data from the slave devices is illustrated by Figure 4.19. All slave data is categorised into two sections:

- New-slave-data: This refers to the latest sample interval (every 5 seconds) data retrieved.
- Interval-slave-data: This refers to the processed data collected over the time span of one log interval (every 1 minute).

As mentioned, if data collection is activated, the MC obtains the 'New-slave-data' from the active slave devices, at a sample rate of five seconds. This data is then processed (determine average, max. and min. values) and logged with a time stamp as 'Interval-slave-data', onto the SD-card at one minute log intervals. With the log interval of one minute and a sampling-period of five seconds, ( $60\text{sec}/5\text{sec} = 12$ ) 12 data samples are recorded per log interval. The user can exercise the option to request New-slave-data at random, thus providing close to a real-time feed of the most recent on-site measurements retrieved by the MC. A user can also access the Interval-slave-data, which is uploaded continuously to the on line database.

The MC requests data from each device in sequence. Should a device fail to respond or the received data's CRC check fails, the MC will initiate another data request, up to a maximum of three requests. If all three data requests made to a slave device fail, the MC moves on to the next slave device and logs the failed attempt. No data entries are made for such a failed attempt. However, should all of the sample-interval (5 sec) data requests fail, zeros are logged to the SD-card and database for this specific device's log-interval data.

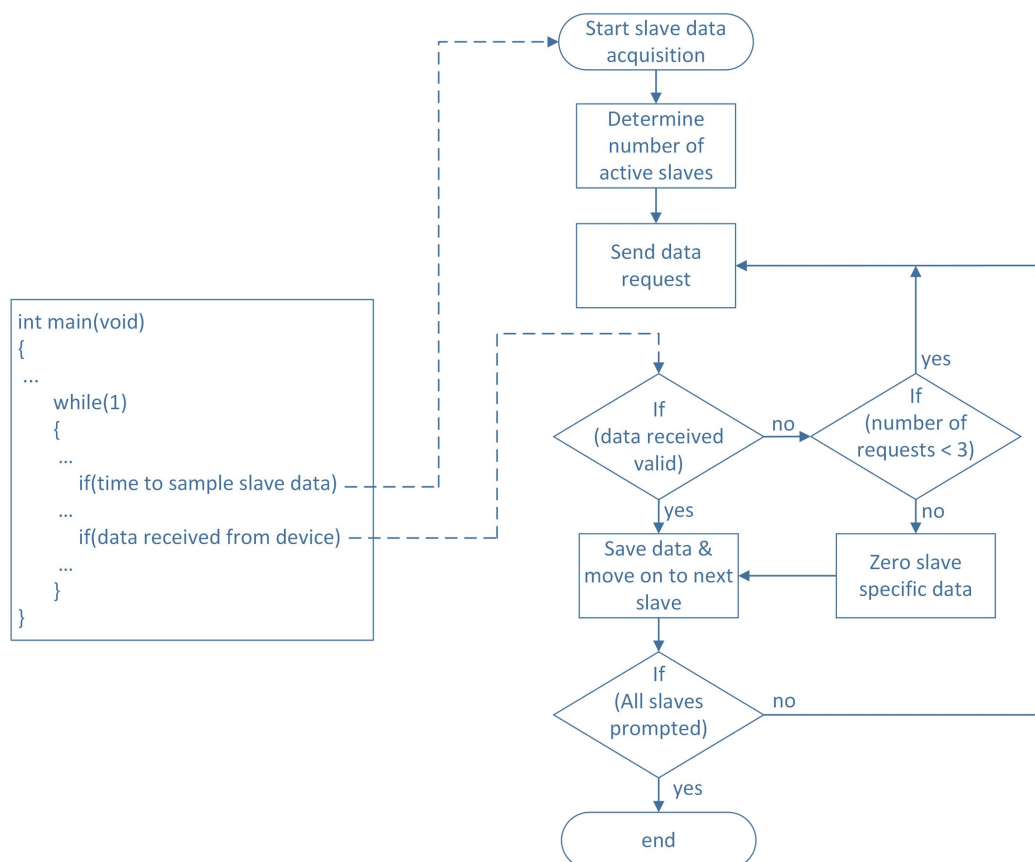


Figure 4.19: Overview of the slave data acquisition process applied by the MC.

**Weather sensor data acquisition**

Communication with the MSO-485 weather sensor is executed via the RS485 protocol, but instead of validating data with CRC bytes, a checksum operation serves as the test for data validation. Although address one is reserved for the weather station, a serial trigger, consisting of the characters 'wsone', is used to initiate communication. The WS responds with a string of bytes in the format as displayed below:

SSS.S, DDD,  $\pm$ TTT.T, HHH, PPPP.P, RRR.RR, XXXX, VV.V, MO, \*CCCCC

Table 4.4 defines each section of the data string received. Also, the checksum operation for data validation is presented by equation (4.10).

Table 4.4: Weather station data recorded after each log interval.

<b>String format</b>	<b>Measurement</b>	<b>Recorded Measurements</b>	<b>Unit</b>
SSS.S	Wind Speed	Avg. Max. Min.	m/s
DDD	Wind Direction	0 – 359	degrees
$\pm$ TTT.T	Ambient Temperature	Avg. Max. Min.	°C
HHH	Relative Humidity	Avg. Max. Min.	%
PPPP.P	Barometric Pressure	Avg. Max. Min.	mbars
RRR.RR	Rain	Interval	mm
XXXX	Optional Field	-	-
VV.V	Voltage	Supply voltage	V
MO	Config. & Status bytes	-	-
*CCCCC	Message Checksum	-	-

$$\sum \text{received bytes} = \text{received checksum CCCCC} \quad (4.10)$$

All weather data recorded during a 24 h day, starts and ends at 12:00 AM. The data received from the WS is processed and saved as presented in the 'Recorded Measurements' column in Table 4.4. In terms of the wind direction, a bin-counter is used, because simply calculating an average wind direction angle, for the various directions [degrees], is irrelevant. If the wind blows 9/10 times 0° and 1/10 times at 360°, an average direction of 36° will be recorded, which is not an accurate estimate of wind-direction. Thus, a bin counter is used, to give an accurate depiction of the dominating wind direction. In total 16 wind directions are defined. As mentioned, 12 data samples are recorded per log interval. This concept of a bin counter is illustrated by Figure 4.20.

Rainfall is measured as a quantity, which is reset to zero after each log interval. Thus, only the rainfall received during a log interval is recorded. If the entire day's rain fall is to be determined, all of the log interval rain measurements are added together.

**Irradiance instruments data acquisition**

As mentioned, the MC is programmed to allow a total of three pyranometers and one pyrhe-liometer to be installed, each with dedicated addresses. As mentioned, communication takes place over the USART1 communication port for all MODBUS devices. The device addresses, as well as communications set up (baud rate, parity etc.) are pre-configured with

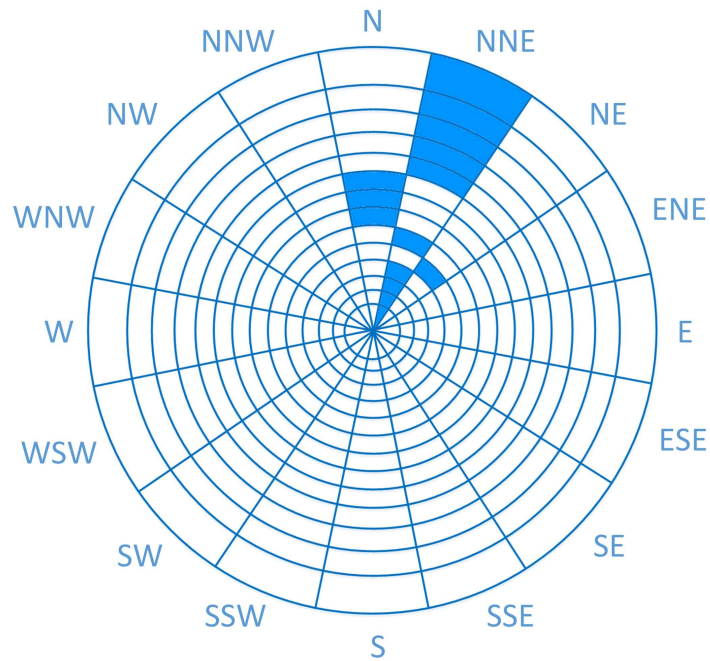


Figure 4.20: Illustration of how wind direction is recorded by means of a bin counter, where several sample measurements are made during a log interval.

the Kipp&Zonnen Smart Sensor Demo software package (refer to [61]). Data captured from the pyranometer and pyrhemliometer, is saved as presented in Table 4.5. As mentioned, the irradiance is recorded at the same instant as when the I-V curves are measured by the AL devices. The maximum and minimum irradiance is also recorded over the duration of the log interval. The pyranometer and pyrhemliometer device temperatures are recorded purely for diagnostic purposes.

Table 4.5: List of the data collected from the pyranometer and the pyrhemliometer.

Pyrano & Pyrhelio information	Unit	Interval Data Collected		
Body Temp.	C°	Average	Max.	Min.
Irradiance	W/m <sup>2</sup>	Instant	Max.	Min.

The data packet sent to the irradiance devices by the MC, is displayed in Figure 4.21. This data packet represents hexadecimal (HEX) values and the command specifies that the device's input register should be read [61, p.45][83, p.37]. Of the received bytes, bytes 14 and 15 provide the actual temperature compensated irradiance [W/m<sup>2</sup>], with temperature [°C] provided by bytes 20 and 21. The decimal value of the measured irradiance and temperature is retrieved by converting the received data into decimal values, with bytes 14 and 20 as the Most Significant Byte (MSB).

Slave address	04 00 00 00 0A	CRC1	CRC2
---------------	----------------	------	------

Figure 4.21: Format of the data sent to the pyrhemliometer and pyranometer, which requests the processed (not raw) irradiance data from the irradiance device.

### Single-axis-tracker data acquisition

As mentioned, the SATs provide the current angle of tilt [deg] and mode of operation. SAT data is however only collected just before the new minute starts. A tracking interval, with a minimum value of one minute, is defined for the trackers, which results in the SATs changing position, at most, once every minute. Thus, it is redundant to prompt the trackers every sample period (five sec.). Tracker data is requested and saved just before the start of a new minute at hh:mm:55. When data is requested by the MC from any of the SATs, then the data packet must conform to the MODBUS format presented by Figure 4.22. The MC's role of data logger and intermediate device (for user to SAT communication) is illustrated in Figure 4.23.

SAT address	SAT Command	SAT Sub-command	Data...	CRC1	CRC2
-------------	-------------	-----------------	---------	------	------

Figure 4.22: MODBUS data packet format as sent from the MC to a SAT.

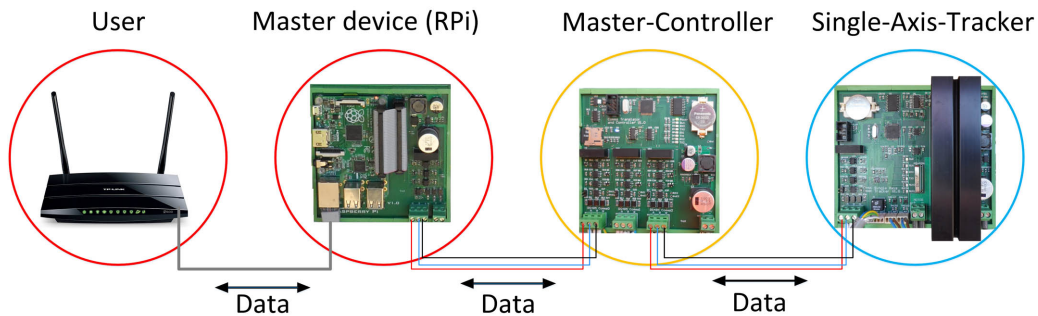


Figure 4.23: Communication interaction between the user and a SAT. *Source:* Wifi-router as found at [84]

The available primary user commands, which enable a data transaction between the user and the SATs, are shown in Table 4.6. The commands can be separated into two sets of communication:

- Command based: Data is sent to the SAT, with no information expected in return, other than the slave MODBUS reply message.
- Interactive: A specific set of data is requested from the SAT by the user.

Table 4.6: MC's user commands available to exchange information with the SAT.

Command	Description
Order-All-SAT-Data()	Order all of the available data from the SAT
Get-All-SAT-Data()	Retrieve all the data received from the SAT
Pass-Data-To-SAT()	Send data to the SAT

The Order-All-SAT-Data() and Get-All-SAT-Data() command are interactive commands. When the Order-All-SAT-Data() command is sent to the MC, the MC collects the required

data fields from the SAT. Then, if the `Get-All-SAT-Data()` command is executed by the user, the MC sends all of the SAT collected data to the user. Thus, the combination of these two commands can be regarded as a two stage communication between the user and a SAT. More detail with regards to the SAT commands is provided in Chapter 5, Section 5.5.7.

#### 4.6.5 MasterController user interface commands

The RPi enables user access to the MC device itself. Various commands are readily available for user interaction and allows users to send or retrieve device specific data. The user commands are separated into three groups, namely HEX-41 (Hexadecimal), HEX-42 and HEX-43 commands. Within these three groups, subcommands are dedicated with specific functionalities. The HEX-41 and HEX-42 command list is dedicated to standard set up and data retrieval commands, with the HEX-43 commands dedicated to special functions. The functions are listed and described in Table 4.7. Whenever a command is sent to the MC, it must conform to the data packet format as in Figure 4.24. The MC always returns a MODBUS reply message to ensure data credibility, which conforms to the same format as presented by Figure 4.25. Only the data and CRC bytes returned differ. The software routine executed by the MC when a user sends a command is displayed in Figure 4.26. The MC's internal `ServiceComms()` function essentially performs data validation and `ServiceSerial()` proceeds with the data received, executing the corresponding behaviour as received by the data packet.

MC address	MC Command	MC Sub-command	Data to MC...	CRC1	CRC2
---------------	---------------	-------------------	---------------	------	------

Figure 4.24: Data packet format where data is sent from the RPi to the MC.

MC address	MC Command	MC Sub-command	Data from MC...	CRC1	CRC2
---------------	---------------	-------------------	-----------------	------	------

Figure 4.25: Data packet format where the MC replies to the RPi.

A python based interface is created to interact with the MC. This code is integrated into the research facility's on-line, graphic user interface <sup>1</sup>. An example of the graphic interface is displayed in Figure 4.27. The list of all the available MC commands are presented in Table 4.7.

<sup>1</sup>This user interface is accessed at [www.pvsoiling.co.za](http://www.pvsoiling.co.za) and was developed by Malem Heymans and revised and expanded by Tashriq Pandy, both Master's degree students

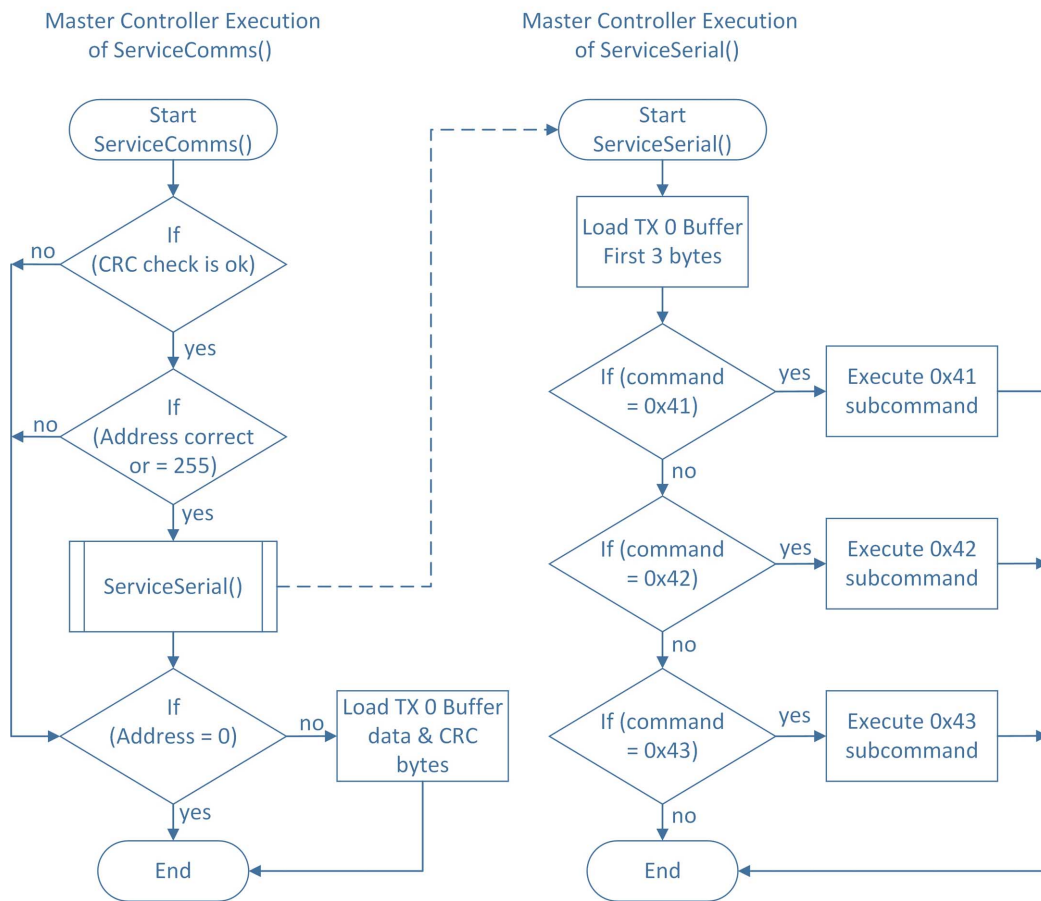
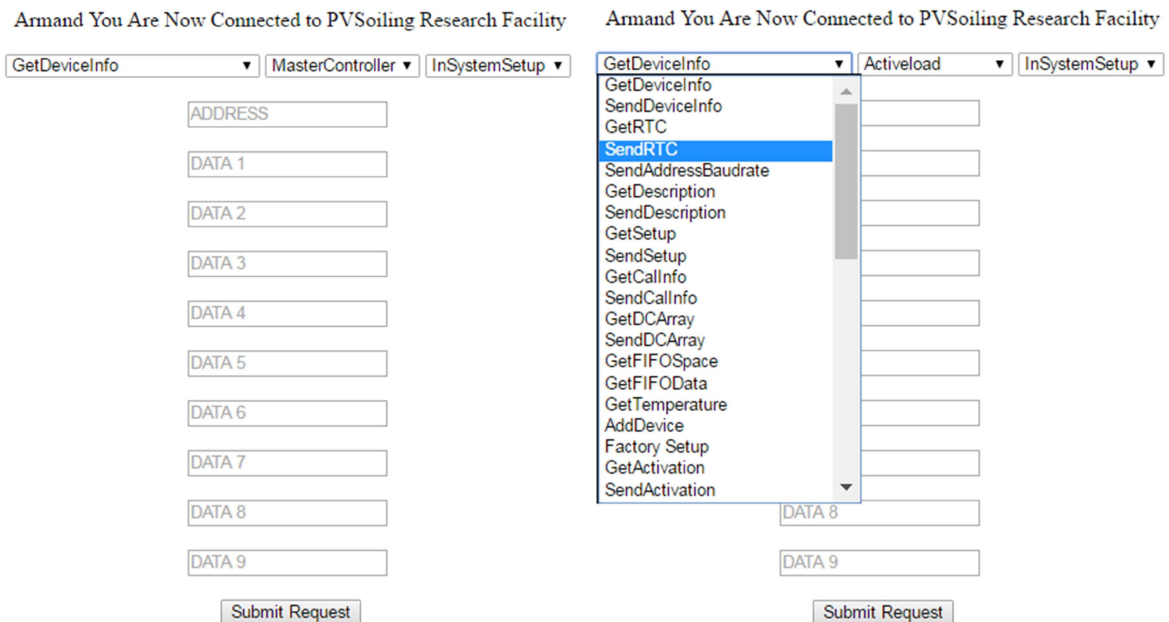


Figure 4.26: Basic software process for executing master device commands received.



(a) Online graphic interface.

(b) Drop down menu options.

Figure 4.27: Graphic user interface to communicate with the MC, as well as ALs.

Table 4.7: List of the available python HEX-41 and HEX-42 MC commands.

Command 0x41		Command 0x42	
Sub-command	Function()	Sub-command	Function()
0x01	Get-Device-Info()	0x01	Get-Setup()
0x02	Send-Device-Info()	0x02	Send-Setup()
0x03	Get-RxBuf()	0x03	Get-SAT-Weather-Control-Setup()
0x04	Get-RTC()	0x04	Send-SAT-Weather-Control-Setup()
0x05	Send-RTC()	0x08	Get-Fifo-Index()
0x06	Send-Address-Baudrate()	0x09	Get-Fifo-Data()
0x07	Get-Description()	0x0B	Get-Latest-WS-Data()
0x08	Send-Description()	0x0C	Get-Latest-Pyrano-Data()
		0x0D	Get-Latest-Pyrhelio-Data()
		0x0E	Get-Saxis-Angle()
		0x0F	Get-Daxis-Angles()

### HEX-41 commands

**Send-Device-Info():** Sends a serial number to the MC, so that it is identifiable. The serial number consists of YYMMXXXX with YY as the year after 2000 (16 for 2016) and MM as the month when device set up is completed. The device number XXXX represents the production number.

**Get-Device-Info():** Retrieves the MC's firmware version, the serial number and the device-ID, which is 2020 for the MC and represents the type of device.

**Return-RxBuf():** This is a diagnostic function which returns the data that was received by the MC.

**Send-RTC()** and **Get-RTC():** The real time clock (RTC) is adjusted with the Send-RTC() function to a new date and time. The Get-RTC() function simply returns the MC's time and date (year, month, date, hour, minute, second) that is presented by the RTC at the specific moment in time when the query is made.

**Set-Address-Baudrate():** The MC's address and baud rate is set with this function. If the address of the device is unknown, then address 0 or 255 can be used to communicate with the device and assign a new address. The difference between all-call addresses 0 and 255 is that, when communication is initiated with address 0, no MODBUS reply is sent to the master-device. However, for address 255, a MODBUS reply message is sent from the slave device.

**Send-Description()** and **Get-Description():** The description of the MC is 'MasterController n' with 'n' as any number designator. This allows a user to distinguish between different MC devices from one another, where more than one MC device is present in a system.

### HEX-42 commands

**Send-Setup()** and **Get-Setup():**

The MC's process of data acquisition is largely defined by this set up. Table 4.8 presents the set up values that are applied to the MC. The Get-Setup() function simply returns the value of each set up variable.



Table 4.8: List of items that define the set up of the MC.

Set-up	Value	Description
Log-Data	0-1	Permits data to be saved to SD card.
Log-interval	0-59	Defines the length [minutes] of a log interval.
Number of WS	0-1	Defines the number of active weather stations.
Number of Pyrano	0-3	Defines the number of active Pyranometers.
Number of Pyrhelio	0-1	Defines the number of active Pyrheliometer.
Number of SAT	0-3	Defines the number of active Single-Axis-trackers.
Number of DAT	0-1	Defines the number of active Double-Axis-Trackers.

**Send-SAT-Weather-Control-Setup()** and **Get-SAT-Weather-Control-Setup()**: The MC is responsible for sending the SATs a warning when wind speeds are high. Also, when rainfall is detected, the MC also informs the trackers. This function allows two variables to be set, starting with 'max-wind-speed', which defines the maximum wind speed allowed before the trackers have to level out. Secondly, the 'weather-control-activation' which enables the MC to issue a warning to the trackers. Details regarding this set up is retrieved from the MC with the `Get-SAT-Weather-Control-Setup()` function.

**Get-Fifo-Index()**: The SD-card saves data according to a FIFO (First In First Out) process. For each set of data stored, which represents a log interval, a FIFO-index number is assigned. When this function is called by the master-device, the MC sends the latest FIFO-index number. When the master-device updates the database, the FIFO-Index number serves as a reference point to identify whether or not the most recently logged data has been retrieved.

**Get-Fifo-Data()**: When this function is called, the data logged on the SD-card, which is associated with a certain FIFO-Index number is sent to the user. The user must provide the FIFO index number as an input.

**Get-Latest-WS-Data()**: When executed, the MC sends the most recent recorded weather data. The value of the rain-fall, presents the amount of rain fall received from 12:00 AM on the particular day, up to the moment in time when the request is made. This data is updated every five seconds (sample interval).

**Get-Latest-Pyrano-Data()**: This function retrieves the latest GHI, temperature and voltage supply values recorded by the specified pyranometer, which is also updated every five seconds.

**Get-Latest-Pyrhelio-Data()**: This function returns the latest DNI, temperature and voltage supplied values retrieved from the pyrheliometer, by the MC.

**Get-Saxis-Angle()**: The most recent recording of the SAT tilt angles and modes of operation is retrieved from the MC when this function is called.

**Get-Daxis-Angles()**: The altitude and azimuth angles of the double-axis-tracker are sent by the MC, when this function is called.

Table 4.9: List of the available HEX-43 special commands list, for the MC.

Command 0x43	
Subcommand	Function()
0x01	Get-Activation()
0x02	Send-Activation()
0x03	Order-All-SAT-Data()
0x04	Get-All-SAT-Data()
0x05	Pass-Data-To-SAT()
0x06	Get-SAT-MODBUS-Reply()
0x07	Switch-Off-On-WS()

The special commands are reserved as Hex43 commands. These commands are presented by Table4.9.

**Send-Activation()** and **Get-Activation()**: The Send-Activation() function permits the slave data collection process and the Get-Activation() command simply confirms whether or not data collection is activated or de-activated.

**Operate-Remote-Supply-Switch()**: The RSS is activated by this function for a brief moment, so that a hardware reset can be applied to the WS, if necessary.

The rest of the HEX-43 commands are directed towards the operation of the SAT. Whenever a command is sent from the master-device, to a SAT the data packet must conform to the format presented by Figure 4.28.

MC address	MC Command	MC Sub-command	SAT address	SAT Command	SAT Sub-command	SAT Data...	MC CRC 1	MC CRC 2
---------------	---------------	-------------------	----------------	----------------	--------------------	-------------	-------------	-------------

Figure 4.28: Data packet format applied when data is sent by the user, via the RPi, to a SAT through the interface provided by the MC.

**Order-All-SAT-Data()**: Direct real time communication between the user (via the master-device) and the single axis trackers is not available, since this might interrupt and delay the process of data-collection from the other slave devices. Therefore, a two stage communication is established between the master-device and each SAT. When data is to be requested from a SAT, an 'order' is placed by the master-device, which informs the MC to collect data from a specified SAT. This 'order' is advanced towards the SAT and when the reply is received from the SAT, the MC saves the data to temporary variables.

**Get-All-SAT-Data()**: This function is called after the Order-All-SAT-Data() function has been initiated, so that the two stage communication process is completed. Thus, when data has been received by the MC from the SAT, as a result of the execution of Order-All-SAT-Data(), a user can request this data which will activate the MC's Send-All-SAT-Data() command. The information provided by the SAT is listed in Chapter 5.5.7.

**Pass-Data-To-SAT()**: The Pass-Data-To-SAT() command, is not a user available command, but is an internal command executed by the MC, whenever a command intended for a SAT is executed by a user. The list of available user commands are presented in Table 4.10. For more specific detail with regards to these functions, please refer to Chapter 5.5.7.

Table 4.10: Functions that allow a user to send and request data to and from a SAT.

<b>Command Name</b>	<b>Description</b>
Send-RTC-To-SAT()	Update SAT clock time
Send-Address-Baudrate-To-SAT()	Set SAT baud rate and address
Send-Setup-To-SAT()	Send set up to SAT
Send-Tracker-lengths-To-SAT()	Define tracker dimensions and distance
Send-Set-Tilt-Angle-To-SAT()	Force stationary tilt angle
Send-Resume-Tracking-To-SAT()	Allow tracker to resume normal tracking
Send-Motor-Setup-To-SAT()	Define motor specifications
Send-Deactivate-Motor-To-SAT()	Deactivate motor operation
SAT-Adapt-To-Weather()	Force tracker into position due to weather
Send-Activation-To-SAT()	Activate tracker
Get-All-SAT-Info()	Retrieve latest tracker processed data
Set-Zero-Calibration-Angle()	Calibrate zero reference angle
Send-Reset-SAT-Software()	Force tracker to perform a software reset

# Chapter 5

## Single axis tracking

### 5.1 Introduction and chapter overview

As mentioned in Chapter 1, it is a research goal of this thesis to investigate different PV soiling mitigation methods on tracker mounted PV modules. To accomplish this goal, two SATs are implemented, which serve as an experimental platform to gather field generated data. A question that might come to mind is why it is necessary to design and implement the SAT infrastructure, when there are commercial trackers available for purchase on the open market? The reason for a self designed SAT system is to enable the tracking system to be integrated with the rest of the remote communications infrastructure. Secondly, a self designed system also expands the experimental manoeuvrability regarding the research.

With the fundamental theory of Earth and Sun movement presented in Chapter 2.3, this chapter starts by further adding to the theory, and presents the required concepts to formulate the tracking algorithms. Next, a discussion on backtracking and the derivation of the backtracking algorithm. This is followed by a detailed hardware and software design, which enables the successful operation of the two SAT systems installed at the PVRF. The software implementation of the backtracking and normal tracking algorithms are also presented.<sup>1</sup>

### 5.2 Sun tracking fundamentals of the SAT system

The equations presented for the basic earth and sun movement in Chapter 2.3, are repeated again for the reader's convenience:

$$\delta = 23.45 \left[ \frac{360}{365} (n - 81) \right] \quad (5.1)$$

$$\beta = \sin^{-1}(\cos L \cos \delta \cos H + \sin L \sin \delta) \quad (5.2)$$

$$\Phi_S = \sin^{-1} \left( \frac{\cos \delta \sin H}{\cos \beta} \right) \quad (5.3)$$

$$\text{if } \cos H \geq \frac{\tan \delta}{\tan L} \text{ then } |\Phi_S| \leq 90^\circ \text{ else } |\Phi_S| > 90^\circ \quad (5.4)$$

---

<sup>1</sup>To the reader. This chapter consists of a rather large amount of information regarding the single axis tracking system. Omitting too much information to an appendix, would result in a watered-down description which might leave the reader with unanswered questions and a lack of insight, regarding system operation.

$$H = \left( \frac{15^\circ}{\text{Hour}} \right) (\text{Hours Before Solar Noon}) \quad (5.5)$$

$$\text{Hours Before Solar Noon} = 12 : 00 - ST \quad (5.6)$$

$$ST = CT + \frac{4[\text{min}]}{1^\circ} (\text{Local Time Meridian} - \text{Local Longitude})^\circ + EOT \quad (5.7)$$

$$EOT = 9.87 \sin 2B - 7.53 \cos B - 1.5 \sin B \quad (5.8)$$

$$B = \frac{360}{364} (n - 81) \quad (5.9)$$

Where the variables in (5.1) - (5.9) are defined as:

$L$	= Latitude [deg]
$H$	= Hour angle [deg]
$\delta$	= Declination angle [deg]
$EOT$	= Equation Of Time [min]
$n$	= Day number [day]
$\Phi_S$	= Sun azimuth [deg]
$\beta$	= Sun altitude [deg]
$ST$	= Solar Time [min]
$CT$	= Civil/Clock Time [min]
$B$	= ST and CT correction factor angle [deg]

Representative of the commercial SAT systems employed in South Africa, the single axis tracking topology used by by this research is based on a horizontal, North-South layout. Figure 5.1 illustrates a trigonometric interpretation of the relationship between the various angles, as discussed by G. Masters [44, p. 224]. The derivation of these angles is presented in Appendix C. By interpreting the trigonometric relationship of the angles presented by Figure 5.1, the tilt angle of the tracker can be derived as presented by equation (5.10) [44, p.224].

$$\cos \varepsilon = \frac{\sin \beta}{\cos \theta} \quad (5.10)$$

Where  $\varepsilon$  represents the tilt angle of the SAT. The value of  $\cos \theta$  is derived from a normal Pythagoras triangular relationship of:

$$\cos \theta = \sqrt{1 - (\cos \beta \cos \Phi_S)^2} \quad (5.11)$$

The goal of the SAT system is to continuously adjust the modules to the ideal tilt angle, so that the maximum irradiance [ $\text{kW}/\text{m}^2$ ] is received. Thus, a Tracking Algorithm (TA) is formulated for a horizontal, North-South SAT, which executes the following chronological process of equation solving:

1. Determine the day number  $n$ .
2. Define  $B^\circ$  from equation (5.9).

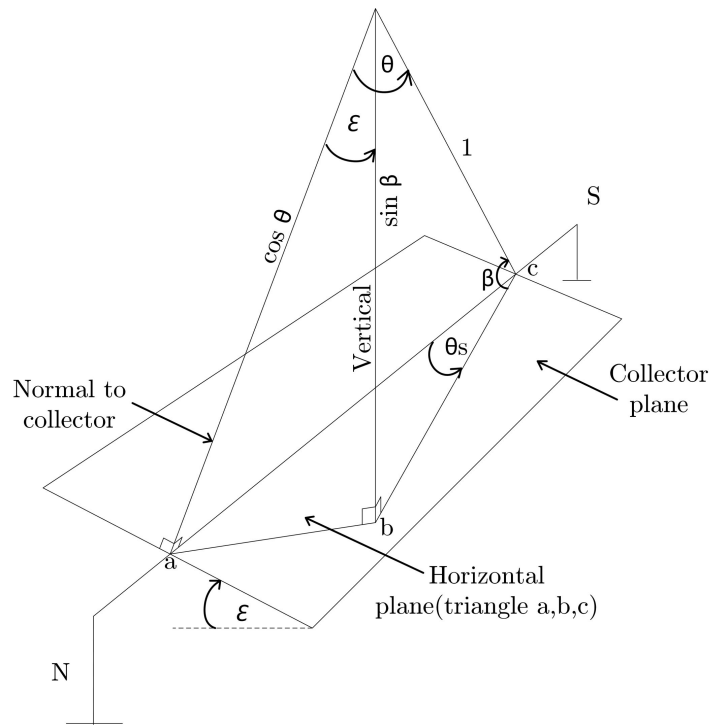


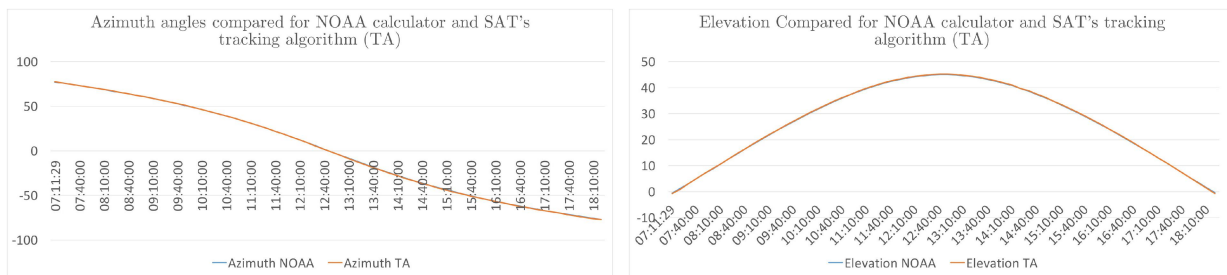
Figure 5.1: Trigonometric relationship of the relative position of the Sun to the angle of tilt for the SAT. *Source:* Redrawn image as illustrated by [44, p. 224]

3. Find the EOT value with equation (5.8).
4. Calculate ST (Solar Time) with equation (5.7).
5. Get the hour angle  $H$  from (5.5). *Hours before solar noon* is positive before a ST of 12:00AM.
6. Find the altitude angle of the sun  $\beta$  from (5.2).
7. Find the azimuth angle of the sun  $\Phi_S$  with equations (5.3) and (5.4).
8. Determine the value of  $\cos \theta$  with (5.11).
9. Determine the ideal tilt angle  $\varepsilon$  with equation (5.10).

A comparative study is undertaken to relate the accuracy of the derived TA, to that of the highly accurate NOAA Earth System Research Laboratory solar position calculator [86]. The graphs illustrated in Figures 5.2a and 5.2b illustrate the accuracy with which the derived TA (implemented for the SAT system) is able to predict the  $\Phi_S$  and  $\beta$  angles of the sun, as opposed to the NOAA calculator. The largest difference between the NOAA calculator and the TA is  $0.3^\circ$  and  $0.24^\circ$  for the  $\Phi_S$  and  $\beta$  angles. This demonstrates the accuracy of the algorithm, used for the SAT, to determine the position of the sun. It should be noted that the objective of the thesis is not to build a 100 % accurate sun tracking algorithm. The goal is to implement an accurate enough sun tracking algorithm that requires minimal processing power, which can direct the PV modules to the sun with a relatively high degree of accuracy.

### 5.2.1 Backtracking fundamentals

Backtracking has been proven to increase PV array energy yield and ensures PV module reliability, by avoiding hot spots due to shading [87]. Backtracking is a strategy utilised by



(a) Azimuth angle comparison.

(b) Altitude angle comparison.

Figure 5.2: Results comparing the SAT implemented TA to that of the NOAA Earth System Research Laboratory solar position calculator.

sun tracking systems to optimise energy yield. Essentially, backtracking allows an array of PV modules to avoid inter shading during low sun altitudes, which occurs during sunrise and sunset [7]. Shading is avoided by flattening out the SAT panels so that the shadow projected by a panel does not fall onto another panel, as shown in Figure 5.3.

In terms of commercial application, there will always be a play-off between the height of the sun (at a given time) and the available inter row spacing between single axis trackers. Ideally, the trackers would follow the sun from sunrise to sunset, which can be accomplished only when one row of trackers are installed. However, commercial application of single axis tracking is usually restricted by availability of space, as well as a simple matter of practicality.

The illustrations presented by Figures 5.3 and 5.4 are essential for implementing the backtracking algorithm. Figure 5.3 illustrates the available distance, denoted by  $d_{\text{row}}$ , between the panels for a specific tilt angle of  $\varepsilon^\circ$ . The  $x$  and  $y$  dimensions represent PV module length and tilted height, respectively. The distance from the SAT axis to the furthest module point is presented by  $z$ . This distances of  $d_{\text{row}}$  and  $z$  changes as the tilt angle  $\varepsilon^\circ$  changes. On the other hand, Figure 5.4 demonstrates shadow length of a module and how the  $\beta$  and  $\Phi_S$  angles determine the position of the shadow. The shadow distance of importance is the distance defined by  $d_S$ , and not the actual length of the shadow, displayed as  $L_S$ . Reason being that  $d_S$  is the absolute distance of the inter row shadow from one panel to another.

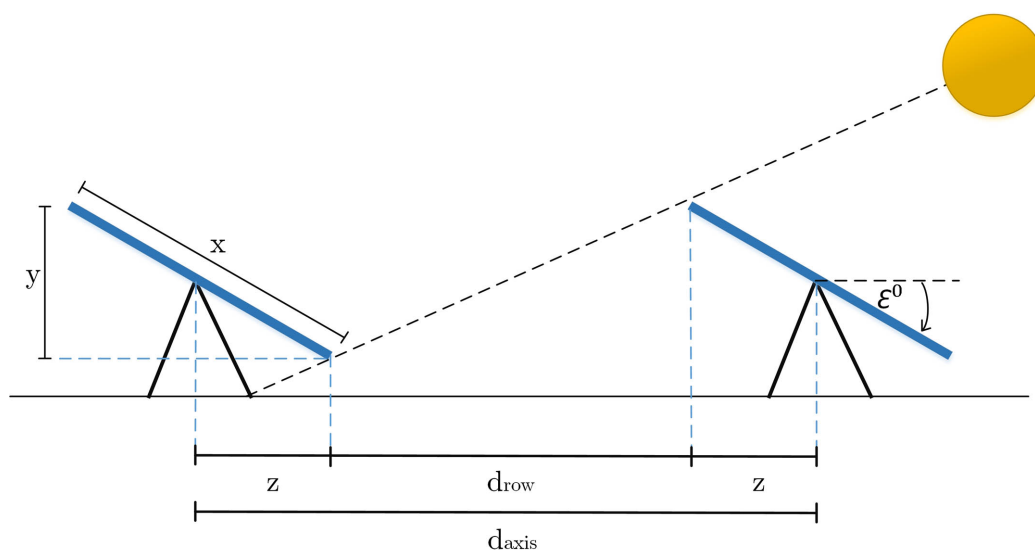


Figure 5.3: Backtracking in progress, where modules avoid table-on-table shading with a determined tilt angle of  $\varepsilon^\circ$ .

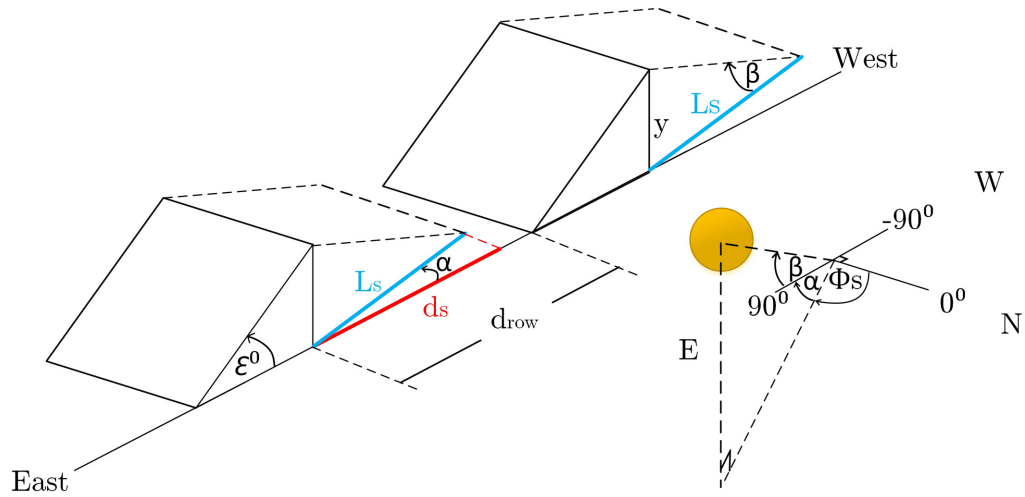


Figure 5.4: Shading distance as a result of the position of the sun.

The following equations are derived from Figures 5.3 and 5.4. From Figure 5.3 equations (5.12) to (5.14) are derived:

$$\varepsilon = \arcsin\left(\frac{y}{x}\right) \quad (5.12)$$

$$z = \cos \varepsilon \left(\frac{x}{2}\right) \quad (5.13)$$

$$d_{\text{row}} = d_{\text{axis}} - 2z \quad (5.14)$$

From Figure 5.4,  $L_S$  is the projected shadow length of the module, whereas  $d_S$  is the normal component of the inter row shadow projected. The angle between the eastern reference line and the angle  $\Phi_S$  is described by  $\alpha$  and the height of the PV module is defined by  $y$ . From this illustration in Figure 5.4 the following equations are derived:

$$L_S = \frac{y}{\tan \beta} \quad (5.15)$$

$$d_S = L_S \cos \alpha \quad (5.16)$$

$$\alpha = 90^\circ - \Phi_S \quad (5.17)$$

Essentially, the Backtracking Algorithm (BTA) applies these equations to determine whether or not backtracking should be initiated and if so, also determines the backtracking tilt angle. From equations (5.15) and (5.16), it is determined whether backtracking should be initiated. Equation (5.16) provides the minimum distance ( $d_S$ ) required to avoid inter row shading. The maximum available distance between the rows ( $d_{\text{row}}$ ) at a tilt angle of  $\varepsilon$ , is determined with equation (5.14). Thus, the following logic is applied to determine if backtracking should be initiated:

$$d_{\text{row}} > d_S : \text{Tracking proceeds, with no risk of inter row shading.} \quad (5.18)$$

$$d_{\text{row}} < d_S : \text{Backtracking is initiated.} \quad (5.19)$$



Should backtracking be initiated, the BTA makes use of an iterative process, where the tilt angle  $\varepsilon$  is incremented/decremented until the condition of (5.18) is satisfied. The iterative process of the BTA sequentially executes equations (5.13) to (5.16) when a new tilt angle  $\varepsilon$  is calculated. Further details with regards to the exact implementation of the backtracking functionality is provided in Section 5.5.2.

## 5.3 Hardware design

### 5.3.1 Conceptual hardware design

A microcontroller based sun tracking system is designed, which incorporates both open-loop and closed-loop feedback. A clock driven open-loop control strategy is used to determine the position of the sun, whereas axis mounted position sensors are used, to establish the closed-loop control feedback, as displayed in Figure 5.5. In essence, the tilt angle is determined for a particular moment in time and the trackers are adjusted until the reference angle is reached. In Figure 5.5 variable  $\theta_{err}$  is the difference between the measured tilt angle,  $\theta_{pos}$  and the desired tilt angle  $\theta_{ref}$ .

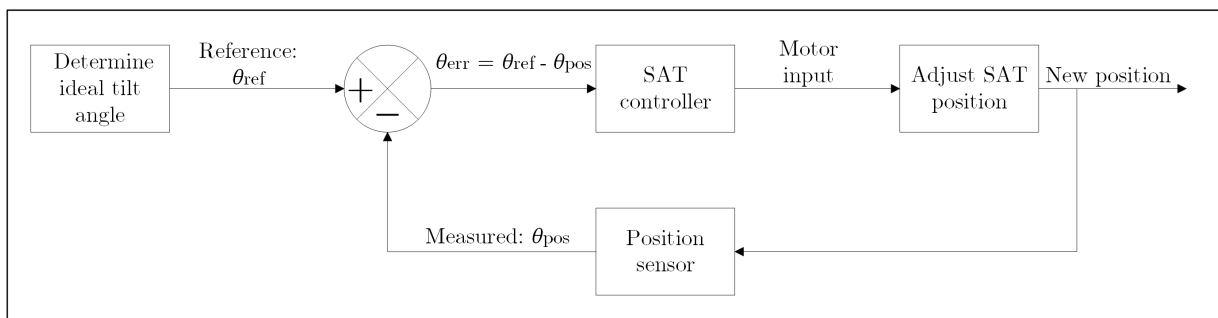


Figure 5.5: Illustration of the applied control system used to ensure the modules are tilted towards the desired tilt angle.

The tracking system implemented at Kalkbult, is a passive system and does not rely on light sensors to determine the optimal tilt angle. Therefore, to allow the SAT to function as intended and to utilise the control system presented in Figure 5.5, the SAT must have the following functionality:

- A microcontroller capable of performing the necessary tracking algorithms.
- Position sensors which provide feedback regarding the tilt angle of the tracker tilt.
- A DC motor which receives a PWM signal to enable the modules to be rotated in either direction.
- Proximity sensors to avoid potential over-tilt.
- An RS485 MODBUS interface, which enables communication with the SAT.

### 5.3.2 Microcontroller

The same Atmel manufactured ATmega 1284P-AU microcontroller [65] is used, which is also used for the MC device as discussed in Chapter 4.3.2.

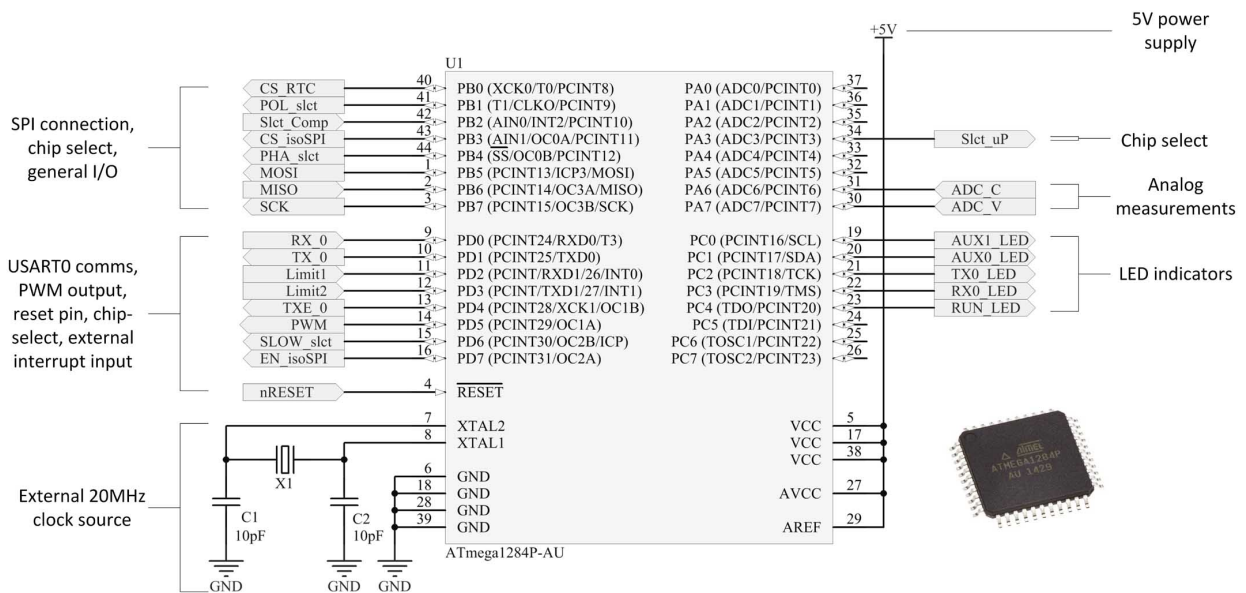


Figure 5.6: Illustration of the ATmega 1284P-AU MCU pin connections for the SAT. *Source:* ATmega1284P as found at [68].

This microcontroller is primarily responsible for the following processes:

- Establish RS485 communication and SPI device communication.
- PWM output control for H-bridge and DC motors.
- ADC measurement of received DC motor voltage and current.
- Execution of all sun tracking algorithms.
- Interpreting positional feedback from position sensors.
- Execution of control system presented in Figure 5.5.

### 5.3.3 Power supply

The SAT power supply circuitry is designed to accommodate a DC input voltage of either a 12V or 24V battery configuration. The input voltage from the battery bank also serves as the direct supply for the 24 V DC motor. The same supply voltage circuit, which uses an MC33063A step down switching regulator [69], as presented in Chapter 4.3.3, is used to establish an on-board 5 V DC supply voltage. From this 5 V supply a TME0515S DC-DC converter [88] is used to create a 15 V voltage line, required by the HIP4082 H-bridge FET driver [89]. Once again an isolated 5 V is also established for the RS485 circuitry, with a TMA0505S isolated DC-DC converter [75].

### 5.3.4 USART communication

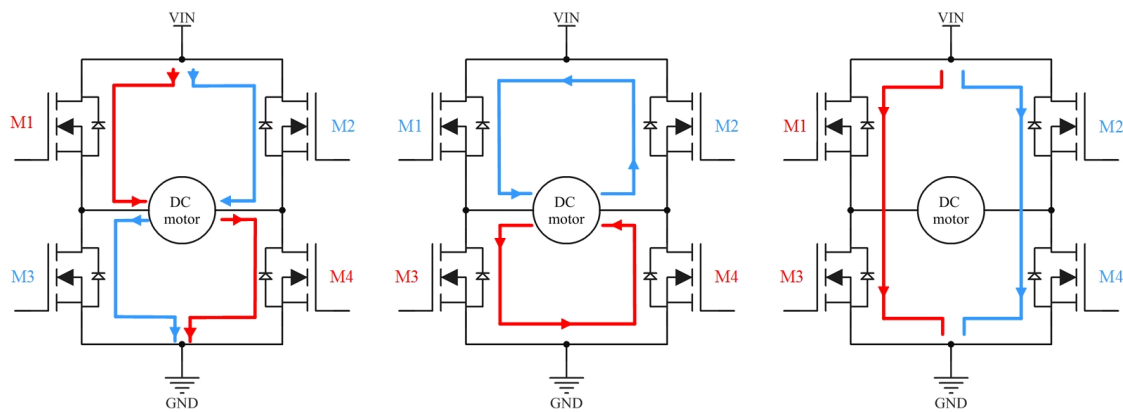
Communication is established with the SAT by means of an RS485 line. Only the USART0 of the MCU is necessary to establish this communication line. The circuit design is the same as for the MC, which is described in Chapter 4.3.4.

### 5.3.5 Real time clock

The real time clock used is the exact same DS3234 [82] which is used on the MC as well as the AL devices. Detail with regards to this chip is provided in Chapter 4.3.6. The RTC is a principal component in the design of the SAT, since this serves as the source of the tracking algorithms applied.

### 5.3.6 Full H-bridge driver circuit

A full H-bridge design, which allows the bidirectional rotation of the connected DC motor as displayed in Figure 5.7a, is applied by making use of a HIP4082 H-bridge FET driver [89]. This IC drives four dedicated channels independently and is provided with a 15 V supply. The basic operation of an H-bridge and how the logic states of the transistors determine this operation, is displayed in Figure 5.7. Figure 5.7b also displays how the rotation of a connected motor can be stopped.



(a) Rotate connected motor. (b) Restrict motor movement. (c) Dynamic shoot through.

Figure 5.7: Illustration of the resulting H-bridge circuit behaviour for various activated transistor combinations.

To prevent dynamic shoot through, as presented in Figure 5.7c a dead time is implemented by connecting a delay resistor to pin5 of the HIP4082 driver. For this application, a dead time of  $0.5 \mu\text{s}$  is selected, which is 2 % of the selected 20 kHz switching frequency, which is small enough to avoid affecting this switching frequency. Based on the datasheet [89] recommendations a delay resistor value of  $10 \text{ k}\Omega$  is selected.

The MOSFETs used for the H-bridge are the IRFB4115PbF, International Rectifier, N-channel power MOSFETs [90]. These MOSFETs have a high voltage and current capability of 150 V and 104 A respectively, with a max. gate threshold voltage  $V_{\text{GTH}}$  of 5 V. A gate voltage of 15 V is applied by the HIP4082 FET driver. Ringing on the output line of the MOSFETs, due to the gate capacitance and line inductance, is reduced with a gate resistor of  $30 \Omega$  added in series.

The schematic design of enabling the H-bridge topology is presented in Figures 5.8 and 5.9. A single PWM signal is applied to the H-bridge driver, as seen in Figure 5.8. Thus, the direction of the DC motor, as connected in Figure 5.9 is reliant on the duty cycle of the PWM signal. The direction of rotation for the applied duty cycle is indicated in Table 5.1.

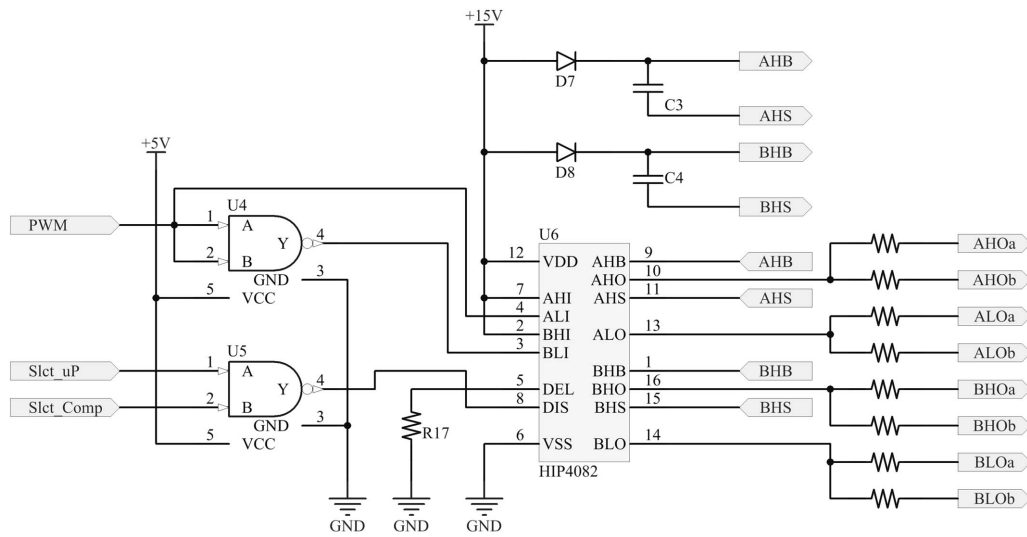


Figure 5.8: Schematic design of the HIP4082 driver circuitry.

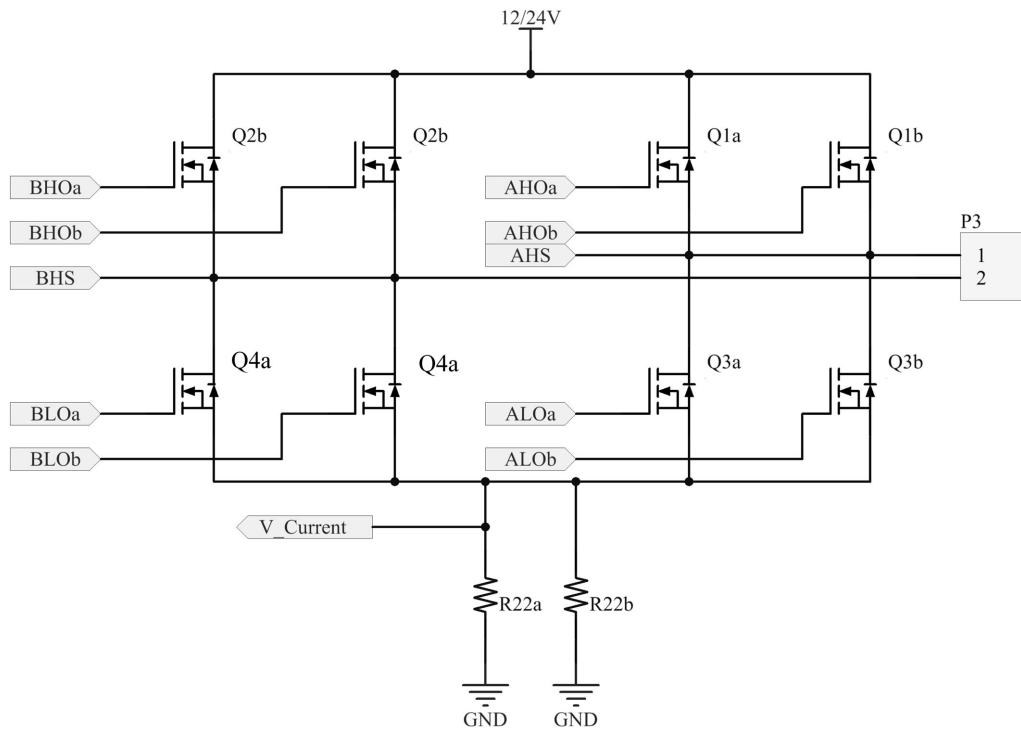


Figure 5.9: Schematic design of the MOSFET H-bridge topology.

Table 5.1: Truth table of the applied H-bridge MOSFET signals.

PWM Duty Cycle [%]	ALI PWM Input	ALO Out Q3a,Q3b	AHO Out Q1a,Q1b	BLI PWM Input	BLO Out Q4a,Q4b	BHO Out Q2a,Q2b	Dir.
$50 < D \leq 100$	0	0	1	1	1	0	Fwd.
$0 < D \leq 50$	1	1	0	0	0	1	Rev.

### 5.3.7 Heat sink design

Thermal management is applied to allow the MOSFETs, in the H-bridge set up, to operate within the specified thermal limit. The required thermal resistance [C°/W] of the heat sink is calculated with an equivalent electrical model, as seen in Figure 5.10 [91, p. 568], which is used to facilitate the design process.

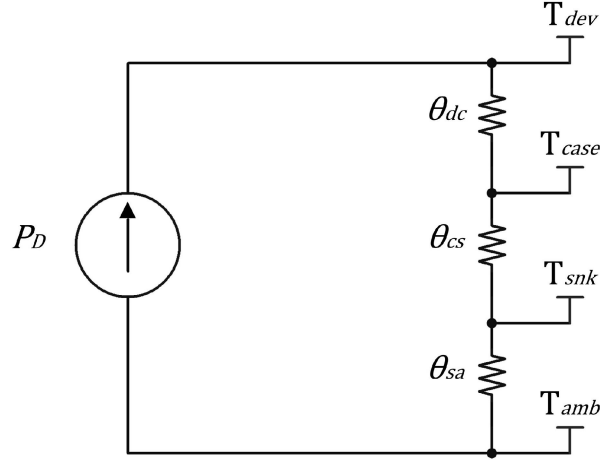


Figure 5.10: Equivalent electrical model for the applied heat sink design, as presented in [91].

From this electrical model, equation (5.20) is derived, which is used to define the value of the required thermal resistance of the heat sink as in  $\theta_{sa}$ .

$$T_{dev} - T_{amb} = P_D(\theta_{dc} + \theta_{cs} + \theta_{sa}) \quad (5.20)$$

$$\theta_{sa} = \frac{T_{dev} - T_{amb}}{P_D} - \theta_{dc} - \theta_{cs} \quad (5.21)$$

In equations (5.20) and (5.21)  $P_D$  is the power dissipated and  $T_{dev}$ ,  $T_{case}$ ,  $T_{snk}$ ,  $T_{amb}$  are the device, case, sink and ambient temperatures, respectively. The thermal resistances of the device-to-case, case-to-sink and sink-to-ambient values are presented by  $\theta_{dc}$ ,  $\theta_{cs}$  and  $\theta_{sa}$  [92].

Firstly, the power dissipated ( $P_D$ ) by the switching MOSFETs, is determined. Both conduction and switching losses are considered. The conduction losses take place during steady state operation, where power dissipation occurs due to the on resistance of the MOSFETs,  $R_{DS(on)}$ , which is 11 m $\Omega$  [90].

$$P_{cond} = R_{on} I_{SW}^2 \quad (5.22)$$

$$I_{SW}^2 = \frac{1}{T_S} \int_0^{DT_S} i_{SW}^2 dt \quad (5.23)$$

To allow for a degree of design safety, an extreme case where a current,  $i_{SW}$ , of 20 A and a duty cycle ( $D$ ) of 100 % is assumed, together with an H-bridge supply voltage of 30 V. The MOSFET switching frequency of 20 kHz, is defined as  $f_s = 1/T_S$ . However, in a full H-bridge configuration the high side arm and low side arm MOSFETs are active when the

motor is activated. Therefore, the instantaneous dissipated power for these two MOSFETs should be considered. The conduction loss for one MOSFET is calculated from equations (5.22) and (5.23) as:

$$P_{cond} = R_{DS(on)} \times f_S \times D \times T_S \times i_{SW}^2 \quad (5.24)$$

$$= 11 \text{ [m}\Omega] \times 20 \text{ [kHz]} \times 100 \text{ [%]} \times 50 \text{ [\mu s]} \times 20^2 \text{ [A]} \quad (5.25)$$

$$= 4.4 \text{ [W]} \quad (5.26)$$

Thus, with two MOSFETs activated the total conduction losses equate to  $P_{cond} = 8.8 \text{ W}$ . In terms of the switching losses, the worst case scenario occurs when a MOSFET is switched on, with a total rise time of 73 ns. Only two MOSFETs will be switching, due to the dead time of  $0.5 \text{ }\mu\text{s}$  applied by the HIP4082 FET driver. The switching losses for one MOSFET are defined by equation 5.27 [92].

$$P_{sw} = \frac{1}{2} \times (t_{rise} + t_{fall}) \times V_{DD} \times I_{SW} \times f_S \quad (5.27)$$

$$= \frac{1}{2} \times (73 \text{ ns} + 39 \text{ ns}) \times 30 \text{ [V]} \times 20 \text{ [A]} \times 20 \text{ [kHz]} \quad (5.28)$$

$$= 0.672 \text{ [W]} \quad (5.29)$$

Thus, with two MOSFETs activated at a time, the total switching losses equate to  $P_{cond} = 1.34 \text{ W}$ . The total dissipated power is calculated as:

$$P_D = P_{cond} + P_{sw} = 10.1 \text{ [W]} \quad (5.30)$$

Therefore, with  $\theta_{dc} = 0.4 \text{ [C}^\circ/\text{W]}$  and  $\theta_{cs} = 0.5 \text{ [C}^\circ/\text{W]}$  as determined from the MOSFET datasheet [90], the required thermal resistance is calculated with equation (5.21) as:

$$\theta_{sa} = \frac{T_{dev} - T_{amb}}{P_D} - \theta_{dc} - \theta_{cs} \quad (5.31)$$

$$= \frac{80 \text{ [C}^\circ] - 45 \text{ [C}^\circ]}{10.1 \text{ [W]}} - 0.4 \text{ [C}^\circ/\text{W]} - 0.5 \text{ [C}^\circ/\text{W]} \quad (5.32)$$

$$= 2.57 \text{ [C}^\circ/\text{W]} \quad (5.33)$$

Therefore, a heat sink with a maximum thermal resistance of  $2.6 \text{ C}^\circ/\text{W}$  is required. However, due to cost and size considerations, it is decided to make use of parallel MOSFET pairs. Thus, the conduction losses  $P_{cond}$  are halved to  $4.4 \text{ W}$ , due to the parallel  $R_{DS(on)}$  combination, which is then effectively reduced to  $5.5 \text{ m}\Omega$ . The switching losses  $P_{sw}$  are however doubled to  $2.68 \text{ W}$ , due to the extra switching parallel MOSFETs. Thus, when a value of  $P_D = 4.4 + 2.68 \simeq 7 \text{ W}$  is substituted into 5.31, the new required maximum heat sink thermal resistance is defined as  $4.1 \text{ C}^\circ/\text{W}$ . A heat-sink is used with a thermal resistance of  $4.08 \text{ C}^\circ/\text{W}$  [93].

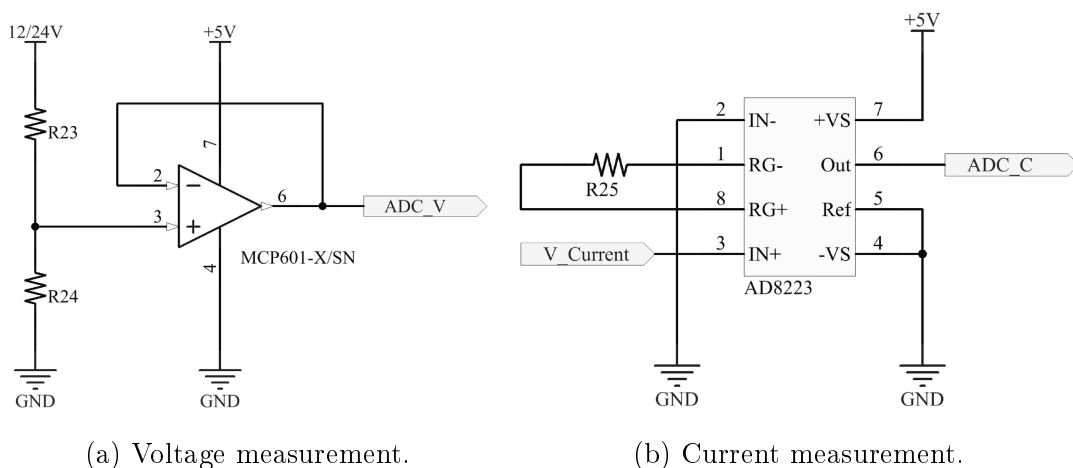
### 5.3.8 Analogue measurement circuitry and over current detection

#### Analogue voltage supply and current measurement

Analogue-To-Digital (ADC) measuring circuits are required to ensure that the DC motor is operated within the rated 24 V and 13.6 A supply values. The input voltage from the battery bank (24 V), which serves as the power source of the DC motor, varies when the MPPT charge controller is active. This is due to the charge controller, which makes use of an absorption voltage of 28.8 V and a float voltage of 27.6 V to maintain battery capacity. Before the H-bridge is activated, a limit must be applied to the PWM signal, which prevents the supply voltage of the DC motor from being exceeded. The input voltage is monitored via one of the ADC pins on the MCU, which is rated at a 5 V input. Thus, to measure the battery input voltage, with the ADC pins, the voltage reading must be stepped down to 5 V. A voltage divider circuit is used in conjunction with an MCP601 [94] operational amplifier (Op-Amp), as a means of protecting the MCU. With the circuit design as applied in Figure 5.11a. The output voltage  $V_{out}$  is determined with (5.34) as :

$$V_{OUT} = V_{BAT} \frac{R_{24}}{R_{23} + R_{24}} \quad (5.34)$$

The design accepts a battery input voltage of 30 V, which is stepped down to 5 V, with a resistors  $R_{23}$  and  $R_{24}$  chosen as 100 k $\Omega$  and 20 k $\Omega$ .



(a) Voltage measurement.

(b) Current measurement.

Figure 5.11: Analogue measurement circuits to read battery supplied voltage and current supplied to the DC motor.

#### Over-current safety detection circuitry

Should a motor stall, excessive current can be drawn which could destroy the MOSFETs. A rated current value of 13.5 A is imposed on the DC motor, by this design. Should this limit be exceeded, the MCU will disable the DC motor by activating the disable pin (DIS), on the HIP4082 H-bridge driver. The supply current is detected by means of a 15 m $\Omega$ , 5 W, current sensing shunt resistor [95]. This resistor is used together with the high gain AD8223 [96] instrumentation amplifier, presented by Figure 5.11b. Although a 13.5 A limit is imposed, the over-current circuitry is designed for a maximum current of 15 A, which equates to a maximum possible voltage reading of 0.225 V (15 A  $\times$  15 m $\Omega$ ). Therefore, to establish a higher resolution of up to 5 V for the ADC input pin of the MCU, a gain of at least 22 is required (5V/0.225V  $\simeq$  22). As provided by the datasheet [96], the output voltage is determined as:

$$V_{OUT} = G(V_{IN+} - V_{IN-}) + V_{REF} \quad (5.35)$$

$$= G(V_{IN+}) \quad (5.36)$$

Thus, a gain resistor ( $R_{25}$  in Figure 5.11b) of  $20 \Omega$  is chosen, which from (5.36) equates to a max. of 4.5 V. However, should a current of 13.5 A. be exceeded, or the MCU fails to disable the DC motor, then hardware will be engaged to physically disable the DC motor. An LM311D voltage comparator, by Texas Instruments [97] is used to implement this second stage safeguard, as presented in Figure 5.12. An op-amp is not used for this detection, since the reaction time of the voltage comparator is much faster.

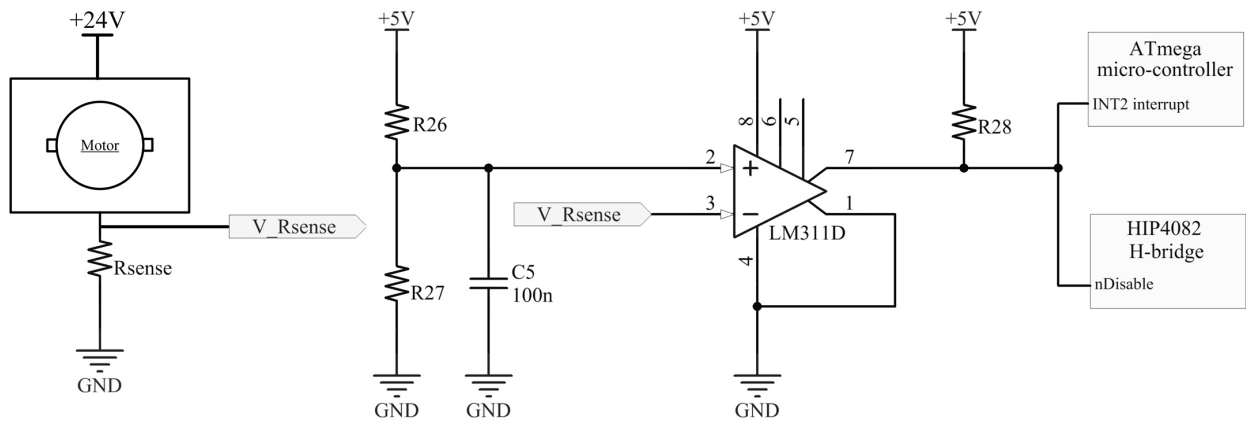


Figure 5.12: Illustration of how the LM311D comparator circuit is connected to the MCU and H-bridge, to enable a second stage hardware reset.

The output pin of the comparator is connected to the interrupt pin PA6 of the MCU, so that a falling edge logic change, will initiate an interrupt routine, which disables the DC motor. For a 15 A current, the comparator will see a max. of 0.225V over the  $R_{sense}$  resistor. The comparator circuit changes its output state when the voltage between its inputs crosses through approximately zero volts as according to equation (5.37):

$$V_{in+} - V_{in-} \leq 0V \quad (5.37)$$

The value of  $V_{in+}$  is received from the voltage divider circuit consisting of  $R_{26}$  (91 k $\Omega$ ) and  $R_{27}$  (3.9 k $\Omega$ ) which provide an input ( $V_{in+}$ ) of 0.21 V. Thus, when the current extracted by the DC motor exceeds 14.7 A ( $\simeq 15$  A), a 100 mV differential voltage is detected by the comparator and the circuit will be activated<sup>2</sup>. The timing diagram of the LM311D comparator is presented in Appendix C, Figure C.3. To allow an input signal, received from either the comparator circuit or the MCU, to Disable the H-bridge, the logic circuit in Figure 5.13 is used. A logic NAND gate is used, since the Disable pin is active low. Table 5.2 presents the logic.

<sup>2</sup>To be clear. The heat-sink design is conducted for a 20 A DC motor current. The DC motor rated current is selected by design as 13.5 A, although it is in actual fact 13.6 A. The circuitry is designed to function at a 15 A current. The second stage emergency hardware is effective when current drawn is  $\sim 15$  A.



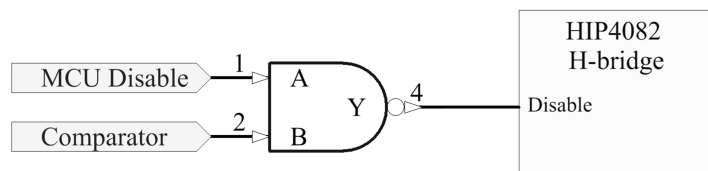


Figure 5.13: Signal input from MCU and comparator to disable H-bridge.

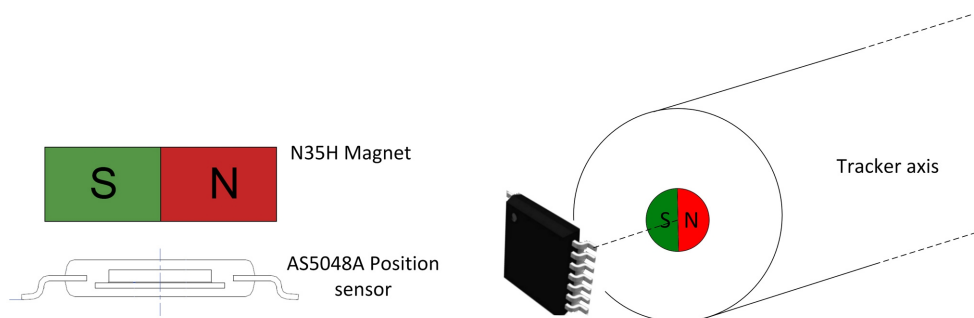
Table 5.2: Truth table logic for H-bridge disable pin

MCU Output	Comparator Output	NAND Output	Disable pin
0	0	1	1
0	1	1	1
1	0	1	1
1	1	0	0

### 5.3.9 Position sensor and isolated SPI design

The tilt angle of the SAT is measured with a non-contact AMS AS5048A, 14 bit angular position sensor [98]. This position sensor relies on a disc magnet to effectively determine the angular information, which is provided as an angle ranging from 0 to 360° [98]. Information is accessed from this device by means of an SPI interface and it is supplied with a 5 V input voltage, consuming a total of 150 mW. The primary reason for selecting this sensor is due to its robustness and accuracy, with the sensor capable of tolerating air gap (up to 2.5 mm) and temperature (-40 C° to +150 C°) variations, as well as misalignment and external magnetic fields [98].

From recommendation an 8 x 2.5 mm disc, N35H grade magnet is used [99], to allow the AS5048A sensor to determine the tilt angle of the tracker. For this particular set up, the magnet is placed in the centre of the trackers axis, with the position sensor also centered over the magnet, as displayed in Figure 5.14.

Figure 5.14: Illustration of the application of the AS5048A magnetic position sensor. *Source:* Left section of figure redrawn as illustrated in [98].

To avoid measurement uncertainty with regards to angular measurements, an isolated-SPI (isoSPI) communications interface is established, with an LTC6820 device [100]. As seen in the recommended set up in Figure 5.15, this device allows a bidirectional SPI communication

network to be established between devices. The set up of this isolated interface requires two LTC6820 devices, where one serves as the master and the other as a slave.

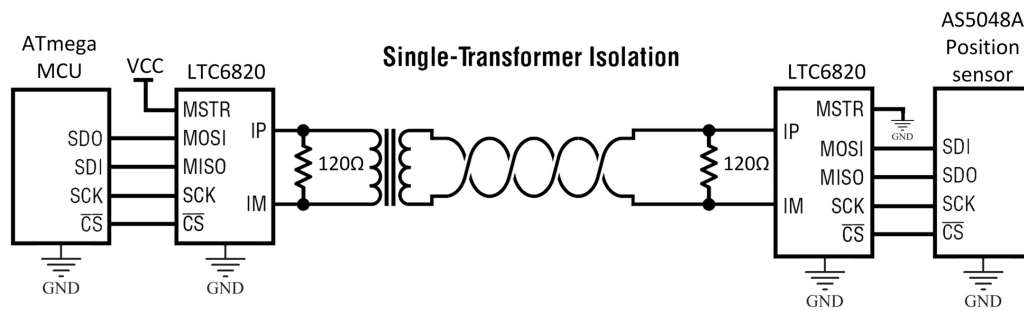


Figure 5.15: Recommended layout for a single-transformer isolation set-up. *Source:* Redrawn as illustrated in [100].

This layout in Figure 5.15 requires a 1:1 Current transformer to isolate the IP and IM signals between the two isoSPI devices. As recommended by the datasheet the Murata 78613/3C center tapped transformer is chosen [101]. The cable used to link the two separate devices is a six core, screened cable, of which the characteristic impedance is terminated on each side by a 120 Ω resistor.

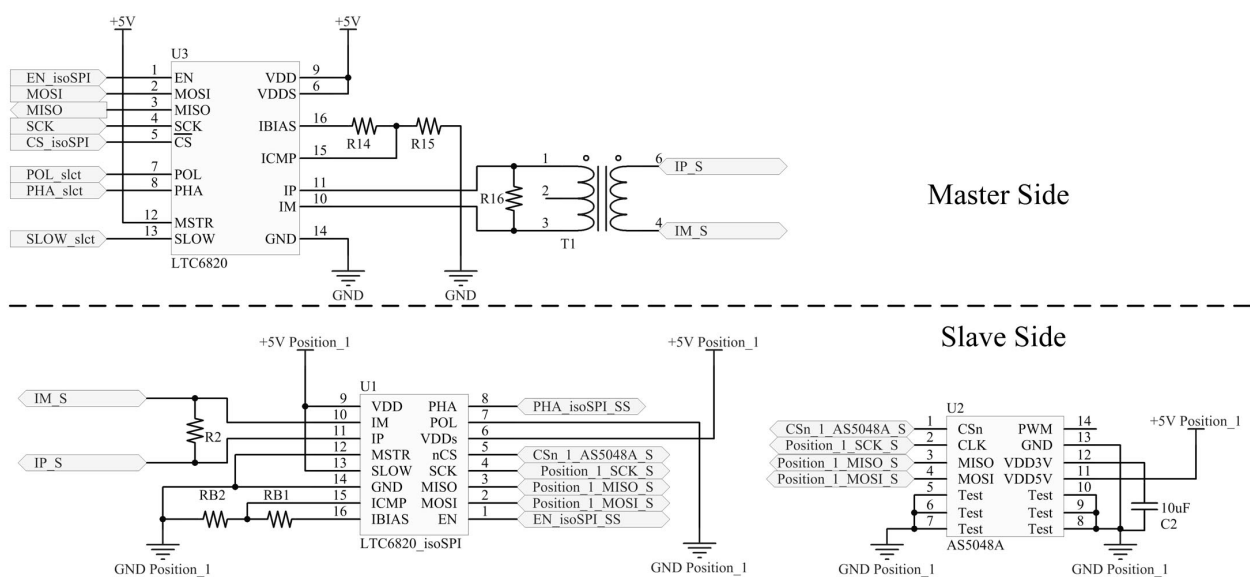


Figure 5.16: Circuit design of the master and slave side implementation of the LTC6820 (isoSPI) and the AMS5048A position sensor.

It is important to distinguish between the master and the slave side of this isolated communication line, as in Figure 5.16. In terms of the SPI communication, the MCU and isoSPI are set up according to the position sensor (AS5048A), since it only has one SPI mode. This SPI mode is defined for a clock that idles low and latches on the falling edge. The isoSPI operates in this mode by assigning the polarity pin (POL) and phase pin (PHA) to 0 and 1 respectively. A 156 kHz SPI clock is defined, which allows the isoSPI to operate in slow mode (SLOW pin high). In slow mode the MCU, isoSPI and position sensor are all in agreement regarding the SPI communication interface. As recommended by the datasheet [100] the appropriate pull up resistors are applied to the MISO and MOSI pins. The value of the  $R_{B1}$

and  $R_{B2}$  resistors are chosen as  $2.7 \text{ k}\Omega$  and  $1.3 \text{ k}\Omega$ . This allows effective communication of up to 50 m distances.

### 5.3.10 Proximity sensors

The SAT has a rotation limit of  $\pm 90^\circ$ . Two magnetic proximity switches (IP68 compliant) [102], which are essentially reed switches, are used to detect when the SAT has surpassed the tilting limit. Since two sensors are used, it is possible to determine the direction of the over-tilt. Knowing on which side the SAT has over-tilted allows a user to remotely steer the SAT back into place, by using one of the commands, as described in section 5.5.7. The conceptual and circuit design is presented in Figure 5.17. Two dedicated MCU external interrupt pins (EXT0, EXT1) are assigned to each of these sensors. When the SAT over tilts, a magnet activates the proximity sensor and an interrupt is generated which deactivates the DC motor. As the switch of the proximity sensor closes, the input signal towards the AND gate [103] is changed to a logic low, with the  $R_{PU}$  ( $10 \text{ k}\Omega$ ) limiting the current flow. When a sensor is not activated, the  $R_{PU}$  resistor keeps the AND gate logic input high. Thus, the external interrupt of the MCU reacts on a falling edge only. This is essential, because if the SAT is moved back into position, so that the logic input to the external interrupt pin changes from low to high (normal operation), then an interrupt is not generated.

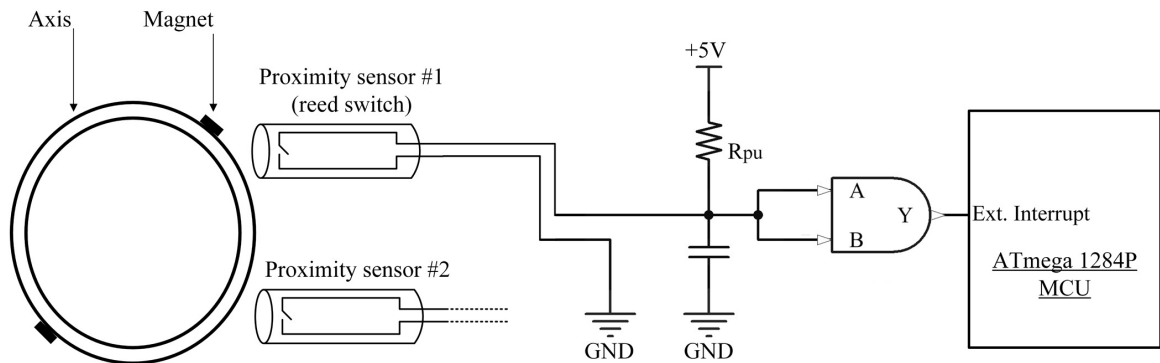


Figure 5.17: Circuit design of the proximity sensor circuit which generates an interrupt when over tilt occurs.

### 5.3.11 LCL filter and input bus capacitor design

The PWM signal provided from the H-bridge to the DC motor is smoothed out by making use of an LCL (inductor-capacitor-inductor) filter. By means of simulation, performed with a basic LT-SPICE simulation package, the value of each inductor and the capacitor is determined as  $50 \text{ }\mu\text{H}$  and  $40 \text{ }\mu\text{F}$ , respectively.

For the inductor, a FS-1RN-131-26 series toroidal core, of iron powder-26 [104] is used. The inductor windings consist of a 2 mm (diameter) copper wire. This toroidal core is selected due to its high magnetic flux capability [104]. However, to ensure the appropriate toroidal core is selected for the design, the core must not saturate for a chosen DC motor current value of 13.5 A. If equation (5.38) is adhered to, then the toroidal core selected is appropriate for the specified design criteria [105]:

$$B \geq \frac{\mu N i}{l_c} \quad (5.38)$$

Where the variables in (5.38) are defined by equations (5.39) to (5.41):

$$B = \mu H \quad (5.39)$$

$$H = \frac{Nl_c}{i} \quad (5.40)$$

$$\mu = \mu_0\mu_r \quad (5.41)$$

In equations (5.39) to (5.41) the variables represent [105]:

- $B$  = magnetic flux density [T]
- $N$  = number of turns [turns]
- $i$  = maximum current [A]
- $l_c$  = length of the core [m]
- $\mu_r$  = relative permeability of material [H/m]
- $\mu_0$  = permeability of air which is  $4\pi \times 10^{-7}$  [H/m]
- $H$  = Magnetic Field Intensity [A/m]

This toroidal core has an inductance rating  $A_l$  of 116 [nH/N<sup>2</sup>] [104]. Therefore, the number of turns required is calculated as:

$$L = \frac{\mu_c N^2 A_e}{l_c} = N^2 A_l \quad (5.42)$$

$$N = \sqrt{\frac{L}{A_l}} \quad (5.43)$$

$$N = \sqrt{\frac{50 [\mu\text{H}]}{116 [\text{nH}/\text{N}^2]}} \quad (5.44)$$

$$N = 21 [\text{Turns}] \quad (5.45)$$

With the relative permeability defined as 75, [104, p. 27] at 20 kHz and the magnetic flux density defined as 1.2 T, it is determined that the toroidal core will not saturate with equation (5.38):

$$B \geq \frac{\mu N i}{l_c} \quad (5.46)$$

$$B \geq (4\pi \times 10^{-7}) \times 75 \times 21 \times \frac{15}{0.0772} = 0.385 \text{ T} \quad (5.47)$$

Thus, with B equal to 0.385 T, this is well below 1.2 T and the core will not saturate.

With the inductor design finalised, only the capacitor is still to be selected. Two 22  $\mu\text{F}$  Polyester (PET) Film Capacitor (Epcos FB32524) [106] are added in parallel. With a DC voltage rating of 63 V, this capacitor is chosen due to the ability to be used in applications where sharp, fast rise time spikes are present, as these capacitors are able to accommodate high dV/dt figures.

Upon start-up, to prevent the DC motor from withdrawing too much current at once, which would cause the rest of the circuitry to possibly lose power, a series of bus capacitors are installed. Four electrolytic 1 mF Aluminium capacitors [107] are added in parallel, together with a 10  $\mu\text{F}$  polyester film capacitor [108].

## 5.4 PCB design

### 5.4.1 SAT PCB board

With regards to the PCB design of the SAT board, it is important to separate the high current and voltage circuitry from the digital, analogue and communications circuitry. The RS485 communication circuitry is completely separated from the rest of the PCB, with an isolated ground and voltage supply. The analogue and digital circuitry, is separated by distance and strategic component placement. Wide copper traces are used to accommodate the flow of current from the power supply to the DC motor. The requirements for the PCB layout, with regards to the isoSPI device and the 1:1 transformer are also adhered to, as recommended by the application notes of the LTC6820 datasheet [100]. The PCB design schematics are provided in Appendix C.3.

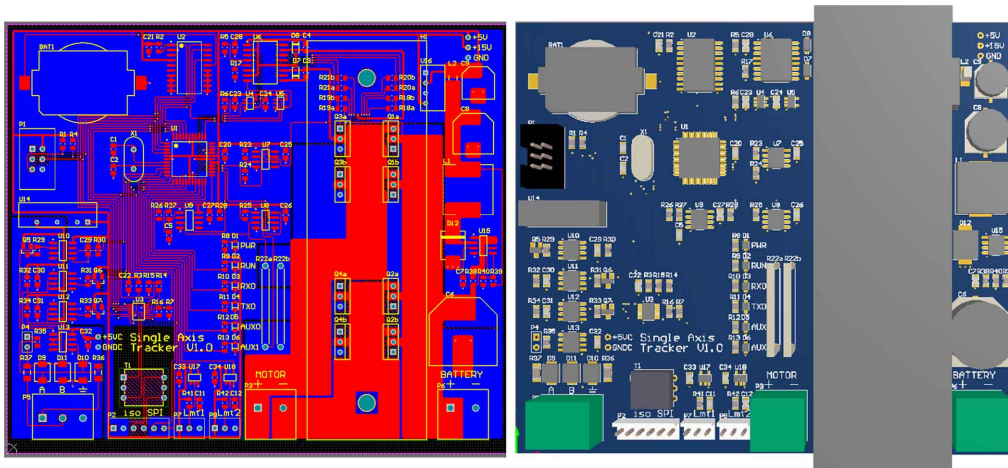


Figure 5.18: Illustration of the completed SAT PCB design .

### 5.4.2 Position sensor

The position sensor PCB is designed so that the AS5048A position sensor itself is separated from the rest of the components, by placing it on the backside of the PCB. This is illustrated in Figure 5.19. This is done so that the PCB can be mounted onto the gearbox of the DC motor and the magnet on the axis can be read easily. With this design the position sensor board can be easily exchanged with another, should an issue arise. The PCB design schematics of the position sensor board are also provided in Appendix C.3.

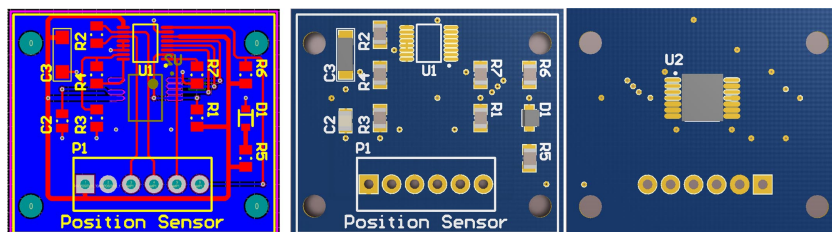


Figure 5.19: Illustration of the SAT position sensor PCB board.

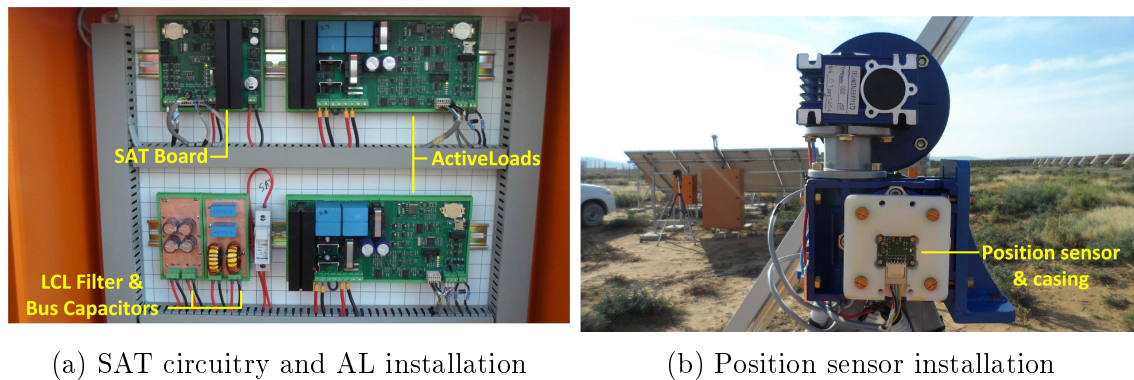
### 5.4.3 SAT circuit problems encountered

Substantial ringing is measured on the output signals of the H-bridge MOSFETs, as well as voltage spikes over the current sensing resistor. The ringing was significantly reduced

with the addition of a  $30\ \Omega$  gate resistor. A snubber circuit is also added in an attempt to eliminate further ringing, but this did not help to resolve the issue of the voltage spike seen over  $R_{sense}$ . Therefore, the current detection circuitry unfortunately could not be utilised. However, to eliminate the possibility of an undetected over current event, a 15 A fuse is installed between the battery supply and the SAT circuit board.

#### 5.4.4 Electronic installation of the SAT system

With the PCB design of the SAT and position sensor boards completed, these boards are installed as displayed in Figure 5.20. The complete electronic set up of the SAT board, the LCL filter, input bus capacitors together with the AL boards are shown in 5.20a. The position sensor circuit board mounted onto the SAT gearbox is displayed in Figure 5.20b.



(a) SAT circuitry and AL installation

(b) Position sensor installation

Figure 5.20: Electronic installation of one of the SAT systems systems.

#### 5.4.5 SAT Mechanical and structural assembly

##### DC motor and gear configuration

An F7147H series King DC motor is used on each tracker. This is a brushed DC motor with the rated values as presented in Table 5.3. After several tests are performed, it is determined that the speed of rotation is to be reduced to less than one r.p.m. to allow for a smooth rotation, without inducing any whiplash on the mounted tracker modules. Therefore, a reduction gear ratio of at least 1:4000 is required.

Table 5.3: DC motor rated values [109]

	Speed	Voltage	Current	Input	Torque
<b>No Load</b>	4105 r.p.m.	24.18 V	1.37 A	33.1 W	0.28 kg-cm
<b>Full Load</b>	3268 r.p.m.	24.09 V	13.63 A	328.3 W	7.07 kg-cm

It is decided to make use of a worm gear configuration. Worm gears have the advantage of large gear reduction ratios and a locking capability, which prevents the shaft connected load to turn the gear. This ensures minimal inertial backlash. Only the worm, connected to the shaft of the DC motor can turn the gear. This is ideal, since it is necessary for the SAT axis to stay in place at all times, irrespective of any external force applied to it (such as wind). As presented in Figure 5.21b, two worm gears are attached to execute a double reduction gear ratio of 5000:1, which equates to a 0.8 r.p.m. rotation speed at most. This

is accomplished with a 50:1 NMRV030 63B5 and a 100:1 NMRV050 63B5 worm gear [110] connected to one another with an NMRV030 to NMRV040 coupling<sup>3</sup>.

## SAT system assembly

The mechanical assembly of the SAT system is displayed in Figures 5.21b to 5.21d. As can be seen from these images, each SAT consists of three A-frames, secured onto a concrete block foundation. On top of each A-frame is a pillow block bearing and housing for the axis. In Figure 5.21b the worm gear combination is illustrated. Two stainless-steel (50 mm  $\phi$ ) axis are connected by means of a universal mechanical joint, which is housed by the middle A-frame's pillow block bearing. The rail-to-axis clamps, in Figure 5.21c, also allow a margin of adjustment, to ensure the horizontal alignment of the PV modules.

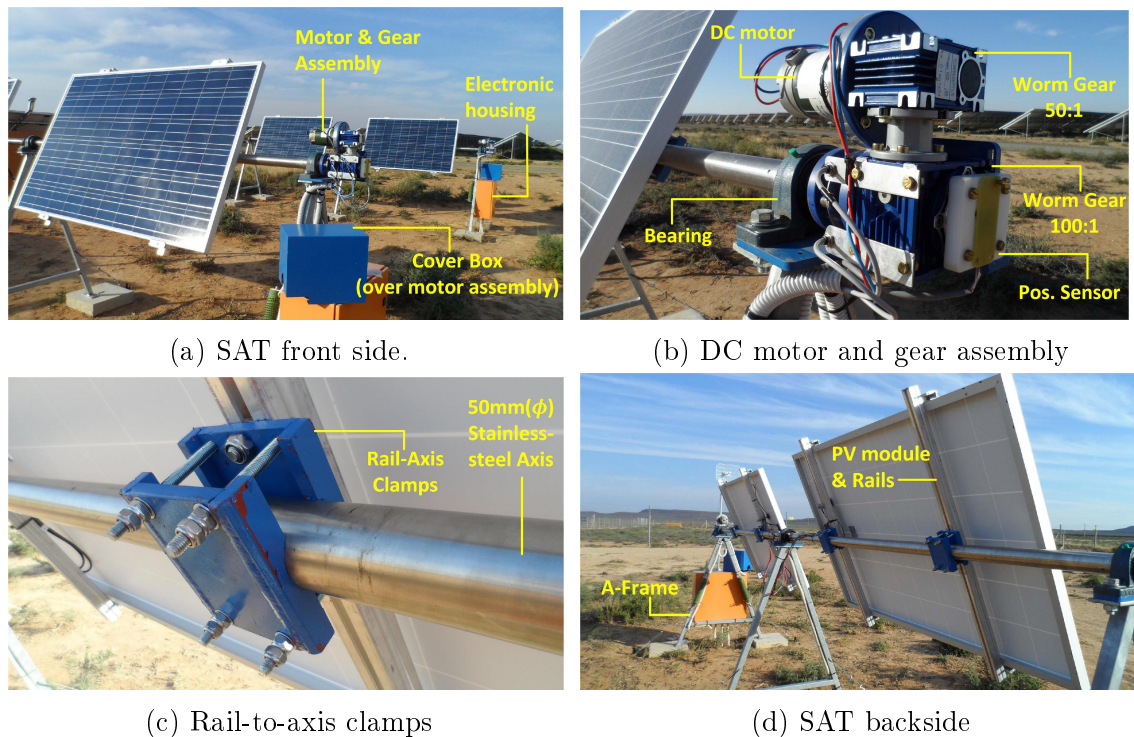


Figure 5.21: Mechanical assembly and installation of the SATs.

## 5.5 Software design

### 5.5.1 SAT software design overview

This section presents a conceptual overview of the algorithms and software routines implemented, which allow the SAT system to operate as intended. As with the firmware implementation of the MC device, Atmel-Studio 6.2 is also used as the software development platform. Therefore, all code is written in the C programming language, with further details as already presented in Chapter 4.6.1.

The firmware routine of the SAT system is divided into three categories and each will be discussed in this section:

<sup>3</sup>Due to time constraints, it was the responsibility of another student, L. Joubert to do the required calculations regarding the details of the mechanical design.

1. Single-axis-tracker modes: Presents all of the different operation modes which provide the tracker's dynamic behaviour.
2. Motor control: Reveals how the control system feedback routine is applied, where the trackers are aligned to a pre-determined tilt angle.
3. User access/control and communication: Presents the active-communication interface, which allows the MC and a user to extract or send information and commands to the SAT.

### 5.5.2 Software application of the tracking algorithm

The SAT tilt angles are defined with respect to the  $0^\circ$  reference line, as indicated in Figure 5.22. As evident from this tilting diagram, the following relationships are established between the collector direction of the PV module and tilt angle:

$$-90^\circ \leq \varepsilon^\circ < 0^\circ : \textit{East} \quad (5.48)$$

$$0^\circ < \varepsilon^\circ \leq 90^\circ : \textit{West} \quad (5.49)$$

$$\varepsilon^\circ = 0^\circ : \textit{Solar Noon} \quad (5.50)$$

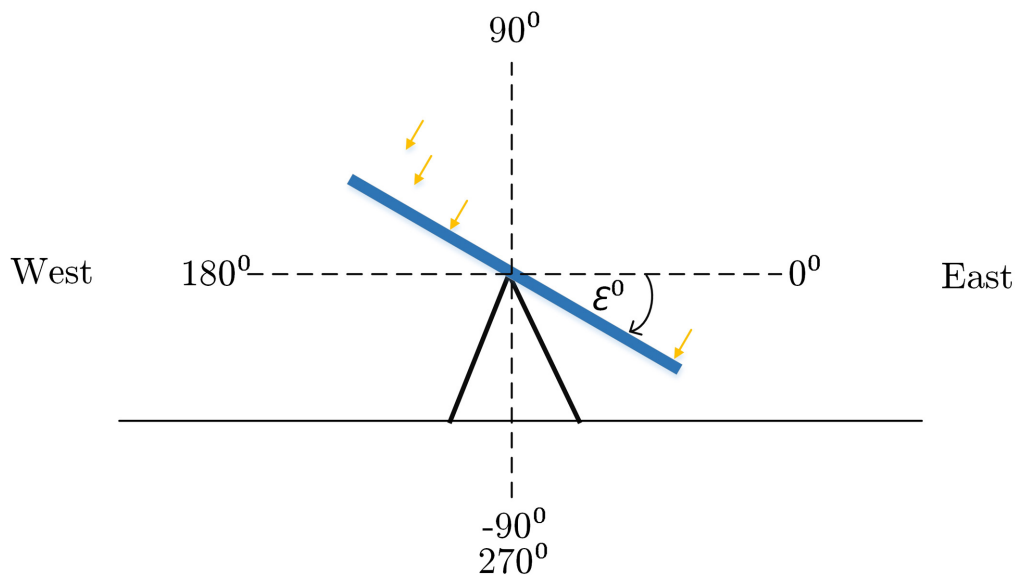


Figure 5.22: Illustration of the SAT defined tilt angles.

The tracking algorithm consists of three segments as illustrated in Figure 5.23. The first part of the tracking algorithm sequentially applies the equations 5.1 to 5.9, as presented in Section 5.2 to find the ideal tilt angle  $\varepsilon^\circ$ . Below is the simplified flow-diagram of the TA applied to determine the ideal tilt angle.



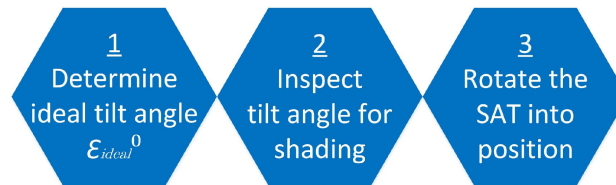
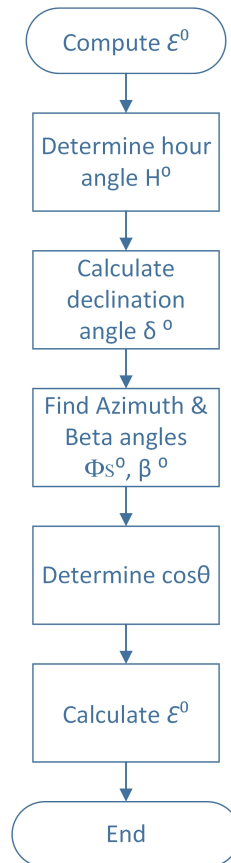


Figure 5.23: Illustration of the SAT defined tilt angles.

Figure 5.24: Flow diagram of the tracking algorithm which determines the ideal SAT tilt angle  $\varepsilon^\circ$ .

Tracking initiates the moment when sunrise starts and ends with sunset. However, due to the complexity of inter-module shading during the early morning and late afternoon hours, the tracking algorithm is separated into two parts, namely normal tracking and backtracking. With backtracking applied during periods of low sun altitudes and normal tracking during periods where table-on-table shading is not of concern.

As mentioned, the TA is executed once every minute, which is found to be adequate for accurate tracking. It is redundant to continuously calculate the optimal tilt angle, since the position of the sun progresses gradually over time. The TA also aims to reduce motor activity, by allowing some degree of deviation ( $\omega^\circ$ ) from the ideal tilt angle  $\varepsilon_{ideal}^\circ$ . The allowed degree of deviation  $\omega^\circ$  is set at  $2.5^\circ$  for this system. This is found to provide a good balance between reduced motor activity and a negligible loss to received irradiance.

### Normal tracking routine

Normal tracking simply refers to the tracker being aligned with the optimal tilt angle ( $\varepsilon_{ideal}^\circ$ ). The TA compares the current position of the SAT, denoted by  $\varepsilon_{now}^\circ$ , to  $\varepsilon_{ideal}^\circ$  and when the condition of equation (5.51) is no longer true, will the SAT be realigned.

$$(\varepsilon_{ideal}^\circ - \omega^\circ) < \varepsilon_{now}^\circ < (\varepsilon_{ideal}^\circ + \omega^\circ) \quad (5.51)$$

Where the variables in equation 5.51 represent:

- $\varepsilon_{ideal}^\circ$  = Ideal tilt angle
- $\varepsilon_{now}^\circ$  = Current tilt position of the tracker
- $\omega^\circ$  = allowed deviation from the ideal tilt angle

As mentioned, when (5.51) is no longer valid, the SAT is realigned to a tilt angle of  $\omega^\circ$  ahead of  $\varepsilon_{now}^\circ$ . This movement is illustrated in Figure 5.25a. As the sun progresses, the ideal tilt angle will eventually come into alignment with the tracker's current angular position, as demonstrated in Figure 5.25b. Finally, the sun will then move past the position of the SAT as shown in Figure 5.25c. Then, when the Sun has moved  $\omega^\circ$  degrees ahead of  $\varepsilon_{now}^\circ$ , equation 5.51 will be violated and the SAT will once again be moved at a position of  $\varepsilon^\circ + \omega^\circ$ , which is  $\omega^\circ$  degrees ahead of the ideal tilt angle, for the particular sun position.

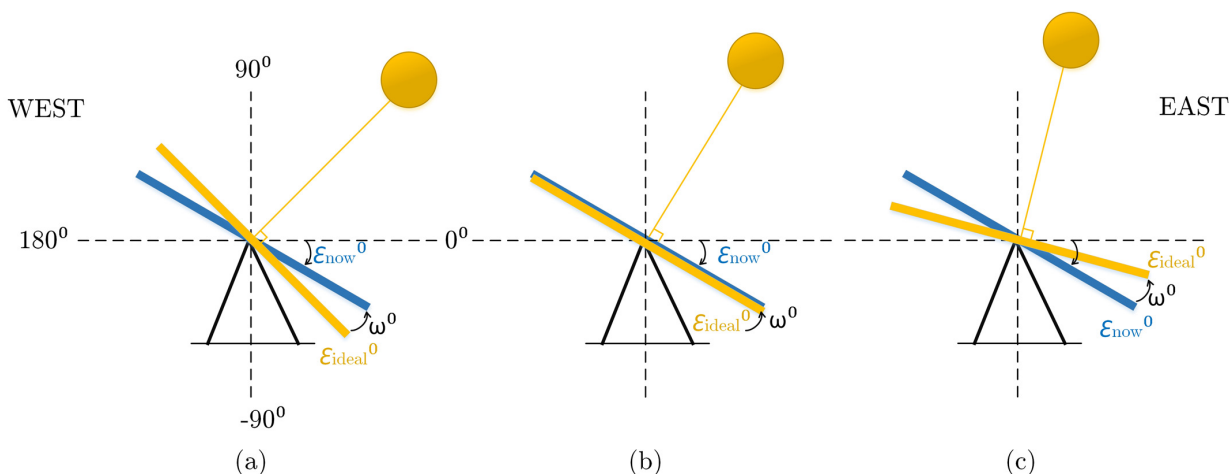


Figure 5.25: Normal tracking illustrated. Illustration a, b and c represents tracker positions as the sun progresses during hours associated with normal tracking.

The conceptual software routine applied to implement the normal tracking routine, is illustrated by Figure 5.26. From this flow-diagram it can be seen that even during the normal tracking mode, the TA still accounts for potential inter-module shading. If shading does occur, the TA shifts to a backtracking routine, which is explained in the text to follow.

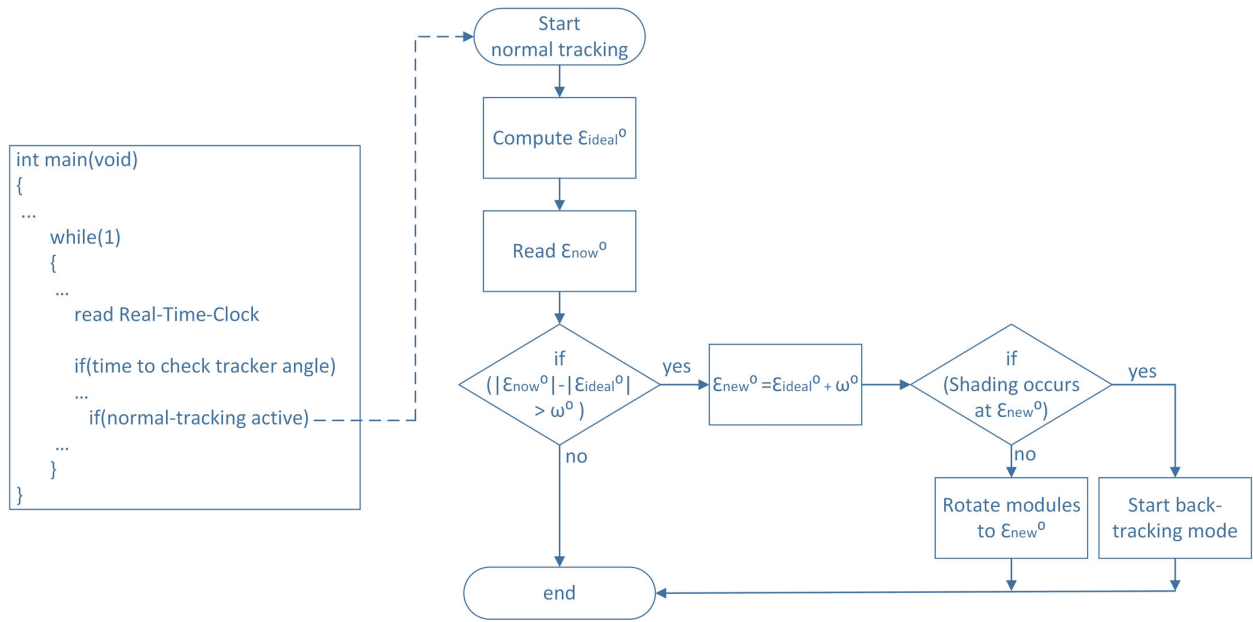


Figure 5.26: Overview of the software routine used to apply the normal tracking procedure.

### Backtracking routine

Backtracking is an iterative process where a tilt angle is identified that will avoid panel-on-panel shading. Backtracking is applied during periods of low sun altitudes, namely early morning hours (sunrise) and late afternoon (sunset). The backtracking strategy for sunrise and sunset is different from one another, but the concept remains the same.

#### Backtracking during sunrise:

When the time of geometric sunrise appears, which is when the sun's midpoint is on the Horizon [44, p. 209], the SAT is set at zero degrees (horizontal). Then, the algorithm searches for a tilt angle which will not result in inter-shading, starting from zero degrees. It must be noted that, although the sun may visually appear earlier in time on the horizon, due to atmospheric refraction [44, p. 209], the algorithm does not react on this, but only accounts for geometric sunrise and sunset. By not accounting for atmospheric refraction and using the geometric sunrise and sunset as reference point, a small degree of safety is gained, which further ensures that the panels will not cast a shadow onto one another. When the ideal backtracking tilt angle  $\varepsilon_{bt}^{\circ}$  is found, the SAT will not be tilted towards this angle immediately, since this would result in a more frequent use of the motor, as previously mentioned. Only when the difference between the current tilt angle  $\varepsilon_{now}^{\circ}$  and the backtracking angle  $\varepsilon_{bt}^{\circ}$  is greater than the allowed degree of deviation,  $\omega^{\circ}$ , will the SAT tilt towards  $\varepsilon_{bt}^{\circ}$ . In backtracking mode the, allowed degree of deviation is determined by the condition of 5.52 In Figure 5.27 the backtracking strategy during early morning hours is illustrated. As depicted by Figure 5.27, three angles are essential for the backtracking algorithm, which are: The ideal tilt angle  $\varepsilon_{ideal}$ , which results in maximum irradiance exposure; the ideal backtracking angle  $\varepsilon_{bt}$ , which avoids inter-module shading and applies maximum irradiance exposure; current module tilt angle  $\varepsilon_{now}$ .

$$|\varepsilon_{bt}^{\circ}| - |\varepsilon_{now}^{\circ}| \leq \omega^{\circ} \quad (5.52)$$

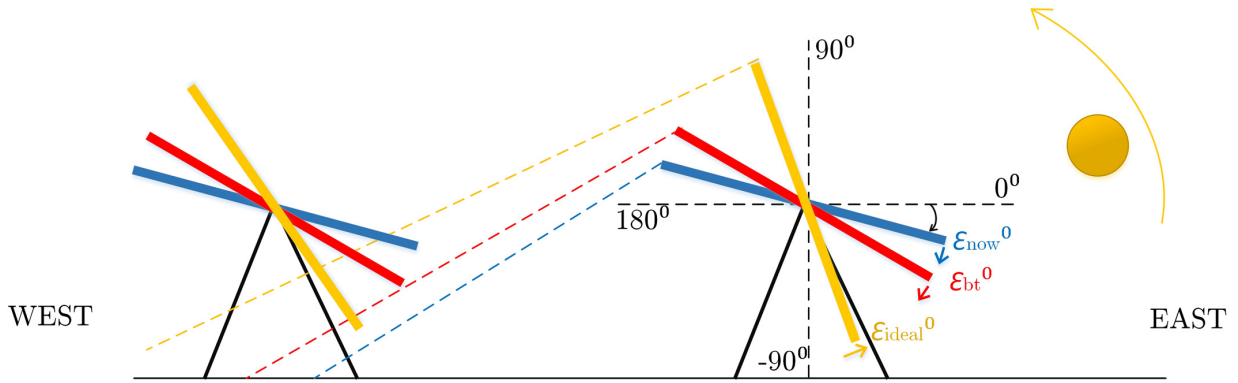


Figure 5.27: Backtracking during sunrise, with the difference in projected shadows for the three different tilt angles. The arrows refer to direction of movement.

The movement of the tracker with regards to the three angles, is illustrated by Figure 5.27. During backtracking, the PV module's tilt angle and the backtracking angle advances towards a bigger absolute tilt angle (descend), to allow for maximum irradiance exposure. On the other hand, should the tracker follow the ideal normal tracking angle  $\varepsilon_{bt}^{\circ}$ , the PV module's absolute tilt angle would gradually decrease (ascend towards horizontal position), but this would result in module shading. Backtracking during sunrise is ended when the condition of equation 5.53 is true:

$$|\varepsilon_{bt}^{\circ}| \geq |\varepsilon_{ideal}^{\circ}| \quad (5.53)$$

An overview of how the backtracking algorithm calculates and implements backtracking during the morning, is displayed in Figure 5.29.

#### Backtracking during sunset:

During the afternoon, backtracking is initiated when the first inter shadow is projected for the  $\varepsilon_{ideal}^{\circ}$  tilt angle. The TA, executed during normal tracking, always factors in the possibility of a new tilt angle casting a shadow onto another module. With  $\varepsilon_{bt}^{\circ}$  determined as the absolute maximum tilt angle, where shading is still avoided, the SAT is tilted  $2.5^{\circ}$  ( $\omega^{\circ} = 2.5^{\circ}$ ) ahead ( $\varepsilon_{now}^{\circ}$ ), as displayed in Figure 5.28. The tracker is moved ahead of  $\varepsilon_{bt}^{\circ}$  by  $2.5^{\circ}$  to avoid regular motor activity, as well as to account for the tracking interval, which is monitored only once every minute. The SAT is then kept stationary at this tilt angle ( $\varepsilon_{now}^{\circ}$ ), until  $\varepsilon_{bt}^{\circ}$  has caught up with  $\varepsilon_{now}^{\circ}$ . As soon as the condition of equation 5.54 is true, the panels are tilted ahead to  $\varepsilon_{bt} - \omega^{\circ}$ . Backtracking for the late afternoon ends, when  $\varepsilon_{bt}$  settles at  $0^{\circ}$  (horizontal).

$$\varepsilon_{bt}^{\circ} - \varepsilon_{now}^{\circ} \leq 0^{\circ} \quad (5.54)$$

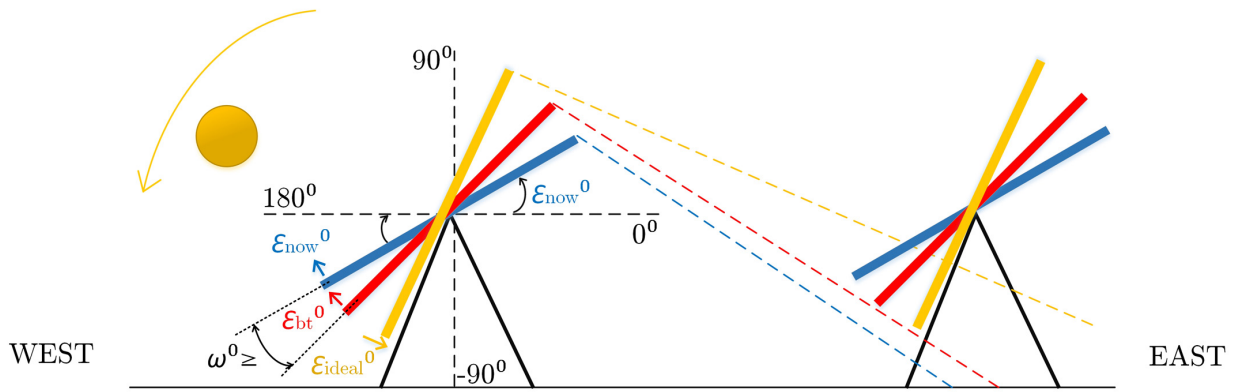


Figure 5.28: Backtracking during sunset, with the shadow position indicated for the three different tilt angles  $\epsilon_{ideal}^0$ ,  $\epsilon_{now}^0$  and  $\epsilon_{bt}^0$ .

**Software implementation of the backtracking algorithm:**

As mentioned, calculating the backtracking angle is an iterative process, based on the relationship between the shadow projected between the trackers, as well as the physical available distance between the trackers. Equations 5.1 to 5.19 are all utilised to implement the normal tracking and backtracking algorithms, as explained. This is demonstrated by the software flow diagrams in Figure 5.29. It should be noted that, the backtracking algorithm makes use of  $0.25^\circ$  increments, to test for a new potential tilt angle  $\epsilon_{bt}$ . This  $0.25^\circ$  increment value is determined from iterative testing.

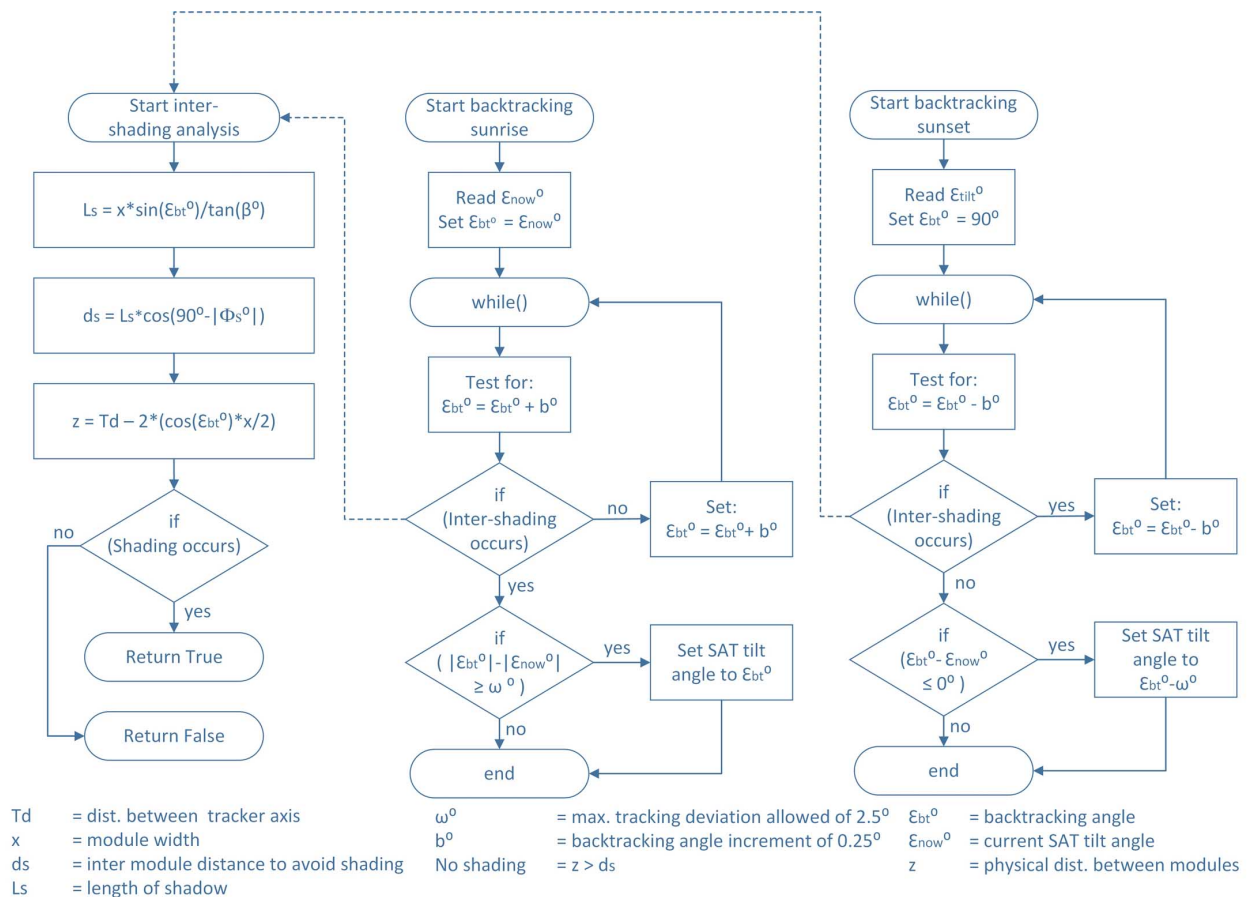


Figure 5.29: Backtracking algorithm flow diagram for sunset and sunrise.

### 5.5.3 SAT operation modes

The SAT system has six modes of operation, each with a unique functionality and accompanying software routine to execute the desired behaviour.

- Mode 1: Normal tracking mode
- Mode 2: Backtracking mode
- Mode 3: Stationary mode
- Mode 4: Night mode
- Mode 5: Safety mode
- Mode 6: Self-cleaning mode

#### Mode 1: Normal tracking mode

As discussed in Section 5.5.2, during this mode the SAT aligns the modules with the ideal tilt  $\varepsilon_{ideal}^{\circ}$  angle that results in the highest exposure of irradiance.

#### Mode 2: Backtracking mode

As discussed in Section 5.5.2, during this operation mode panel-on-panel shading is avoided during periods of low solar altitude (sunrise and sunset).

#### Mode 3: Stationary mode

The SAT system provides the user with the option of assigning a fixed tilt angle, which will force the SAT to remain stationary in position. Only if one of the following conditions occur, will the SAT abandon the stationary mode:

- Emergency safety routine is initiated.
- Tracking is resumed.
- A software or hardware reset is executed.
- When self-cleaning mode (refer to Section 5.5.3) is initiated due to rainfall or morning dew. It should be noted that this self-cleaning mode can only commence if the SAT is enabled for this mode, otherwise this will not affect the operation of Mode 3.

#### Mode 4: Night mode

Night mode is initiated when the altitude angle  $\beta^{\circ}$  of the sun is determined as equal to or below zero degrees. During this mode the SAT is tilted into a horizontal ( $\varepsilon = 0^{\circ}$ ) position. Night mode is ended when sunrise occurs and  $\beta > 0^{\circ}$ . Only if the following events occur, will the SAT be taken out of or prohibited from executing night mode:

- A fixed tilt angle is assigned (Mode 3 active)
- If a safety mode is imposed (Mode 5 active). Should the safety mode be ended, during the night, then the tracker will move into the default tracking routine for that moment in time, which is night mode.
- Temporarily interrupted when self-cleaning mode (Mode 6) is initiated.

### Mode 5: Safety mode

Any irregular internal behaviour will initiate a safety routine. This mode has the highest authority and overrides all other system functionality. To protect the tracking system, only a hardware or software restart, or a dedicated user command (Resume-Tracking(), Set-Tilt-Angle()) can retire the SAT out of safety mode. The scenarios presented below, will cause the safety mode to be activated. In the firmware routine, each scenario also receives a dedicated variable to identify the origin of the safety mode being initiated.

**Over-tilt:** As mentioned in Section 5.3.10, the SAT has two proximity sensors. Each sensor generates an external interrupt when the SAT rotates beyond  $\pm 90^\circ$ . Over-tilt may occur due to a faulty position sensor reading, where either the position sensor itself is faulty, has been removed or is no longer in close proximity with the rotating magnet. When the external interrupt vector executes, the H-bridge MOSFET driver is disabled and a 50 % duty cycle is applied (should the driver fail to be disabled). The tracker's operation mode is changed to mode five and a flag is set to indicate on which side the tracker over-tilted.

**Immobility:** If the SAT fails to rotate or the time elapsed to reach the intended angle exceeds 50 sec, the SAT is placed into safety mode. This event can occur if the motor is either stuck in position, or movement is restricted so that the tracker rotates slowly. If the motor is physically obstructed and the over-current detection is not triggered, this ensures that the fault is identified.

**High wind speeds:** For wind speeds greater than 12 m/s (user-defined), the panels are tilted into a flat horizontal ( $0^\circ$ ) position as demonstrated in Figure 5.30. The master-controller monitors the wind-speed and takes control of the SAT, should the wind speed exceed the limit. Even if a user resumes normal tracking (by applying a restart), the MC will force the SAT to default back into safety mode. The SAT has a waiting period of 20 minutes (user defined) after which no more high wind speeds ( $\geq 12$  m/s) have been identified. If the waiting period is exceeded, normal operation is resumed by the SAT system. Figure 5.30 illustrates the position adopted during high wind speeds.

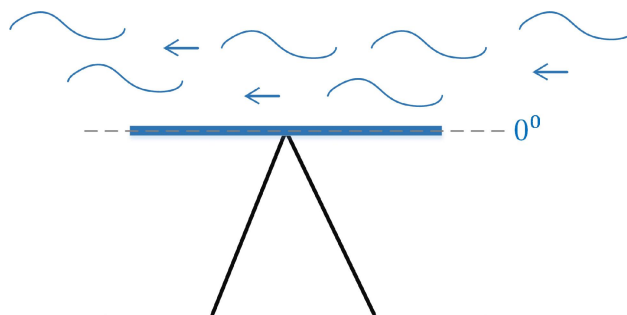


Figure 5.30: Emergency  $0^\circ$  tilt initiated during high wind speeds.

**Over-current detected:** Over current detection is set as 13.5 A as discussed in Section 5.3.8. If the MCU reads a high ADC voltage input over the  $R_{sense}$  resistor or receives an external interrupt from the comparator circuitry, the DC motor is disabled and the safety mode is activated.

### Mode 6: Self-cleaning mode

As part of the dust-mitigation strategy, this mode allows a tracker to make use of natural occurring precipitation (rainfall and morning dew) to initiate a self-cleaning process. When

rainfall occurs the MC informs the SAT, which then rotates the modules into the direction of the rain, at a  $\pm 45^\circ$ . In the morning, Figure 5.31 illustrates the self-cleaning tilt positions.

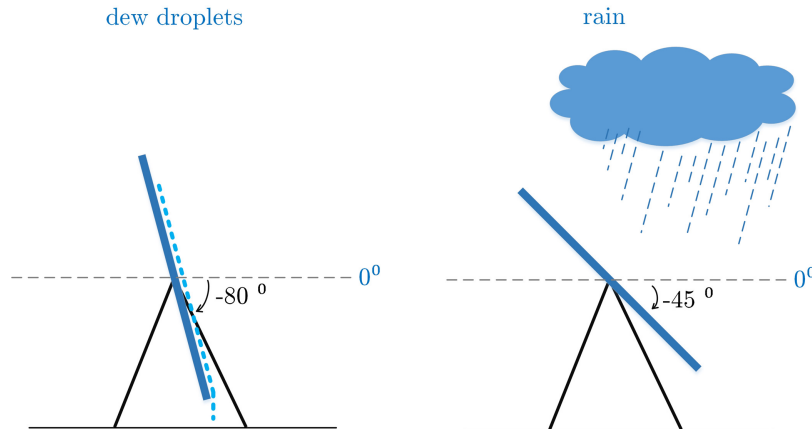


Figure 5.31: SAT tilt angles adopted for self-cleaning mode.

### 5.5.4 Motor control and SAT positioning

The algorithm responsible for rotating the SAT consists of three segments:

A PWM signal generated by the OC1A output pin of the MCU, is applied to the H-bridge (HIP4082) MOSFET gate-driver, which in turn controls the input to the DC motor. The direction of tilt is determined by  $D$  as demonstrated in Table 5.4. However, the value of  $D$  [%] is also determined by the input voltage  $V_{BAT}$  of the battery bank. As demonstrated by equation 5.55, the value of  $D$  is firstly adjusted to stay within the DC motor's rated voltage restriction  $V_{DC(rated)}$ . Equations 5.56 and 5.57 are applied afterwards, to define the direction of rotation. The frequency of the PWM signal is set at 20kHz.

Table 5.4: SAT direction of rotation for applied duty cycle ( $D$ )

Direction Of Rotation		
Forward (East-West)	Backward (West-East)	Stationary
$D < 50\%$	$D > 50\%$	$D = 50\%$

$$D_{rated} = \frac{V_{DC(rated)}}{V_{BAT}} \times 100\% \quad (5.55)$$

$$D_{max} = 50\% + \frac{D_{rated}}{2} \quad (\text{Forward rotation}) \quad (5.56)$$

$$D_{max} = 50\% - \frac{D_{rated}}{2} \quad (\text{Backward rotation}) \quad (5.57)$$

Details regarding the software set up of the PWM signal are presented in Appendix C (Section C.4). The assigned maximum duty cycle of the PWM signal is not immediately applied. Instead  $D$  is slowly ramped up and stops to increase when either the  $D_{max}$  value is reached or the tilt angle has been reached. This is done to decrease the stress on the mechanical parts, by allowing the tracker system to slowly come into motion. It is also



found that by not allowing the PWM signal's duty-cycle to be ramped up slowly, a high initial current ( $\sim 10$  A) is drawn.

### 5.5.5 ADC set up

Pin-30 (ADC6) and pin-31 (ADC7) of the MCU are dedicated to reading the current  $I_{BAT}$  and voltage  $V_{BAT}$  input to the DC motor, from the battery bank. As mentioned, the voltage measurement is ultimately required to ensure the maximum rated voltage is not exceeded by the PWM signal. The current value is required to ensure that over current is detected. The ADC functionality of the SAT system is set to operate at a 10 bit resolution. More details regarding the software set up are provided in Appendix C, section C.4.

### 5.5.6 Reading the position sensor

The SAT tilt angle is retrieved from the AS5048A position sensor, by means of an SPI connection. It is important to consider that the position sensor only has one SPI mode of operation. The SPI interface of the position sensor reads on every falling edge and writes on the MISO line every rising edge, with the SPI clock (SCK) pin idling low [98, p.10]. Thus, to accommodate this interface, both the isoSPI (LTC6820) and the ATmega1284 MCU is set up accordingly. Finally, due to the reasons mentioned in Section (hardware LTC6820), the clock frequency is set as 156 kHz.

When the angular data is requested from the position sensor the isoSPI is first enabled and then selected by assigning a logic high and low to the EN (enable) and CSn (chip select low) pins. It must be noted that after each 16 clock cycles the CSn has to be set back to a high status, as advised in datasheet [98, p.10]. The process of retrieving the angle data from the position sensor is displayed in Figure 5.32

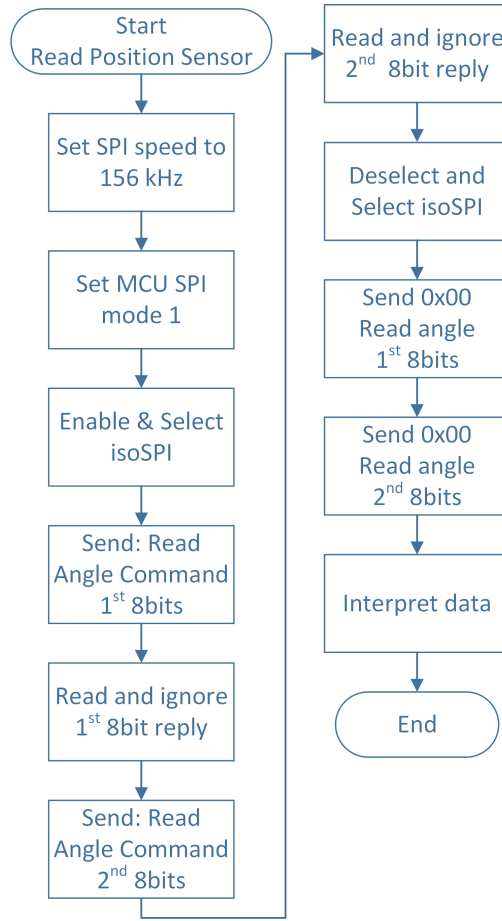


Figure 5.32: Overview of the software routine applied to collect angular data from the position sensor (AS5048A) via the isoSPI (LTC6820) chip.

When the 14-bit data angle is finally received, a parity check is performed to ensure data validity. If successful, the value of the angle read  $Angle_{True}$ , which is anything from  $0^\circ - 359.978^\circ$  (14 bit resolution), is calculated as follows:

$$Angle_{True} = Angle_{RAW} - \frac{1}{16384.0} \times 360.0^\circ \quad (5.58)$$

The angle convention used for the SAT system, is different to the reference point of the position sensor, as indicated in Figure 5.33. To adapt the desired SAT tilt angle, to the angle convention of the position sensor, equations 5.59 and 5.60 are applied:

$$\text{if } 0^\circ < \varepsilon_{SAT} \leq 90^\circ : \Phi_{POS} = 360^\circ - \varepsilon_{SAT} \quad (5.59)$$

$$\text{if } -90^\circ \leq \varepsilon_{SAT} < 0^\circ : \Phi_{POS} = |\varepsilon_{SAT}| \quad (5.60)$$

When an angle is read from the position sensor and the angle is to be translated to represent the physical tilt angle of the SAT, equations (5.61) and (5.62) are applied.

$$\text{if } 0^\circ < \Phi_{POS} \leq 180^\circ : \varepsilon_{SAT} = -(\Phi_{POS}) \quad (5.61)$$

$$\text{if } 180^\circ \leq \Phi_{POS} < 360^\circ : \varepsilon_{SAT} = 360^\circ - \Phi_{POS} \quad (5.62)$$

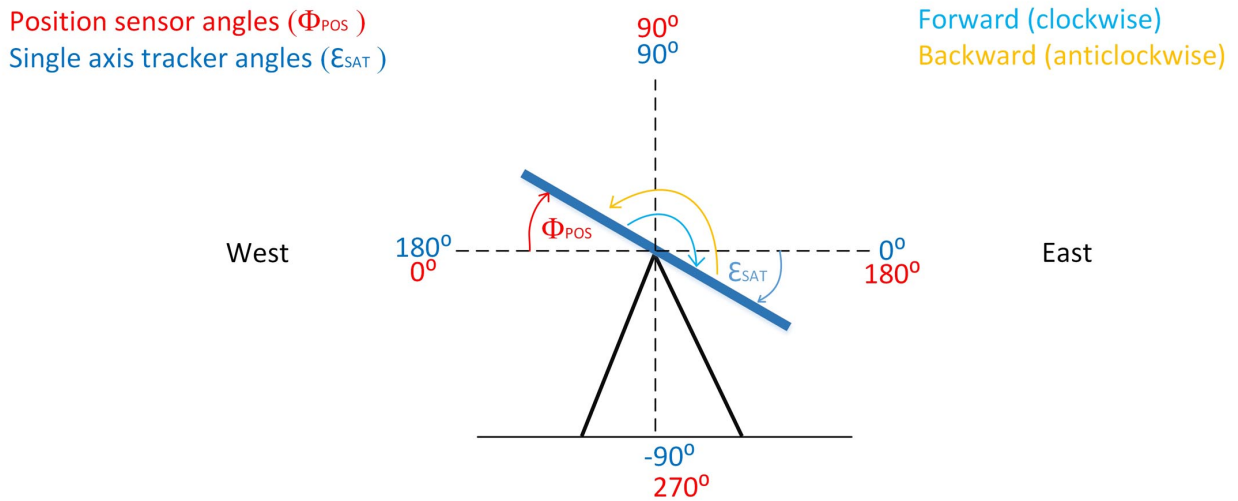


Figure 5.33: Illustration of the reference angles of the SAT system and the position sensor.

When the SAT is to be set to a specific tilt angle  $\epsilon_{SAT}$ , then the desired SAT angle is converted to the angular reference of the position sensor, as illustrated by Figure 5.34a. However, when the angle is read from the position sensor  $\Phi_{POS}$ , then it is translated accordingly to the angle of the defined SAT position  $\epsilon_{SAT}$  as depicted in Figure 5.34b.

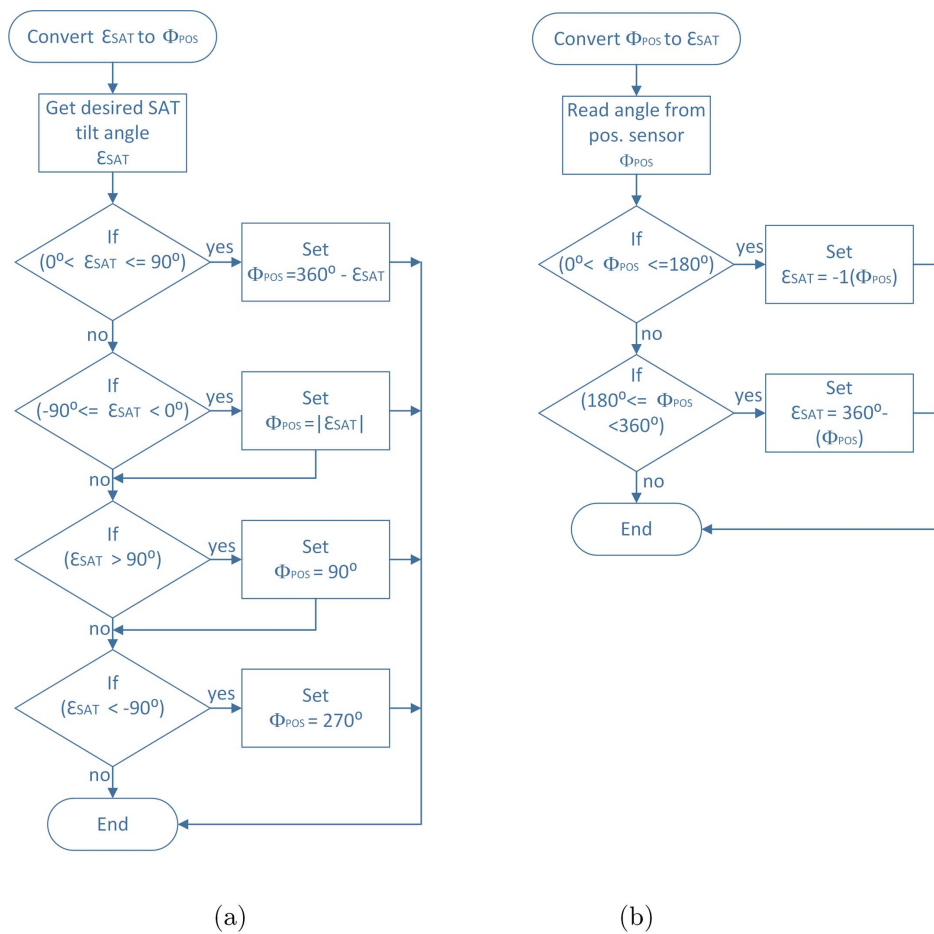


Figure 5.34: Software routines of angular translation. a) Routine to translate  $\epsilon_{SAT}$  to angular reference of position sensor  $\Phi_{POS}$ . b) Translation of  $\Phi_{POS}$  to  $\epsilon_{SAT}$ .

### 5.5.7 SAT communication and software commands

Each tracker is regarded as a slave device, with the MC serving as the master device. Communication with the tracker(s) is established with an RS485 connection and the USART of the MCU. USART0 of the MCU on the SAT circuit board is used to transmit and received data and the set up is exactly the same as for the MC device, described in Chapter 4.6.3. The goal of the SAT communication is firstly to provide angular data to the MC, which is requested every minute. Secondly, the MC serves as intermediate device for communication between a user and a SAT.

The same command structure is replicated as applied for the MC. This refers to the commands separated into three groups namely HEX-41, HEX-42 and HEX-43 commands. The HEX-41 and HEX-42 commands are standard set up and data retrieval commands, whereas the HEX-43 commands are listed as special commands. As with the MC, a python based interface is developed and integrated with the on line graphic user interface, for the website that hosts access to the research facility. The available user functions and descriptions are provided below.

#### HEX-41 and HEX-42 commands

Table 5.5: HEX-41 and HEX-42 commands

Command 0x41		Command 0x42	
Sub-command	Function()	Sub-command	Function()
0x01	Get-Device-Info()	0x01	Get-Setup()
0x02	Send-Device-Info()	0x02	Send-Setup()
0x03	Get-RxBuf()	0x03	Get-Tracker-Lengths()
0x04	Get-RTC()	0x04	Send-Tracker-Lengths()
0x05	Send-RTC()	0x05	Get-Angle-Position()
0x06	Set-Address-Baudrate()	0x06	Set-Tilt-Angle()
0x07	Get-Description()	0x07	Resume-Tracking()
0x08	Send-Description()	0x08	Send-Tracker-Status()
		0x09	Get-Motor-Setup()
		0x0A	Send-Motor-Setup()
		0x0B	Get-Position-Sensor-Details()
		0x0C	Deactivate-Motor()
		0x0D	Adapt-To-Weather()

**Get-Device-Info():** Retrieves the following SAT information:

- Device ID: This specifies the type of device. For a SAT the device ID is 2030.
- Software version: Specifies the running software version on the SAT.
- Serial number: The serial number format is YYMMNNNN with YY as year (16 for the year 2016), M as Month and NNNN as the device number .

**Send-device-info():** This function allows the user to specify a serial number for the SAT, which serves as a unique number that differentiates one SAT from another. Example of a serial number is: 16030002. Therefore, the serial-number informs the user that the device

was manufactured in the year 2016, during March and it was the second (02) SAT board manufactured during this month.

**Get-RTC():** Provides the current date and time that resides on the SAT itself. The RTC is provided in the following format: Weekday, YYYY-MM-DD, hh:mm:ss for example: Sunday 2016-05-15 21:59:20

**Send-RTC():** Updates the RTC of the SAT, thus synchronising the clock of the SAT. When the RTC is sent, the position of the sun is recalculated and the tracker will be advanced to the appropriate tilt angle. Normal tracking will however not be resumed when the RTC is sent to the SAT and the SAT is operating in either safety mode (Mode 5) or stationary mode (Mode 3). Should the SAT be in self-cleaning mode (Mode 6) and a new RTC is received, then normal tracking will be resumed as the SAT will exit self-cleaning mode.

**Send-Address-Baudrate():** Updates the device address and the baud rate of the SAT. Addresses 6, 7 and 8 are reserved for a connected SAT system. For this function only, the MODBUS reply message will be a 7 digit (instead of 5 digit) MODBUS reply, if this set up has been received. The format of the MODBUS reply is as follows:

SAT address	Command	Sub-command	New SAT address	Baudindex	CRC 1	CRC 2
-------------	---------	-------------	-----------------	-----------	-------	-------

Figure 5.35: MODBUS reply message of SAT after address and baud-rate are set.

**Send-description()** and **Get-description():** Different SAT devices are distinguished from one another with a user defined description (name). When the description of the SAT is retrieved with Get-description(), an example of the description would be: *Single Axis Tracker 1*

**Send-Setup()** and **Get Setup():** Each SAT has a set up (defined by user entry) regarding basic operation and information about the location of the SAT. The following information is provided/retrieved when Send-Setup()/Get-Setup is executed:

- Track interval : Specifies the interval [minutes] when the tilt angle of the SAT must be monitored and adjusted if necessary.
- Degrees ahead ( $\omega^\circ$ ): This is the number of degrees  $\omega^\circ$  by which the SAT is allowed to be ahead or behind the ideal tilt angle, as determined by the tracking algorithm.
- Degrees to iterate shading ( $b^\circ$ ): When backtracking is in progress, the algorithm must identify an angle at which shading will be avoided. This is however an iterative process. The value of  $\omega^\circ$  defines the increments of this iterative process.
- Latitude ( $L^\circ$ ): Refers to the latitude angle of where the SAT is physically placed. L is defined as positive for the Northern hemisphere and negative for the Southern hemisphere.
- Longitude: Refers to the longitude angle of where the SAT is physically placed. Angles in the Eastern hemisphere are regarded as negative and positive in the Western hemisphere.
- Time Meridian: Refers to the local time meridian of the location where the SAT is placed. Locations east of the meridian are regarded as negative, with west as positive. Thus, for any location in South Africa this angle will always be  $-30^\circ$ .

- Self cleaning mode: This setting activates or deactivates the self cleaning mode (Mode 6) of the SAT.

**Get-Tracker-Lengths()** and **Send-Tracker-Lengths()**: **Get-Tracker-Lengths()** retrieves the lengths of the SAT set up. The only two dimensions of importance in terms of the physical set up of the SAT is:

- The distance between the one axis to the other axis of each SAT [m].
- The module length (width) of the PV panels from east to west [m].

**Send-Tracker-Lengths()** allows the user to specify the above mentioned dimensions. These dimensions are illustrated in Figure 5.36. These dimensions are used by the tracking algorithm to ensure that inter shading is avoided.

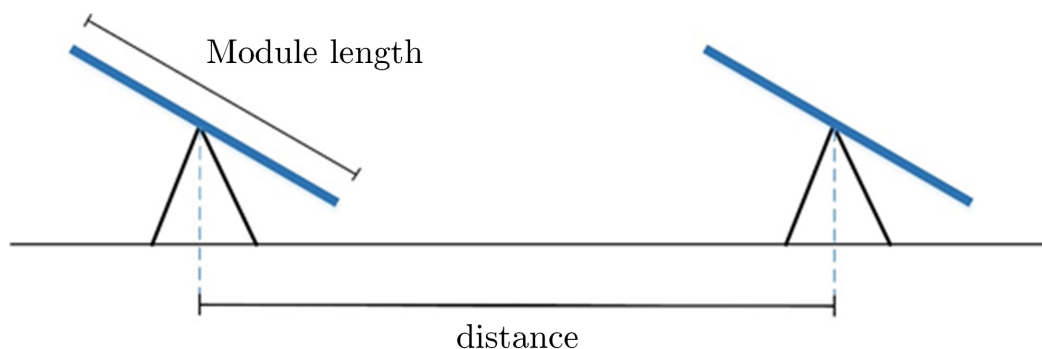


Figure 5.36: User defined tracker lengths of SAT set up.

**Get-Angle-Position()**: Retrieves the current tilt angle and mode of the SAT. Table 5.6 clarifies the different modes of operation:

Table 5.6: Different SAT modes of operation

Mode	Description
1	Normal Tracking
2	Backtracking mode
3	Stationary mode (tilted at specified angle)
4	Night mode
5	Safety mode
6	Self-cleaning mode

**Set-Tilt-Angle()**: The single axis tracker provides the user with the option of assigning a fixed tilt angle. When executed, the SAT operates in Mode 3.

**Resume-Tracking()**: Allows the SAT to synchronise with the normal tracking routine. This mode would be initiated, by the user, when the SAT is either operating in Mode 3, Mode 5 or Mode 6.

**Get-Tracker-Status()**: This function provides the state of operation for the SAT. The details provided are presented below:

- SAT operation: Warning and possible cause is provided should the SAT be in any other mode other than tracking the Sun.
- Supply voltage [V]: Voltage input from battery bank.
- Supply current [A]: Current input from battery bank.
- Tracking mode description: Normal tracking, Backtracking, Stationary, Self-Cleaning, Night-Mode, Safety-Mode

**Send-Motor-Setup()** and **Get-Motor-Setup()**: The DC motor connected to the SAT has its own rated voltage and current values. Therefore, to avoid exceeding these rated values, a motor set up must be completed by executing the Send-Motor-Setup() command. The following set-up values are sent to the SAT:

- DC motor rated voltage [V]
- DC motor rated current [A]

Get-Motor-Setup() simply provides information regarding the rated voltage and current set up of the DC motor. This function also returns the value of the Duty cycle currently applied to the DC motor. If the supply voltage is more than the rated voltage of the DC motor, then the Duty cycle will be less than 100 %, otherwise, it should be 100 %.

**SAT-Adapt-To-Weather()**: Specifies whether or not the SAT must react to specific weather conditions. If high wind speeds occur, this setting allows the MC to take control of the SAT and guide it to safety. If a tracker is activated for the self cleaning mode, this once again allows the MC to inform the SAT of the event and to react accordingly. 1 = activated and 0 = deactivated.

### HEX-43 commands

The available HEX-43 user commands are displayed in Table 5.7:

Table 5.7: HEX-43 user commands list.

Command 0x43	
Sub-command	Function()
0x01	Get-Activation()
0x02	Send-Activation()
0x03	Get-Sun-Tracking-Parameters()
0x04	Check-Back-Tracking()
0x05	Get-All-SAT-Info()
0x06	Calibrate-SAT-Zero-Position()
0x07	Get-Zero-Cal-Constant()
0x08	Soft-Reset-SAT()

**Send-Activation()** and **Get-Activation()**: Send-Activation() defines if tracking is activated 1 = activated and 0 = deactivated. Get-Activation() specifies whether or not tracking is activated.

**Get-Sun-Tracking-Parameters():** SAT sends all of the necessary information with regards to solar tracking, as listed in Table 5.8

- Get-Device-Info()
- Get-Setup()
- Get-Motor-Setup()
- Get-Zero-Cal-Const()
- Get-RTC()
- Get-Tracker-Lengths()
- Get-Sun-Tracking-Parameters()
- Get-Description()
- Get-Tracker-Status()
- Get-Activation()

Table 5.8: Tracking data provided by the SAT.

Variable	Description
Day number	$n$ -th day of the year
EOT	Equation Of Time
Delta ( $\delta$ )	The declination angle
Hour-Angle (H)	The number of hours before or after solar noon
Azimuth ( $\Phi_S$ )	Represents the Azimuth angle of the sun's position
Beta ( $\beta$ )	Represents the altitude angle of the sun's position
E ( $\varepsilon_{ideal}$ )	The ideal tilt angle that will result in optimal irradiance
Ebt ( $\varepsilon_{bt}$ )	If backtracking is in effect, the backtracking angle is provided
Enow ( $\varepsilon_{now}$ )	This is the current tilt angle of the SAT
d-max	Max. available distance between the SATs for the specific tilt angle
dist	Min. distance required between the panels to avoid inter-shading
Sunrise time	Time of geometric sunrise (where midpoint of sun is on the horizon)
Solar noon time	Time of day when the sun will be directly over the SAT
Sunset time	Time of geometric sunset

**Check-Back-Tracking():** This is primarily a function for diagnostic testing. The function returns all information regarding the backtracking algorithm. This information is displayed in Table 5.9:

Table 5.9: Active backtracking details.

Backtracking details	
Variable	Description
Mode	SAT operation mode
Azimuth ( $\Phi_S$ )	Azimuth angle of the sun
Altitude ( $\beta$ )	Altitude angle of the sun
E ( $\varepsilon_{ideal}$ )	Ideal tilt angle
Ebt ( $\varepsilon_{bt}$ )	Backtracking angle
Enow ( $\varepsilon_{now}$ )	Current tilt angle of SAT
d-max	Maximum physical distance between SAT modules
dist	Distance required between modules to avoid shading

**Get-All-SAT-Info():** When the user requests information from a SAT, via the MC (user executes MC functions Order-All-SAT-Info() and Get-All-SAT-Info() as described in Chapter 4, section 4.6.5) the SAT will respond by executing the Get-All-SAT-Info() user command. This function returns all of the necessary information regarding the complete set-up and



operation of the SAT. The information returned by the SAT, when this function is executed, is the same information as returned by a user request for all of the following SAT functions, simultaneously:

**Calibrate-SAT-Zero-Pos():** The position sensors rely on an input from the magnet, fixed on the axis, to indicate the tilt of the PV modules. However, for the position sensor to read the correct value from the magnet, which represents the true tilt angle, the magnet must be exactly aligned, so that the horizontal position of the tracker is also the zero tilt degree position of the magnet. Instead of following an iterative and tedious process to align the magnet physically, the zero position is simply calibrated in software. The zero position angle cannot be calibrated if the tracker is in normal or backtracking mode, but only when in stationary mode (Mode 3). The new zero calibration angle is saved to the EEPROM.

**Send-Zero-Cal-Const():** This command is primarily for diagnostic purposes. It sends the zero calibration angle of the magnet.

**Soft-Reset-SAT():** A software restart is initiated by this command.

# Chapter 6

## Experimental set up and methodology

### 6.1 Overview

As mentioned, the dust mitigation initiative of this research, serves to investigate different methods of reducing dust soiling on PV modules. The formulation of the Dust Mitigation Strategy (DMS), as well as the implementation thereof, is presented by this chapter. A complete description of each individual mitigation method is provided, as well as the delegation of these methods to specific modules. Details with regards to the coating applied are also discussed, as well as the complete procedure followed to apply the coating. Finally, the periodic cleaning procedures and the stepwise execution of these cleaning routines are provided.

### 6.2 Dust mitigation strategy applied

#### 6.2.1 Stationary PV modules

Two individually tailored DMSs are formulated for both the stationary PV modules and the SATs. The process of thought applied to develop the DMS for this research study, is based on the questions presented below. The resulting DMS is presented by Figure 6.1.

1. Does cleaning PV modules substantially increase PV module power output?
2. How do coated PV modules compare to uncoated modules?
3. How do different cleaning intervals compare to one another and to modules that are left indefinitely?
4. How does water based (wet) cleaning compare to a dry cleaning strategy?

Firstly it is asked whether or not cleaning PV modules will substantially increase PV module power output? From this question, it is asked whether or not coated modules perform better than uncoated PV modules? This could be investigated by comparing coated to uncoated modules for short (1-2 weeks), medium (1-3 months) and long term (6-12 months) cleaning routines, as well as an indefinite period, where modules are never actively cleaned. However, because of a limited number of modules available, it is decided to only include the short and long term cleaning routines in the DMS. It is assumed that this might provide a bigger contrast, if any, between the results for the periodic cleaning routines. The short term for

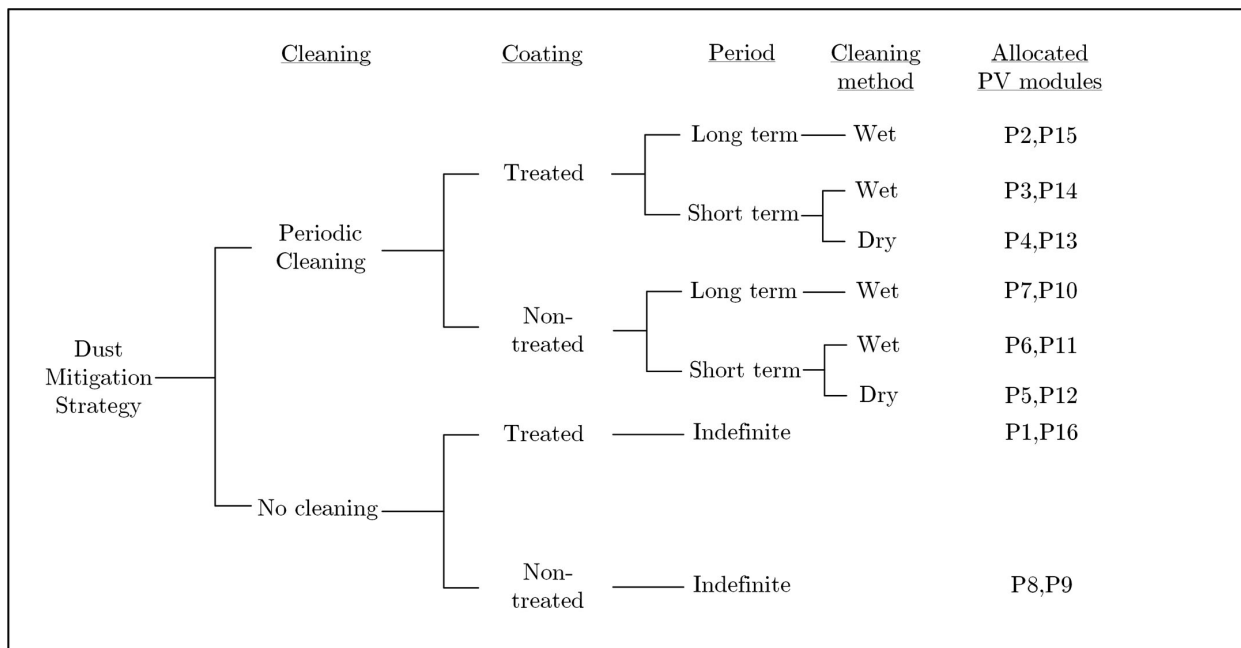


Figure 6.1: Framework of the DMS, consisting of various dust mitigation methods applied to the allocated stationary PV modules.

this project is defined as a biweekly cleaning routine and the long term is defined as a six month interval cleaning routine.

Another question to ask is how a water-based (wet) cleaning strategy compares to a dry cleaning strategy. These two cleaning approaches are therefore also integrated into the DMS. Thus, a wet and dry cleaning strategy is implemented over a short and long term period, on both treated and non-treated PV modules. However, because there are only two sets of long term modules (coated and uncoated) available, only a wet or dry cleaning routine can be allocated. It is decided to only implement a wet cleaning strategy on the modules exposed for six months. This allows a potential comparison to be made between modules which are water washed, to modules naturally cleaned by rain, after a long term period of exposure. Table 6.1 establishes each dust mitigation method. Figure 6.2 indicates the dust mitigation method applied to each corresponding PV module.

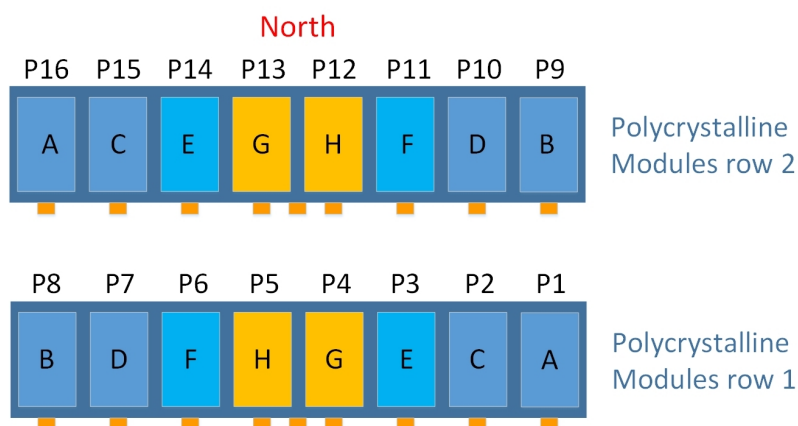


Figure 6.2: Layout of the applied dust mitigation methods to allocated stationary modules.

Table 6.1: Applied dust mitigation methods to individual stationary PV modules

Mitigation method	Treatment	Duration
A	Hydrophobic coating applied.	Left indefinitely
B	Untreated PV module	Left indefinitely
C	Hydrophobic coating applied. Wet clean process.	Long term exposure 6 months
D	Untreated PV module Wet clean process	Long term exposure 6 months
E	Hydrophobic coating applied. Water clean process.	Short term exposure 2 weeks
F	Untreated PV module Water clean process	Short term exposure 2 weeks
G	Hydrophobic coating applied. Dry clean process	Short term exposure 2 weeks
H	Untreated PV module Dry clean process	Short term exposure 2 weeks

Each method of dust mitigation is applied opposite and across from one another. For example, method A is applied in row one, on the far right, whereas this same method is applied in row two, on the far left. Then, once again for method B, the same approach is followed where the two panels, to which the same mitigation strategy is applied, are located opposite and across from one another.

Apart from the fact that all analytical comparisons, between PV modules, are normalised to STC conditions, the reason for this 'opposite-and-across' approach is to minimise the effects of external influences. These include factors such as the influence of wind and rain and more specifically, the direction of the wind and rain received by the PV module surfaces. It is in the opinion of the author that this approach allows general dust deposition to be less partial, which therefore decreases sampling bias. For example, if it is hypothetically assumed that more direct wind contact decreases dust deposition and that the general wind direction is from the East (or West), PV modules located more to the Eastern (or Western) side of the facility, might therefore be subjected to more advantageous conditions. Thus, by placing two PV modules, with the same mitigation method next to one another, it might result in sampling bias.

## 6.2.2 Dust mitigation method applied to SAT system

The development of a DMS for the SATs, is formulated as indicated in Figure 6.3. The mitigation strategy for the trackers is focused on answering the following:

- Investigate how coated modules compare to uncoated modules, in terms of dust soiling.
- Determine the influence of a self-cleaning functionality on dust soiling, where trackers utilise natural occurring precipitation to displace dust particles.

In Figure 6.3 the formulation of the DMS for the SAT modules is presented. Self-cleaning refers to the ability of the SAT to make use of natural precipitation to provoke the removal

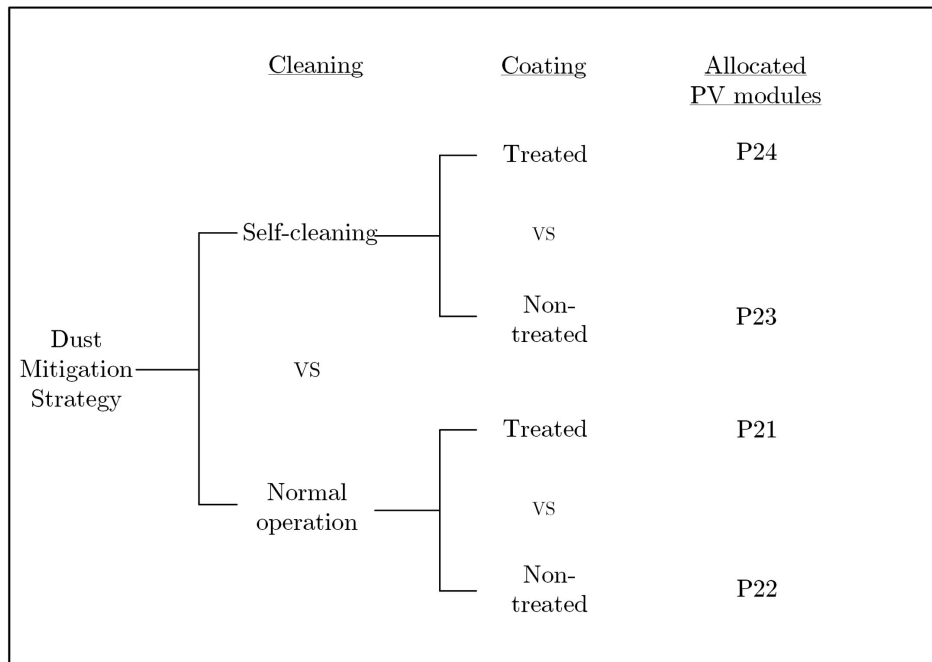


Figure 6.3: Formulated DMS for the single axis tracking PV modules as indicated.

of accumulated surface dust. SAT one is activated for the self-cleaning mode, whereas SAT two is deactivated. Details regarding the self-cleaning mode have been discussed in Chapter 5.5.3. Essentially, the self-cleaning mode instructs the SAT to react to rainfall, by tilting at a  $45^\circ$  angle, into the direction of the rain. This allows rain droplets to collide directly with the PV module glass surface. If the wind is in any direction East of the line defined by North and South, (such as NNE, ESE) then the tracker will tilt  $45^\circ$  towards the Eastern side. The self-cleaning mode also instructs the tracker to tilt  $80^\circ$  towards East, every morning, five minutes before sunrise. This movement motivates droplets, formed by dew, to roll off the side of the module, eliminating dust. When self-cleaning commences in the morning, the SAT (if activated for this mode) always tilts towards the same side for the dew cleaning, so that the dust gathered on the module surface can be intentionally manoeuvred towards a dedicated side. This is done in case the dew droplets are not enough to completely remove the dust in one session. Therefore, the next morning when the self-cleaning mode commences once again before sunrise, the remaining dust can be further displaced by the dew.

The mitigation methods are applied as shown in Table 6.2 and Figure 6.4. With the assignment of each mitigation method to a module, the same principle of applying the coating "opposite-and-across" is used, as is done with the stationary modules. Also, suppose that both modules on the self-cleaning tracker are coated with a dust removal product. This would make it virtually impossible to distinguish whether or not the resulting effect on dust accumulation, would be due to the coating applied, or the self-cleaning functionality. Therefore, with the mitigation methods as assigned in Figure 6.4, this topology allows for a non-ambiguous comparison between the modules on the self-cleaning tracker and the modules on the normal tracker.

Table 6.2: Applied dust mitigation methods to individual SAT PV modules

Mitigation method	Treatment	Tracker operation	Duration
I	Hydrophobic coating applied	Self-cleaning	Indefinitely
J	Untreated PV module	Self-cleaning	
K	Untreated PV module	Normal	
L	Hydrophobic coating applied	Normal	

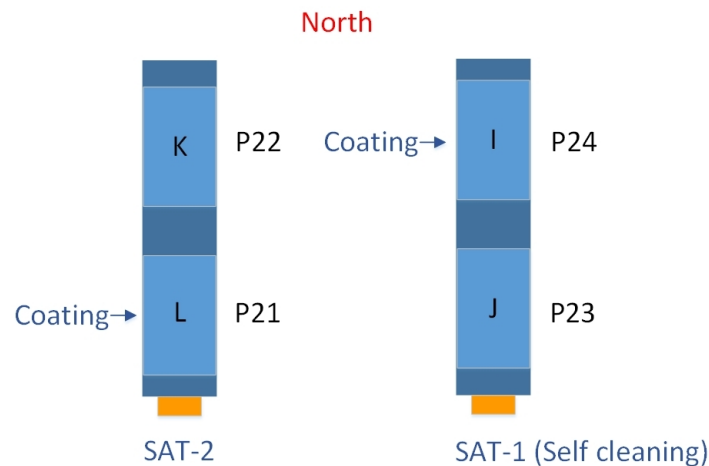


Figure 6.4: Illustration of the dust mitigation methods applied to the single axis tracking PV modules as indicated.

## 6.3 Application of the module coating

### 6.3.1 Coating product specifications

Before selecting a coating product, the following objectives are set, with which the product must preferably comply:

- Must be eco-friendly.
- Should be easy to obtain and affordable.
- Coating must be hydrophobic.
- Should be able to apply the product during any time of the day.
- Lifetime, of at least 12-18 months once applied.

The reasons for the above mentioned criteria are self explanatory, except maybe for specifying a hydrophobic coating. When selecting between a hydrophobic and hydrophilic coating, the decision is based on the environment, which is hot, dry and has a low rainfall. Hydrophobic anti-soiling coatings are capable of repelling a broader range of organic contaminants than hydrophilic coatings, which also prefer environments with a more frequent exposure to water (rain) [111]. With this criteria in mind, a commercial glass surface coating is selected. This product is hydrophobic and the coating itself is invisible. The product is also eco-friendly

and easily obtainable from a local supplier, at a reasonable cost. The product is developed for PV modules, as well as any glass surface that needs to stay clean for pro-longed periods of time, such as the glass windows of buildings. The product is also non-flammable. Finally, a 24 hour period is required before any stress testing can be performed and the lifetime of the applied coating is estimated at 18 months.

### 6.3.2 Applying the hydrophobic coating

As presented in Tables 6.1 and 6.2, the hydrophobic coating is applied to the PV modules assigned to one of the following mitigation methods: A, C, E, G, I and J, as indicated in Figure 6.5.

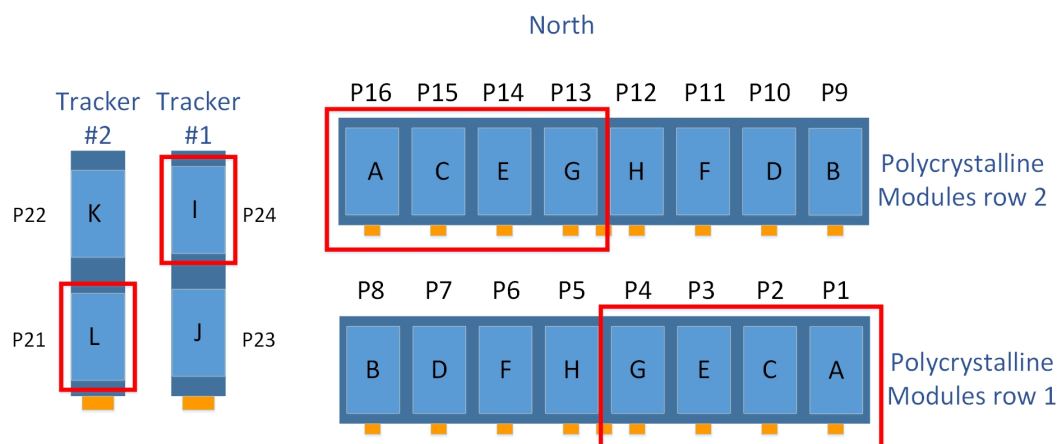


Figure 6.5: PV modules (in red block) to which the coating is applied.

The product is applied to the stationary modules, on the 16th of February 2016, whereas the SAT modules are only coated on the 4th of June 2016. The exact procedure of applying the coating to the PV modules is described below. Before application of the product precautionary measures are taken. Firstly, it is determined that there is no chance of rainfall within a 24 hour period, to allow the product to completely settle onto the module. Secondly, the product is also applied early in the morning, before the wind speed starts to increase, which might introduce wind-borne dust and sand particles during the process of applying the coating.

#### List of items

The list of items required for the application of the hydrophobic coating is listed below.

- 2 x Microfibre cloths dedicated for spreading the surface coating.
- 1 x Microfibre cloth dedicated for removing excess product on the PV module surface.
- 2 x Microfibre cloths dedicated for cleaning the PV module glass surface with water.
- 2 x Sponges for isopropyl alcohol cleaner.
- Coating (approximately 35 mL - 60 mL for each PV module).
- An isopropyl alcohol cleaner such as general purpose window cleaner (approximately 50ml per PV module).

- Distilled water (approximately 1.5 - 2 L per module).
- Time keeping device (watch)
- 1 x 20 L bucket for water
- 1 x Stepladder
- Appropriate safety clothes

### **Application onto the PV modules**

#### **Step 1: Wash module with distilled water.**

The water found in the surrounding area of the research facility is brackish and leaves white stains on the module surface. Therefore, all PV modules are cleaned with distilled water, sold locally at most hardware shops in 5 L cans as distilled battery water. Approximately 1.0 L to 1.2 L of water is thrown into the 20 L bucket. The microfibre cloths, dedicated for cleaning the PV module surfaces, are soaked and used to clean the glass surface. With one person on the step ladder and the other on the ground, the PV module is cleaned from the top to the bottom, as shown in Figure 6.6a.

#### **Step 2: Application of the isopropyl alcohol cleaner.**

Remove the excess of water on the panel after the completion of step one. After removing the excess water, apply the alcohol cleaner by spraying it across the surface, as demonstrated in Figure 6.6b. Softly (to avoid damage to PV module surface), use a wet sponge to gently clean away stubborn dirt particles.

#### **Step 3: Wash module with distilled water again.**

Repeat Step 1. Be sure to remove any excess water and ensure that the surface is completely dry.

#### **Step 4: Application of the coating.**

With the PV module glass surface completely dry and clean, spray the coating onto a microfibre cloth. As advised by the user guide, do not use too much (approximately 35ml-50ml), since the coating is meant to be spread and all excess must be removed. Spread the coating across the PV module surface so that it is evenly distributed, by making circular movements across the surface, as shown shown in Figure 6.6c.

#### **Step 5: Remove excess coating.**

Ensure that the product is left for at least 1 minute (use timer), before using a clean microfibre cloth to gently remove, any residue left on the surface. After the completion of these steps, the PV modules are left untouched for the next 24 hours, to allow the product to cure. Figure 6.6d shows a coated PV module.





Figure 6.6: Illustrations of the process for applying the hydrophobic coating.

### 6.3.3 Execution of the cleaning routines

The official cleaning routines, as prescribed by the DMS, are implemented from the 21st of April 2016. As according to the DMS, the PV modules with a short term scheduled cleaning routine are cleaned once every 2 weeks. The PV modules assigned to mitigation methods H and G are dry-cleaned and the PV modules assigned to methods E and F are cleaned with distilled water. The following steps outline the process of both the dry and wet cleaning process. It should be noted that during both the cleaning and drying process, one person stands on top of the step ladder and the other on the ground. The person on the ground, continuous the action of cleaning/drying from the section on the panel (about half way downwards) where the person on the ladder can no longer reach.

#### Water-cleaning:

**Step1:** Pour approximately 1.5 L of distilled water, into the clean 20 L bucket and soak two of the microfibre cloths.

**Step2:** Clean the glass surface of the PV module by starting from the top first, cleaning the PV module with downwards strokes. Soak the cloths as much as required, to ensure that all visible dust is removed. It is essential to make smooth, slow movements with the wet cloths to avoid water droplets from splashing onto the adjacent PV modules.

**Step3:** Dry the modules by making use of the super-absorbent cloths. Ensure that all moisture is removed, to prevent any incentive for airborne dust to rapidly attach to the module surface. When drying, the action is once again performed with downwards strokes, to further remove any dust particles still present on the module.

#### Dry-cleaning:

**Step1:** Ensure that the microfibre cloths, dedicated for the dry-cleaning, are dry.

**Step2:** This process is also performed with one person on top of a ladder and the other on the ground. With a light downwards sweeping action, the modules is cleaned so that all visible dust particles are removed. The idea is not to scrub the stubborn or infused dust

particles off of the module, since this might scratch/damage the surface. The aim of the dry-cleaning is merely to remove most of the superficial dust from the surface. After completion of this step, the dry-cleaning is completed.

After performing the periodic cleaning routines on the appropriate modules, log the exact time and date during which the modules are cleaned.

To ensure that these cleaning routines are completed adequately as according to the prescribed methodology above, the following proactive measures are taken:

- Firstly, the scheduled cleaning routines are always executed by the same two people, whom are part of the on-site staff at the Kalkbult PV power plant.
- Secondly, the staff are provided with the necessary cleaning equipment which includes: 2x microfibre cloths for the dry cleaning, 2x microfibre cloths for the water cleaning, 2x special super-absorbent cloths for drying the PV modules, several 5 L cans of distilled water, a 20 L water bucket.
- On the back of each biweekly cleaned module, the assigned mitigation method is written, which is either a wet or dry cleaning process.
- Finally, a job completion list is also provided, which is to be filled in after the completion of the scheduled cleaning routines.

# Chapter 7

## Results and Analysis

### 7.1 Overview

In this chapter, the results presented focus on the real world performance of 16 stationary and four single axis tracking, 250 W pc-Si modules. The data presented for the stationary modules is recorded over a period of six months, which ranges from 4th of May to the 31st of October 2016. Data for the SATs is presented for a three month period, which includes the months and days of 14 August to 18 November 2016. This chapter starts off with defining the chosen Performance Ratio (PR), which is used to evaluate PV module performance. This is followed by a discussion regarding the systematic process of raw data extraction and data validation. The final part of the chapter presents the results of the analysis performed regarding the influence of dust soiling on the stationary and tracking modules.

### 7.2 Performance ratio defined

Instead of pursuing a PV module  $I_{SC}$  analysis, an efficiency calculation or a or an energy yield [kWh] approach it is the aim of this thesis to focus on power output, determined from the extracted I-V curve measurements. Several authors [21, 23, 37, 41] have also used output power as the criteria for analysing module performance. A Performance Ratio (PR) is defined and serves as a metric to characterise the effect of soiling on a PV module. The PR defined by equation (7.3) is adopted from authors [41] and is adjusted to determine an averaged PR over a specific time span. This PR is based on the two fundamental equations (7.1) and (7.2), which allow both temperature and irradiance correction to be applied. The PR corrects measured PV module performance to the rated PV module characteristics as defined at STC conditions. The PR is defined in equation (7.3). Evidently, this formula provides a temperature and irradiance corrected power output value to be retrieved, which allows a PV module to be compared with itself and other modules with different power ratings, over a range of varying conditions.

$$P_{DC} = P_{STC} \left( \frac{G_{POA}}{G_{STC}} \right) \quad (7.1)$$

$$P_{DC} = P_{STC} \times (1 + \delta(T_{cell} - T_{STC})) \quad (7.2)$$

$$PR = \frac{1}{N} \sum_{i=1}^N \frac{P_{DC\_i}}{P_{STC} \frac{G_{POA\_i}}{G_{STC}}} \frac{(1 + \delta(T_{cell\_i} - T_{STC}))}{G_{STC}} \quad (7.3)$$

Where the variables in (7.3) are defined as:

- $P_{DC\_i}$  = recorded MPP of PV module in the  $i^{th}$  minute of the day [W].
- $G_{POA\_i}$  = measured POA irradiance in the  $i^{th}$  minute of the day [ $W/m^2$ ].
- $G_{STC}$  = irradiance at STC [ $1 \text{ kW}/m^2$ ].
- $T_{cell\_i}$  = measured back-plate PV module temperature [ $C^\circ$ ].
- $T_{STC}$  = PV module cell temperature at STC conditions [ $25 \text{ C}^\circ$ ].
- $\delta$  = temperature coefficient for power of the PV module [ $-0.4 \text{ \%}/C^\circ$ ].

Power, irradiance and module temperature is measured at an instance, from which the PR for that specific moment in time is determined. The performance ratio's power value is derived from the measured I-V curve. Several researchers have proposed analysing the effects of dust analysis on the I-V curve's short-circuit current value alone, due to the direct relationship between  $I_{SC}$  and irradiance. However, as concluded by [9], it is found that the short-circuit current of a PV module is proportional to irradiance (at a given temperature), whereas for the maximum power of a PV module, this is found not to be the case. This finding is also confirmed in a study conducted by E. Lorenzo et al. [18], where it is concluded that investigating the effect of soiling losses in terms of  $I_{SC}$  alone, is not enough. Voltage losses are observed to be several times larger than the  $I_{SC}$  losses, which ultimately leads to higher losses in terms of power output as compared to  $I_{SC}$  losses only [18].

## 7.3 Raw data validation

### 7.3.1 Overview

Various steps are taken to ensure that data uncertainty is minimised with regards to the raw data collection process, since this serves as the foundation of the data analysis. The performance monitoring of the PVRF is mainly formulated to adhere to the guidelines for measurement, data exchange and analysis as prescribed by the IEC61724 standard [59].

### 7.3.2 PV module data

All 20 of the PV modules (255W Renesola Virtus II series) installed at the research facility are brand new and from the same manufacturer and supplier. The exposure time of all 16 stationary PV modules is synchronised with the modules installed on the same day, which is 1 Aug 2015. The remaining four 255 W pc-Si PV modules, dedicated to the SATs, are installed on the 1st of June 2016. Additionally, as specified by the IEC60891 standard [48], the backplate temperature of each PV module is also recorded, at the same instance when the I-V curve and irradiance measurements are recorded.

To abstain from sampling bias regarding the performance of one PV module to another, all modules are normalised to one another regarding power output. Initially, the PV modules are installed on the 1st of August 2015, which equates to an exposed period of nine months, before data analysis is commenced. However, due to the lengthy installation and testing

phases of the data logging devices, initial rated PV module performance is not determined. Instead, the STC power rating of each module is determined on the 11th of May 2016, between 12:30-13:10 PM. During this period of time, the wind speed is low (average of 1.09m/s) and dominantly from the North and NNW direction, therefore slowed down further by the thin-film row furthest to the north. The irradiance is also very close to STC conditions at an average of 975 W/m<sup>2</sup> recorded and an ambient air temperature recorded at an average of 17.5 C° for this period. The process of normalising the PV modules accounts for temperature and irradiance compensation, relative to STC conditions. Most importantly, this day is chosen, because before the 11th of May a total of 24.5 mm and 8.5 mm of rain is received on the 9th and 10th of May, respectively. From a thorough visual inspection, it is concluded that all modules are in the same physical condition at this moment in time. The argument could be made that microscopic dust particles are still present on these modules, even after the heavy rain, but the uncertainty provided by these dust particles are negligible, compared to the uncertainty of assuming that all PV modules are rated at 255 W. Also, due to the fast and non-linear degradation of the PV modules during the first year of exposure, characterising the rated power values of each module during May 2016 (start of the measurement period) has some advantage. This eliminates uncertainty in the sense that modules that might have degraded faster than others during the first nine months, are now normalised appropriately. This argument is based on the PV module datasheet, which indicates a drastic 2.5 % degradation from initial performance, during the first 12 months [52]. Thus, the long term decrease in the PR of a module, due to dust, is now more dependent on the effect of dust itself and less reliant on the rapid initial material degradation of the PV module.

The normalisation process of the power output of each PV module is determined by four I-V curve measurements, which consists of a period of over 40 minutes. Each measurement is corrected to STC conditions by means of equation (7.4).

$$P_{STC} = \frac{1}{4} \sum_{i=1}^4 \frac{P_{DC\_i} \times G_{STC}}{(1 + \delta(T_{cell\_i} - T_{STC}))G_{POA\_i}} \quad (7.4)$$

Each I-V curve is curve fitted, according to the single diode model presented in section 7.8, and the maximum power output  $P_{DC}$  is determined. The results obtained for the rated power are presented in Table D.1, Appendix D.

To further subject the PV modules to a real world scenario, the maximum available power is continuously extracted from the PV modules, which is deposited into a dumping resistor, mentioned in Chapter 3.

### 7.3.3 ActiveLoads

The AL devices, as described in Chapter 3.5.1, are responsible for extracting the I-V curves. These devices are carefully calibrated to minimise measurement uncertainty. The calibration process eliminates the offset and gain errors presented by the I-V curve measurements, which results in a maximum measurement uncertainty determined as 0.5 %.

### 7.3.4 Weather station and irradiance measurements

As required by the IEC 61724 standard, total irradiance in the plane of the array, ambient air temperature (protected by a radiation shield) and wind speed is recorded. The weather station and the pyranometer are placed at a height and location, which is representative of

the actual array conditions, as mentioned in Chapter 3 , section 3.4.6. The measurement accuracy of the instruments are also well within the minimum requirements of the IEC61724 standard, as shown in Table 7.1. Weather and irradiance data, collected from the MSO-485 weather sensor and Kipp&Zonnen SMP10-Pyranometer, is monitored at a sample rate of five seconds and logged every minute. An instant irradiance measurement is recorded at the exact moment when the I-V curves are measured. Calibration dates of the weather sensor, pyranometer and the rain-gauge are also valid for the entire measurement period.

Further uncertainty with regards to accurate irradiance measurements is minimised with the pyranometer cleaned every week-day, except on weekends. Any specifics with regards to the acquisition of the weather and irradiance data is discussed in Chapter 4.6.4.

Table 7.1: Instrument measurement accuracy and IEC 61724 standards.

Measurement	Unit	Accuracy	IEC61724 accuracy
Wind-Speed	[m/s]	$\pm 2\%$ for speeds of 0-50m/s	0.5m/s for speeds < 5m/s 10% for speeds > 10m/s
Wind Direction	[deg]	$\pm 5^\circ$	
Ambient Temperature	[C°]	$\pm 0.4$ C°	$\pm 1$ C°
PV module temp	[C°]	$\pm 0.5$ C°	$\pm 1$ C°
Relative Humidity	[%]	$\pm 4$ %	
Barometric pressure	[mbar]	$\pm 2$ mbar	
Rain	[mm]	$\pm 1$ %	
Irradiance	[W/m <sup>2</sup> ]	0.2 %	5 %
I-V curve	[V],[A]	0.5 %	1 %

## 7.4 Data alignment, storage and monitoring

With multiple devices continuously collecting data, data alignment is guaranteed by regularly (minimum of once a month) synchronising all the RTCs of each device to that of the master device (Raspberry-Pi). A time stamp linked with each measurement also ensures cohesion between all I-V curve and meteorological data measurements.

With regards to data storage, all data measurements gathered are processed and recorded onto an on-board SD-card, as well as an online MySQL (Structured Query Language) database<sup>1</sup>. The data captured in the online database, is continuously synchronised with the data on the local SD-cards of each device. This avoids data loss when an internet connection is unavailable. In adherence to the IEC61724 standard, as mentioned above, a time and date stamp is provided with each recording, at the end of the period during which measurements are taken. Each set of data is differentiated by means of a column header, so that each measurement is recorded as a single entity.

The status of all of the devices active on the research facility is monitored via a website<sup>2</sup>. This website, provides a live feed of the latest online database entries. This helps to avoid the tedious process of analysing each database table individually. A dedicated monitor is set-up in the office, which displays the status web page continuously, so that the data logging process and system operation is confirmed throughout the day. This is found to be a great

<sup>1</sup>The infrastructure regarding the online database was created by Malem Heymans and revised by Tashriq Pandey. The database is registered under the domain name of [www.pvsoiling.co.za](http://www.pvsoiling.co.za).

<sup>2</sup>This website is created by Tashriq Pandey and can be viewed at [www.pvsoiling.co.za/status](http://www.pvsoiling.co.za/status).

method of system monitoring since it minimises response time and allows any system failure to be identified rapidly. Figure 7.1 presents a screen shot of this web page:

### Kalkbult Plant

Device	FIFO Space	Date	Time	Temperature	Voltage0	Current19	MPP 1 Or DC Array Voltage
Polycrystalline1	5920	2016/11/9	11:30	53.31 °C	33.58 V	10.74 A	248 W
Polycrystalline2	3898	2016/11/9	11:30	53 °C	33.56 V	10.64 A	246 W
Polycrystalline3	45397	2016/11/9	11:30	52.63 °C	33.72 V	10.74 A	252 W
Polycrystalline4	46625	2016/11/9	11:30	51.25 °C	33.7 V	10.61 A	247 W
Polycrystalline5	11809	2016/11/9	11:30	52.63 °C	33.59 V	10.82 A	252 W
Polycrystalline6	46552	2016/11/9	11:30	51.44 °C	33.6 V	10.71 A	249 W
Polycrystalline7	2752	2016/11/9	11:30	50.5 °C	33.95 V	10.85 A	253 W
Polycrystalline8	22845	2016/11/9	11:30	50.44 °C	33.93 V	10.44 A	248 W
Polycrystalline9	29337	2016/11/9	11:30	53.44 °C	33.55 V	10.87 A	250 W
Polycrystalline10	47037	2016/11/9	11:30	53.06 °C	33.88 V	10.87 A	253 W
Polycrystalline11	46815	2016/11/9	11:30	52.56 °C	33.7 V	10.85 A	252 W
Polycrystalline12	33264	2016/11/9	11:30	51.38 °C	33.69 V	10.87 A	253 W
Polycrystalline13	47008	2016/11/9	11:30	52.44 °C	33.63 V	10.74 A	250 W
Polycrystalline14	29242	2016/11/9	11:30	51.75 °C	33.67 V	10.74 A	249 W
Polycrystalline15	43683	2016/11/9	11:30	50 °C	33.71 V	10.79 A	252 W
Polycrystalline16	47069	2016/11/9	11:30	49.75 °C	33.87 V	10.72 A	253 W
ThinFilm17	876	2016/11/9	11:30	51.75 °C	79.35 V	1.86 A	103 W   96 W
ThinFilm18	5033	2016/11/9	11:30	52.25 °C	79.48 V	1.98 A	106 W   104 W
ThinFilm19	47030	2016/11/9	11:30	48.13 °C	79.5 V	2.01 A	112 W   102 W
ThinFilm20	1280	2016/11/9	11:30	47.44 °C	79.95 V	1.95 A	108 W   102 W
STracker21	12914	2016/11/9	11:30	45.5 °C	34.05 V	9.37 A	223 W
STracker22	22846	2016/11/9	11:30	47 °C	34.14 V	10.33 A	244 W
STracker23	12778	2016/11/9	11:30	48.25 °C	34.15 V	10.6 A	248 W
STracker24	12929	2016/11/9	11:30	48.5 °C	34 V	10.74 A	250 W
Master Controller25	83269	2016/11/9	11:35	30.5917	N/A	N/A	27.4 V

### Kalkbult Weather

Date: 2016/11/9
Time: 11:35
Wind Speed (m/s): 4.58
Temperature (°C): 30.59
Humidity (%): 19
Pressure (mbar): 892.3
Rain Fall (mm): 0

### Single Axis Trackers

STracker 1 Angle: -8.25439°
STracker 1 Mode: 1°
STracker 2 Angle: -8.8916°
STracker 2 Mode: 1°

Date: Wednesday, 9 November 2016

Time: 11:35:32

Figure 7.1: Monitoring website, which displays the status and most recent measurement entries from all devices.

## 7.5 Data related documentation

To account for any known irregular activity that might influence data, a log file is kept according to the IEC 61724 standard. All unusual events, problems encountered, sensor and system operation changes and faults are explicitly documented. This log file also contains comments that might be considered useful for the process of data extraction and interpretation.

A cleaning and maintenance log file is also maintained, so that scheduled cleaning routines are both monitored and recorded. The staff at the Kalkbult site, recorded the date and time of all scheduled cleaning routines executed. Inspection of the PV modules for bird droppings is also performed on a daily basis and should a PV module be exposed to a bird dropping it is recorded. The date and time when the bird dropping is removed is recorded and the size of the dropping is also recorded, as well as the PV module ID number, on which the dropping is found. The sizes are defines as presented by Table 7.2.

Table 7.2: Bird-dropping size definition

Definition	Size
Small	Dropping $\leq 1\text{cm}^2$
Medium	Dropping $\leq 5\text{cm}^2$
Large	Dropping $> 5\text{cm}^2$

## 7.6 Problems encountered during the process of data acquisition

As can be expected, some challenges were faced with the data collection process.

### SD-cards

Data captured by the SD-cards would occasionally fail. At most five SD-cards, out of the 25 logging devices, would fail on average once a month. Data is only lost for the time during which the SD-card is not active. This issue is solved with a simple reformat of the SD card by the on-site staff at Kalkbult. The reason for this seems to be a potential low-level hardware issue. It is also found that only 4 Gigabyte Scandisk, class 4 micro-SD cards can be used.

### Weather station

Another issue that occurred during the period of 11-18 January 2016, was the fact that the weather station's temperature reading constantly recorded a 999.99°C. This resulted because of a firmware issue on the weather sensor's side. It was however resolved by uploading a HEX-file with a new firmware version that was provided by technical staff of Met One Instruments.

The biggest issue with regards to data logging is the fact that approximately every 4 hours and 20 minutes, the weather station provides no feedback for approximately 5-10 minutes. At first, it was thought that the issue is with the MC board itself. However, after extensive testing, this theory was refuted when another PCB board was programmed to reply as if it was the weather station. No data loss occurred and it was concluded, to the best knowledge of the author, that there is definitely a firmware issue with regards to the weather station. Since weather data (ambient temp. wind speed, wind direction, humidity, etc.) does not change as frequently, this 5-10 minute loss of data still complies with the IEC61724 standard's sampling interval of 10 minutes for data that is not directly affected by irradiance.

To try and counter this irregular behaviour from the MSO weather sensor, a remote supply switch was added, which enables the weather station to be reset either remotely by a user, or by the MasterController itself at specific intervals. This however, proved not to solve the problem of a no reply issue every odd 4 hours. However, should there be any reason to reset the weather sensor, the capability is still available.

### Pyranometer

Irradiance measurements were also lost for the period of 21 June - 12 July 2016. The Kipp&Zonen SMP10 pyranometer was exposed to water damage, which caused the connector attachment of the cable to corrode. The connector of the pyranometer was repaired and silicon was used to insulate the pyranometer from any possible future water damage. The calibration and operation of the device is confirmed by a local engineering company who



specialise in these irradiance instruments. The lost irradiance data for this period is provided by Scatec's on-site weather-data collection system.

### Battery-bank

As mentioned in Chapter 3.4.4, a lightning strike is also presumed to have struck the power-station, which caused both of the MPPT charge controllers to be destroyed. This led to a complete discharge of the 12 V lead-acid batteries. These batteries and the MPPT charge controllers were replaced, however no data is available from 13th March to 21st March 2016.

### Bird droppings

Due to frequent bird droppings, bird-spikes are also installed. A drastic decrease in bird droppings are seen due to this addition.

### ActiveLoads

It was also noticed that PV modules' measured currents were clipped at 9.3 A by the ALs. This is due to a gain resistor for the INA111 operational amplifier [112], that is too small at 900  $\Omega$ . Thus, the  $R_G$  resistor is substituted for a 1k5  $\Omega$  resistor to ensure that high currents would not clip. Due to the change of this resistor, the operational amplifier gain had to be adjusted, which means that the ALs had to be recalibrated in terms of current offsets.

On several occasions some of the ALs would produce  $I_{SC}$  and  $V_{OC}$  readings, but would however not deliver any power from the PV module to the resistor load. This was usually due to a faulty load connection caused by a bad solder connection. On several occasions the ALs would simply stop producing any  $I_{SC}$  or  $V_{OC}$  values, which was usually due to defective MOSFETS.

In terms of the ALs that measured the I-V curves for the Thin film modules, the measurements had to be aborted, due to faulty measurements. The open circuit (OC) current readings ( $I_{OC}$ ) for the thin-film modules do not record zero Ampere readings, but instead record current at open-circuit conditions as 0.6 A, which is almost 50 % of the  $I_{sc}$  value. The reason for this behaviour is undetermined and requires further investigation. The measurements also had a large noise factor, which only contributes further to the uncertainty of the PV thin-film module measurements.

### Temperature sensors

Another issue was with regards to the temperature sensors. Problems ranged from inconsistent temperature readings to constant measurements of zero degrees. The solution was to insert a terminating 47  $\Omega$  (line impedance) resistor in series with the MISO and MOSI lines of the SPI cable connection.

### Single Axis Trackers

The data acquisition of the single axis tracker ALs (Numbers 21-24) was stopped after logging data successfully from the 4th June to 22 July 2016. Unfortunately, the position sensor of a single axis tracker became faulty. It was replaced by a new position sensor, but due to a calibration offset of 10 degrees introduced by the new sensor, both single axis trackers were stopped. New code was implemented to allow remote calibration to be performed, should one of the position sensors be misaligned. The modules on the trackers were cleaned and the overall process of data collection was restarted again on the 13th of July 2016.

## 7.7 Process of data extraction and filtering

### 7.7.1 Data extraction

The process of data extraction is executed by means of a script written in Python2.7. This script integrates the functionality and processing power of the MySQLdb python library, to allow for a more powerful execution of online data extraction. The Python script for the data analysis and parameter optimisation is performed on an ordinary PC which consists of a 3.6 GHz, i7 CPU, with 16 GB of RAM and a 64-bit Windows 7 Operating System. An internet connection is required, since the accumulated raw data is to be obtained from the online database (DB).

### 7.7.2 Data filtering

The ultimate goal of the data analysis is to determine the effect of dust soiling, on PV module output power. With the process of raw data acquisition, clearly defined in section 7.3 the next phase of the data analysis can commence. To introduce a data set that is accurate and a true representation of PV module behaviour, any particulars that might alter data credibility, is filtered out. This process of filtering is performed by asking a series of questions to define how valid data is to be discerned from invalid data.

- *In terms of data measurements, what is the criteria for a measurement day to be regarded as valid?*

This question serves as the foundation for identifying the necessary criteria to define a valid day. More questions are asked to answer this question holistically.

- *Which hours of a day will be used for the PV module performance analysis?*

Firstly, it is decided to avoid low light conditions, which typically refers to one hour after and before the sunrise and sunset, respectively. The shading profile of the research facility, provided in Appendix D.3, also only allows a valid all year round period for measurements between sunrise up until 16:00 PM. According to the datasheet of the 255 W, Renesola Virtus II modules, the efficiency of the modules varies with the level of irradiance to which the modules are exposed as presented in Table 7.3. Thus, to avoid the effects of a varying efficiency, it is decided to apply the PR for relatively constant levels of irradiance. From inspection of the recorded GHI data, it is determined that irradiance levels with a small variance ( $< 150 \text{ W/m}^2$ ) are observed from 11:00AM-14:00PM for a clear day. This is also the time of day when the highest levels of irradiance are available and power output for the stationary PV modules are at a maximum. Based on these two factors the hours regarded for the performance analysis of a PV module is the hours of 11:00AM to 14:00PM.

Table 7.3: Renesola VirtusII PV module datasheet specifics for irradiance and efficiency .

Irradiance [ $\text{W/m}^2$ ]	200	400	600	800	1000
Efficiency [%]	15.8	16.2	16.2	16.1	16.0

- *From a meteorological perspective, what weather conditions will disqualify the recorded measurements of a day?*

To avoid irregularities with regards to irradiance and maintain a uniform approach in terms of analysing the PR of modules, only clear days are examined. A clear day is characterised by two criteria, namely:

- (a) The difference between consecutive GHI measurements, recorded at one minute intervals, must not vary by more than 30 %.
- (b) An irradiance measurement of at least  $800 \text{ W/m}^2$  must be recorded during the 11:00AM - 14:00PM time period.

Thus, from condition (a), if a GHI measurement deviates more than 30 % from the previous measurement, then it is regarded as an invalid day. Deviation from this 30 % tolerance implies cloud cover. The reason for selecting 30 % as the tolerance is based on inspection, as presented in Figure 7.2. This graph displays the power output of six consecutive days where different levels of irradiance are recorded. Each power curve in Figure 7.2 represents the maximum tolerance required for a measurement day to be defined as valid. Condition (b) ensures that the minimum irradiance is high enough so that a 30 % tolerance is applied to days of high irradiance. If a specific day is cloud covered and irradiance levels are low, then condition (a) might be fulfilled, but condition (b) will ensure that high levels of irradiance are indeed experienced during this day.

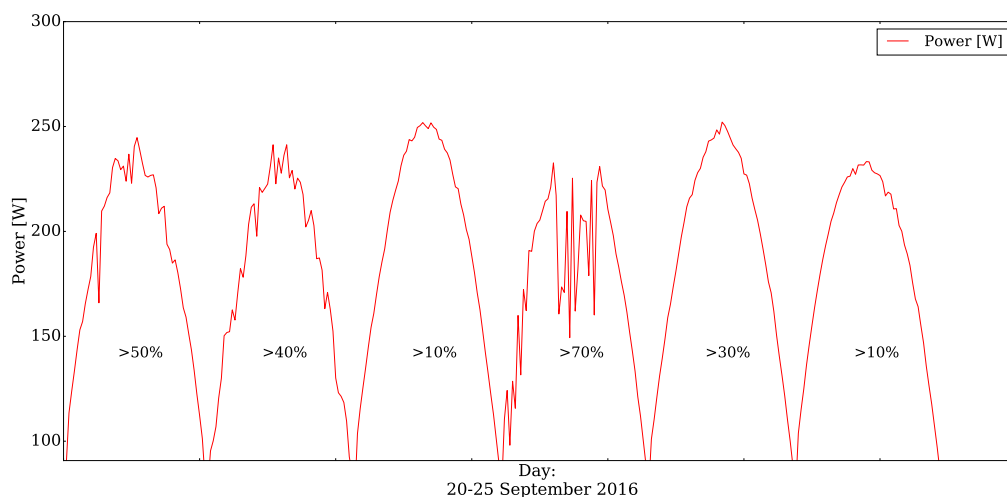


Figure 7.2: Illustration of the power curve limitation, imposed by the condition of a maximum GHI deviation.

- *How will days or log intervals be managed, where there are either missing or no irradiance ( $G_{POA}$ ), module temperature ( $T_{cell}$ ) or I-V curve measurements available for a specific data recording?*

As defined by equation (7.3), the PR is the recorded average of the temperature compensated power, divided by the irradiance adjusted power, as measured over a defined period (11:00 AM to 14:00 PM). Should any of the data samples retrieved fail to produce a  $G_{POA}$ ,  $T_{cell}$  or  $P_{DC}$  value from which the power is determined, then it is not included in the PR equation. For example, if there is no irradiance measurement available for the log interval of 11:10 AM, on a specific day, then it is ignored by the PR equation, to avoid the PR value from being skewed. Should no data be available for the entire measurement day, for either

of these entries, then a PR of zero is logged.

- *How is on-site human interference, which may corrupt recorded data, avoided?*

As mentioned, a log file is kept according to the IEC 61724 standard, where all on-site maintenance and irregular activity is recorded. Days on which on-site installations and general work are done, are ignored where necessary. In terms of the scheduled cleaning, if the modules are cleaned during the period of 11:00 AM-14:00 PM, this day will be discredited and a PR will not be presented for this day.

- *How does the data analysis account for bird droppings?*

As mentioned, part of the daily maintenance routine is to ensure that there is no bird droppings. Should a bird dropping be recorded, data for the specific module for that day will be disregarded.

- *How is I-V curve measurement noise and accompanying measurement uncertainty filtered out?*

This is meticulously explained in section 7.8. In summary, a single diode curve fitted model is applied over the measured points. If the fitted curve is unable to appropriately fit the measured data, for example in the case of momentary shading (displayed by Figure 7.7) the recorded measurement is ignored.

- *How are scheduled cleaning days and days that received rainfall accounted for in the analysis?*

These days are indicated on all graphs where necessary, to give an indication of these events. Cleaning routines are also mostly executed outside the measurement period of 11:00 AM to 14:00 PM, if possible. However, should a cleaning routine be executed during these hours, the measurements are disregarded.

- *How is the difference in tilt angle of the two SATs accounted for?*

As seen in section 7.9.9, the calculation to translate measured irradiance ( $G_{POA}$ ) to that of the SAT modules, does consider the angle of tilt of each module. This eliminates further uncertainty regarding SAT module performance.

## 7.8 Curve fitting

### 7.8.1 Introduction

With the necessary raw data validation and process of data filtering addressed, it is still not guaranteed that the measured data points provide an accurate depiction of PV module behaviour. This is why the single-diode equation is used to apply a curve fitted model, on top of the measured data points. This section is dedicated to the process of applying the single-diode curve fitted model.

### 7.8.2 Single-diode curve fitting model

The raw I-V curve measurements recorded, consists of 20 sample points each. Thus, to eliminate measurement noise, provide a higher resolution of available data points, as well as

confirm that raw data measurements conform to typical PV module behaviour, it is necessary to apply a fitted trend line. There are powerful Python functions available, for exactly this purpose such as the Spline interpolation and Savgol filtering and smoothing functions. However it is found that the approach of interpolation and filtering/smoothing simply defines how the function behaves between data points, but does not modify or validate data points. In other words, these functions simply attempt to go through each and every measured point. Although these curve fitting tools might work for most of the data samples, it unfortunately does not represent true PV module behaviour, and does not provide a method to discern between normal and abnormal data points. More detail is provided regarding this in the pages to follow.

It is required that raw I-V curve data points are fitted with a model which defines a relationship between the voltage and current measurements. A decision is made to apply a non-linear curve fitted model to raw I-V curve measurements, based on the single-diode equation.

There are a variety of proposed models for solar panels, one of which is the double-diode model. The double-diode model has been proclaimed [113–115] to provide a more accurate description of the dark I-V curve characteristics and other physical phenomena of a PV module. However, authors such as M. Villalva, et al. [116] and C. Carrero et al. [117] have reported that the single-diode model provides a good balance of simplicity and accuracy. This model is also used as a standard model in photovoltaics, for example the IEC 60891 standard [48], which further attests to its reliability. The single-diode model is applied by this thesis.

From the electrical equivalent circuit of a solar cell, as presented by Figure 7.3, the single-diode model equation (7.8) is derived. The variable  $I_{PV}$  is the current source.  $I_D$  is the current through the diode,  $R_S$  is the series resistance and  $R_{SH}$  represents the shunt resistance. Finally, the terminal output current and voltage is labelled as  $I_T$  and  $V_T$  [118].

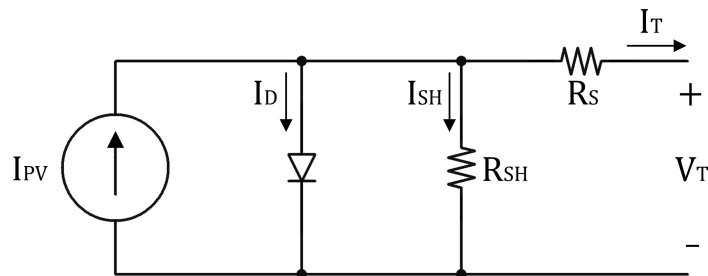


Figure 7.3: Equivalent circuit of a solar cell.

Using the indicated sign convention and applying Kirchoff's current law, equation (7.5) is derived from this circuit.

$$I_T = I_{PV} - I_D - I_{SH} \quad (7.5)$$

Equation (7.8) is derived by substituting the diode current  $I_D$  with the Shockley diode equation (7.7) [44, 266] and  $I_{SH}$  with equation (7.6), which is derived from the circuit in Figure 7.3.

$$I_{SH} = \frac{V_T + I_T R_S}{R_{SH}} \quad (7.6)$$

$$I_D = I_O \left[ e^{\left( \frac{V_T + I_T R_S}{a} \right)} - 1 \right] \quad (7.7)$$

$$I_T = I_{PV} - I_O \left[ e^{\left( \frac{V_T + I_T R_S}{a} \right)} - 1 \right] - \frac{V_T + I_T R_S}{R_{SH}} \quad (7.8)$$

In equation 7.8,  $I_O$  is the saturation current of the diode and variable  $a$  represents the following:

$$a = \frac{nN_S k T}{q} \quad (7.9)$$

The variables in (7.9) are defined with  $n$  as the diode ideality factor, and  $V_t$  is the thermal voltage of the diode, which is temperature ( $T$ ) dependent and also defined by the Boltzmann constant,  $k = 1.38064852 \times 10^{-23} [\text{m}^2][\text{kg}][\text{s}^{-2}][\text{K}^{-1}]$ , and the charge of the electron,  $q = 1.60217662 \times 10^{-19} [\text{C}]$ . The number of cells in series are represented by  $N_S$ , but  $N_S$  is considered to be one in subsequent calculations. The equivalent parallel and series resistance is represented by  $R_{SH}$  and  $R_S$ , respectively. [118]

### 7.8.3 Parameter extraction

The formula derived as (7.8) for the single-diode equivalent circuit model, involves five unknown parameters:  $I_{PV}$ ,  $R_S$ ,  $R_{SH}$ ,  $I_O$  and  $a$  to be determined, to accurately represent an I-V curve. Therefore, with five unknown variables, it is implied that at least five I-V curve boundary conditions must be obtained. An analytical approach, based on either provided PV cell manufacturer data, or experimental data can be employed to determine the I-V curve parameters [118]. Solar cell manufacturers provide electrical performance data, which usually includes the  $I_{SC}$ ,  $V_{OC}$ ,  $I_{MPP}$  and  $V_{MPP}$  values. Nevertheless, this information is not enough to identify the five mentioned parameters and requires further parameter estimation [118]. Also, PV module manufacturer data does not necessarily represent typical PV module behaviour under real world operating conditions, which includes varying irradiance as well as temperature changes [119].

An optimisation algorithm is therefore used to execute a curve fitting routine which extracts the values of the unknown parameters. The process of parameter extraction presented by this thesis, utilises measured I-V data, from each corresponding module. A conceptual illustration for the approach of parameter extraction is displayed in Figure 7.4a and 7.4b.

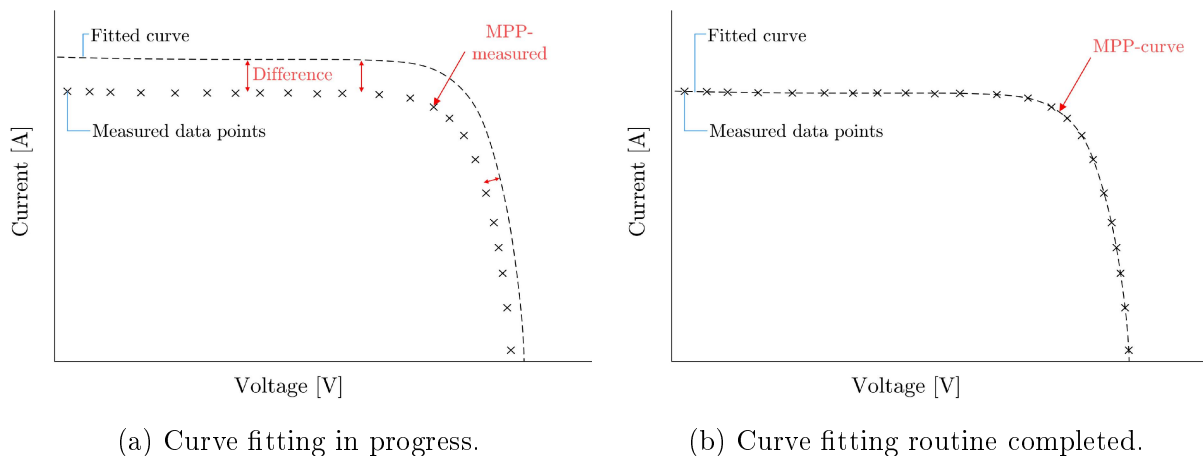


Figure 7.4: Illustration of the curve fitting routine.

As the optimisation algorithm adjusts the parameters, it attempts to fit the I-V curve over the measured data points, with a minimum difference between the fitted curve and the measured curve as result. As presented in Figure 7.4a, the difference between the fitted curve and the data points is much bigger than that of the curve presented by Figure 7.4b. Also notice how the fitted curve in Figure 7.4b provides a higher resolution, with the MPP found between two measured points and not necessarily at a single measured point as indicated in Figure 7.4a.

### Equation set for parameter extraction

The process of parameter extraction requires a set of equations, based on the electrical equivalent PV module circuit. The particular set of equations required are derived as follows:

For the short-circuit ( $I_{SC}$ ) condition, equation (7.8) is rewritten as:

$$I_{SC} = I_{PV} - I_O \left[ e^{\left( \frac{V_T + I_{SC}R_S}{a} \right)} - 1 \right] - \frac{V_T + I_{SC}R_S}{R_{SH}} \quad (7.10)$$

As presented by author M.G. Villalva et al. [116], equation (7.10) can be simplified to:

$$I_{PV} = \frac{R_{SH} + R_S}{R_{SH}} I_{SC} \quad (7.11)$$

For the open circuit voltage ( $V_{OC}$ ) condition, (7.8) can be rewritten as:

$$0 = I_{PV} - I_O \left[ e^{\left( \frac{V_{OC} + I_T R_S}{a} \right)} - 1 \right] - \frac{V_{OC}}{R_{SH}} \quad (7.12)$$

As presented by author D. Sera [120] equation (7.10) can be simplified to:

$$I_O = \frac{(R_{SH} + R_S) I_{SC} - V_{OC}}{e^{\left( \frac{V_{OC}}{a} \right)} R_{SH}} \quad (7.13)$$

As with most non-linear optimization algorithms, an educated guess for the initial parameter values should be made, since an inappropriate selection of initial values will result in non-convergence of the algorithm. Thus, for this particular curve fitting approach, only three parameters have to be estimated, since the  $I_O$  and  $I_{PV}$  parameters are dependent on the other three parameters  $a$ ,  $R_{SH}$ ,  $R_S$  as well as the measured  $I_{SC}$  and  $V_{OC}$  values, as presented by equations (7.11) and (7.13).

- The initial guess for  $R_{SH}$  is approximated by calculating the gradient of the I-V curve's slope, found between markers  $I_1$  and  $I_2$  in Figure 7.5 with:

$$R_{SH} = \left| \frac{V_1 - V_2}{I_1 - I_2} \right| \quad (7.14)$$

- The value of  $R_S$  is approximated by calculating the gradient of the slope after the MPP point, towards the  $V_{OC}$  point. As demonstrated in Figure 7.5 the initial guess for  $R_S$  is determined as

$$R_S = \left| \frac{V_3 - V_4}{I_3 - I_4} \right| \quad (7.15)$$

- The value of  $a$ , which represents  $nV_t = nN_S kT/q$ , with  $N_S = 1$  is approximated by assuming a diode ideality factor of  $1 \leq n < 1.5$  [116] and with the constant values of  $k = 1.38064852 \times 10^{-23}$  J/K and  $q = 1.60217662 \times 10^{-19}$  °C, the cell temperature is estimated as 30 °C, which results in  $T = 30 + 274.15 = 304.15$  K.

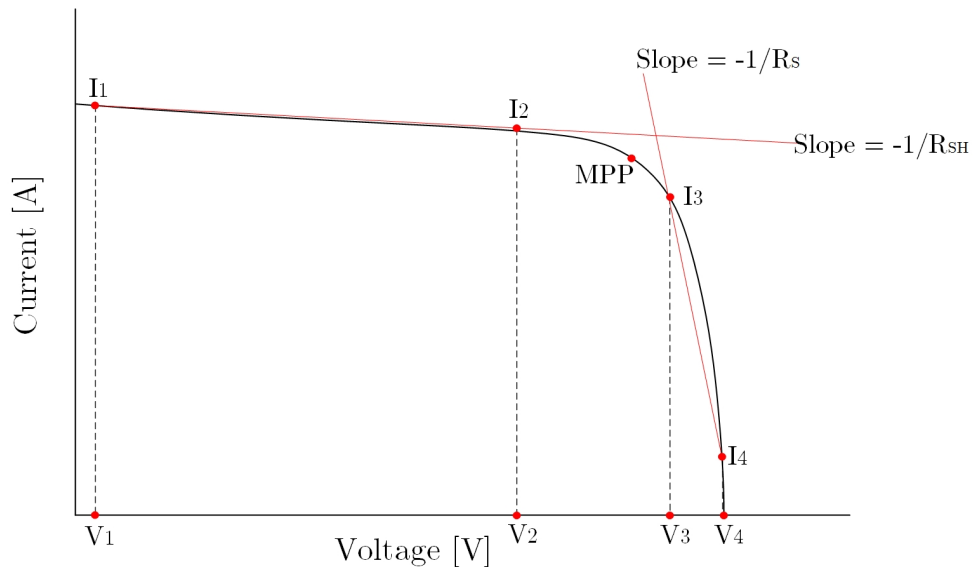


Figure 7.5: Demonstration of how the shunt,  $R_{SH}$ , and series,  $R_S$ , resistances are approximated for an initial value guess, used by the optimisation algorithm.

#### 7.8.4 Software implementation of PV module parameter extraction

A python script, which utilises the SciPy library is used to implement the parameter extraction algorithm which employs the `optimize.minimize` module [121]. The single-diode model is then solved in the form of equation (7.8). Specifically, after testing various optimisation methods the COBYLA (Constrained Optimization BY Linear Approximation) optimization method is found to be the most suitable. As previously mentioned, other standard curve



fitting functions are used such as the Spline interpolation and Savgol filtering and smoothing techniques, but these routines simply aim to strike through each data point, but do not represent true PV module behaviour, especially when irregularities occur. An example of this is shown in Figures 7.6 and 7.7. As seen in Figure 7.6 all three methods fit the curve almost exactly. However, in Figure 7.7 a shaded module I-V curve is fitted by the Spline and Savgol methods, but the single-diode curve fitting routine has returned an error and failed to plot due to an irregular data set. Therefore, only two lines are plotted in Figure 7.7.

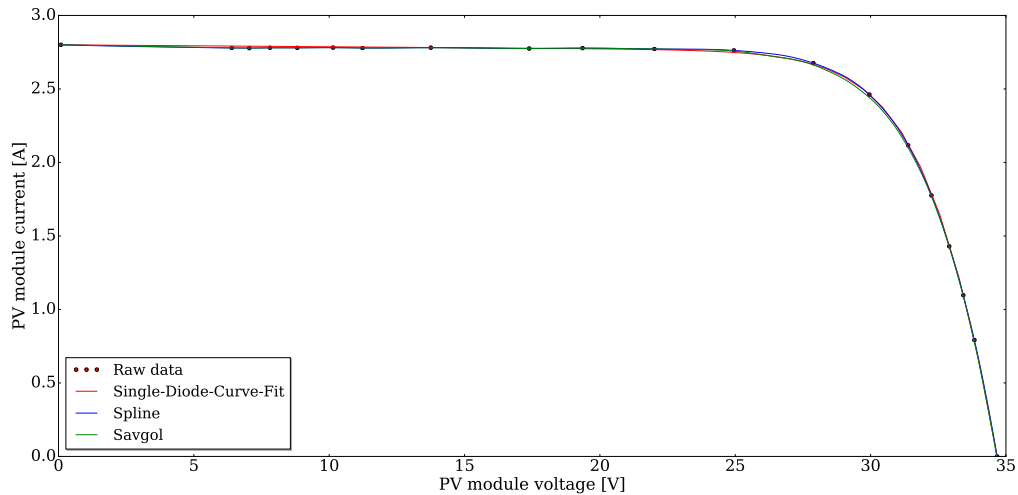


Figure 7.6: Illustration of a curve fitted routine applied by the Spline, Savgol (3rd order) and Single-diode curve fitting routines, onto a regular set of measured data points.

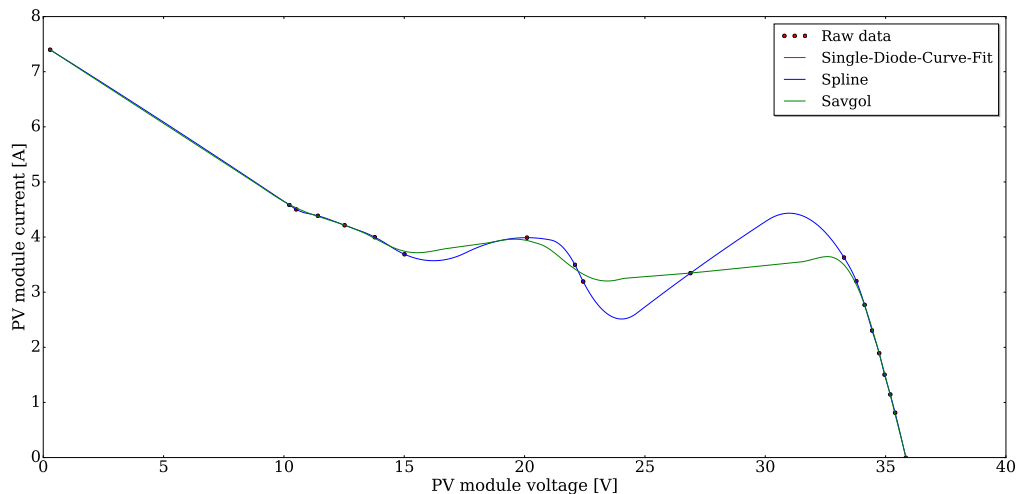


Figure 7.7: Illustration of a curve fitted routine applied by the Spline, Savgol (3rd order) and Single-diode curve fitting routines, onto a shaded module.

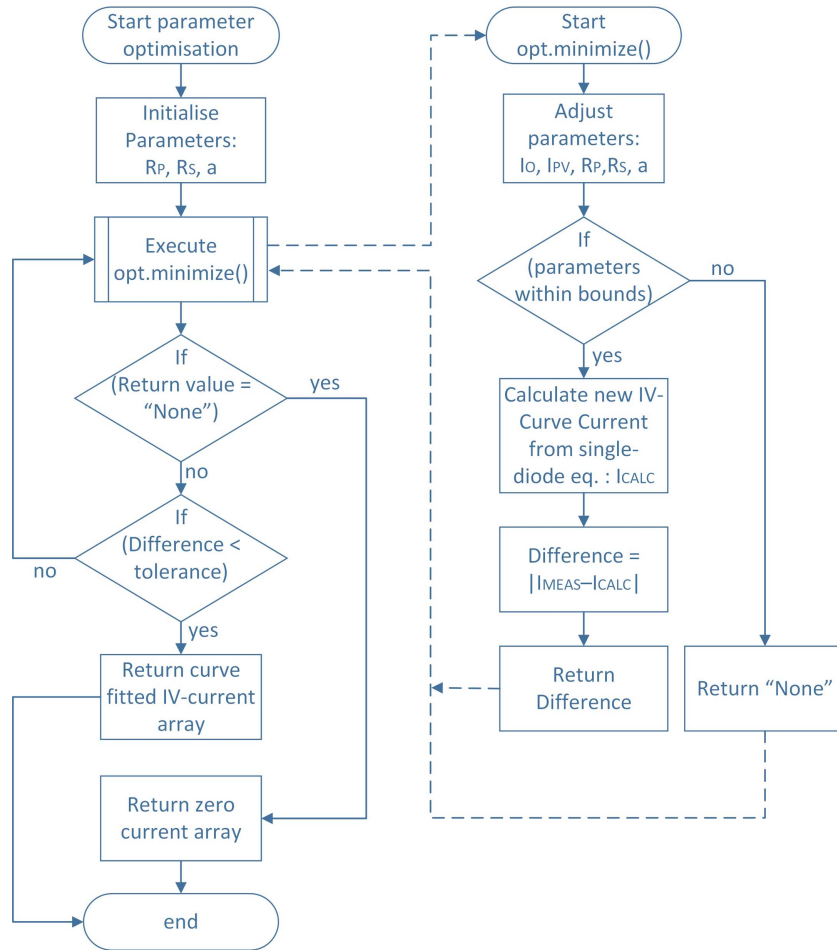


Figure 7.8: Software flow diagram illustrating the process of parameter extraction for the Single-diode curve fitting algorithm.

As presented by the flow chart of Figure 7.8, the Python script optimises the parameters continuously, until a new set of parameters is found, which allows the difference between the measured and the newly calculated current values to converge. Initially, all five parameters are estimated by the python script, but it is found that adjustments are made in such a way that some parameters are over or under estimated. Therefore, with the use of equations (7.11) and (7.13), which define  $I_O$  and  $I_{PV}$ , only parameters  $R_S$ ,  $R_{SH}$  and  $a$  have to be estimated.

The required  $I_{SC}$  and  $V_{OC}$  values are set as the actual measured  $I_{SC}$  and  $V_{OC}$  values. The value of parameter  $a$  is estimated by assuming a diode ideality factor of one and a module temperature of  $30\text{ }^\circ\text{C}$ . The initial value of  $R_{SH}$  and  $R_S$  is defined by acquiring the gradients of the I-V curve by applying equations (7.14) and (7.15).

A predefined tolerance, which specifies the desired accuracy for the process of convergence, is applied and is set at 0.001. As presented by (7.8), the single-diode equation requires an iterative process to solve the value of the terminal output current  $I_T$  of the PV module. This is achieved by adopting the Newton-Raphson method. Firstly, this method requires that the equation to be solved is in the form  $f(x) = 0$ , with  $x$  as the variable to be determined [122, pp.312,313]. The Newton Raphson recursion formula is presented by equation (7.16) [122].

$$x_{n+1} = x_n - \frac{f(x_n)}{f'(x_n)} \quad (7.16)$$

The single diode equation (7.8) is rewritten into the specified Newton Raphson format of  $f(x) = 0$  as shown in (7.17). However, for the recursive formula to converge, the derivative of  $f(x)$  is required as well, as defined in (7.18).

$$f(x) = f(I_T) = I_T - I_{PV} + I_O \left[ e^{\left( \frac{V_T + I_T R_S}{a} \right)} - 1 \right] + \frac{V_T + I_T R_S}{R_{SH}} = 0 \quad (7.17)$$

$$f'(I_T) = 1 + I_O \frac{R_S}{a} \left[ e^{\left( \frac{V_T + I_T R_S}{a} \right)} - 1 \right] + \frac{R_S}{R_{SH}} \quad (7.18)$$

Therefore, when equation (7.16) is recursively applied the new value of the terminal current  $I_T$  is determined as:

$$I_{T(n+1)} = I_{T(n)} - \frac{I_{T(n)} - I_{PV} + I_O \left[ e^{\left( \frac{V_T + I_{T(n)} R_S}{a} \right)} - 1 \right] + \frac{V_T + I_{T(n)} R_S}{R_{SH}}}{1 + \frac{I_O R_S}{a} \left[ e^{\left( \frac{V_T + I_{T(n)} R_S}{a} \right)} - 1 \right] + \frac{R_S}{R_P}} \quad (7.19)$$

The Newton Raphson method stops approximating the value of  $I_T$  when the difference between determined values starts to converge to satisfy the condition of (7.20).

$$|I_{T(n+1)} - I_{T(n)}| \leq \textit{tolerance} \quad (7.20)$$

Thus, with the parameters now known, as defined by the curve fitting process, an I-V curve with a higher resolution can be obtained by applying the defined parameters to equation (7.8) and providing a set of input voltage values. It is found that 40 generated data points, as opposed to the measured 20, provide a high enough resolution to determine the MPP of the I-V curve.

## 7.9 Results and discussion

### 7.9.1 Overview

All results and discussions are presented by this section. Firstly, the analysis of the stationary modules is performed, which is followed by the analysis of the SAT modules. Dust soiling is quantified and the applied dust mitigation methods are compared.

### 7.9.2 Holistic data representation for stationary modules

Before the data analysis proceeds into a more detailed investigation, it is important to firstly gain an overall perspective of the data captured. This is necessary so that the reader is acquainted with the general movements of the data set and to prevent focus of diverting from the more in depth discussions, due to unknown data behaviour. A holistic view of the

PR of all the PV modules (except PV modules two and seven), is presented by Figure 7.9, with Figure 7.10 representing an enlarged view of the PR data set.

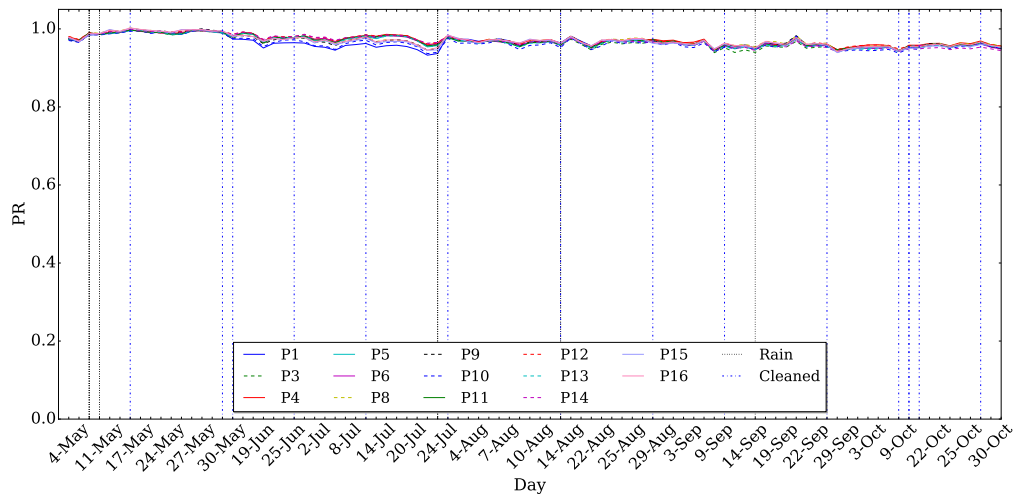


Figure 7.9: Extracted PR values of all the stationary PV modules, with rainfall and cleaning sessions indicated.

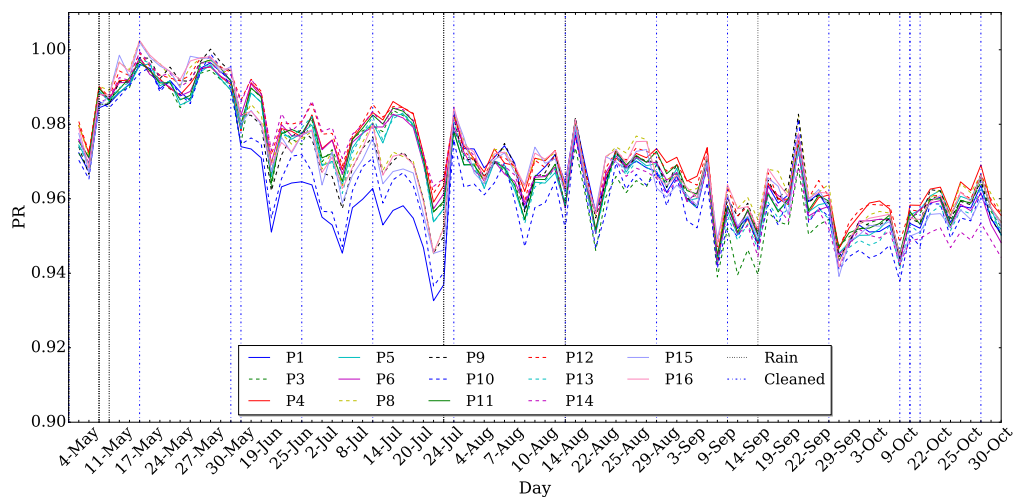


Figure 7.10: Amplified view of the extracted PR values.

Firstly, data retrieved from PV modules two and seven is not presented due to the insufficient extraction of I-V curve data from these modules. With the holistic illustration of data in Figures 7.9 and 7.10, characterising the PV modules' behaviours in terms of PR, there are some components of the data set to be considered:

- Days on which the modules are washed or rainfall occurred.
- PR fluctuation.
- An overall gradual decline in PR.

All days where the PV modules are exposed to rainfall, or a scheduled cleaning routine is performed, are indicated on the graphs. However, notice that the time-line of the data presented by Figures 7.9 and 7.10 does not display a chronological sequence of time. This is

because, only the days that are regarded as valid, based on the criteria defined in section 7.7, are considered for analysis. This does however exaggerate the deviation between two data points, since a gradual change in a PV module's PR, is now condensed over a shorter period of time. This is one of the reasons why such a sharp increase or decrease in the PR is seen. In terms of rainfall, not all intermittent days (invalid days) on which rain is received can be displayed. Thus, rainfall and, in some cases cleaning days, are therefore shifted to a data point measured before the rain or scheduled cleaning occurred, as in Figure 7.10. This does give a more logical data representation, since days on which rain occurred, are succeeded by an immediate increase in PR, as seen on the 14th of Sept. for example.

Therefore, to obtain a more synchronised and less exaggerated graphical representation of data, all graphs are displayed in chronological order as in Figure 7.11. With this display format of data, the reader should not be confused with regards to a rain or cleaning routine indicator. For example, in Figure 7.11 the rainfall indicated at marker (a) occurred on the 27th, 28th and 31st of July 2016. However, the first valid day after the 24th of July is 1 Aug. 2016. Thus, between these two measured data points, rainfall occurred, which explains the increase in PR from 24 July - 1 Aug. 2016. The same scenario takes place in terms of rainfall on 17 and 18 Aug. and the cleaning routine of the PV modules on the 15th of August, as indicated at marker (b). Thus, the reader should not be confused with the early increase in PR before rain and cleaning events occur.

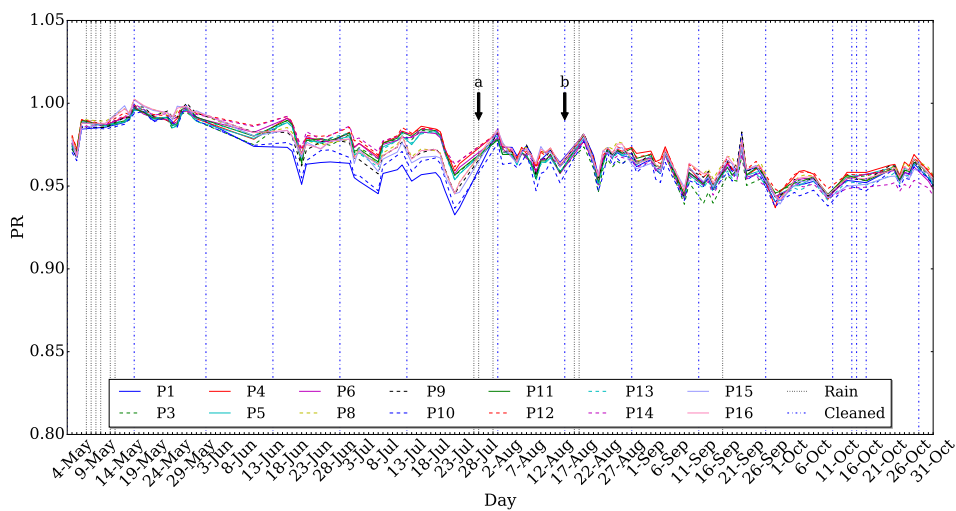


Figure 7.11: Chronologically spaced representation of the measured PR.

### 7.9.3 Performance ratio characterisation

There are two distinctive aspects with regards to the varying PRs as in Figure 7.11. Firstly, the sudden increase and decrease at specific moments, not preceded by rainfall or module cleaning. Secondly, the gradual decline in PR, as seen from the beginning of May to August. Upon first inspection the occurrence of rapid fluctuation in the PR could possibly be prescribed to a varying level of PV module surface soiling. On the other hand, the gradual decline in PR could be due to a stubborn accumulation of dust particles, or the natural degradation of the PV modules. Before a conclusion can be made regarding these events, the main question of concern here is whether the formulated PR normalises PV module output as expected? Mathematically, the PR should normalise PV module behaviour with regards to module temperature and irradiance at STC conditions. The question therefore is, why is there such a definitive variation in the PR of the modules? For example, in Figure 7.11 on the 21st to 22nd of Sept., a PR change of 2.3% is observed, for almost all modules.

With further examination of the data, this question of a varying PR is mostly answered. Evaluation reveals that, the received irradiance ( $G_{POA}$ ) has the most significant correlation with the change in the PR, as indicated in Figure 7.12. The irradiance presented by this graph is averaged for the daily hours of 11:00 AM-14:00 PM. This is the same period which is used to determine the PR. From this comparison it is concluded that  $G_{POA}$  and the PR are inversely proportional to one another. Further analysis, also indicates some correlation between wind-speed, humidity and ambient temperature, but the influence of these data sets are not nearly as obvious, as can be seen in the figures of Appendix D.4.

There are some points of interest indicated on the graph of Figure 7.12, which need to be addressed. Firstly, the gradual decline in PR, can largely be attributed due to the gradual incline of the irradiance. Secondly, to substantiate the argument of the inverse relationship between  $G_{POA}$  and the PR, points (c) and (d) clearly indicate a drastic increase in PR, in the absence of a preceding cleaning routine or rainfall. However, the sharp increase does correlate with a decrease in irradiance. At marker (e2) the PR does however not increase with a decrease in irradiance. This is because, the irradiance measured for the period of 21 May to 12 July, is received from another pyranometer, due to the malfunction of the research facility's own pyranometer, as previously mentioned. Points (e1) and (e2) indicate this period, where the other pyranometer's data is merged with the research facility's data. This should however not affect the PRs measured between these points ((e1) and (e2)), since the irradiance correction of the PR is applied equally to all of the PV modules. Marker (b) refers to the largest difference in measured PRs, during the entire research period. The curve of the PR graph does correlate well with the change in irradiance, but further investigation is required to determine the difference in performance amongst the modules. Finally, point (a) is regarded as an anomaly, since the average irradiance is very low, but an expected inverse response from the PR is not seen. This particular data point does however present a rather low irradiance level ( $\sim 700 \text{ W/m}^2$ ), which is speculated to contribute to this behaviour.

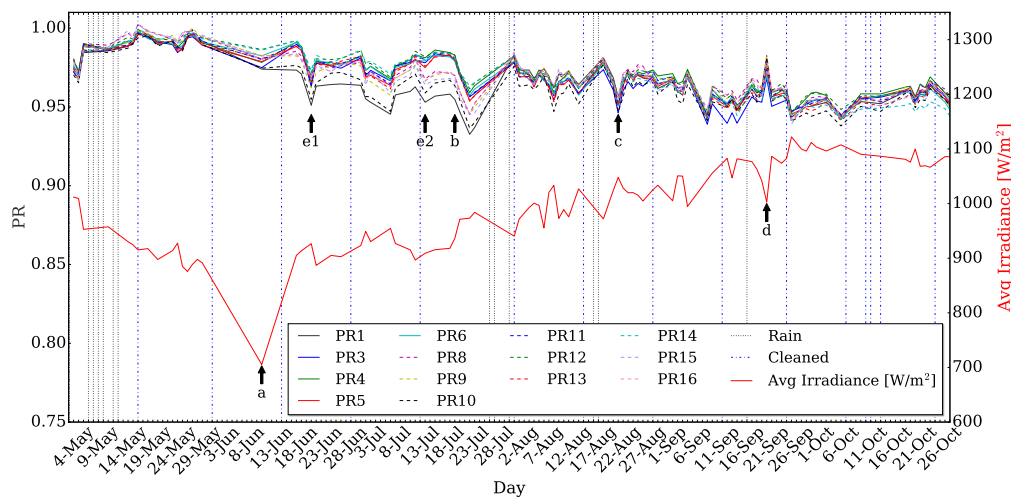


Figure 7.12: Relationship between the measured plane of array irradiance ( $G_{POA}$ ) and the measured PR values.

It is concluded that the change in the PR, is due to the varying efficiency of the PV modules at different irradiance intensities, as previously indicated in Table 7.3. Thus, to obtain a better representation of PV module performance, less sensitive to a variation in irradiance and more representative of the effects of PV soiling, a Clearness Ratio (CR) is defined. This ratio is defined by equation 7.21:

$$CR = \frac{PR_{Tcell-G-corrected}}{PR_{Tcell-G-corrected-clean}} \quad (7.21)$$

Where  $PR_{T_{cell}-G-corrected}$  represents the temperature and irradiance corrected PR of a module and  $PR_{T_{cell}-G-corrected-clean}$  presents the corrected PR of a cleaned reference PV module.

The CR minimises the effect of a changing irradiance, by comparing the PR of a module to that of a set of cleaned modules, subjected to the same exposure of irradiance and other environmental factors (wind, temperature, etc.). Therefore, any change in PV module behaviour can be largely attested to the influence of dust soiling.

The  $PR_{T_{cell}-G-corrected-clean}$  value of the CR, as in 7.21 is chosen as the average of the combination of modules P6 and P11. Reason being that these two modules are both untreated (no surface coating applied) and cleaned with distilled water once every two weeks, restoring the surface conditions of the modules. The CR of each module is represented in Figure 7.13, with P6 and P11 as reference. Therefore, a CR of one, presents the value of  $PR_{T_{cell}-G-corrected-clean}$

$$PR_{T_{cell}-G-corrected-clean} = \frac{PR_{P6} + PR_{P11}}{2} \quad (7.22)$$

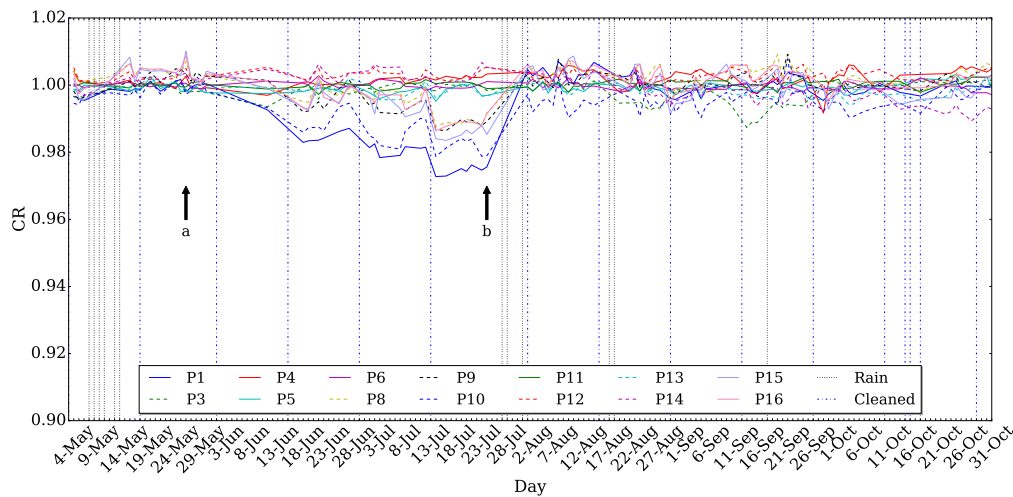


Figure 7.13: Clearness ratio represented for each module over a six month period, with PV modules P6 and P11 as reference modules.

### 7.9.4 Quantifying the effect of dust soiling

Evident from the graph presented in Figure 7.13, the CR filters out the data sensitivity to irradiance. As seen, there are several PV modules that deviate from the ideal CR of one. Particularly of interest is the section between markers (a) and (b) in Figure 7.13. It is visible from the graph that this time period has provided circumstances which amplifies the effect of dust soiling on PV module output power. Particularly, a 75 day absence of rainfall is what primarily separates this section from the rest of the graph. As previously mentioned, it is not the aim of this thesis to provide an in depth study with regards to the influences of weather, but rather to produce a holistic perspective on the influence of weather factors, where identified. The aim of the thesis is primarily to identify the effects of dust soiling on PV module surface area and not so much the identification of external influences on the accumulation of dust. The aim is however to identify the effects of soiling and how various dust mitigation strategies affect the behaviour of modules, subjected to the environment.

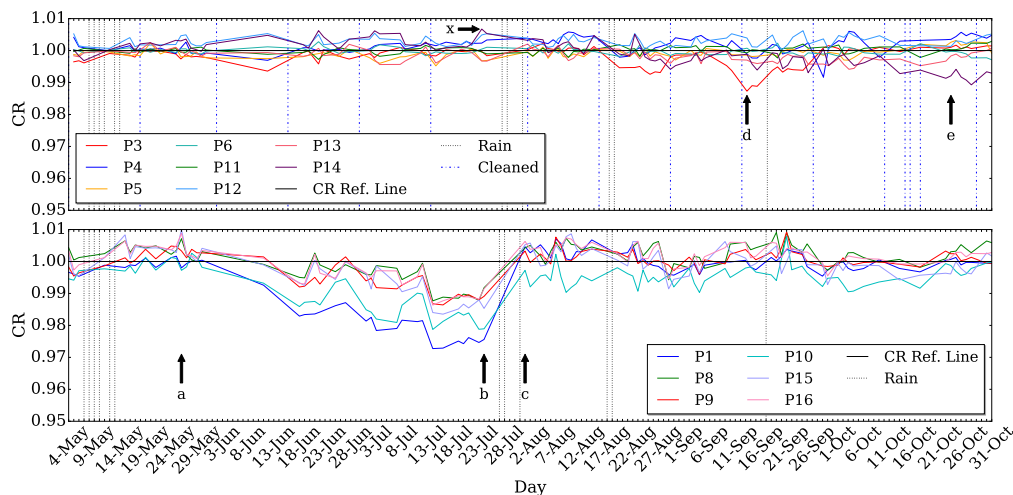


Figure 7.14: CR represented for two groups of regularly cleaned and non-cleaned modules. Top: CR of PV modules cleaned regularly. Bottom: CR of non-cleaned PV modules.

In Figure 7.14 the short term cleaned modules are compared to the non-cleaned PV modules. It is observed that the CR is exceeded on several occasions by both groups (cleaned and non-cleaned). This indicates that the reference modules (P6 and P11) are in fact not the cleanest, or most ideal in terms of surface clarity, all of the time. PV modules P4, P12 and P14 outperform the reference modules most of the time. However, it should be noted that the highest CR is recorded at 1.0067, indicated by marker (x) in Figure 7.14, which is only 0.67 % higher than that of the reference modules. Thus, for practical reasons this is negligible. However, it should be noted that the long term modules also outperformed the reference modules of the CR, especially during the period of August to September. The highest CR measurement is recorded on 26 May, indicated by marker (a), with PV module P15 exceeding the CR of the reference modules by  $\sim 1\%$ .

It can be seen that the CR of the PV modules are either below or above the ideal CR value of one. This is simply a result of using reference modules, which occasionally perform better or worse than the other PV modules. It is evident from these graphs that the PV modules, which are not cleaned bi-weekly, exhibit the largest decrease in terms of the CR. Particularly, the largest decrease in CR is seen during the 13th to the 24th of July.

Also interesting is how after a two week cleaning session is executed, as for example on the 1st, 15th and 29th of June, one can clearly identify how the CR of the modules, which are not cleaned, decreases. This is of course attributed to the CR's point of reference, which is reset after the cleaning routines are executed. Therefore, the measurements recorded soon after the completion of a cleaning routine, presents the most realistic representation of a cleaned module as compared to a non-cleaned module. After almost two and a half months of no rain, the rainfall of the 27th, 28th and 31st of July, indicated by marker (c), clearly allows the non-cleaned modules' performance to be restored in terms of the CR. Only module P10 does not seem to recover quite as well, but is still within  $\sim 0.3\%$  of the reference modules' CR. In Table 7.4, the maximum decrease in CRs for the non-cleaned modules are shown, which essentially quantifies the difference in module performance due to dust soiling, as compared to a set of normal, cleaned PV modules.



Table 7.4: Maximum decrease in clearness ratio for unclean modules, as extracted from Figure 7.13.

PV module	P1	P8	P9	P10	P15	P16
Max. decrease in CR [%]	2.72	1.24	1.36	2.13	1.65	1.37

From the top graph in Figure 7.14, the CR of the cleaned PV modules remains within a maximum deviation of 1%. The largest deviation amongst the cleaned PV modules, occurs at markers (d), which points to 12 Sep. and marker (e), denoting the period between 17 and 28 October. At marker (d) a maximum decrease of 1.3 % is seen for PV module P3. This behaviour is associated with a bird dropping, since the CR of the module decreases right after being cleaned on 12 September, therefore eliminating the possibility of dust soiling. It is interesting to note how the rainfall on 17 September (6.5 mm) does largely restore module P3's CR, but still not as effectively as the cleaning routine performed on 28 September. This does give an indication of how rainfall is not able to effectively eliminate the bird dropping. With regards to point (e), module P14 indicates a CR drop of 1.1 %. As mentioned, the non-routine cleaning sessions indicated for 14, 15 and 17 October are only applied to PV modules P3, P4, P5 and P6. Thus, with module P6 as reference module, the CR's reference point is effectively raised, which does contribute to some of the decrease of module P14's CR. A definitive conclusion regarding module P14's decrease in CR cannot be made due to uncertainty. The biggest contributor to this uncertainty is the module's reaction after the cleaning routines are executed on the 10th and 28th of October, which does not seem to restore module P14's CR.

Over all, apart from the time period between markers (a) and (b) in Figure 7.14, the data indicates that a frequent and sufficient rainfall is enough to maintain PV modules to within 1 % of rated performance. A frequent rainfall refers to approximately four to six weeks. No conclusion can be drawn with regards to the quantity [mm] of rainfall required to restore a PV module surface completely. This is due to all rainfall events equating to more than 6.5 mm of rain, which restored all of the modules' performances, except for the two events discussed regarding modules P3 and P14.

To conclude, for the period of 24 May to 24 July, the modules cleaned biweekly, outperformed the PV modules that are not cleaned during the research period. However, it is evident from the data set presented that some modules, for the majority of time, perform better or worse than other modules. An example of this is modules P4, P12 and P14, which outperform most modules, in the top graph of Figure 7.14, for a number of weeks. On the other hand in the bottom graph of Figure 7.14, modules P8, P9 and P16 seem to perform the best. The question is now to determine, whether or not this can be attested to the mitigation methods applied and if so, to determine which dust mitigation methods performed better. Further investigation, regarding the mitigation methods applied, is presented in Section 7.9.5.

### 7.9.5 Analysis of dust mitigation methods

#### Important details regarding the data analysis

With the influence of dust quantified in section 7.9.4, it is still within the interest of this thesis to determine which dust mitigation methods performed the best. Figure 7.15 serves as a reminder of the DMS, with the applied stationary module mitigation methods. With regards to any analysis of long term modules, modules P1, P8, P9 and P16 are also considered, even though no cleaning routines are allocated to these modules. Reason being that, the analysis

is conducted, within the first six months after applying the anti-soiling coating. Thus, the long term and indefinite modules are still synchronised with regards to exposure time, up until the 28th of October, when modules P10 and P15 are washed, after a six month exposure period (long term). The addition of modules P1, P8, P9 and P16 to the analysis, in effect reconciles for the data absence of modules P2 and P7, which are long term assigned modules.

The PR, which is recorded at the same instance for all modules, under the same circumstances, is used for the comparison of the different mitigation methods. The CR could also be utilised for the analysis, but the PR allows for an easier visual interpretation of the data set.

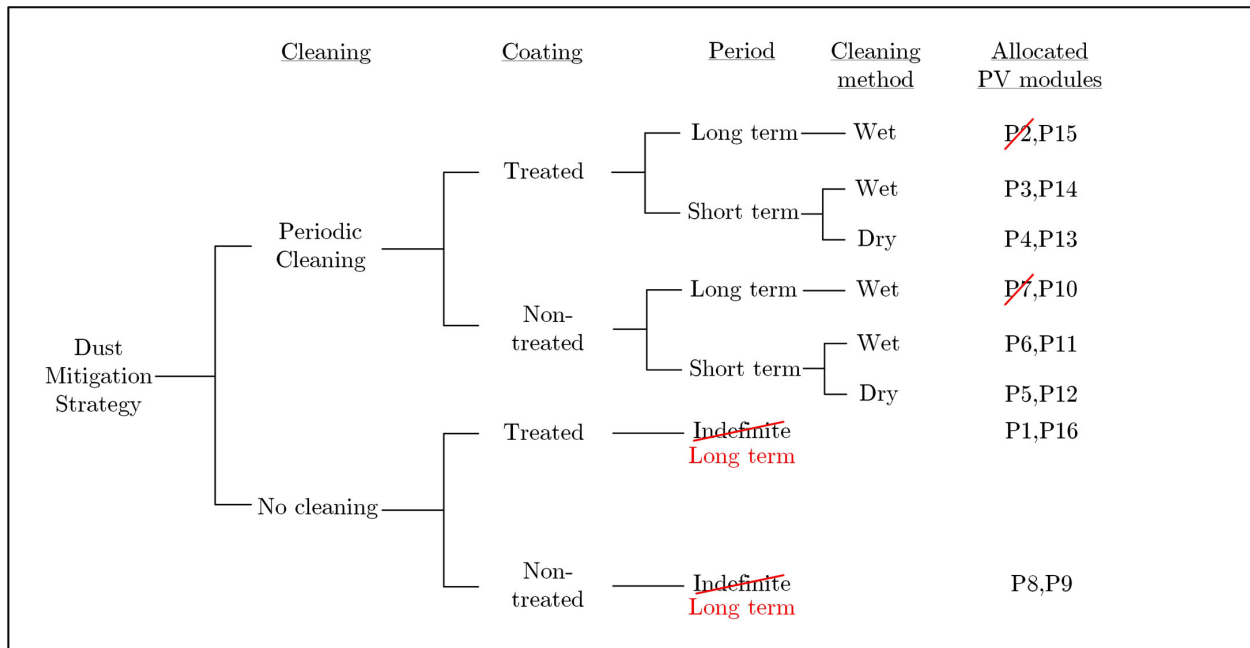


Figure 7.15: Illustration of the adjusted DMS for the analysis.

As explained in Chapter 6.2.1, each mitigation method is applied to a set of two modules. The approach of calculating the performance of the different mitigation methods, is based on a comparison of averages, as will be seen throughout this analysis. A histogram plot is then used to illustrate the mathematical distribution of the module sets compared.

With regards to the histogram distribution plots. It is necessary to portray a weighted data set, which is representative of a fairly distributed data set. Due to the criteria mentioned in section 7.7.2, not all days are regarded as valid data points for the analysis. This does occasionally result in unavailable data points between two consecutive PR measurements. Figure 7.16 provides an illustration of how days, for which a PR value is unavailable, are added into the data set, to allow for a more representative histogram data distribution. With points A and B as measured data points and  $y_1$ ,  $y_2$ ,  $y_3$  as unavailable data points, the values of  $y_1$ ,  $y_2$  and  $y_3$  are calculated and added into the PR data set. This allows for a fair weight distribution of the histogram data plots.

When two data sets are compared, a percentage difference is provided as an indication of performance. Figure 7.17 aids the explanation of defining the definitions for an ideal and a relative PR comparison made. When the analysis refers to an ideal PR difference, denoted by  $PR_{ideal}$ , then this is where two data points (A and B) are compared to one another, with reference to the ideal scenario where  $PR = 1.0$ . This is presented in equation (7.23). The relative PR difference  $PR_{relative}$  compares the difference in performance of one module

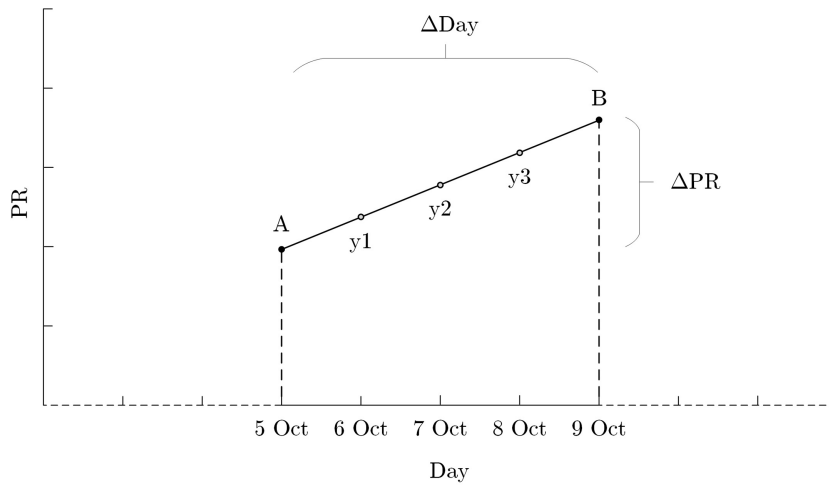


Figure 7.16: Illustration of how unavailable PR data points are added to the measured PR data set.

set relative to another. For example the PR difference of point B relative to point A is presented by equation (7.24). Therefore,  $PR_{ideal}$  is used for a direct comparison with respect to PV module power output performance, and  $PR_{relative}$  is used for a direct inter-module performance comparison.

$$PR_{ideal} = \left( \frac{A - B}{1.0} \right) \times 100\% \quad (7.23)$$

$$PR_{relative} = \left( \frac{A - B}{A} \right) \times 100\% \quad (7.24)$$

For example, in the graph of Figure 7.17 on the 9th of Oct. Module 1 delivers 95 % and Module 2 delivers 80 % of the ideal module output power. Thus, the difference in module performance between Module 1 and Module 2 (in terms of PR) is measured as 15 % higher for point A than for point B, as according to (7.23). In terms of the performance of Module 1 relative to Module 2, on the 9th of October, a difference of 18.75 % is calculated with equation (7.24). Thus, with reference to Module 2, Module 1 outperformed Module 2 by 18.75 %. It is important that the reader is able to clearly differentiate between the two PR definitions.

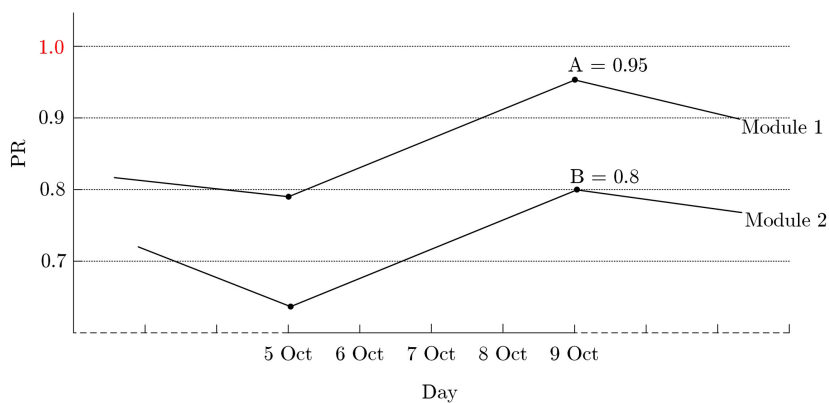


Figure 7.17: Illustration of two measured PR data sets.

Important dates to consider are as follows:

- 14, 15 and 17 Oct. 2016: This is when modules P3, P4, P5 and P6 are cleaned, for a day to day comparison.
- 28 Oct. 2016: This is when the Long term modules P10 and P15 are cleaned after six months of exposure.

The analysis of the PR graphs for all of the modules is presented for the period of 4 May to 31 Oct, unless otherwise specified. Although the modules affected by the activity of either 14, 15, 17 or 28 October may be presented, the reader should keep these dates in mind when viewing the PR graphs. Nevertheless, all of the histogram plots, presenting the difference in performance amongst modules, will disregard any of the days which might alter results.

A final remark about the histogram distribution plots. The bin-width of each histogram bar is 0.5, which is chosen based on the accuracy of the measurement instrumentation and visual preference, in terms of presenting data that is easily interpretable. Thus the histogram bin presenting 1 % values, actually encapsulates values between 0.75 % and 1.25 %.

### 7.9.6 Long term vs. short term

This section compares the performance of modules that are exposed over a long term, without any periodic cleaning executed, to modules cleaned biweekly. This comparison of the coated and non-coated PV modules is also presented. The analysis also investigates the performance of the wet and dry cleaning routines.

#### Comparison A: Short term and long term coated PV modules

Two sets of comparisons are formulated for this particular analysis as shown in Table 7.5. The PRs of sets A-1 and A-2 are compared in Figures 7.18 and 7.19. It is evident that the short term modules clearly outperformed the long term modules during the months of June and July. However, in both cases the short and long term modules perform within close proximity for the period after the rainfall on 31 July. The results of the graphs in Figures 7.18 to 7.20 are summarised in Table 7.6.

Table 7.5: Long term allocated modules compared to short term PV modules.

Comparison	Set	Exposure time	PV modules	Coating
A	1	Long term	P1,P16,P15	yes
		Short term(Wet)	P3,P14	yes
	2	Long term	P1,P16,P15	yes
		Short term(Dry)	P4,P13	yes

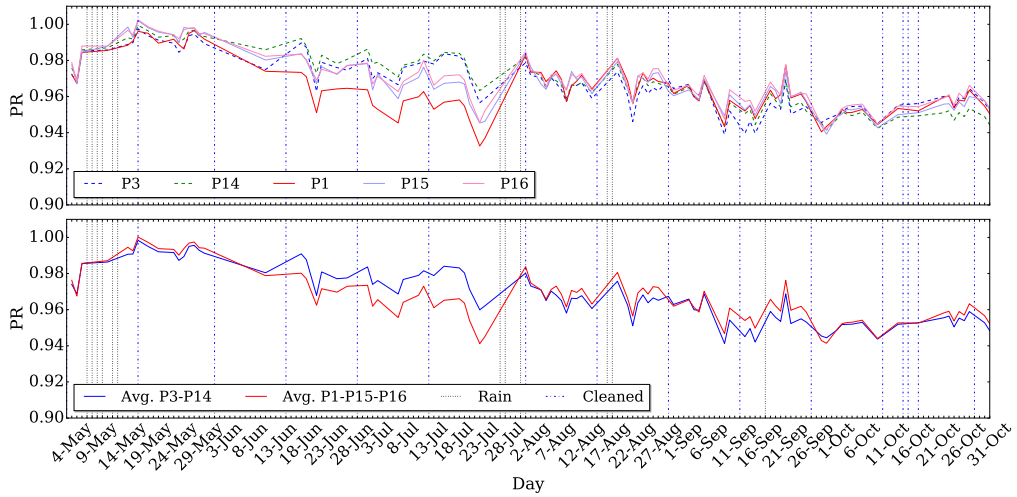


Figure 7.18: Comparison set A-1. Coated modules. Top: PR of long term and water cleaned short term modules. Bottom: Avg. PR of long term and short term modules.

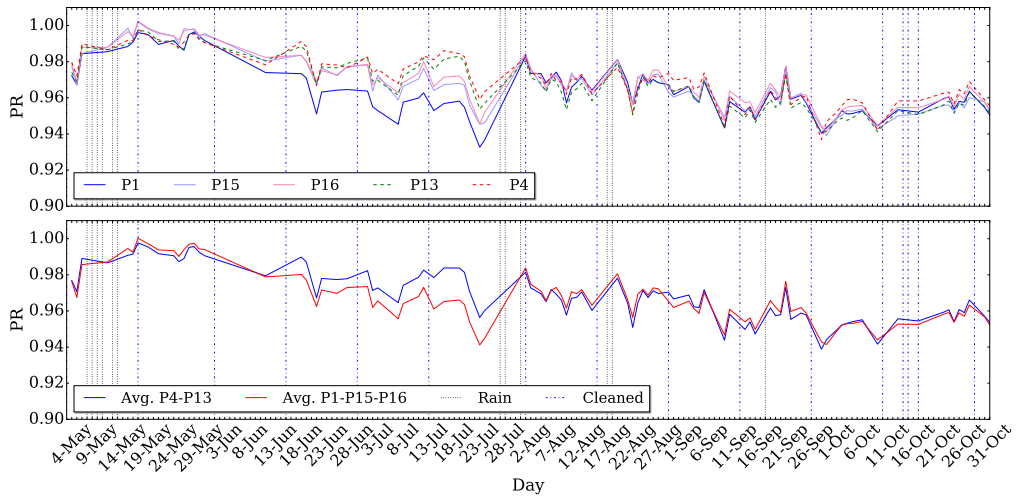


Figure 7.19: Comparison set A-2. Coated modules. Top: PR of long term compared to dry cleaned short term modules. Bottom: Avg. PR of long term and short term modules.

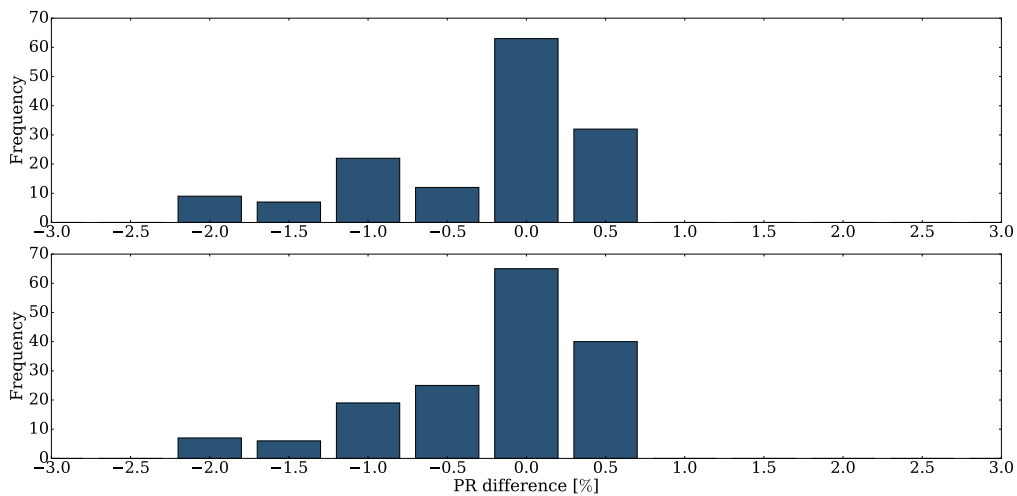


Figure 7.20: Histograms of coated modules. TOP: Set A-1. Long term w.r.t. short term, water cleaned. BOTTOM: Set A-2. Long term w.r.t. short term, dry cleaned.

Table 7.6: Summary of most significant data points for data set A-1 and A-2.

PR	$PR_{ideal}$	$PR_{relative}$	Hist. Days			
			Total	$\geq 1\%$	$\leq -1\%$	$\pm 0.5\%$
Set A-1	1.89% (16 Jul.)	1.96% (23 Jul.)	145	0	38 (26.2%)	107 (73.8%)
Set A-2	1.86% (16 Jul.)	1.89% (16 Jul.)	162	0	32 (19.8%)	130 (80.2%)

The histogram plots in Figure 7.20 presents an accumulated distribution over the course of six months. No unfair advantage is given to either of the modules, with performance comparisons after the 13th of Oct. omitted, due to modules P3 and P4 cleaned on 14, 15 and 17 Oct. 2016. The histogram plot for set A-1, omits the days of 10-26 Sep. due to the bird dropping (mentioned in section 7.9.4) on module P3. In terms of sets A-1 and A-2, the largest data distribution is within the  $\pm 0.5\%$  region of each histogram. However, from the  $\pm 1\%$  region and beyond, the long term exposed modules in both cases tend towards a negative PR, as compared to the short term cleaned modules. For both sets A-1 and A-2 a max. difference in ideal PR ( $PR_{ideal}$ ) is recorded as  $\sim 1.9\%$  on 16 July. Also, the largest relative difference in PR ( $PR_{relative}$ ) is recorded at 1.96% for set A-1, in favour of the short term, water cleaned modules. Thus, from these results it is concluded that the dry and wet cleaned modules, displayed an increased relative performance of  $\sim 2\%$  above that of the long term modules.

### Comparison B: Long term vs. short term uncoated PV modules

As presented by Table 7.7, this analysis investigates the PR of the uncoated (normal) PV modules, which are assigned to long term and short term periodic cleaning routines.

Table 7.7: Details of the uncoated long term allocated PV modules compared to short term PV modules.

Comparison	Set	Exposure Time	PV modules	Coating
B	1	Long term	P8,P9,P10	none
		Short term(Wet)	P6,P11	none
	2	Long term	P8,P9,P10	none
		Short term(Dry)	P5,P12	none

The PRs for the uncoated modules of comparison group B, is displayed in Figures 7.21 and 7.22. As seen from these results, the short term modules once again outperformed the long term modules during the months of June and July, whereas after the rain fall of 31 July, all module performances are within close proximity of one another. Table 7.8 summarises the results obtained for this analysis.

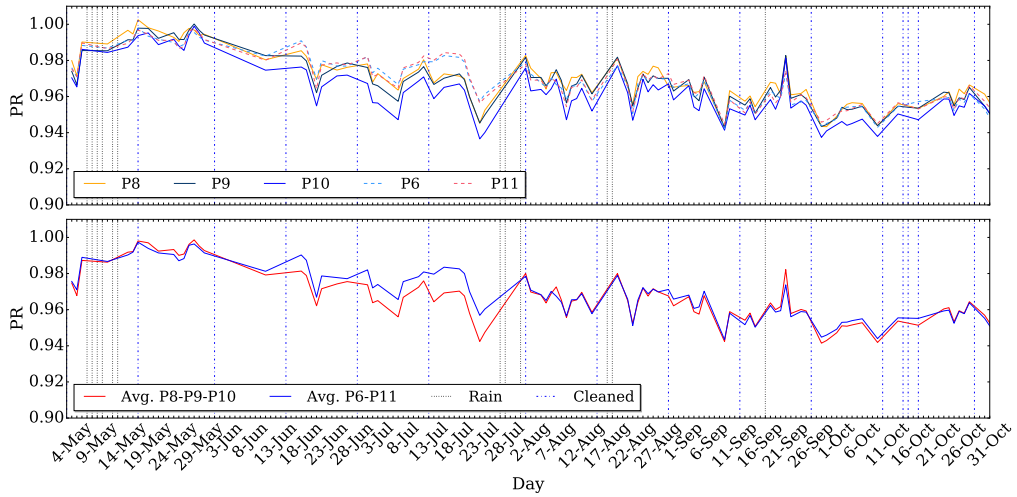


Figure 7.21: Comparison set B-1. Uncoated modules. Top: PR of long and short term (water cleaned) modules. Bottom: Avg. PR of short and long term modules displayed.

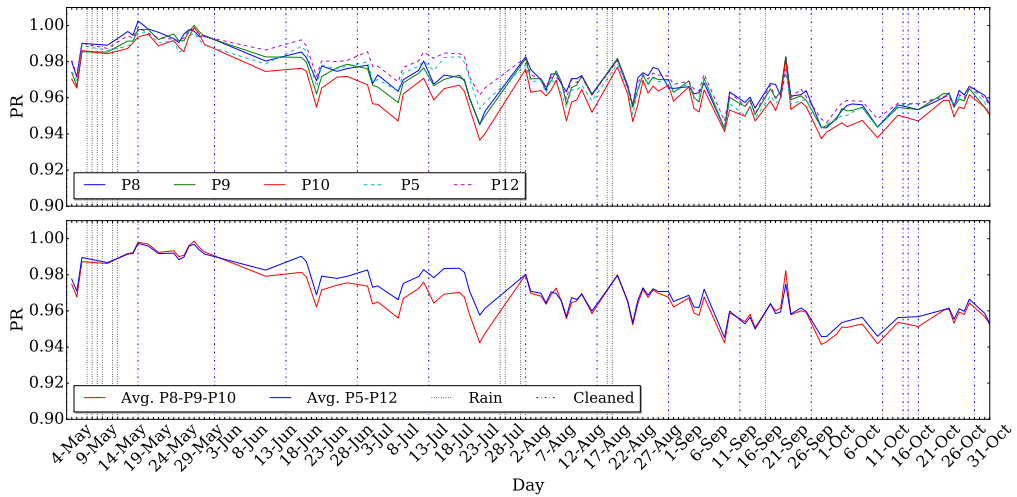


Figure 7.22: Comparison set B-2. Uncoated modules. Top: PR of long and short term (dry cleaned) modules. Bottom: short and long term modules displayed.

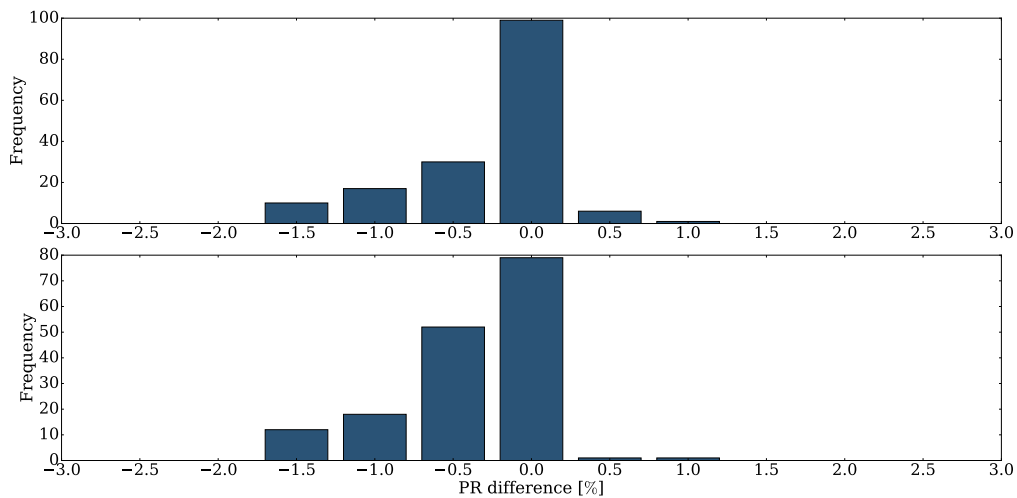


Figure 7.23: Hist. of uncoated modules. TOP: Set B-1. Long term w.r.t. short term, water cleaned modules. BOTTOM: SetB-2. Long term w.r.t. short term, dry cleaned modules.

Table 7.8: Summary of results for the maximum difference in PR values recorded.

PR	$PR_{ideal}$	$PR_{relative}$	Hist. Days			
			Total	$\geq 1\%$	$\leq -1\%$	$\pm 0.5\%$
B-1	1.53% (14 Jul.)	1.56% (14 Jul.)	162	1 (0.6%)	27 (16.7%)	134 (82.7%)
B-2	1.53% (23 Jul.)	1.59% (23 Jul.)	162	1 (0.6%)	30 (18.5%)	131 (80.9%)

From the histogram plots presented in Figure 7.23 it is evident that the short term modules outperformed the long term modules. However, for more than 80 % of the time, the relative difference in PR of both sets B-1 and B-2, is within the  $\pm 0.5$  % region. This indicates that the long term and short term cleaning routines are within a reasonable performance difference of one another.

From the long term and short term analysis conducted for sets A-1, A-2, B-1 and B-2, it is concluded that in the absence of rain over a period of four weeks or more, the short term cleaned modules outperform the long term modules. However, if rainfall is received frequently (four weeks or less) the long term modules perform within an acceptable margin of deviation of less than 1%.

When comparing the results of groups A and B, the long term modules suggest a bigger deviation (max. 1.89 %) for the group of coated modules than for the group of uncoated modules (max. 1.53 %). From the histogram distributions, it is also evident that the coated modules underperformed for a few days more than the uncoated modules. These results are in contrast to the hypothesis made in Chapter 1.2.4, which predicts that the applied hydrophobic coating should allow modules to perform better than uncoated modules. Therefore, with these results in mind, it is speculated that the hydrophobic coating is in fact promoting dust adhesion. This, implies that that long term, coated modules can be expected to be more prone to dust soiling than uncoated modules.

To answer this, it is necessary to make more comparisons, where coated and non-coated modules are directly compared to one another for each exposure period. This analysis is performed in section 7.9.7.

## 7.9.7 Short term PV module analysis

### Short term coated vs. uncoated

Group C is formulated to establish the effectiveness of the applied coating on modules with short term exposure, as presented by Table 7.9. Comparison sets C-1 and C-2 are compared in Figures 7.24 and 7.25.

Table 7.9: Description of the PV module comparison group C.

Comparison	Set	Exposure time	PV modules	Coating
C	1	Short term(Wet)	P14,P3	yes
		Short term(Wet)	P6,P11	none
	2	Short term(Dry)	P4,P13	yes
		Short term(Dry)	P5,P12	none



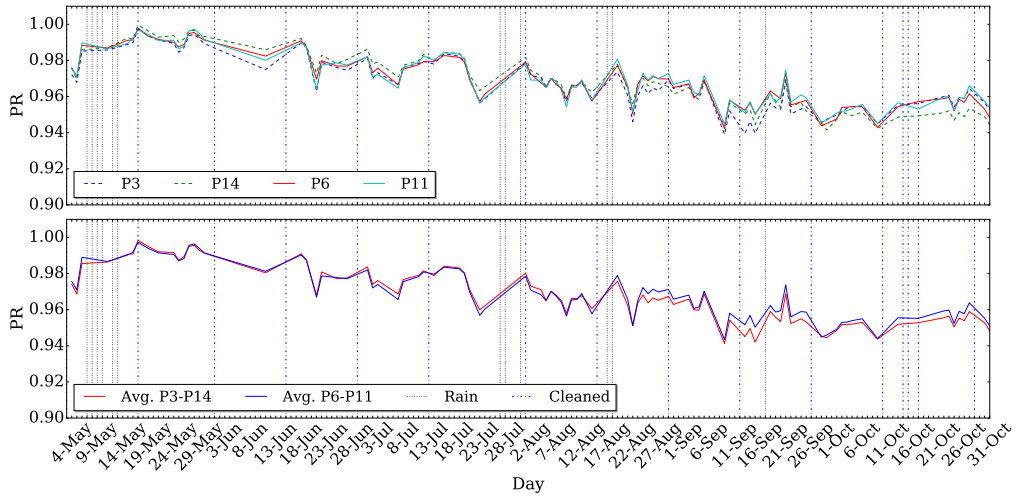


Figure 7.24: Set C-1. Top: PR of short term, water cleaned modules, with P3 and P14 coated and P6 and P11 uncoated. Bottom: Average PR of each set PV modules.

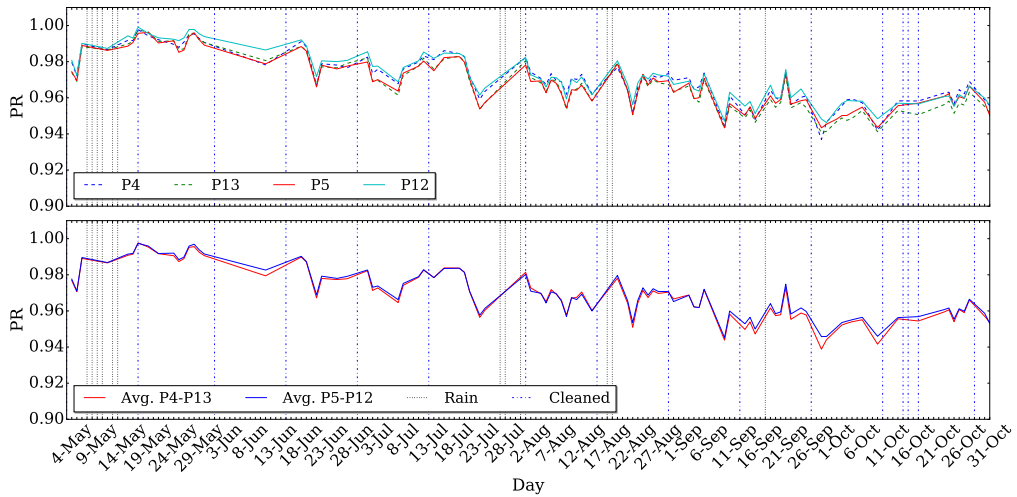


Figure 7.25: Set C-2. Top: PR of the short term, dry cleaned modules, with P4 and P13 coated and P5 and P12 uncoated. Bottom: Average PR of each set PV modules.

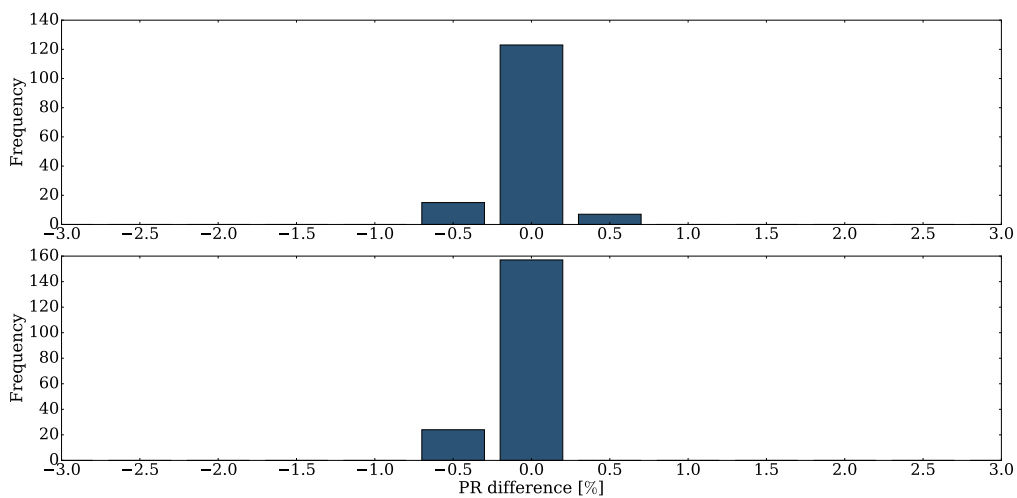


Figure 7.26: Short term module comparison. PR distribution of coated modules displayed w.r.t. non-coated modules. TOP: Set C-1, water cleaned. BOTTOM: Set C-2, dry-cleaned.

Table 7.10: Summary of PR and histogram distribution results for sets C-1 and C-2.

Set	$PR_{ideal}$	$PR_{relative}$	Hist. Days			
			Total	$\geq 1\%$	$\leq -1\%$	$\pm 0.5\%$
C-1	0.5%(25 Aug.)	0.52%(25 Aug.)	145	0	0	145 (100%)
C-2	0.7%(28 Sep.)	0.74%(28 Sep.)	181	0	0	181 (100%)

From the graph presented in Fig. 7.24, it is evident that the water cleaned modules (set C-1) operate within very close proximity of one another's PR. However, the days of 24 Aug. to 2 Sep., 9 - 25 Sep. and 13 - 31 Oct. clearly have the largest PR difference, in favour of the un-coated modules. As previously mentioned, module P3 is affected by a bird dropping for the period of 9 - 25 September, which is ended by the cleaning routine of 26 September. An average  $PR_{ideal}$  drop of 0.82 % is seen for this period, due to the bird dropping. For the period of 13 - 31 Oct. the reason for the difference in performance is due to the PR decrease of module P14. The period of 24 Aug. to 2 Sep. is however a result of dust soiling, since both coated modules under perform at the same moment in time, with a  $PR_{ideal}$  deviation of 0.5 %. However, this statement is inconclusive, due to the measurement uncertainty which is also within  $\pm 0.5$  %.

With regards to group C-2, the biggest difference in ideal PR is measured as 0.7 % on the 28th of September. When considering the average PR of each set (bottom graph of Fig. 7.25) it is apparent that the uncoated modules do seem to consistently perform marginally (0.3 %) better for the period of 10 Sep. and onwards. Results are summarised in Table 7.10

The histogram plots in Figure 7.26 present the coated modules plotted with respect to the uncoated modules. The top histogram plot in Figure 7.26 excludes data for the period of 9 - 25 Sep. and the 13 - 31 October, so that the influence of the bird dropping on P3 and the irregular behaviour of P14 is ignored. The bottom histogram plot for the dry cleaned modules includes all of the days until 31 Oct, since this group is equally affected by the cleaning of modules P3, P4, P5 and P6 during 14, 15 and 17 October. From both histograms it is clear that the deviation seen is within the measurement uncertainty of the ActiveLoad. However, due to the small negative tendency of the histograms, there is some indication that the uncoated PV modules did perform slightly better than the coated PV modules, but no conclusive argument can be made to substantiate this observation.

### Short term dry cleaned vs. water cleaned modules

To examine whether or not the dry or wet cleaning method is superior, comparison group D is established as presented in Table 7.11. The modules are divided into two groups, which consist of uncoated and coated modules, as presented by Figures 7.27 and 7.28, respectively.

Table 7.11: Comparison group D module comparison details.

Comparison	Set	Exposure time	PV modules	Coating
D	1	Short term(Dry)	P5,P12	none
		Short term(Wet)	P6,P11	none
	2	Short term(Dry)	P4,P13	yes
		Short term(Wet)	P3,P14	yes

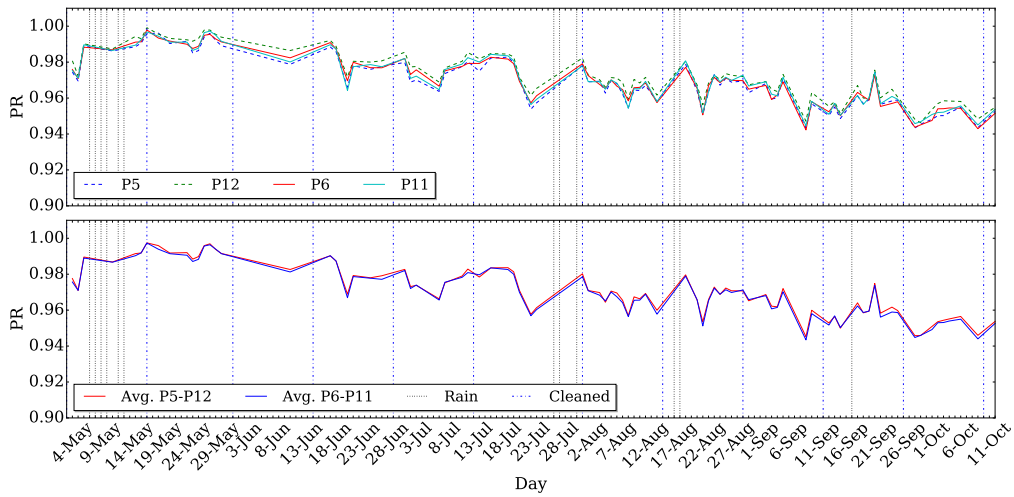


Figure 7.27: Set D-1. Top: PR of short term, uncoated modules, with P5 and P12 dry cleaned and P6 and P11 water cleaned. Bottom: Average PR of each PV module combination set.

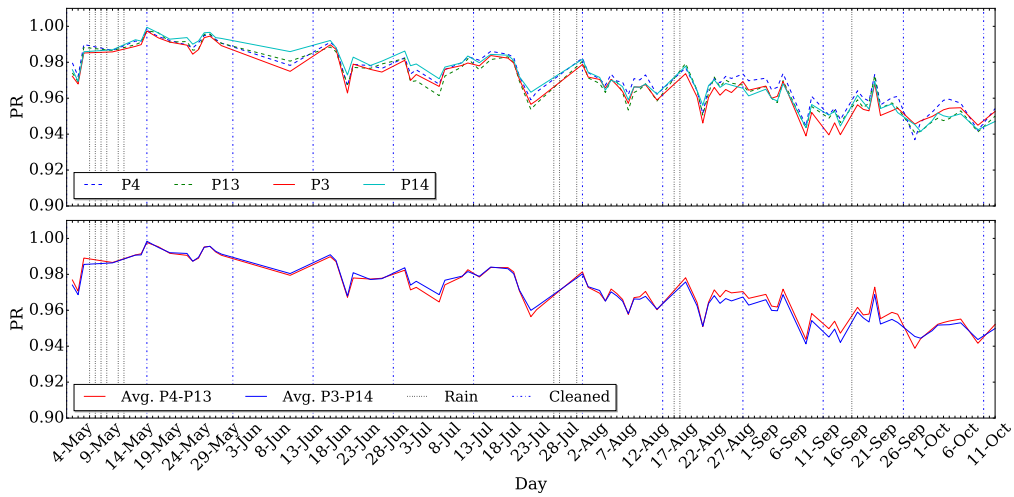


Figure 7.28: Set D-2. Top: PR of short term, coated modules, with P4 and P13 dry cleaned and P3 and P14 water cleaned. Bottom: Average PR of each PV module combination set.

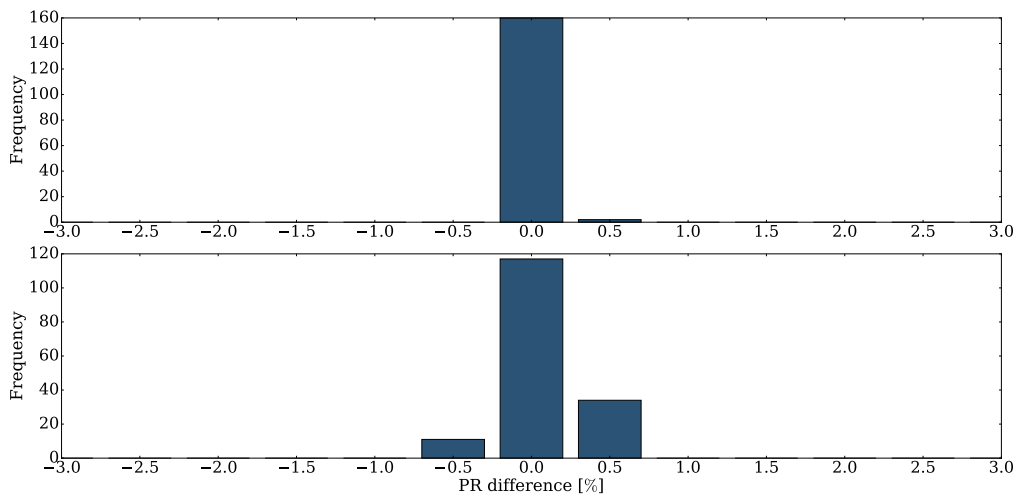


Figure 7.29: Short term module comparison. PR distributions of dry cleaned modules w.r.t. water cleaned modules. TOP: Set D-1, uncoated. BOTTOM: Set D-2, coated.

Figure 7.27 exhibits the comparison of the uncoated modules, which is set D-1. Visible from the graph, there is relatively no difference in performance for these modules. This is confirmed with the histogram distribution presented in Figure 7.29, which indicates almost all of the measurements are within the 0 % bin. From Figure 7.28, there is evidently a small difference in performance seen at the days of 2-8 July, 25 Aug. to 3 Sep. and also 8-25 September. However, as mentioned module P3 is subjected to a bird dropping during the September month. The histogram in Figure 7.29 for set D-2, does not account for the days where the bird dropping is present. At most the performance difference is still within the  $\pm 0.5$  % region. Thus, although there is slightly more variance in the performance of the coated short term modules, none of the cleaning methods present any real advantage above the other. The most significant differences in PR are summarised in Table 7.12. As seen from the results summary, it appears that the uncoated modules performed somewhat better than the coated modules once again, as is seen with comparison sets C-1 and C-2. These results are however only speculative, since difference in performance are within the  $\pm 0.5$  % boundary.

Table 7.12: Summary of PR and histogram distribution results for sets D-1 and D-2

Set	$PR_{ideal}$	$PR_{relative}$	Hist.	Number of days:		
			Days	$PR_{relative}$		
			Total	$\geq 1\%$	$\leq -1\%$	$\pm 0.5\%$
D-1	0.27%(24 Sep.)	0.28%(24 Sep.)	162	0	0	162(100%)
D-2	0.66%(28 Sep.)	0.7%(28 Sep.)	145	0	0	145(100%)

### 7.9.8 Long term PV module analysis

The details of comparison set E-1 is presented in Table 7.13. Figure 7.30 presents the PR values of the long term exposed PV modules. It is evident from Figure 7.30 that the uncoated PV module P10, performs the worst. However, the PV module that performs the second worst is P1, which is in fact a coated PV module. As summarised in Table 7.14 the averaged PR of the two groups (coated and uncoated), as displayed in the bottom graph of Figure 7.30, displays a difference in  $PR_{ideal}$  of 0.6 % on 21 Sep. in favour of the uncoated modules. It is also noted that the uncoated modules perform marginally ( $\sim 0.5$  % at most) better than the coated modules for the period of 20 June to 20 July. However, after the rainfall received at the end of July, a change is observed and the coated modules appear to perform marginally better ( $\sim 0.5$  % at most) than the uncoated modules. However, these are inconclusive observations since the difference is within the  $\pm 0.5$  % measurement range.

Table 7.13: Details of the PV module comparison group E.

Comparison	Set	Exposure time	PV modules	Coating
E	1	Long term	P1,P15,P16	yes
		Long term	P8,P9,P10	none

This vice versa behaviour of performance seen in Figure 7.30 (bottom graph) is affirmed by the histogram plot in Figure 7.30 with the performance of the uncoated modules, relative to the coated modules, almost equal in comparison. The histogram does not include data

points beyond the 27th of Oct, since modules P15 and P10 are cleaned as scheduled after the six month exposure period.

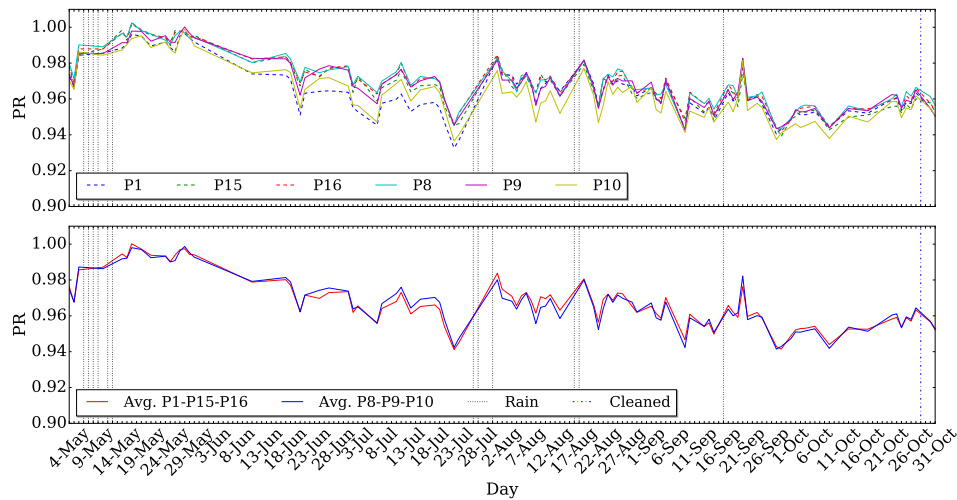


Figure 7.30: Comparison set E-1. Top: PR of long term coated (P1, P15, P16) and uncoated modules (P8, P9, P10). Bottom: Avg. PR of each set of coated and uncoated modules.

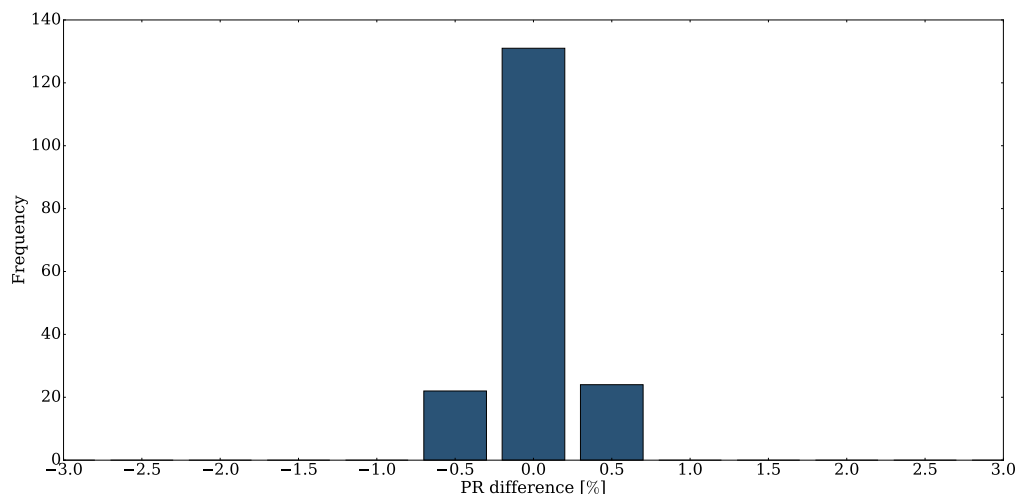


Figure 7.31: Histogram data for the long term PV modules. The PR of coated PV modules P1, P15 and P16 is plotted w.r.t. the uncoated PV modules P8,P9 and P10.

Table 7.14: Summary of the PR results and histogram distribution for set E-1.

Set	$PR_{ideal}$	$PR_{relative}$	Hist.	Number of days:		
			Days	$PR_{relative}$		
			Total	$\geq 1\%$	$\leq -1\%$	$\pm 0.5\%$
E-1	0.6%(21 Sep.)	0.62%(8 Oct.)	177	0	0	177 (100%)

From the presented data, it is evident that for periods with more frequent rainfall ( $\sim 4$  weeks) the coated modules perform marginally better than the uncoated modules. This is however an inconclusive observation, because the data presented by the histogram in Figure 7.30 does not provide measured PR differences above that of the instrumentation accuracy.

### 7.9.9 Defining the single axis tracker performance ratio

The PR equation (7.3) applied, requires a POA irradiance measurement. However, unlike the stationary modules, there is no global plane-of-array irradiance ( $G_{POA-SAT}$ ) measurement available for the tracking modules. This value can however be acquired with the following methodology:

1. Calculate the Sun's incident irradiance ( $G_{incident}$ ), based on the  $30^\circ$  POA measurement ( $G_{POA}$ ) of the pyranometer.
2. Calculate the POA irradiance as received on the surface of the single axis tracker modules, denoted by  $G_{POA-SAT}$ .

$G_{incident}$  is the radiation measured perpendicular to the sun [123], also known as Direct Normal Irradiance (DNI). The formula applied to determine  $G_{incident}$  is presented by equation (7.25) [123][124]. This formula translates the measured  $G_{POA-fixed}$  value, retrieved from the  $30^\circ$  tilted, North facing pyranometer, into the incident irradiance value. Due to a lack of a measurement for the diffused irradiance ( $G_{diffuse}$ ), which is sunlight scattered in the atmosphere [123], the assumption is made that most of the  $G_{POA-fixed}$  consists of the  $G_{incident}$  component. With the PR of the SATs determined during mid-day hours of 11:00AM - 14:00PM, the ground reflected irradiance ( $G_{Reflected}$ ) is assumed to be negligible. Thus equation (7.26) is used to determine the value of direct irradiance component,  $G_{incident}$ .

$$G_{POA-fixed} = G_{incident} \times \cos(\theta_{AOI-fixed}) + G_{diffuse} + G_{Reflected} \quad (7.25)$$

$$G_{POA-fixed} = G_{incident} \times \cos(\theta_{AOI-fixed}) \quad (7.26)$$

The angle-of-incidence, denoted by  $\theta_{AOI-fixed}$ , is required in equation 7.26 which is a function of the  $\theta_S$  and  $\beta$  angles, as well as the tilt angle of the PV module,  $\varepsilon$ , as presented by equation 7.27 [44, p216]:

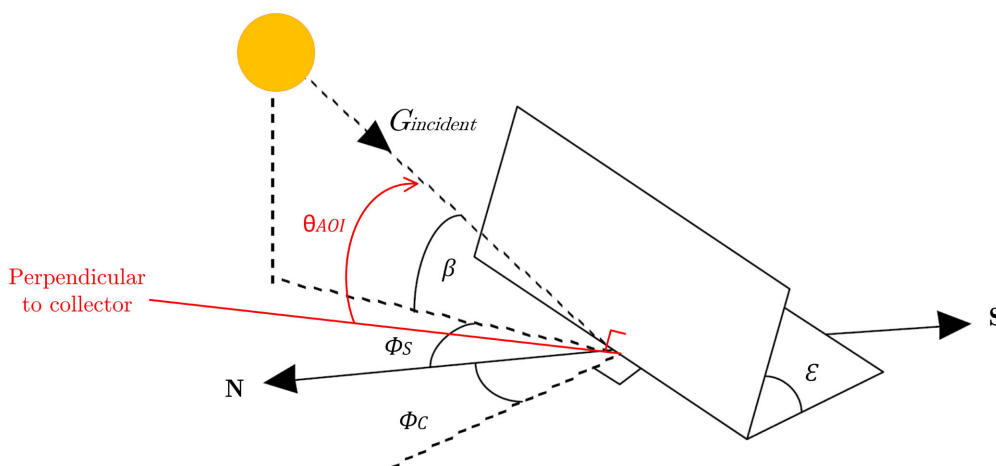


Figure 7.32: Illustration of the various angle positions required for the process of finding the angle of incidence.

$$\cos\theta = \cos\beta\cos(\theta_S - \theta_C)\sin\varepsilon + \sin\beta\cos\varepsilon \quad (7.27)$$

Where:

- $\theta$  = Angle of incidence
- $\theta_S$  = Solar Azimuth defined as degrees East of North (e.g. North = 0°, East = 90°)
- $\theta_C$  = Collector azimuth defined as degrees East of North (e.g. North = 0°, East = 90°)
- $\varepsilon$  = Module tilt angle
- $\beta$  = Solar altitude

The collector azimuth angle adheres to the following condition:

$$\begin{aligned} \text{Time} \leq \text{solar noon} : \theta_C &= 90^\circ \\ \text{Time} > \text{solar noon} : \theta_C &= 270^\circ (-90^\circ) \end{aligned}$$

All of the required angles ( $\theta_S, \beta, \varepsilon, \theta_C$ ) are known since the MasterController actively logs the tilt angle  $\varepsilon$  and the time at which the irradiance measurements are made. Angles  $\theta_S$  and  $\beta$  are determined with the same sun-position algorithm used for the SAT system, as presented in Chapter 5, Section 5.2. Finally, with the incident irradiance  $G_{incident}$  known, the value of  $G_{POA-SAT}$  received on the plane of a SAT is determined as:

$$G_{POA-SAT} = G_{incident} \times \cos(\theta_{AOI-SAT}) \quad (7.28)$$

Where in (7.28)  $\theta_{AOI-SAT}$  represents the angle of incidence for the tracker module:

With  $G_{incident}$  known, the irradiance seen by the PV module of a tracker is determined by calculating the AOI with equation (7.27). Then, (7.28) is applied to determine the effective POA irradiance received by each of the trackers.

It should be noted that this method of acquiring  $G_{POA-SAT}$  is an approximated value. In hind-sight it would have been more advantageous to have had a pyranometer mounted onto the trackers, to acquire a true value for  $G_{POA-SAT}$ . Since a true  $G_{POA-SAT}$  value is unavailable, the capability of directly comparing PR values for stationary and tracking modules is limited. However, it is still possible to effectively determine the performance of tracker modules relative to one another, since the performances of all modules are compared, relative to the same value of received  $G_{POA-SAT}$ .

## 7.10 Performance ratio results of SAT modules

### 7.10.1 Overview

As with the stationary models, different experiments are performed to investigate the feasibility of applying an anti-soiling coating to the tracker modules. The module layout is illustrated in Figure 7.33. As mentioned in Chapter 6.2.2, no physical module cleaning routines are applied to any of the modules. This is due to the interest of this thesis to investigate a DMS for tracking modules, where minimum human interaction is required. Instead, the focus is on the movement of the trackers and how this could possibly be utilised to implement an effective dust mitigation method. Modules P21 and P24 are coated with the anti-soiling

product and SAT-1 is activated for the self cleaning mode, indicated in Figure 7.33. As discussed in Chapter 6.2.2, the self cleaning mode tilts the modules at a  $45^\circ$  tilt angle into the direction of the rain and utilises dew droplets to further assist with displacing dust particles.

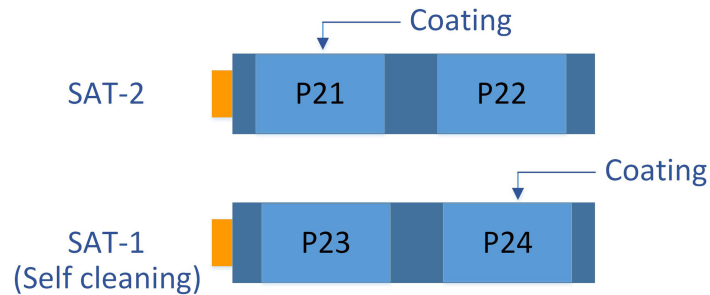


Figure 7.33: Layout of the SAT system and the modules with applied anti-soiling coatings.

### 7.10.2 Comparison of all four tracker module performance ratios

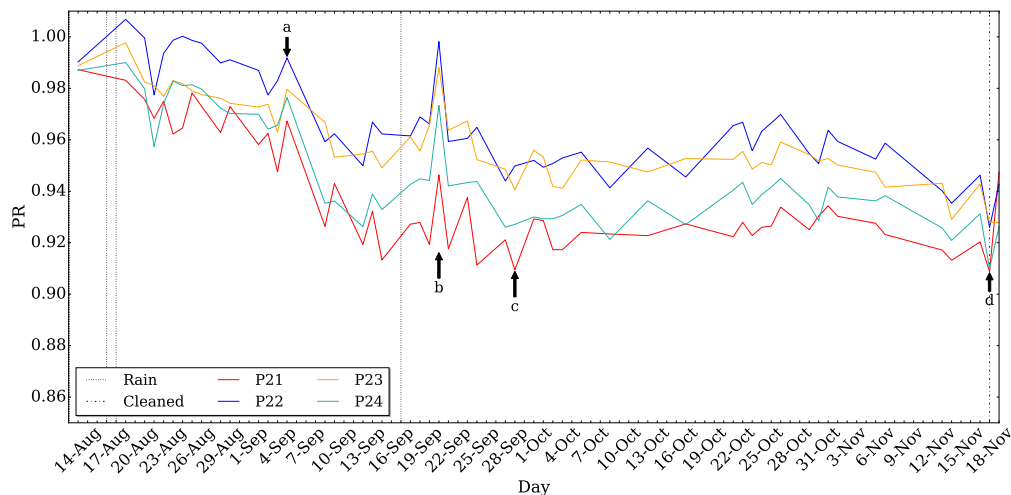


Figure 7.34: Overview of all the measured performance ratios for the four SAT modules.

The PR of each module is once again determined for the period of 11:00 AM to 14:00 PM, for the same reasons as for the stationary modules. From the graph presented in Figure 7.34, modules P21 and P24 have the lowest PR, which evidently decreases further from the 5th of Sep. at marker (a), and onwards. The reason for the rapid increase in PR at marker (b), also occurs as discussed for the data presented for the stationary modules, which is due to a low irradiance measurement, combined with a high average wind speed. It is interesting to note how the reaction of module P21 seems to be exaggerated starting from 14 Aug. up to 29 Sep. at marker (c). The exact reason for this is unknown, but it is assumed to be due to non-uniform shading, provoked by dust soiling. No conclusive remarks can be made regarding the behaviour demonstrated by module P22 during the first few days of 20 Aug. until the beginning of September. Also, from marker (c) and onwards it is evident that modules P21 and P23 are almost synchronised in behaviour, with modules P22 and P24 also displaying the same harmonised movement in terms of PR. The reason for this is concluded to be due to the geographic location of each of these modules. Module P21 and P23 are coated and uncoated, respectively, and are opposite of one another as seen in Figure 7.33. This also accounts for modules P22 and P24, which are both at the North end of the SAT structures. At marker (d) it is seen that the PR of module P21 drastically increases from



0.91 to 0.95. This occurs due to an experimental cleaning routine executed only on module P21, which is a coated module. More details regarding this are provided at the end of section 7.10.3. The next sections aims to quantify the relative difference in performance between the modules.

### 7.10.3 Coated vs. uncoated tracking modules

The first combinations of analysis for tracker module performance is indicated in Table 7.15.

Table 7.15: Module analysis for SAT-1 and SAT-2, comparing coated and uncoated modules.

Comparison	Set	Tracker	PV modules	Coating	Self cleaning
F	1	SAT1	P23	none	activated
			P24	yes	activated
	2	SAT2	P21	yes	deactivated
			P22	none	deactivated

Comparison set F-1 and F-2 differentiates between coated and uncoated tracking PV modules. Figure 7.35 illustrates the PR measured for the modules of SAT-1, which are activated for the self cleaning mode. The data recorded for SAT-2 (Set F-2) is illustrated in Figure 7.36. From these graphs it is evident that the uncoated modules outperform the coated modules. It must be mentioned that a large bird dropping is recorded on the 14th of Oct. on SAT module P21. However, the bird excretion is removed on the 17th of Oct. and is also removed from the data set.

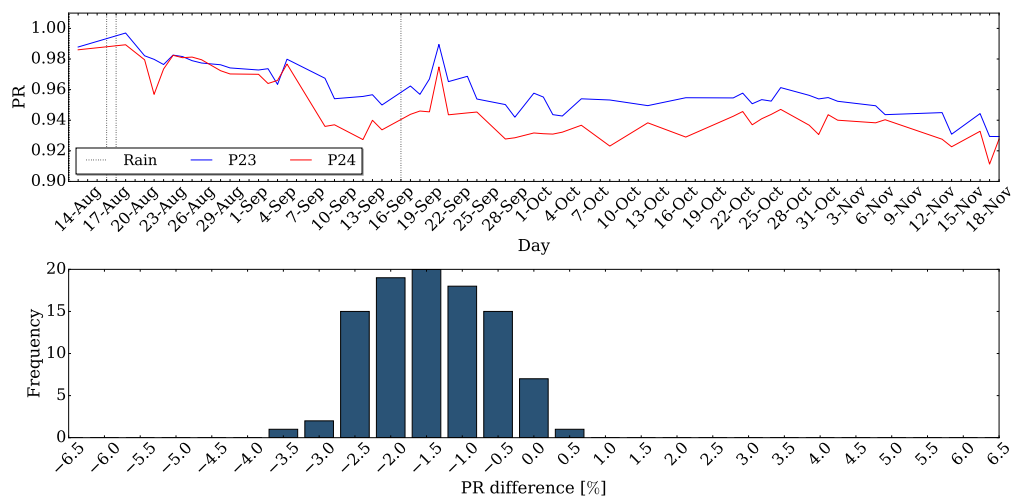


Figure 7.35: Comparisons set F-1. TOP: PR of the coated (P24) and uncoated (P23) modules. BOTTOM: PR distribution of module P24 relative to module P23.

A data summary is provided in Table 7.16 of the results displayed in Figures 7.35 and 7.36. With regards to the distribution of the PR for each data set, set F-2 displays the largest deviation in PR. For set F-2, module P22 outperforms the coated module, P21, by a  $PR_{ideal}$  deviation of 5.54 %. The max.  $PR_{ideal}$  deviation for set F-1 is recorded at 3.15 %, with the weight of the histogram largely distributed between -0.5 % to -2.5 %. This is considerably more than what is recorded for any of the stationary modules. The modules on SAT-2 (Set

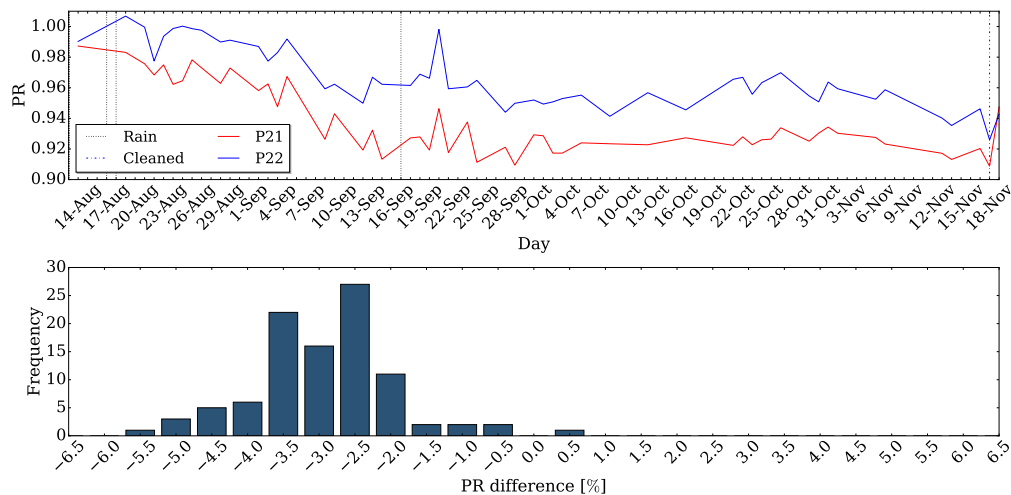


Figure 7.36: Comparisons set F-2. TOP: PR of the coated (P21) and uncoated (P22) modules. BOTTOM: Distribution of module P21's PR relative to module P22.

Table 7.16: Summary of the results obtained for comparison sets F-1 and F-2.

Set	$PR_{ideal}$	$PR_{relative}$	Hist.	Number of days:		
			Days	$PR_{relative}$		
			Total	$\leq -1\%$	$\leq -2\%$	$\leq -3\%$
F-1	3.15%(9 Sep.)	3.25%(9 Sep.)	98	38 (38.8%)	34 (34.7%)	3 (3.1%)
F-2	5.4%(25 Sep.)	5.54%(25 Sep.)	97	4 (4.1%)	38 (39.2%)	53 (54.7%)

F-2) display an even larger deviation in PR, with more than 54 % of the days indicating a  $PR_{relative}$  difference, exceeding 3 %.

The histogram plot of set F-2, in Figure 7.36 has a measurement recorded at +0.5 % on 19 Nov. (not included in Table 7.16) in favour of the coated module. This is due to module P21 cleaned with water to prove that this coated module is in fact subjected to a large deposit of dust soiling. This verifies the results, which indicate that the coated module P21 is much dirtier than the uncoated module P22, as seen in the drastic PR increase measured on the 19th of Nov. A significant increase of  $\sim 2.1$  % relative to module P22 is seen directly after module P21 is cleaned. This verifies that the anti-soiling coating in fact promotes dust deposition. Further reference to this is made in section 7.11.

#### 7.10.4 Self cleaning vs. normal tracking operation

As seen in the graphs of sets F-1 and F-2 in section 7.10.3, the results suggest that the coated modules in fact under performed with regards to the uncoated modules. The question remains whether or not the self cleaning manoeuvre of SAT-1 aids with the removal of dust particles? This is investigated by comparison group G, as detailed in Table 7.17.

The two coated modules of group G-1 (P21, P24) are compared to one another in Figure 7.37. Evidently, coated module P24, on the self cleaning activated SAT1, performs better, with more than half of the histogram distribution indicating a PR between 1 % to 2 % in favour of the module P24. In Table 7.18 a summary of the data is presented both sets G-1 and G-2.

The two uncoated modules are compared for the normal and self cleaning trackers in Figure 7.38. As evident, from the top graph, the difference in performance for these two modules is

Table 7.17: Details regarding comparison group G

Comparison	Set	Tracker	PV modules	Coating	Self cleaning
G	1	SAT1, SAT2	P21	yes	deactivated
			P24	yes	activated
	2	SAT1, SAT2	P22	none	deactivated
			P23	none	activated

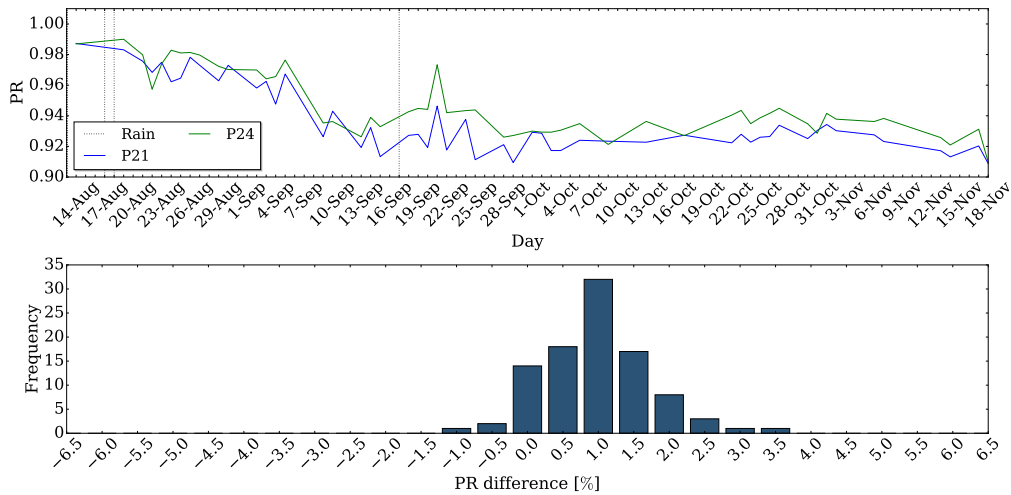


Figure 7.37: Comparisons set G-1. TOP: PR of the coated modules P21 (normal) and P24 (self cleaning). BOTTOM: PR distribution of module P24 relative to module P21.

less than the difference observed for the coated modules. This is confirmed by the histogram distribution in Figure 7.38. Module P22 over-all performs better than P23, with 43 days (97 days in total) indicating a relative PR difference of 1 % - 2 % in favour of module P22.

Therefore, with the analysis of comparison set G-1 and G-2, it is inconclusive whether or not the self cleaning mode did in fact make a difference, since the results of the coated and uncoated modules are not in agreement.

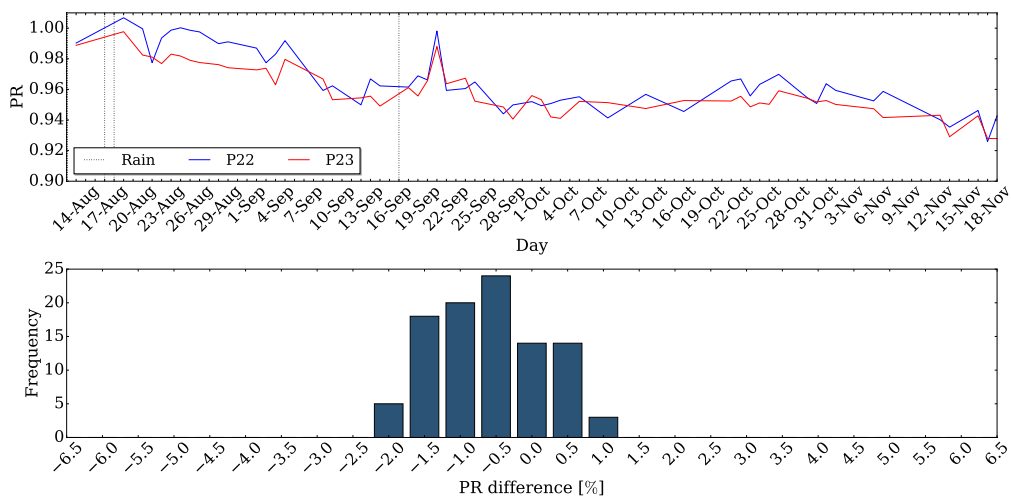


Figure 7.38: Comparisons set G-2. TOP: PR of the uncoated modules P22 (normal) and P23 (self cleaning). BOTTOM: PR distribution of module P23 w.r.t. module P22.

Table 7.18: Summary of the results obtained for the modules compared of Set G-1 and G-2.

Set	$PR_{ideal}$	$PR_{relative}$	Hist.	Number of days:		
			Days	$PR_{relative}$		
			Total	$\leq -1\%$	$\geq 1\%$	$\geq 2\%$
G-1	3.25%(25 Sep.)	3.56%(25 Sep.)	97	1 (1.03%)	49 (50.5%)	13 (13.4%)
			Total	$\leq -2\%$	$\leq -1\%$	$\geq 1\%$
G-2	2.0%(27 Aug.)	2.03%(4 Sep.)	97	5 (5.2%)	38 (39.2%)	3 (3.1%)

As summarised by Table 7.18, the biggest difference in  $PR_{ideal}$  is recorded for modules P21 and P24 as 3.25 %, in favour of module P24. Also, the  $PR_{relative}$  of module P24 outperformed module P21 for more than 63 % of the three month period, by a difference of 1 % or higher. For the uncoated modules of set G-2, module P23 surpassed module P22 with a  $PR_{relative}$  greater than 1 % for about 44 % of the time, over the three month period. However, unlike set G-1, the  $PR_{relative}$  of module set G-2 performed within the  $\pm 0.5$  % range for about 50 % of the time. Contrary to this, the coated modules of set G-1 only performed within the  $PR_{relative}$  range of  $\pm 0.5$  % for 35 % of the time, indicating a larger deviation over a longer time period.

## 7.11 In field visual observations made

### 7.11.1 Overview

This section elaborates on the actual in field observations made during the time spent at the PVRF. The behaviour of the PV modules is captured on photograph to illustrate how coated and non-coated modules react to certain conditions.

### 7.11.2 Stationary PV module observations

From Figure 7.39, the reaction of the PV modules to rainfall is illustrated. As seen in Figure 7.39a the hydrophobic coating allows the rain to accumulate and form water beads (droplets). With the theory presented in Chapter 2.2.3, as these droplets roll off, the dust particles are captured and displaced. On the other hand, Figure 7.39b illustrates how the non-coated module surface, allows for a lower water contact angle, which results in a uniform water distribution across the module surface.



(a) Coated module surface after rainfall.



(b) Uncoated module surface after rainfall.

Figure 7.39: Illustration of the PV module surfaces shortly after rainfall is received.

The reaction of dust particles to these different movements of water displacement (shown in Figure 7.39), is illustrated in Figure 7.40. Figure 7.40a reveals how dust particles react to the water droplets, formed due to the hydrophobic coating. After rain is received, the droplets remove dust by means of rolling off, however there is a problem with regards to the droplets which remain. These droplets, provide a means for dust to be captured and concentrated onto the surface area occupied by the droplets. Ideally, from observation, the droplets should all roll off of the module surface completely. However, once the water quantity on the module decreases as rain stops, the remaining droplets stay in tact due to the 30° tilt angle of the module. Should the angle of tilt increase, the effect of gravity is increased and less, as well as, smaller droplets would remain on the module surface.

The reaction of dust particles on the uncoated PV modules, is seen in Figure 7.40. Evidently, the dust particles combine to form wave shaped lines. From observations made while washing PV modules, two aspects contribute to this phenomena. It is seen that not all of the water disperses from the module and that a remaining layer of water is always left to evaporate. It is this final layer of water which is responsible for the largest amount of dust particle deposition. This layer provides a wet surface for air borne dust to adhere to and also captures the last remaining surface dust, as this water layer gradually moves downwards. Also, as the final layer of water moves downwards, the water layer accumulates and forms wave shaped patterns (as one would see on a beach). However, because this water layer is so thin, it usually evaporates, before it reaches the bottom of the PV module. Ultimately, this behaviour is believed to result in the wave-like dust density line.

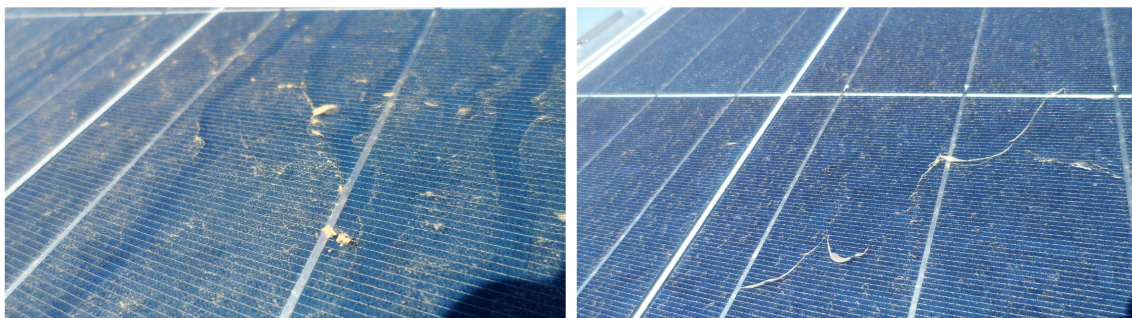


(a) Dry coated module surface.

(b) Dry non-coated module surface.

Figure 7.40: Illustration of the PV modules surfaces, two weeks after rainfall is received.

After the stationary PV modules have been subjected to no rainfall during the two months of June and July, the PV module surfaces appear as displayed in Figure 7.41.



(a) Dry coated module surface

(b) Dry non-coated module surface

Figure 7.41: Illustration of the PV modules surfaces, two months after rainfall is received.

In Figure 7.41a the effect of water droplets rolling off of the module surface, can be clearly seen, which attests to the characteristics of a hydrophobic coating. However, what is alarming is the hard shading caused by the dust patches seen on the module. It can also be seen how the wave shaped dust line of Figure 7.41b is also very dense and results in hard shading. These separate occurrences of hard dust shading is due to the initial onset of dust and the general rule that dust promotes dust [125]. From field observation, it must be mentioned that the wave shaped dust formation is not always present on all modules, however the dust dust patches formed due to the hydrophobic coating are always observed on all coated modules.

It is also worth mentioning the effect of the dust particles during early morning and late afternoon. During these times, it is noticed how the shadows projected by dust molecules, substantially increase during low sun conditions, especially where a concentration of particles is found. This definitely increases the possibility of hot spot formations on the PV module surfaces.

### 7.11.3 Single axis tracker PV module behaviour

After a two month period where no rainfall is received, the reaction of the SAT modules to dust soiling is displayed in Figure 7.42. As seen from the photographs in Figures 7.42a and 7.42b, the coated PV modules indicate a higher degree of dust soiling than the uncoated modules in Figures 7.42c and 7.42d. This correlates with the results presented in section 7.10.3, which conclude that the coated modules under perform with regards to the uncoated modules. Finally, it is noticed that the uncoated tracker modules indicate a slightly larger amount of dust soiling than the stationary modules.

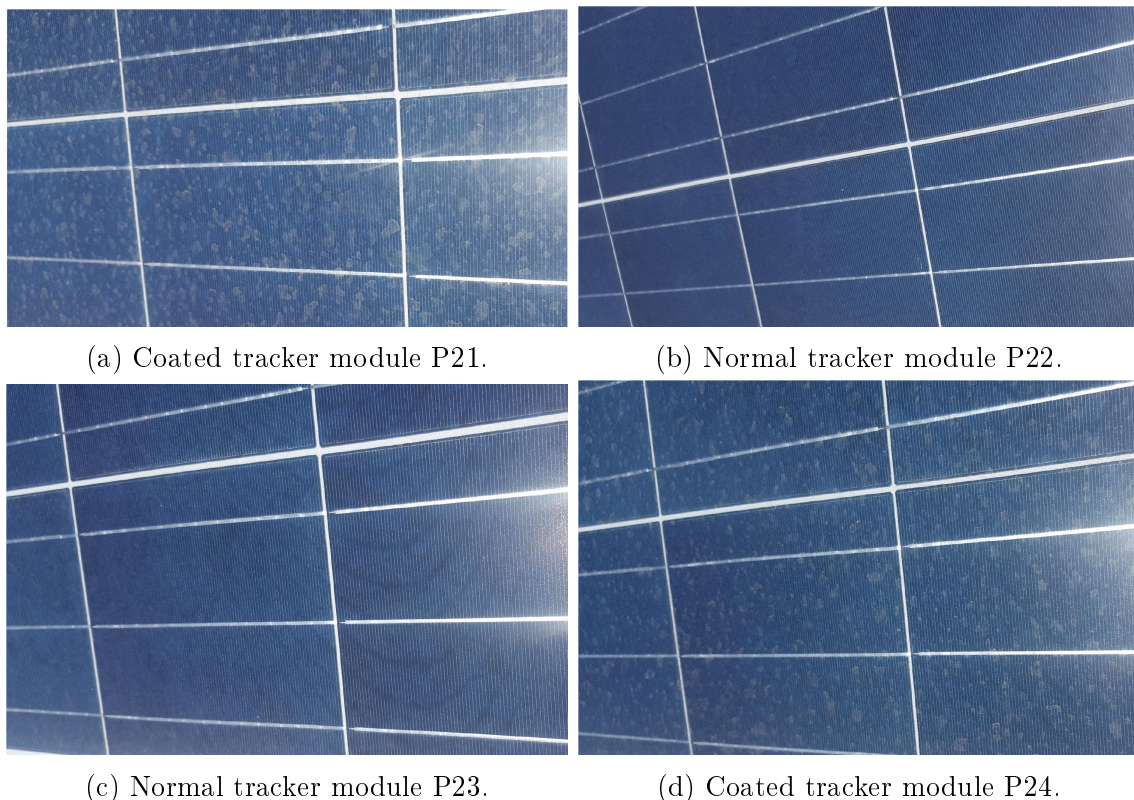


Figure 7.42: Illustration of the single axis tracker PV modules surfaces, after a two month absence of rainfall.

#### 7.11.4 Cleaning routine observations

When short term cleaning routines are executed, it is realised that the dry cleaning procedure does not effectively eliminate all of the dust particles. This is mostly due to the inability of a dry cloth to separate the hardened dust particles from the glass surface, which form what can be described as a dust soiling stain. Only by applying pressure, can these dust stains be removed, but this in turn can damage the glass surface of a PV module. It is however observed that cleaning the modules with distilled water, completely restores the glass surface of a module.

# Chapter 8

## Conclusions and Recommendations

### 8.1 Stationary modules

The results obtained in Chapter 7 produced counter intuitive behaviour with reference to some of the hypothesis statements made in Chapter 1. Where it was expected that the application of an anti-soiling coating would result in an increase in PV module performance, the analysis indicated otherwise. For the evaluation of the stationary modules, different module sets were compared to determined the performance of the various mitigation methods applied. In summary, the following results are obtained for the different comparison sets over the six month period (May-Oct 2016):

- Group A: Long term vs. short term exposed, coated modules. It is concluded that the short term modules outperformed the long term modules. A maximum  $PR_{ideal}$  difference, in favour of the short term modules, of  $\sim 2\%$  was observed for both wet and dry cleaned modules.
- Group B: Long term vs. short term exposed, uncoated modules. Results indicated a max.  $PR_{ideal}$  increase of  $\sim 1.5\%$  for both the wet and dry cleaned short term modules.
- Group C: Short term exposed coated vs. uncoated modules. Results are inconclusive due to the measured difference in performance, recorded within the  $\pm 0.5\%$  boundary of uncertainty.
- Group D: Comparison of short term cleaning routines. No real difference is seen for either the dry or wet cleaning methods applied to the coated and uncoated module sets.
- Group E: Long term exposed coated vs. uncoated modules. Results are once again inconclusive due to the measured difference in performance, recorded within the  $\pm 0.5\%$  boundary.

#### Conclusions on short term exposed modules

Regarding the short term cleaning routines, it is inconclusive whether or not dry cleaning or water (distilled) cleaning is better. Should a short term cleaning strategy be considered, results indicate that stationary PV modules can in fact be left uncoated and dry cleaned, to maintain module performance. This should especially be considered regarding the general water scarcity in the semi-arid areas of the Northern Cape and the cost of labour associated with the application of an anti-soiling coating.



Regarding the short term module performance of the anti-soiling coating, it is perceived that the uncoated modules marginally outperformed the coated modules. This is seen in the results of both comparison sets C and D. The differences are however too small (within  $\pm 0.5\%$ ) to make a definitive statement regarding this topic. Nonetheless, the mere fact that the surface coating made no real contribution to enhance module performance, provides enough reason to conclude that a hydrophobic anti-soiling coating is not required for a short term cleaning strategy. It is also observed, during the actual execution of cleaning routines, that the dust patches formed by the coating resulted in dust stains, which could not be effectively removed by a dry cleaning procedure.

### Conclusions on long term exposed modules

The long term modules were not subjected to any cleaning routines during this research period. These modules displayed a maximum reduction in CR of up to 2.7 %, as compared to the short term, uncoated reference modules. The largest decrease in ideal performance ( $PR_{ideal}$ ) was recorded as  $\sim 1.9\%$ . This was concluded to be due to a 75 day absence in rainfall. However, with rainfall received after this period, the PRs of all long term exposed modules were restored. Concerning the amount of rainfall required to restore module performance, no conclusive statement can be made, since rainfall received always exceeded 6 mm. However, the least amount of rainfall received during the six month period was 6.5 mm, which proved to be enough to restore all module performances. Overall it is concluded that a frequent rainfall, which occurs at least every four to six weeks, is enough to maintain PV module performance, within a 1 % deviation from the rated performance.

Regarding the anti-soiling coating, no real advantage is seen in the performance of the modules exposed over the six month period. Also, the visual observations of Chapter 7 (section 7.11) indicated that the hydrophobic coating stimulated further dust soiling. Small dust patches were seen to appear due to the formation of water droplets, which failed to evaporate within time, to avoid attracting dust. This is concluded to place the modules at risk of possible hot spot formations, since the concentrated dust patches are dense enough to be classified as hard shading particles.

Ultimately, from the results of the data analysis regarding the stationary modules, the following is summarised:

- A hydrophobic anti-soiling coating is not an effective dust mitigation method.
- Long term exposed PV module performance can be sustained within a 1 % deviation, should rainfall above 6 mm be received, within a four to six week time period.
- Over the six month period, the short term dry-cleaning method proved to be superior with regards to restoring PV module performance, as well as the independence on water.

#### 8.1.1 Single axis tracking modules

The analysis continued to investigate the effect of dust soiling on single axis tracking modules, which were exposed for three months (14 Aug. to 18 Nov. 2016). For the experimental set up, a self cleaning manoeuvre was executed on SAT-1 and SAT-2 continued with a normal tracking routine. With two modules coated and two uncoated on each SAT system, the following summary is presented for the results obtained concerning the different SAT comparison sets:

- Group F: Coated vs. uncoated SAT module performance. The largest difference in the ideal performance ratio ( $PR_{ideal}$ ) is recorded at 5.4 %.
- Group G: Self cleaning vs. normal tracking operation. No conclusion is drawn regarding the effect of the self cleaning functionality, since the results of the coated and uncoated modules are not in agreement. The coated modules are in favour of the self cleaning mode with a maximum  $PR_{ideal}$  value of 3.3 %. However, the uncoated modules are in favour of the normal tracking routine with a maximum difference in  $PR_{ideal}$  of 2 %.

From the three months of exposure, it is observed that the applied hydrophobic coating in fact promotes dust soiling on the SAT modules. This is in direct contrast with the expectation that the tracking modules would outperform the stationary modules, regarding surface dust accumulation. As mentioned, a maximum difference of 5.4 % is seen for the ideal PR of coated module P21, as compared to uncoated module P22. To confirm these data observations, coated module P21 is washed and once again compared to module P22. A relative PR increase of 2.1 % is recorded for module P21, with respect to P22. This confirmed the experimental data, which suggests that the anti-soiling coating promotes dust soiling.

It is also seen that the tracking modules (coated and uncoated) are overall more prone to dust accumulation than the stationary modules. Although this cannot be confirmed with a direct PR comparison, due to a lack of a true  $G_{POA-SAT}$  measurement, this conclusion is formulated based on the visual observations made at the PVRF.

The following is a postulation of why the coated modules in fact displayed increased levels of dust soiling. It is believed that the horizontal resting position of the trackers, adopted during night time, creates a stable platform which facilitates the process of dust adhesion onto the modules. This horizontal position, minimises the effect of gravity on larger dust particles, which would normally be displaced by a low wind speed, as is the case for the tilted stationary modules. This thought is also illustrated by the research of E. Klugmann-Radziemska [15], who refers to the ability of gravity to displace dust particles. Further, the formation of dew on the module surfaces, is also believed to act as a catalyst for dust soiling. This thin layer of precipitation allows present dust particles to further merge onto the PV module surfaces. This argument is based on the findings of J. Cano [17] presented in Chapter 2, who quantified the relationship between tilt angle and power loss due to soiling. Cano's study concluded that a decreased tilt angle, resulted in an increased dust accumulation. Cano also concluded that in the event of low rainfall (less than 2mm), particularly with reference to horizontally tilted modules, the formation of mud patches occurred. The research conducted by E. Klugmann-Radziemska also referred to how low amounts of precipitation provokes the formation of adhesive mud patches on module surfaces.

Thus, it is deduced from the in field observations and data presented, that the low amount of precipitation formed by dew, on the SAT module surfaces, enables the dust particles to combine into larger dust-patches.

In summary, the results conclude:

- SAT PV modules, which adopt a horizontal resting position, are more prone to dust soiling than stationary tilted ( $30^\circ$ ) modules.
- A hydrophobic anti-soiling coating is not recommended.

- It is inconclusive whether or not a self-cleaning manoeuvre, to reduce dust soiling, is of any advantage.

### 8.1.2 Conclusive remarks

As presented, the largest deviation in performance (defined by the CR) of an uncoated, long term exposed module as compared to a set of uncoated biweekly cleaned modules, was recorded at 2.1 % (max. of 2.7 % recorded for a coated module). It should however be mentioned that the PVRF is considered to have received an above normal exposure to dust soiling. This is mainly due to the fact that both a rail road and dirt road are located approximately 250 m West of the research site. With a predominant South-West wind direction, dust particles are prone to be distributed towards the PVRF.

It can also be confidently stated that during the six months of analysis, the short term mitigation method that performed the best was the dry cleaning method, applied to uncoated modules. This mitigation method performed equal to the other short term methods, but due to the low labour intensity and cost required to execute this cleaning option, it is regarded as the optimum short term method. However, it cannot be concluded with certainty that this cleaning method is also the best long term method, due to the inability to effectively remove dust stains. Thus, further research is required regarding this topic.

The author's advice to PV system engineers and operators is as follows:

1. Firstly, for modules located in the semi-arid environment of the Northern Cape, it is not recommended that a hydrophobic coating should be applied. The labour intensity, cost and little to no benefit of such a coating (as proved by this research) makes the application thereof highly impractical and expensive.
2. It is advised that PV system operators should continuously monitor PV module performance. Due to uncertainty regarding measurements, it is not advised that a string of modules within a commercial PV power plant is used as reference point for the performance of other strings. The uncertainty regarding this method is simply too high and may not depict the actual loss [%] of PV module performance. An experimental set of normalised reference PV modules (cleaned daily), as well as modules exposed to accumulate dust (representing unclean PV power plant modules), should be utilised. From these modules accurate I-V curve data is to be extracted and analysed. The continuous and accurate monitoring of PV module output power is crucial if commercial PV system operators are to accomplish projected energy yield.
3. An ad hoc cleaning strategy is recommend. With a regularly cleaned set of modules in place, it is advised that an impromptu decision to execute a cleaning routine, must be based on a financial model. This model must account for the decrease in module performance [%], as well as weather predictions regarding rainfall. As seen in this research, rainfall (> 6 mm) every four to six weeks is substantial to recover module performance. Depending on water availability, if a decision is to be made regarding a wet or dry cleaning routine, it is advised that an experimental analysis be performed where both methods are considered. Based on the difference in increased performance, a basic cost analysis can be executed for both routines to make a final decision regarding the method.

## 8.2 Recommendations and future research

- Due to the uncertainty encountered by this research, regarding the irradiance seen by the SAT modules, it is advised that a pyranometer be added to the single axis tracking system. This will allow a true  $G_{POA-SAT}$  irradiance value to be recorded. Such an addition would allow for a direct data related comparison (and not just a visual comparison) between tracking modules and stationary modules in terms of performance.
- In hind-sight, it would have been more advantageous to have had two regularly cleaned reference modules, one coated and one normal, so that a CR analysis could be performed on the trackers. It is also advised that the study regarding the trackers be continued, so that a larger set of data can be analysed.
- It is recommended that research is done regarding the resting position of a single axis tracking system during the night time. This thesis indicated that a horizontal resting position promoted dust soiling. The question remains whether or not a tilted resting position would display a decrease in dust soiling.
- As mentioned, it was seen that the defined PR still displayed a sensitivity to a change in irradiance. Although, the PR does mathematically normalise module performance with regards to both irradiance and temperature, further research is required as to why the PR is still sensitive to changes in irradiance.
- No conclusive remarks beyond six months can be made regarding the mitigation methods. Therefore, it is recommended that the applied dust mitigation strategy for this research be continued. This would allow a conclusion to be drawn regarding the state of the dry cleaned modules after one year of exposure, compared to that of water cleaned modules. Ultimately, this would give a final indication of whether the dry cleaning method truly is superior in terms of maintaining module performance. Such research will also be beneficial for researchers and engineers who are considering the use of robotic systems, which mainly rely on a dry cleaning process.
- It would be interesting to see how modules perform over time which are cleaned when rainfall is in progress. In other words, the study would investigate the efficiency of using rainfall as a potential and natural detergent.
- It is recommended that a study be performed regarding the effect of dust soiling on PV module cell temperature. The research presented by A. Rao et al. [42] and Bing Guo et al. [41] presented different conclusions regarding this topic. Such a study would therefore definitely contribute to the available data on dust soiling and its effect on PV module temperature.
- Ultimately, with the recorded PR and CR deviations as seen in Chapter 7, it is concluded that dust soiling is indeed a highly complex phenomena sensitive to external influences (wind, humidity, rain, irradiance, etc.). It was not within the scope of this research to intensively investigate the effect of weather conditions on PV module performance. Nonetheless, such a study would be of great value regarding the formulation of a highly accurate predictive model, which considers all meteorological influences.

# Appendices

# Appendix A

## Research facility

### A.1 Phase 1: Basic infrastructure

Phase one consists of installing the operational framework of the research facility. Phase one takes place during the week of 18 to 23 May 2015. The following items are installed as indicated by Table A.1:

Table A.1: Active-Load assignments.

Item	Item
26 x orange metal enclosures	4 x 300W PV modules
20 x triangular frames	6 x A-frames (trackers)
21 x small orange metal enclosures	1 x large orange metal enclosure
62 x concrete foundation blocks	1 x WiFi-tower
1 x weather station	Data logger and rain gauge frame
4 x 12 V batteries	2 x MPPT charge controllers
Underground PVC piping	1x wi-fi router & Raspberry-Pi

Day one is dedicated to identifying the the facility's layout and marking off important points of reference before construction commences. The concrete blocks are placed and levelled and trenches for the PVC piping are made. The weather station and WiFi-tower poles are also erected. On day two, the remaining concrete blocks are placed and levelled. The weather station is also installed with the necessary PVC piping. On day three and four, the galvanised steel frames are installed. On day five and six the electronic housings are installed and the weather station and WiFi antenna poles are anchored.

In Figure A.1 the completion of phase one is presented:



(a) Stationary PV module structures. (b) Battery bank after phase 1 installation.

Figure A.1: Images of the PVRF after the completion of Phase 1 construction.

## Phase 1

This phase is described in Chapter 3.

## Phase 2 and 3: Anchoring and PV module installation

Phase two (15 to 17 June 2015) of installations requires that all of the structures installed during phase one, are firmly anchored. This is accomplished with anchor poles, steel vineyard cable and crosby clamps. Every single frame of the fixed rows, trackers and battery bank is anchored on both sides. The weather station and wi-fi towers are also anchored on three sides. In total 54 anchor poles are secured into the ground and fastened to the structure frames as illustrated in figure:

After the frames are securely anchored, the PV modules and wire wound resistor loads are installed during phase three (28 Jul to 1 Aug 2015). The 750 W,  $1 \Omega$  wire wound resistors are also installed. All of the orange metal enclosures are connected with the wire wound resistors, by means of 20 mm sheath and couplings, to allow electrical wiring from each resistor to enter into the corresponding enclosure. In total all 20 pc-Si modules and eight thin-film modules are installed, together with 24 wire wound resistors.

## Phase 4: Installation of electronics

The main focus of this phase (24 to 28 Aug 2015) is the installation of the ActiveLoads and the MasterController. The orange enclosure boxes are connected with one another. Several issues are found with regards to the temperature sensors during this phase. The ALs behind the battery bank, for the SATs are also damaged each time the power is connected. No solution to the problem is found during this phase.

## Phase 5:

Several issues arise during installation phase four, as mentioned above. The primary goal of this phase is to resolve these issues. The problems with regards to communication errors are solved by physically grounding the shield of the RS485 communication line to the structures, which are also grounded via the anchor poles.

A TVS diode is also installed at each input terminal of the ALs, to avoid voltage spikes from damaging circuitry. The temperature sensor issues are still not resolved during this phase.

New software is loaded onto the ActiveLoads and the Raspberry-Pi, to allow for more efficient data management and communication. Also, a new version of the SD-card code allows data to be sampled and stored more accurately, eliminating occurrences of corrupt data. All structures and orange boxes also have to be firmly grounded, to eliminate possible unwanted electric activity on the system, particularly with regards to communication (CRC errors) and also power line grounding issues. The structure of the battery bank is firmly grounded with an earth pick. The RS485 cable's shield is also firmly connected to the earth of the Power Station. This is done to ensure that a single ground is established.

### **Phase 6:**

Phase six takes place during 19 to 23 Oct. 2015. After the completion of phase five, it is noticed that PV module current delivered is clamped at 9.3A. This was due to the fact that the gain originally set with the 900  $\Omega$  gain resistor is too low for the INA111 Instrumentation amplifier [112]. Thus the gain resistor is changed to 1.5 k $\Omega$  to ensure that higher currents do not clip. This mistake is made due to the fact that it is not considered that the irradiance would be more than 1000 W/m<sup>2</sup>. Because of the fact that the INA111's gain is adjusted, the ActiveLoads are recalibrated in terms of current offsets and the calibration constants have to be recoded onto the ActiveLoads. New 47  $\Omega$  resistors are also soldered onto the MISO and MOSI lines of the temperature sensors, in an attempt to acquire more accurate temperature readings. This proved to solve the problem, which was determined to be caused mainly due to the length of the SPI cables.

Bird droppings are an issue and the PV modules are regularly soiled at the top of the module. To maintain data validity, bird spikes are installed to demotivate birds from sitting on the modules. This is found to be an effective solution, since the amount of bird droppings drastically decreased.

### **Phase 7:**

Phase seven(8 Nov. - 12 Nov. 2015) is a critical phase, since this phase marks the start of the official data collection. After completion of this stage, the PVRF is functioning completely. Of course, the trackers are not active yet. Bird spikes are also added to the thin-film modules. All of the PV modules are also washed.

### **Phase 8:**

Is executed between 9 to 11 Dec 2015. It is found that any measurement values larger than 100 are not stored on the SD card of the MC. New code is loaded onto the MC. General site inspection is also conducted.

### **Phase 9:**

The aim of this phase, which takes place 18 January - 20 January 2016, is to upload new firmware onto the weather sensor. The weather sensor is frequently providing a temperature measurements of 999, indicating a faulty measurement. New firmware is uploaded and found to resolve the issue. The MasterController is also found to have an issue. Every 4 h 21 min the WS stops responding for 7-8 minutes, thus failing to reply 11/12 requests per minute, with a request being sent every 5 sec. It is determined that only the very first request is successful during this period of "no reply" from the WS. With various tests it has been determined that the MSO-485 weather sensor is in fact responsible for the problem. With



a log interval of 1 min, the MC's database entries show zero, for 5x entries in a row, every 57minutes. However, the CSV file is updated correctly and contains the correct information. Thus, something is determined to be wrong with the FIFO data on the SD card.

### **Phase 10: Cleaning strategy implemented**

During this phase (15 February - 17 February 2016) the modules are coated and the strategy for dust mitigation is finally implemented. For a detailed description of the mitigation strategy, please refer to Chapter 6. However, due to the malfunction of the battery bank, which is hit by lightning, the official data analysis and implementation of the biweekly cleaning routines are delayed until April.

### **Phase 11: Replace batteries and MPPT charge controllers**

This phase is executed during 20 March to 25 March 2016. Due to a lightning strike, the MPPT charge controllers are destroyed. Thus, new batteries and MPPT charge controllers are installed. The new master device code, revised by T. Pandy, is integrated into the system to allow for a more seamless upload of device data.

### **Phase 12: First official installation attempt of the SAT system**

The SAT system is installed during the week of 19 to 23 April 2016. However, the PV module clamps that connect the modules to the axis are proven to be incapable of securing the modules onto the platform. Several mechanical issues are also experienced regarding the motor couplings. After this first in field testing procedure, the SAT system requires some adjustments concerning the clamps and couplings.

### **Phase 13: Installation of the SAT system**

During the week of 31 May to 5 June 2016, the SAT system is completely installed and several days of in field testing is performed to refine and successfully integrate the SAT system.

### **Phase 14: Installation of pyranometer**

Due to water damage, the pyranometer is reinstalled after being fixed by a local engineering company. This phase is executed during 12 to 15 July. The sensor was also checked for calibration and found to be accurate. A new cable connector is installed for the sensor. General site inspection is performed and firmware updates are uploaded to the MC and SAT boards.

### **Phase 15: Zero position calibration of SAT system**

After a faulty position sensor feedback is received from a SAT, a new position sensor is to be installed. This phase is executed from 11 to 14 August 2016. The new firmware is uploaded to the SAT and MC board, which allows for the remote calibration of a SAT. A new position sensor is also installed and general site inspections are completed.

## A.2 Items installed at Kalkbult PVRF

Table A.2: List of items required for the successful installation of the PVRF.

Item	Item
26 x Orange metal enclosures	4 x 300W PV modules
20 x triangular frames	6 x A-frames (trackers)
21 x small orange metal enclosures	1 x large orange metal enclosure
62 x concrete foundation blocks	1 x WiFi-tower and router
1 x weather sensor	Data-logger and rain-meter frame
4 x 12V Batteries	2 x MPPT charge controllers
Underground PVC piping	1x wi-fi router & Raspberry-Pi
54 x 1m Anchor poles	60 x vineyard anchoring cables
120 x crosby clamps	20 x 250W pc-Si modules
8 x Cd-Te Thin Film modules	24 x Active-loads
1 x Master Controller	1 x Rain gauge
1 x Pyranometer	24 x Wire Wound resistors
1 x Grounding earth-pick	28 x Back-plate temp. sensors
2 x 24V, 4000r.p.m DC motors	2 x 5000:1 Worm Gear combinations
4 x 10m and 1 x 6m cross-beams	4 x single axis tracker axis
80 x pc-Si Module fastening clamps	32 x Thin-Film module clamps
6 x 5 cm diameter bearings	2 x position sensors and enclosures
2 x Single-axis-control boards	Bird spikes on 28 x PV modules

### A.2.1 Photos of PVRF



(a) WiFi antenna.



(b) Weather sensor.



(c) WiFi-router and Raspberry Pi.



(d) Pyranometer mounted at 30° tilt.

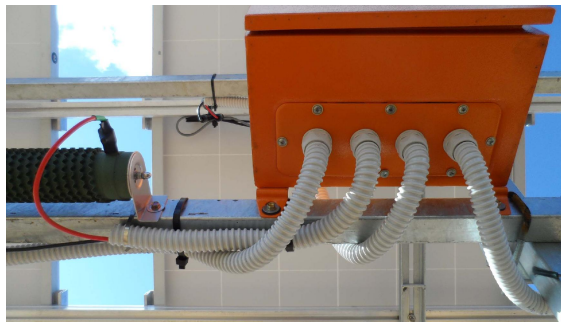
Figure A.2: Communication and meteorological device set-up.



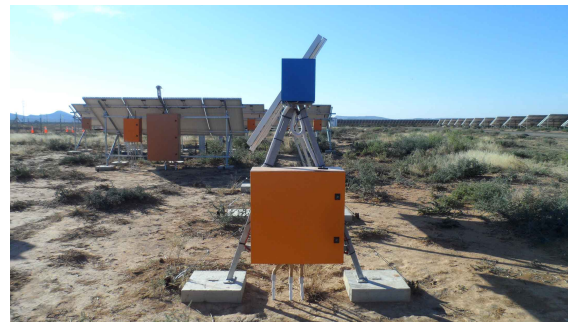
(a) Stationary row with enclosures.



(b) Stationary row from the front side.



(c) Underneath an enclosure box.

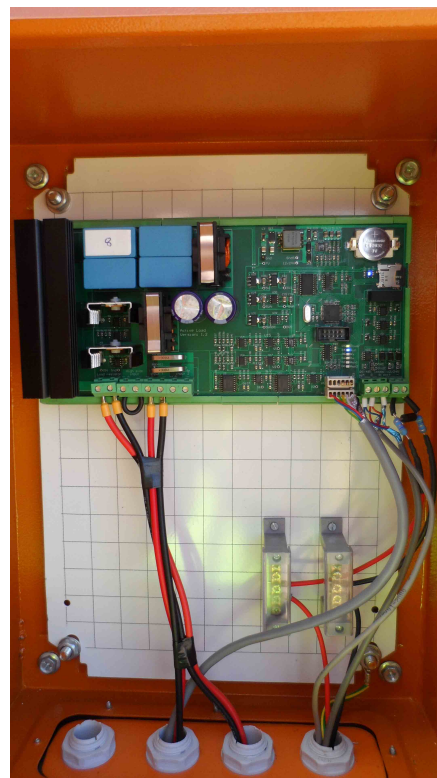


(d) A single axis tracker.

Figure A.3: Images of the stationary rows, one of the SATs and an example of a wired orange enclosure box.



(a) Batteries and MPPT charge controller.



(b) AL connected in an orange enclosure box.

Figure A.4: Images of the battery bank and an AL inside the electronic housings.

# Appendix B

## Master Controller PCB design

### B.1 Relevant datasheet information

#### 6 Typ. drain-source on resistance

$$R_{DS(on)} = f(I_D)$$

parameter:  $V_{GS}$ ;  $T_j = 25\text{ }^\circ\text{C}$

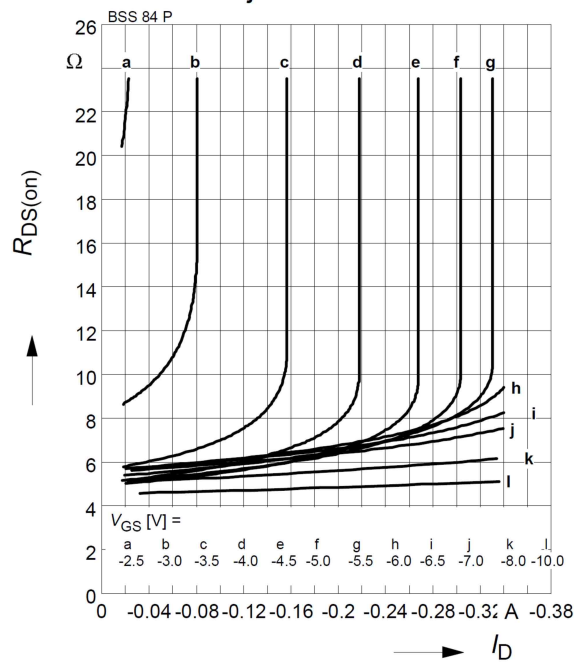


Figure B.1: Value of drain-source on resistance for P-channel BSS84P MOSFET [76, p.5]

### B.2 MC PCB design documents

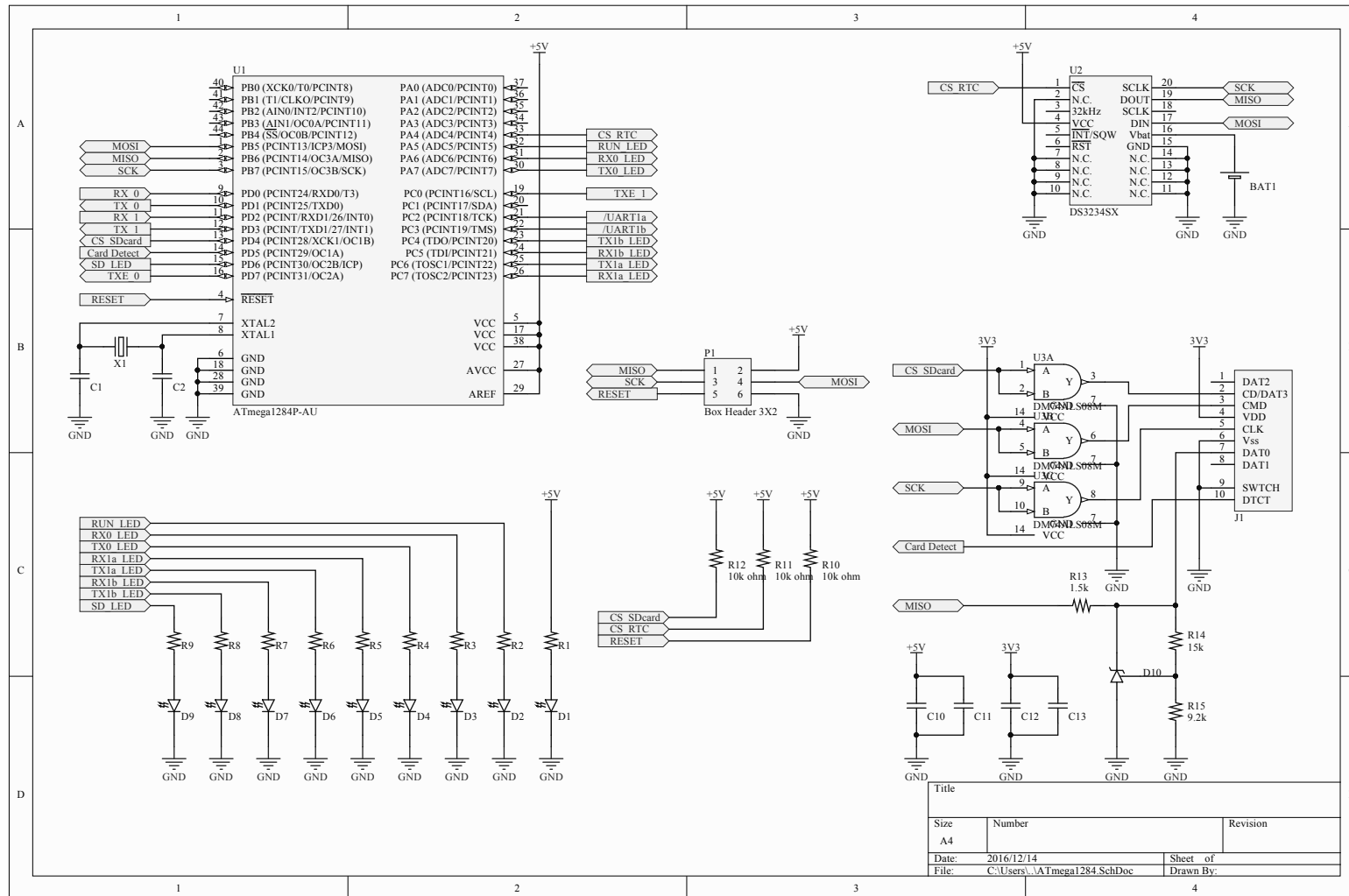
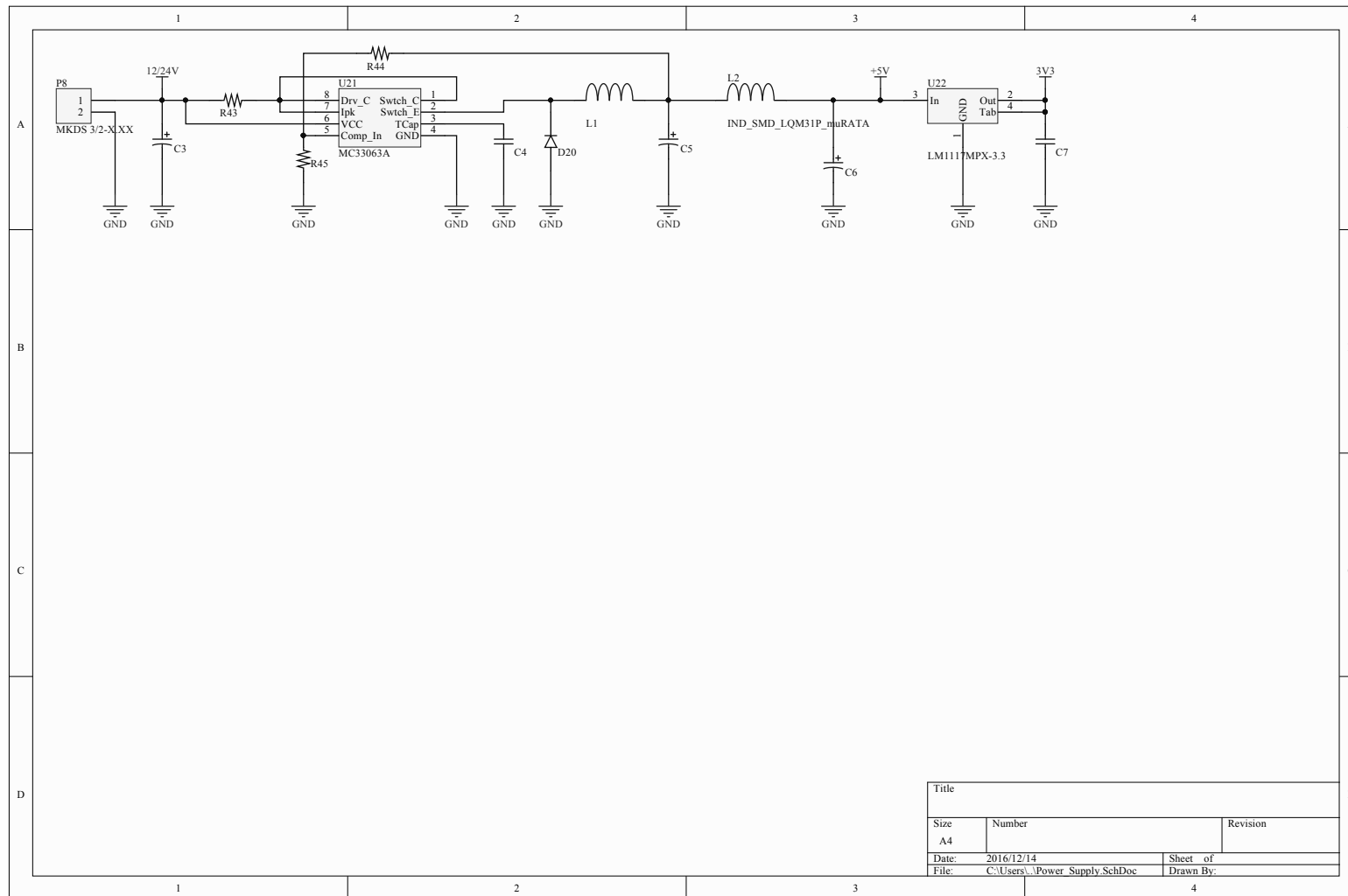


Figure B.2: Schematic design of the MCU circuitry.



Title		
Size	Number	Revision
A4		
Date:	2016/12/14	Sheet of
File:	C:\Users\Power Supply\SchDoe	Drawn By:

Figure B.3: Schematic design of the power supply circuitry.

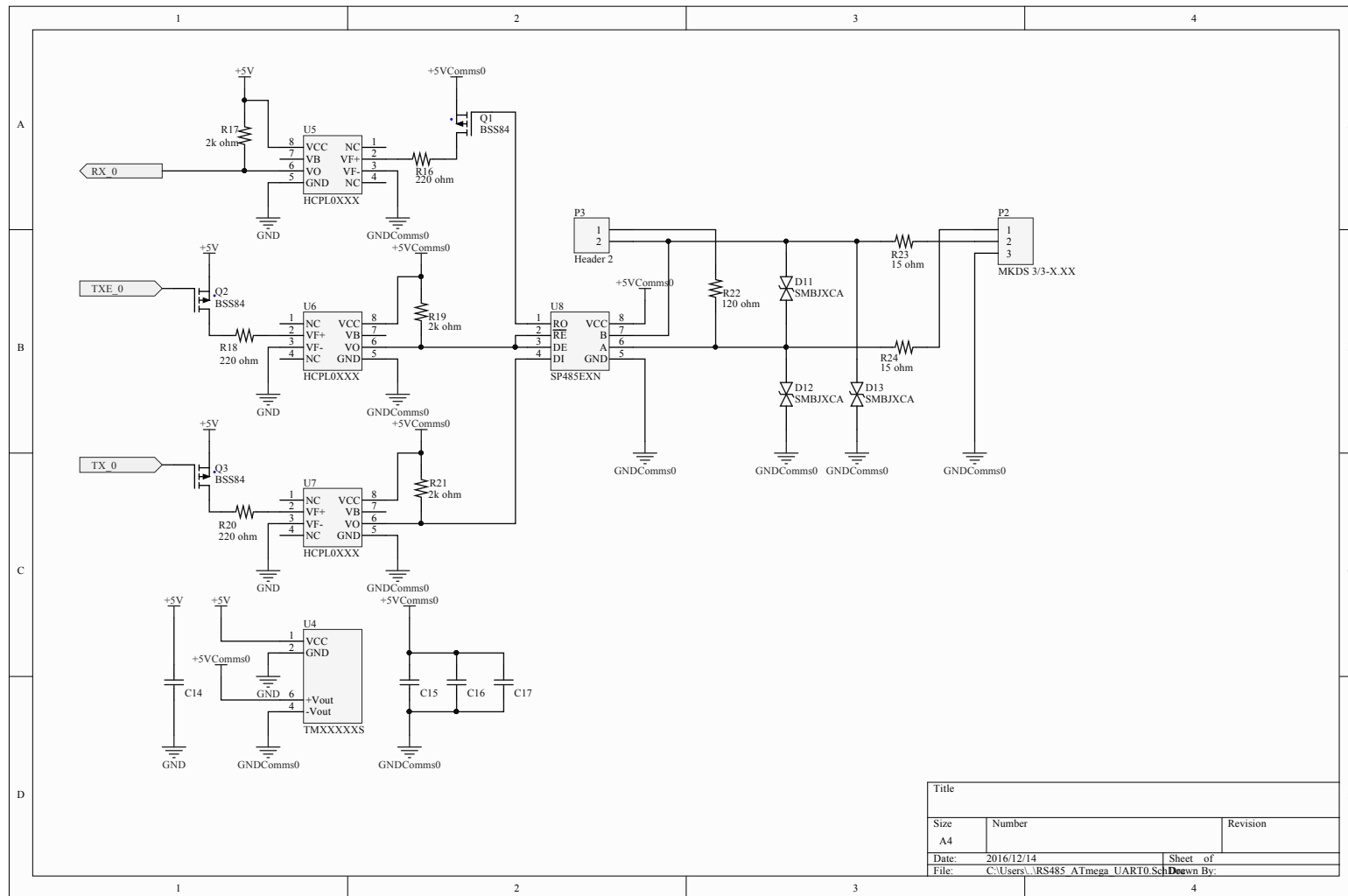


Figure B.4: Schematic design of the RS485 UART0 communication circuitry.

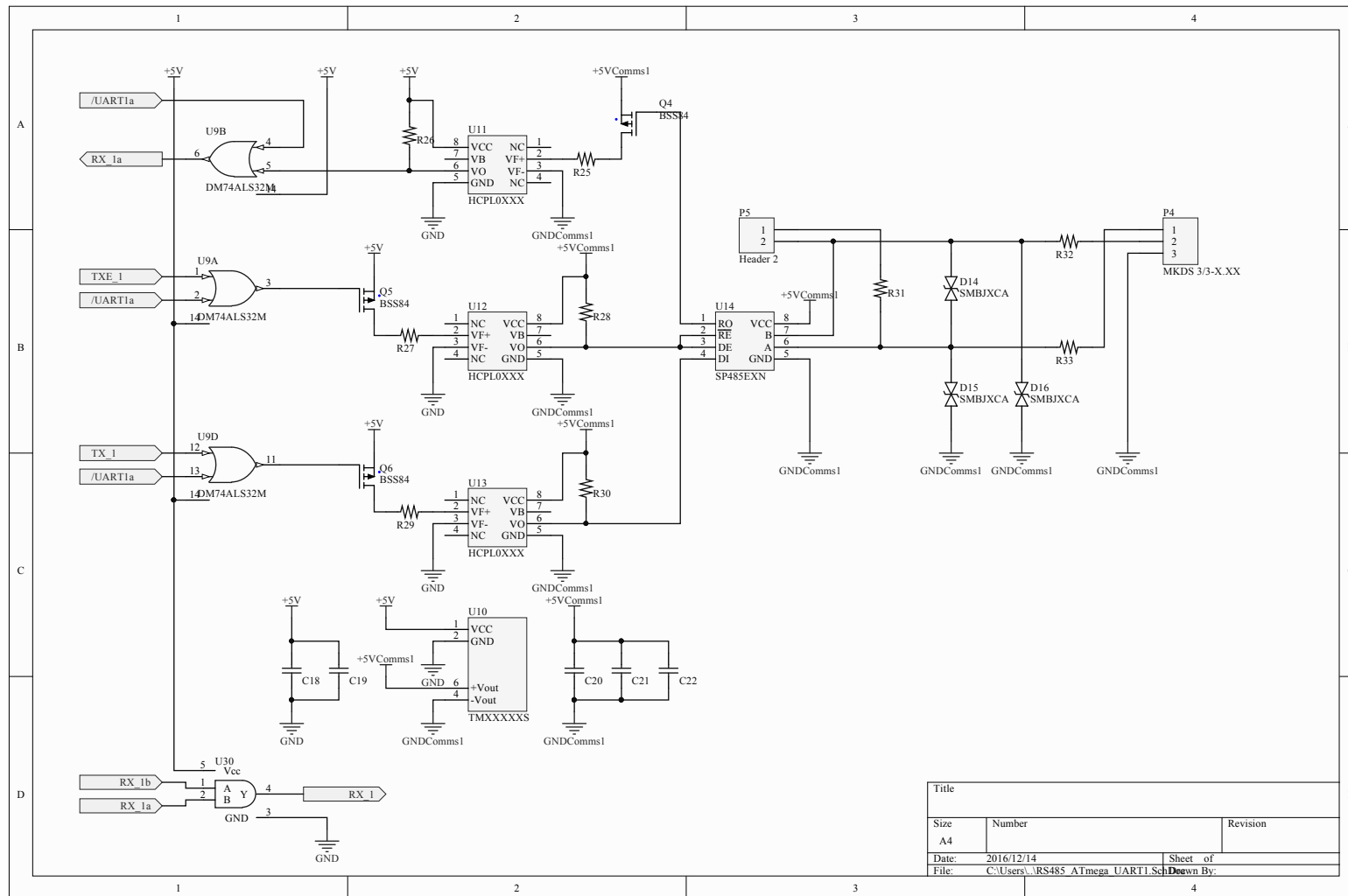


Figure B.5: Schematic design of the RS485 UART1A communication circuitry.



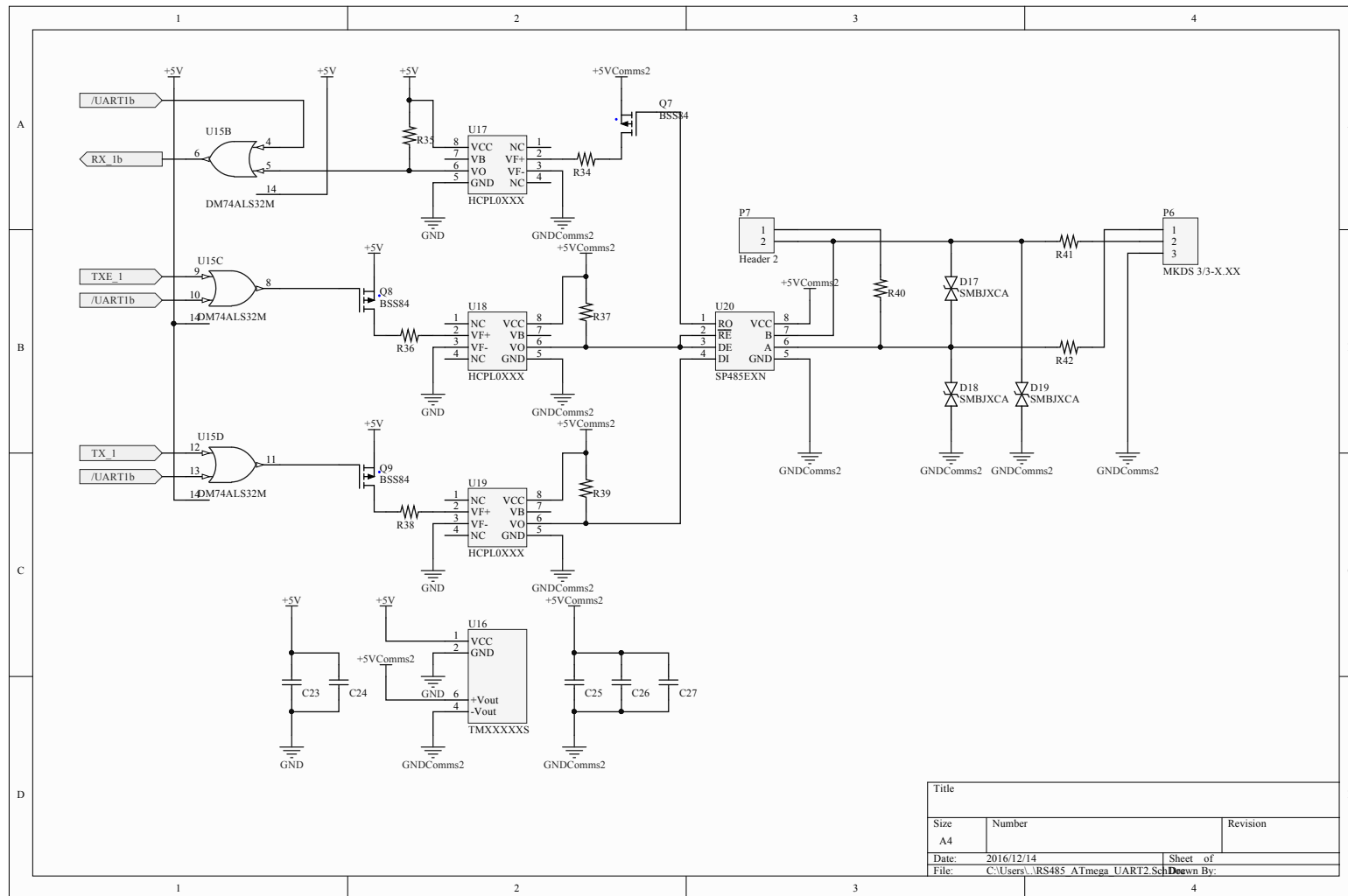


Figure B.6: Schematic design of the RS485 UART1B communication circuitry.

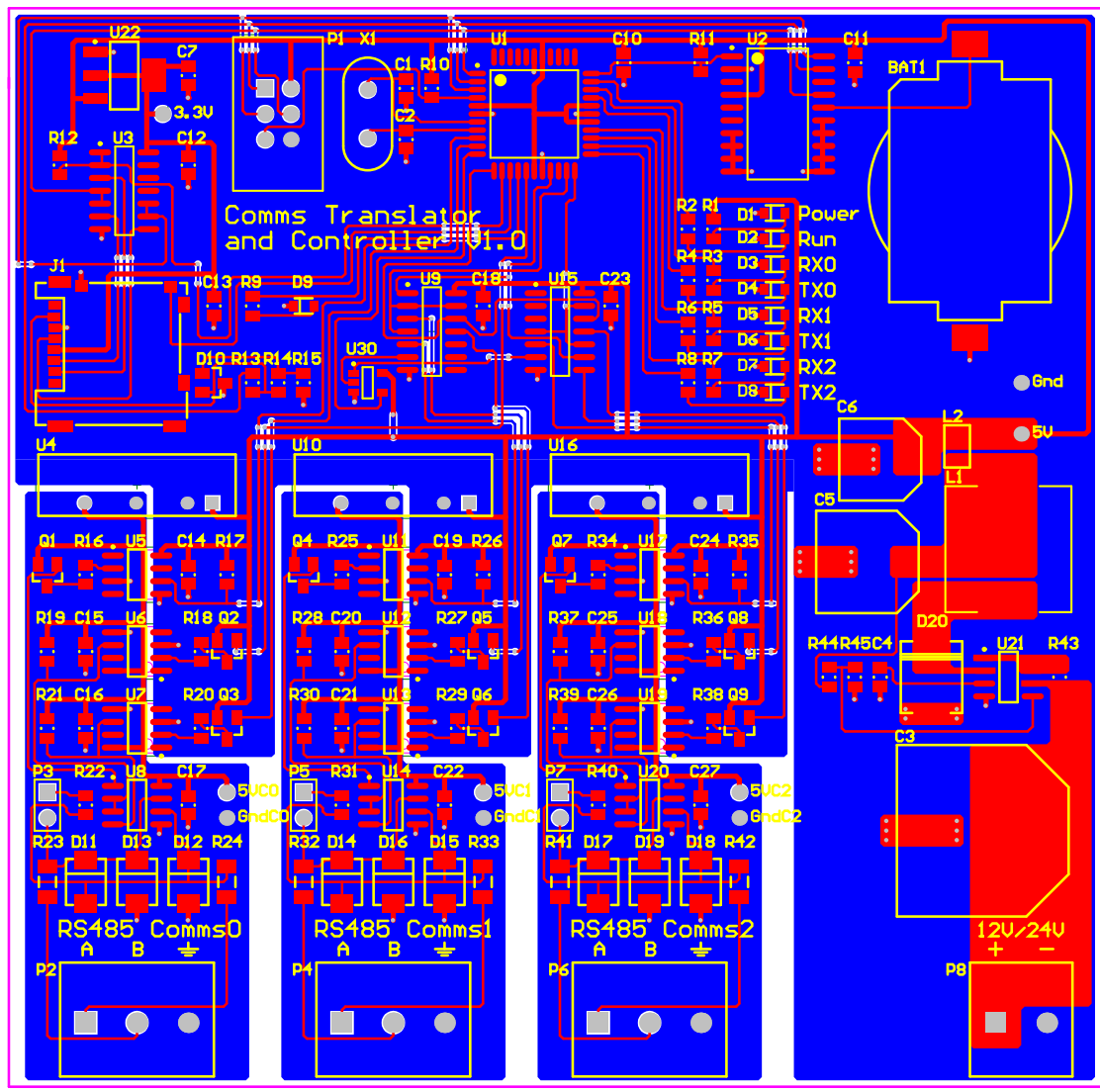


Figure B.7: PCB design of the MC circuit board.



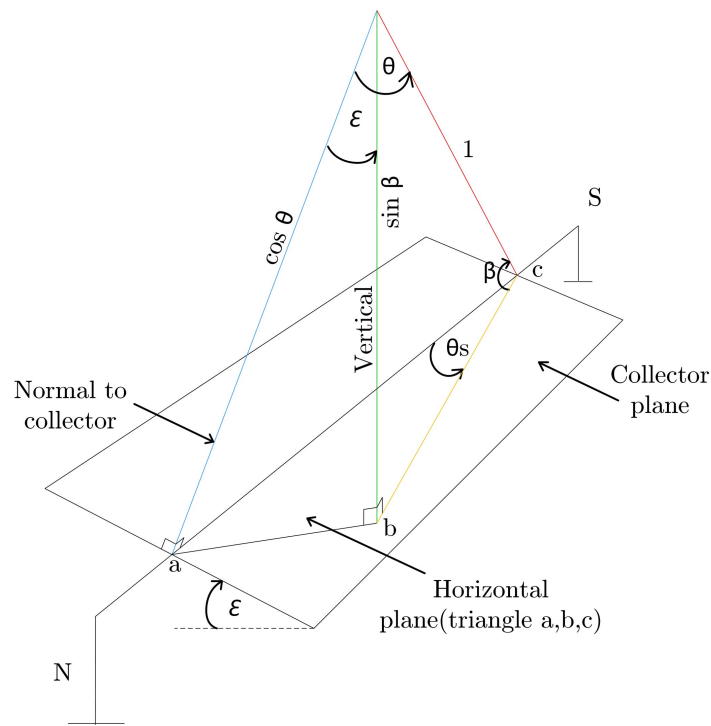


Figure C.2: Trigonometric relationship of the position of the sun relative to the angle of tilt for the SAT. *Source:* Redrawn image as illustrated by [44, p. 225]

## C.2 Hardware design related

### C.2.1 LM311D comparator

In Figure C.3, the timing diagram is displayed for the case where the input voltage  $V_{in-}$  exceeds the reference voltage  $V_{in+}$  by more than 100 mV. The comparator changes its output state from a high output state to a low output state when:

$$V_{in+} - V_{in-} \leq 100 \text{ mV} \quad (\text{C.1})$$

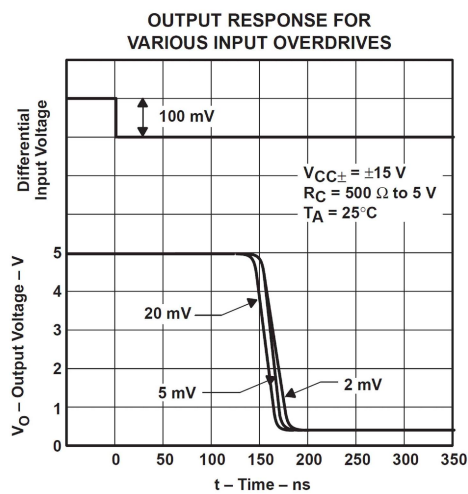


Figure C.3: Timing diagram of the LM311D comparator. *Source:* Extracted from the data sheet [97]

### **C.3 SAT and position sensor PCB design schematics**

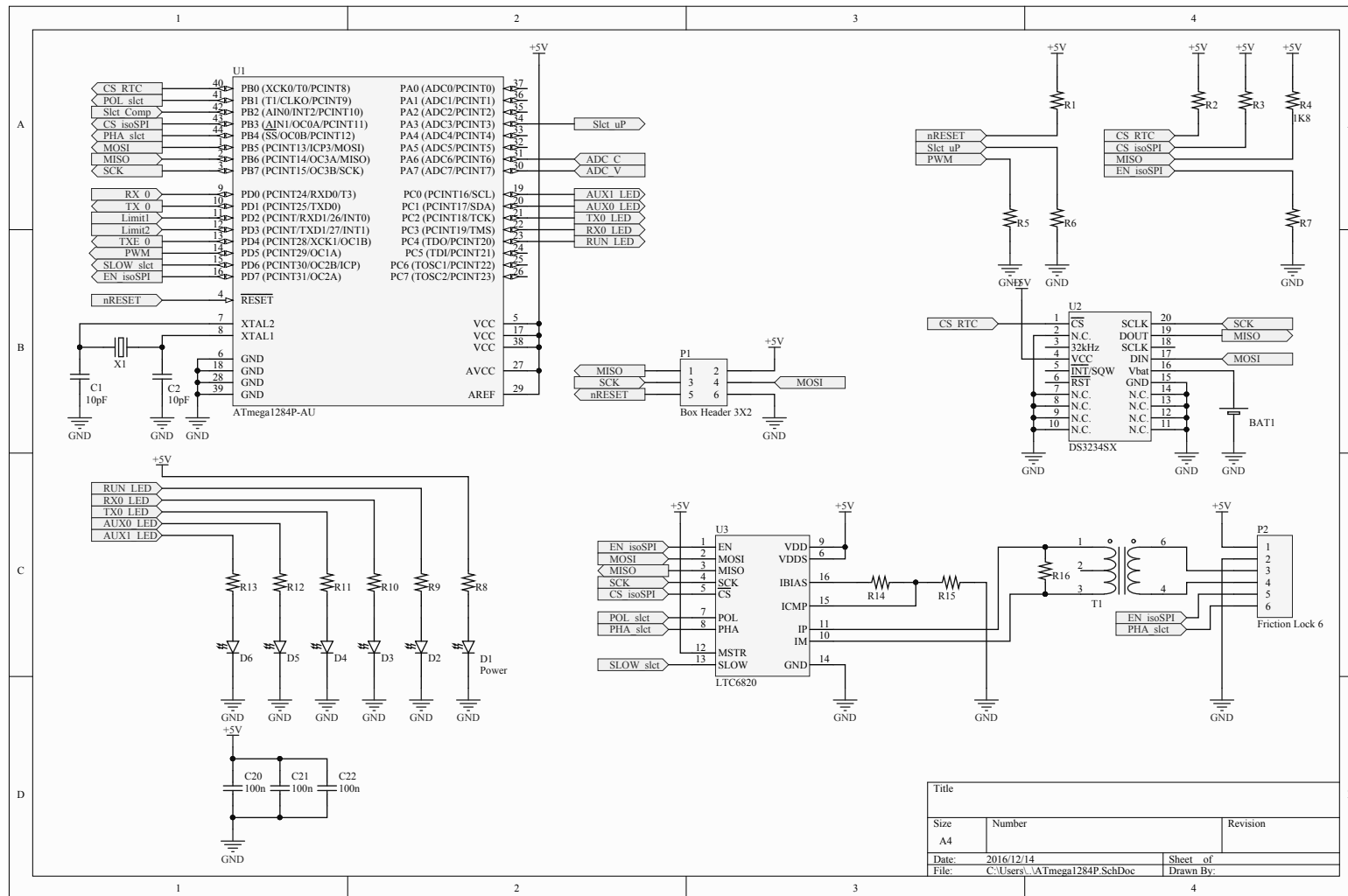


Figure C.4: Schematic design of the MCU circuitry for the SAT PCB board.

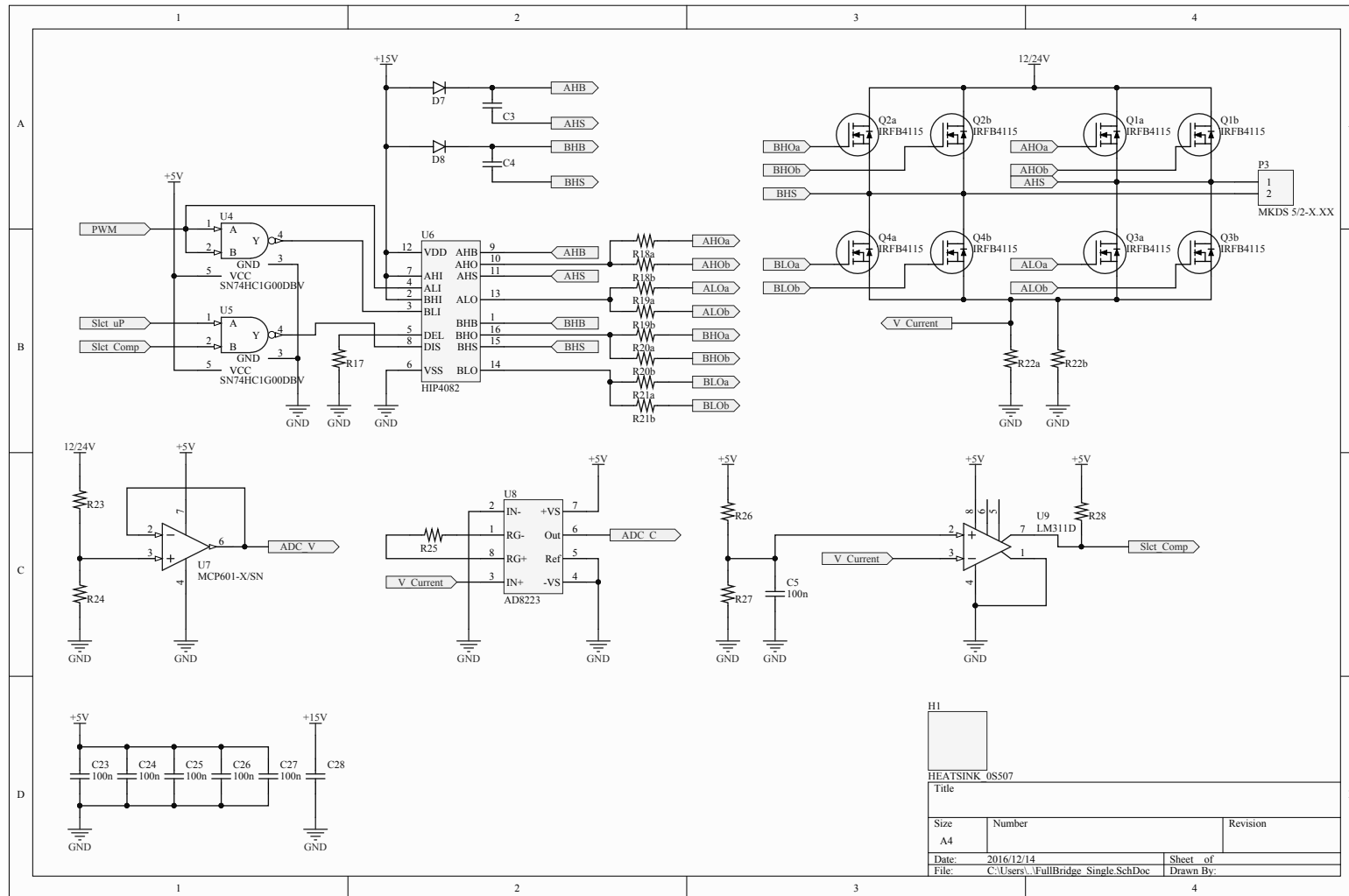


Figure C.5: Schematic design of the H-bridge circuitry.

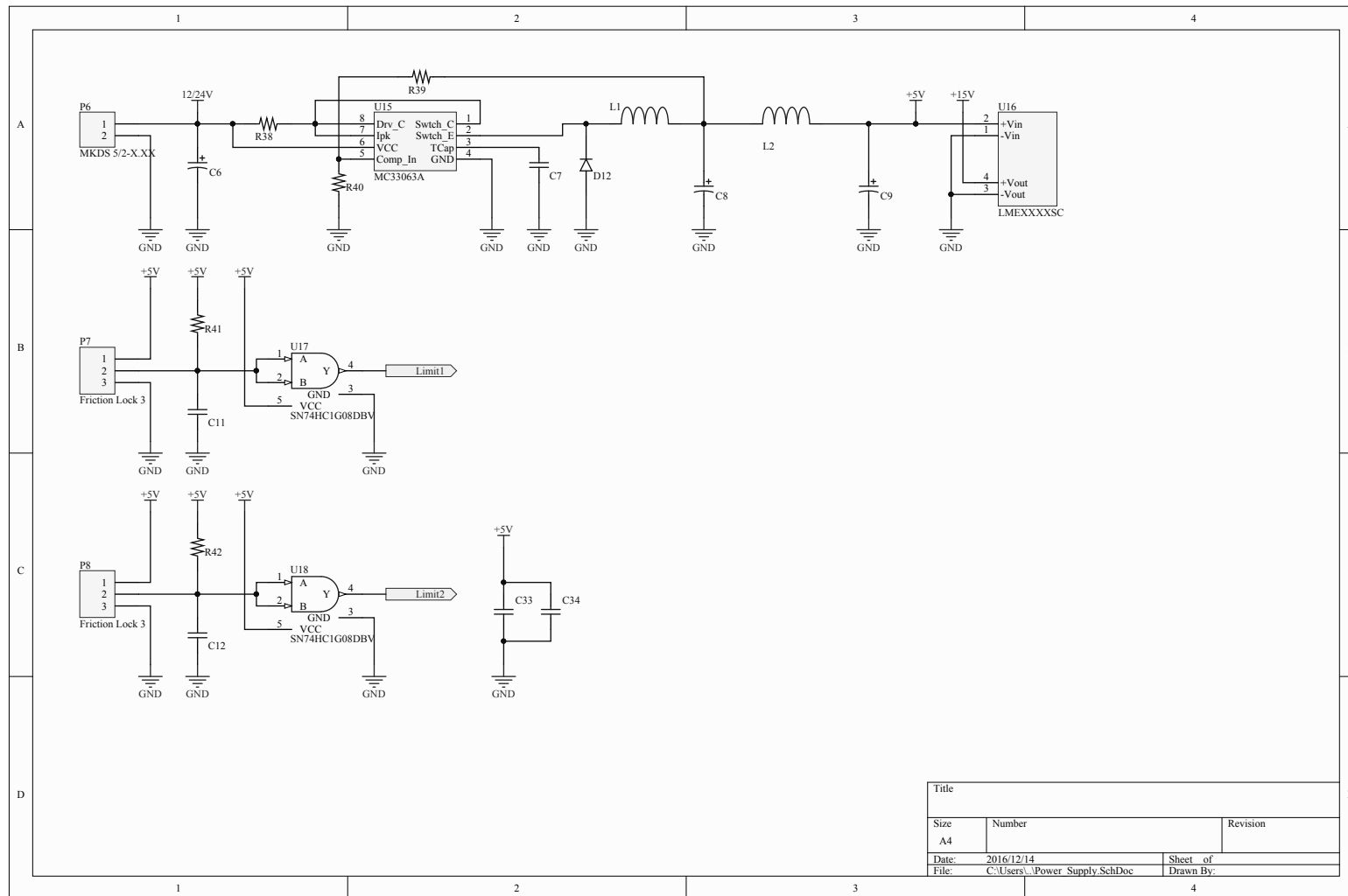


Figure C.6: Schematic design of the SAT power supply and proximity sensor circuitry.



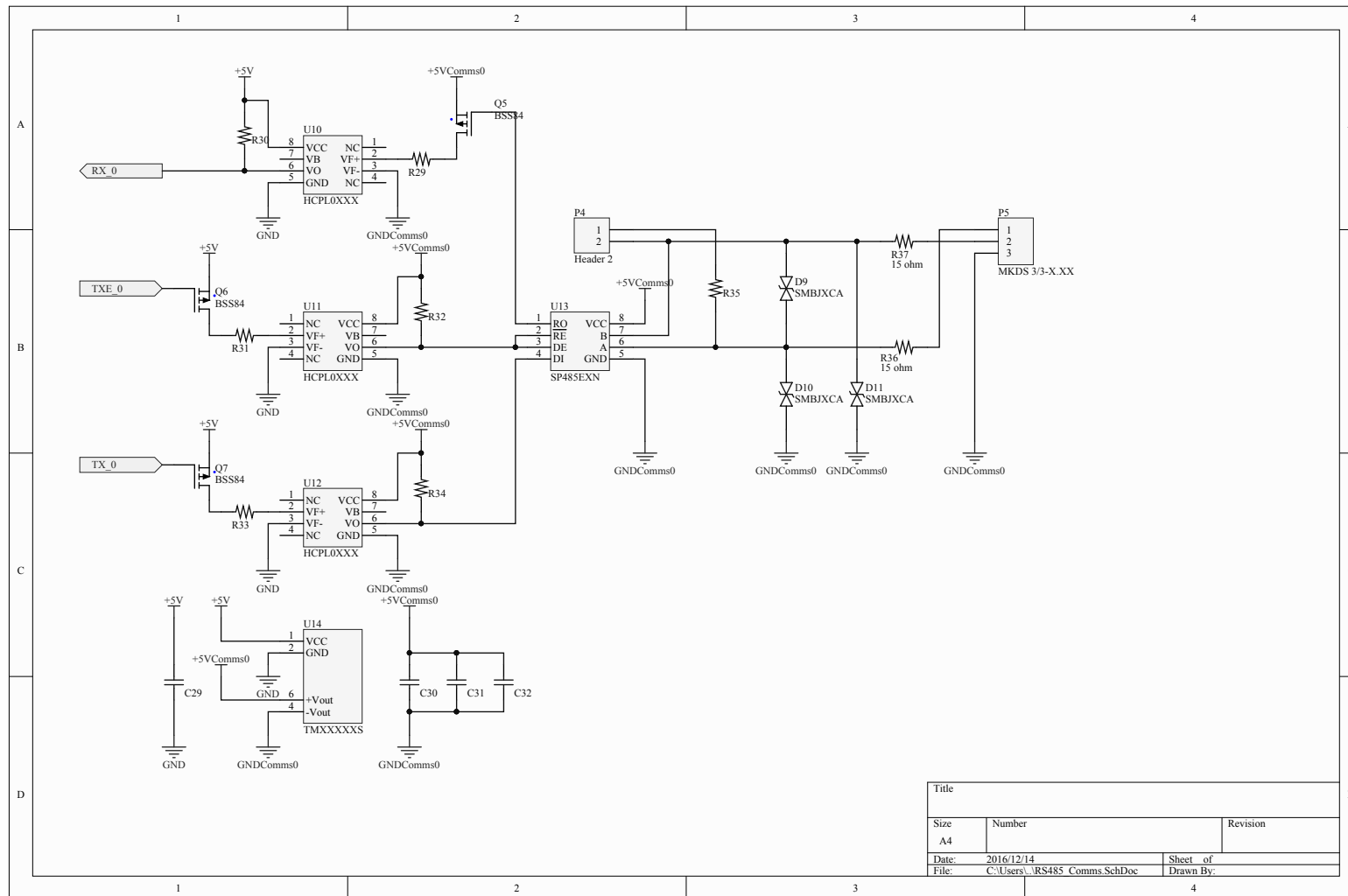


Figure C.7: Schematic design of the RS485 communication circuitry.

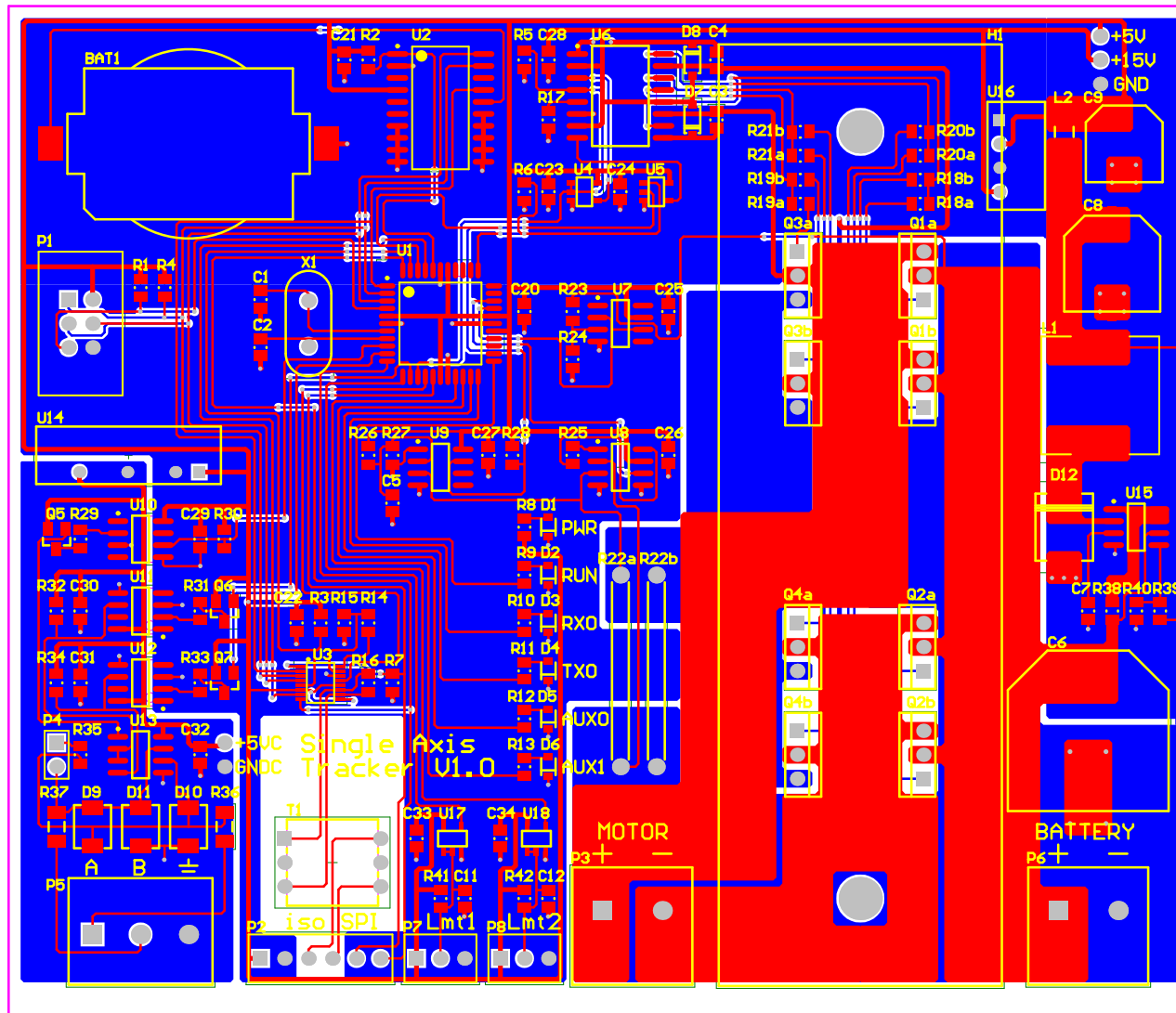


Figure C.8: PCB design of the SAT circuit board.

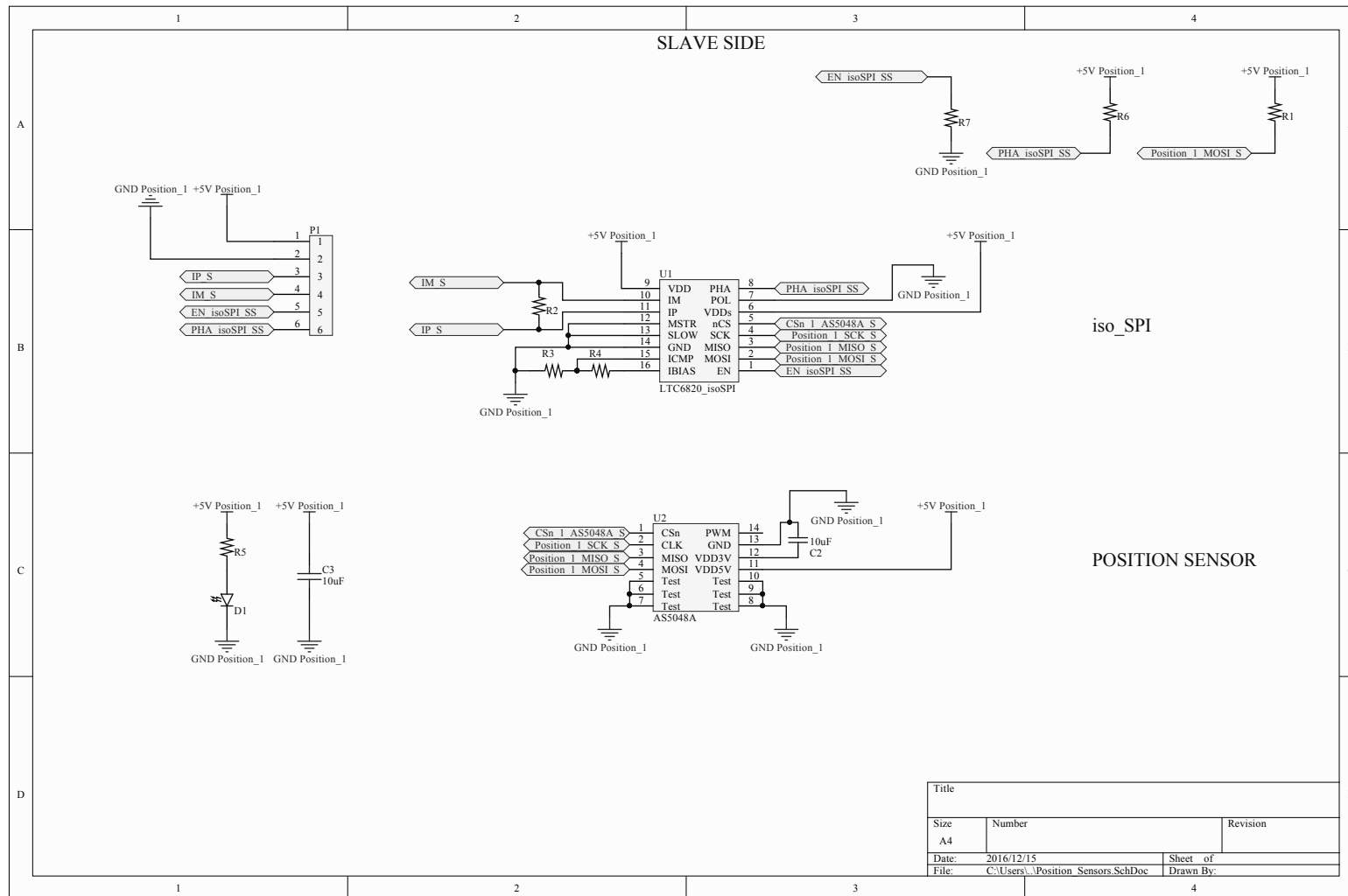


Figure C.9: Schematic design of the SAT position sensor board.

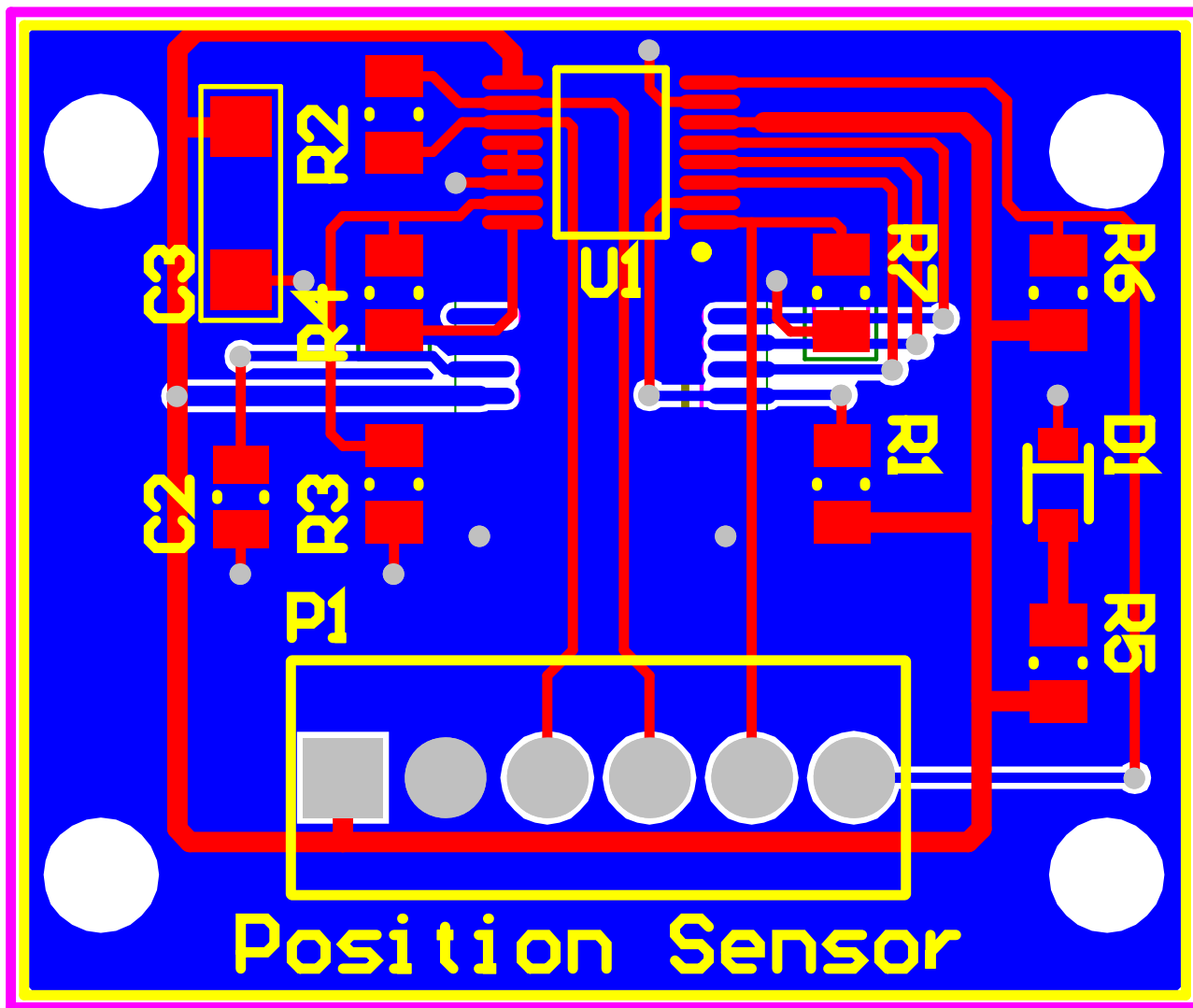


Figure C.10: PCB design of the SAT position sensor circuit board.

## C.4 Software design related

### C.4.1 PWM software set up

The ICR1B register of the PWM signal [85, p. 121] is set up to operate in waveform generation mode 14. Which essentially enables the PWM fast mode, as demonstrated by the timing diagram shown below in Figure C.11. This executes a single-slope operation, where the counter simply counts from BOTTOM to TOP and then restarts again, from BOTTOM. However, with the value of OCR1A set, the counter will stop once the OCR1A value is matched [85, p. 120]. The non-inverting mode is assigned in register TCCR1A. The resolution of the PWM signal is determined as  $9.96 \simeq 9\text{bit}$  resolution by equation (C.2)

$$R_{FPWM} = \frac{\log(TOP + 1)}{\log(2)} \quad (\text{C.2})$$

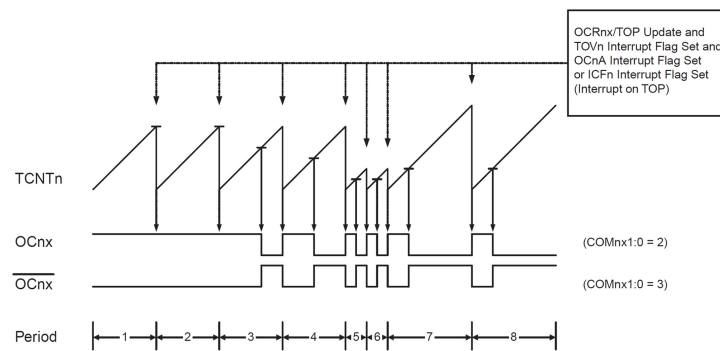


Figure C.11: Fast PWM timing diagram [85, p.121].

Mode	WGMn3	WGMn2 (CTCn)	WGMn1 (PWMn1)	WGMn0 (PWMn0)	Timer/Counter mode of operation	TOP	Update of OCRnx at	TOVn flag set on
14	1	1	1	0	Fast PWM	ICRn	BOTTOM	TOP

Figure C.12: Fast PWM timing diagram [85, p.130].

The 20 kHz frequency is set by assigning the TOP value (999), determined by equations C.4 to the ICR1 register. The N variable is the pre-scaler and is set to one. Equations (C.4) and (C.3) are used to determine the TOP variable.

$$f_{OCnxPWM} = \frac{f_{clk_{I/O}}}{N(1 + TOP)} \quad (\text{C.3})$$

$$TOP = \frac{f_{OCnxPWM} \times 1}{f_{clk_{I/O}}} - 1 \quad (\text{C.4})$$

Where variables  $f_{OCnxPWM}$  and  $f_{clk_{I/O}}$  represent:

- $f_{OCnxPWM}$  = The frequency of the applied PWM signal.
- $f_{clk_{I/O}}$  = The MCU clock frequency, which is 20 MHz.

Finally the applied duty cycle  $D$  is set in the OCR1A register by multiplying the duty cycle with the TOP value of 999, as in equation (C.5):

$$OCR1A = D \times TOP \quad (C.5)$$

### C.4.2 ADC set up

The ADC is enabled by setting the ADC Enable bit (ADEN) in the ADCSRA register. To acquire a conversion resolution of 10 bits, the ADC approximation circuitry requires an input clock frequency between 200 kHz and 500 kHz [85, p.238]. Therefore, a pre-scaler of 128 is used, which results in a 156.25 kHz clock frequency for the ADC sampling rate. The ADC generates a 10-bit result which is presented in the ADC Data Registers, ADCH (ADC higher register) and ADCL (ADC lower register) [85, p.247]. By default, the result is presented right adjusted. For single ended conversion, the result is represented by equation C.6 [85, p.247]. The value 0x000 represents analogue ground, and 0x3FF represents the selected reference voltage minus one LSB, in other words 0 – 1023 (max) which is 0 V – 5 V for this design.

$$ADC = \frac{V_{IN} \times 1204}{V_{REF}} \quad (C.6)$$

In equation (C.6),  $V_{IN}$  is the received voltage at the ADC pin, whereas  $V_{REF}$  refers to the 5 V reference voltage. A single conversion is started by writing a logical one to the ADC Start Conversion bit, ADSC. This bit is cleared when the conversion completes. [85, p.237] In Single conversion mode, the channel must always be selected before starting the conversion. The ADC value read is defined by (C.6) as:

Once the start-conversion bit has been set, the ADC interrupt vector executes and the voltage input is read from the ADCL and ADCH registers. Once ADCL is read, ADC access to Data Registers is blocked (that's why the ADC lower register must be read first). Thus the ADCL register must always be read first and as long as it is not read, the next ADC conversion will not take place. When ADCH is read, ADC access to the ADCH and ADCL registers is re-enabled . [85, p.237].

# Appendix D

## Data-Analysis

### D.1 Rated PV module values of stationary modules

The rated power values determined for each PV module is presented in Table D.1:

Table D.1: Rated power of individual PV modules number 1-16, as determined by measurement.

<b>PV module</b>	1	2	3	4
$P_{STC}$ [W]	240.8497	241.185	244.1529	237.486
<b>PV module</b>	5	6	7	8
$P_{STC}$ [W]	243.4569	241.7745	242.4051	244.0043
<b>PV module</b>	9	10	11	12
$P_{STC}$ [W]	242.4362	245.7874	244.6556	242.9407
<b>PV module</b>	13	14	15	16
$P_{STC}$ [W]	242.1779	242.7734	241.3911	242.4025

### D.2 Rated PV module values of SAT modules

The rated power values determined for each SAT PV module is presented in Table D.2:

Table D.2: Rated power of individual PV modules number 21-24, as determined by measurement.

<b>PV module</b>	21	22	23	24
$P_{STC}$ [W]	230.6035	235.8985	237.9318	233.5762

### D.3 Shading analysis of the PVRF

The only surrounding structure that poses a threat to possible module shading is the substation located West of the PVRF. This is indicated in Figure D.1. Three positions are chosen for the shading analysis, to get a clear indication of when to expect shade to block irradiance from the PV modules. The reason for selecting two locations West of the PVRF (Location 1 and 2) is because the western part of the PVRF will receive the first shadow from this structure. The shading analysis of each location is presented in Figures D.3, D.4 and D.5.

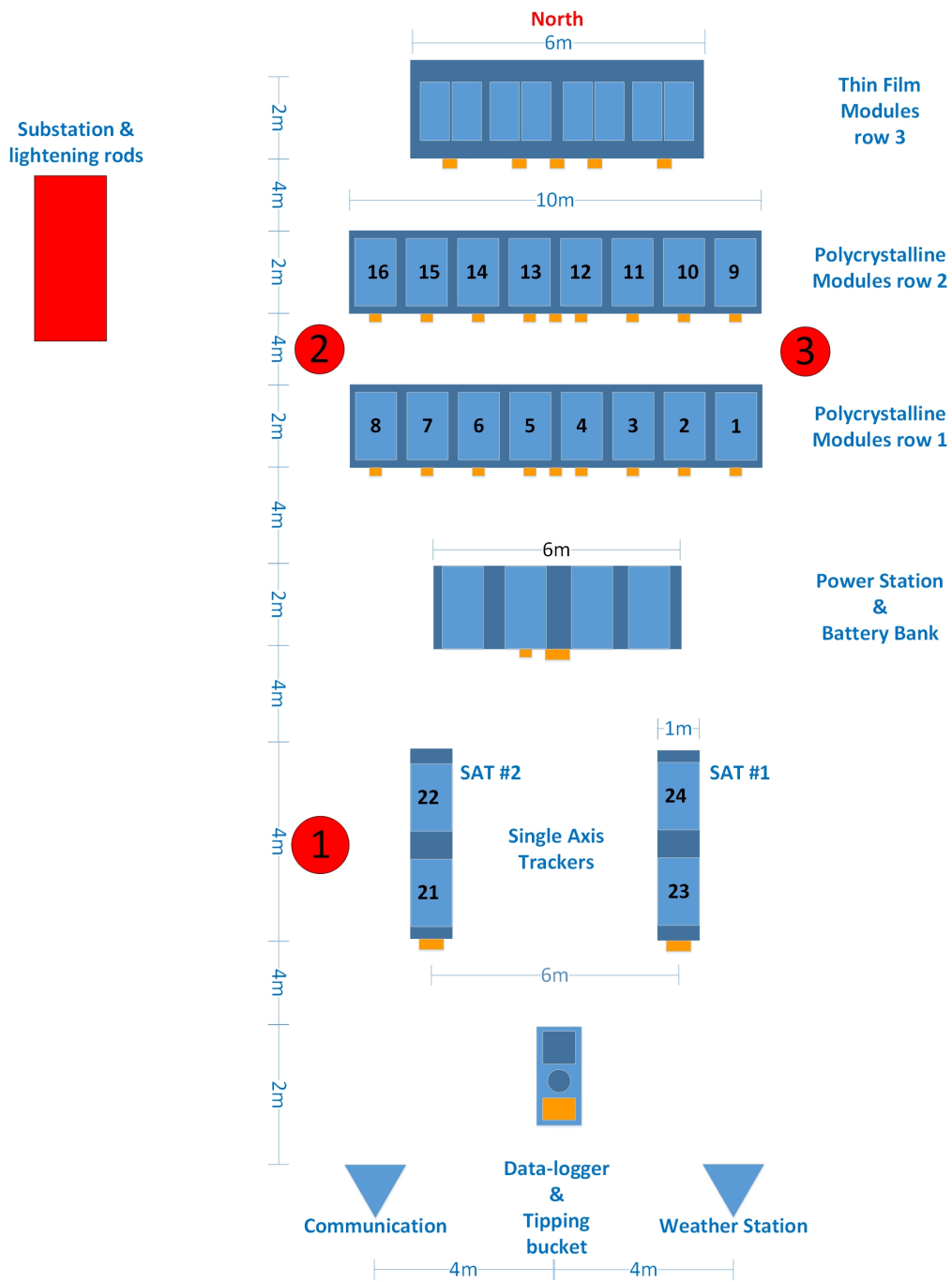


Figure D.1: Facility layout indicating positions from where the shading analysis is conducted.





Figure D.2: Substation and lightning rods which cast a shadow.

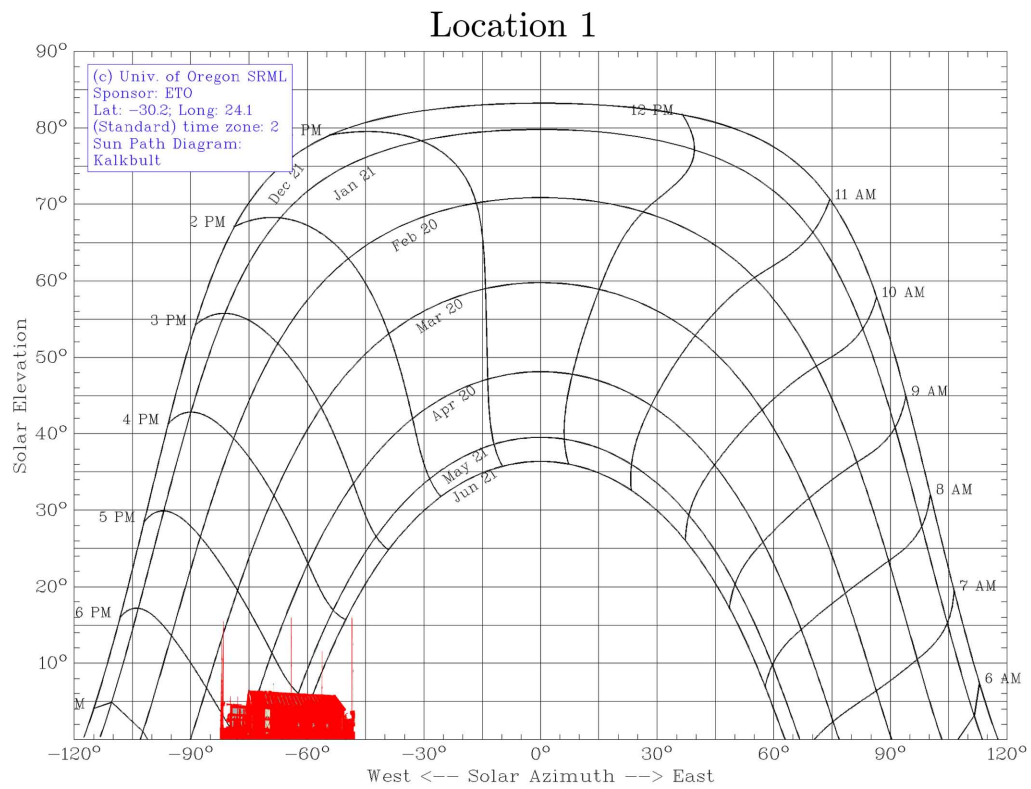


Figure D.3: Shading diagram of location 1.

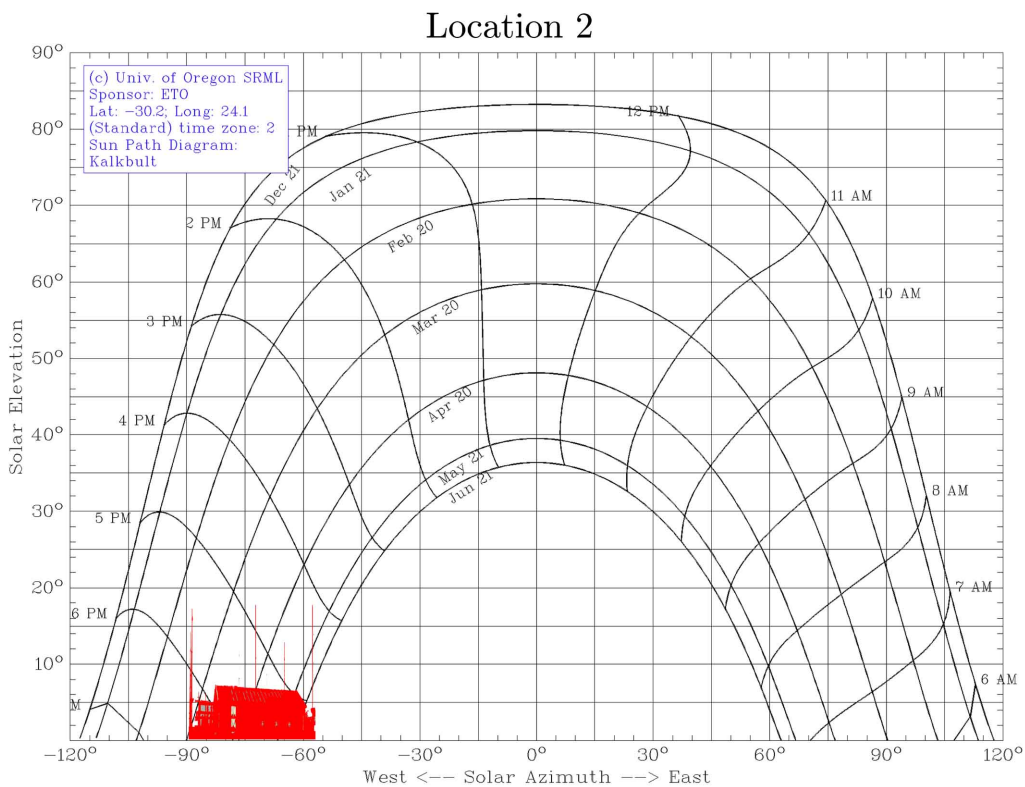


Figure D.4: Shading diagram of location 2.

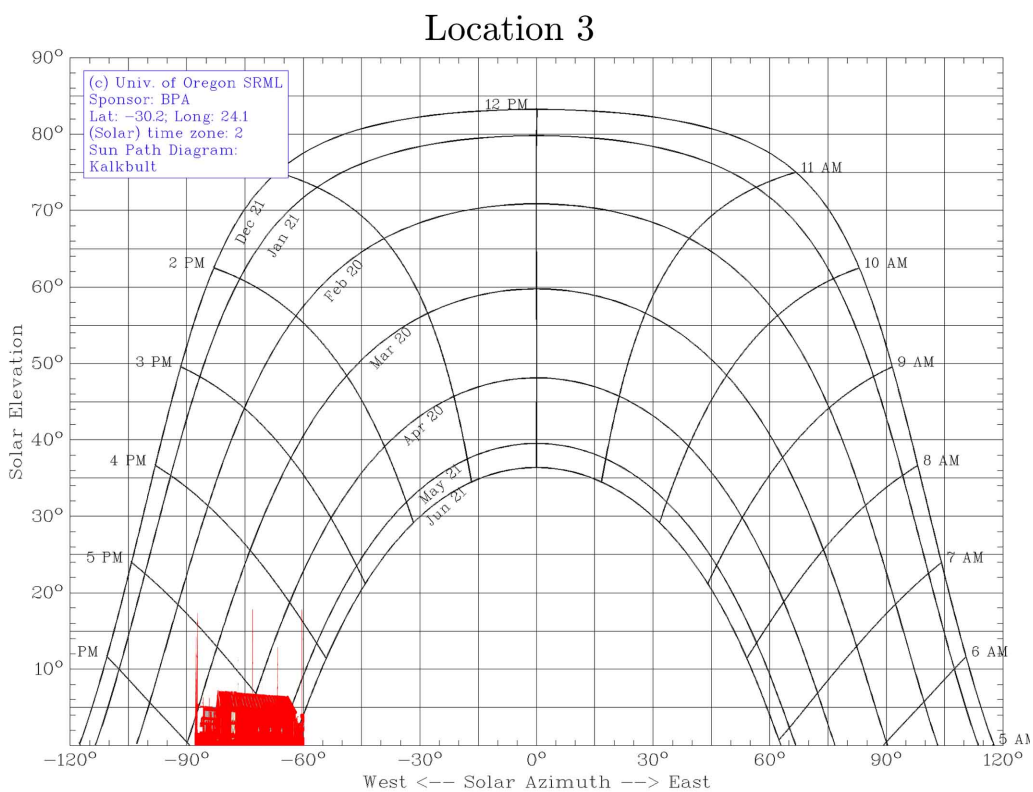


Figure D.5: Shading diagram of location 3.

## D.4 Meteorological data

The figures below present the comparison of the various meteorological data sets, to that of the stationary PV module performance ratios.

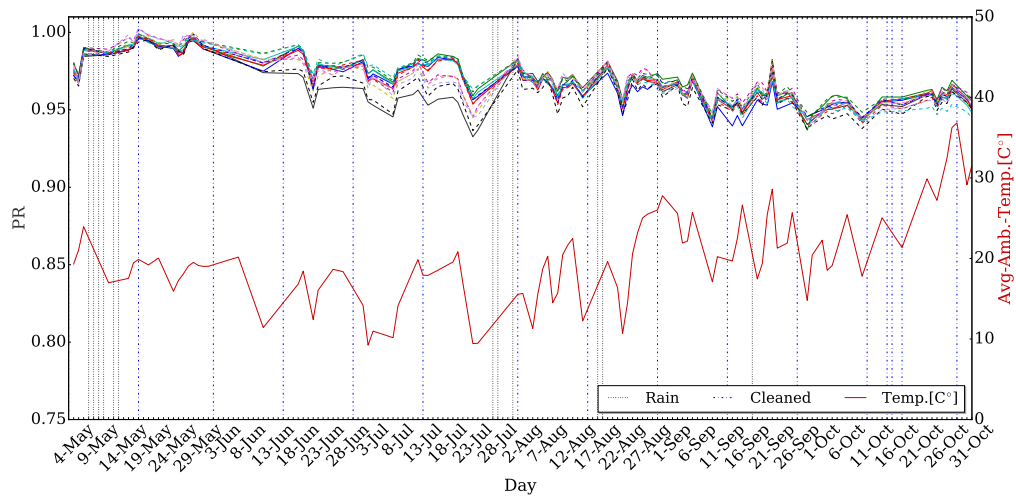


Figure D.6: Average ambient temperature compared to stationary PV module performance ratios.

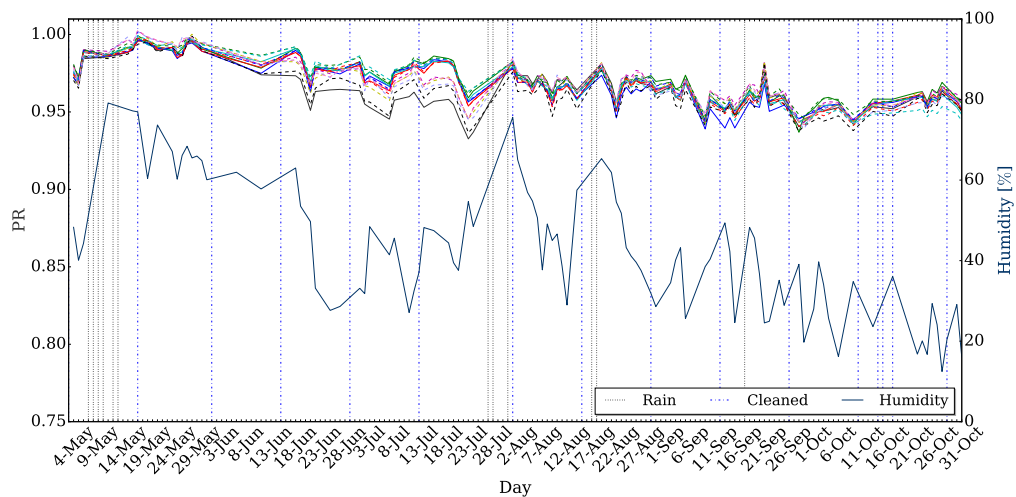


Figure D.7: Average humidity compared to stationary PV module performance ratios.

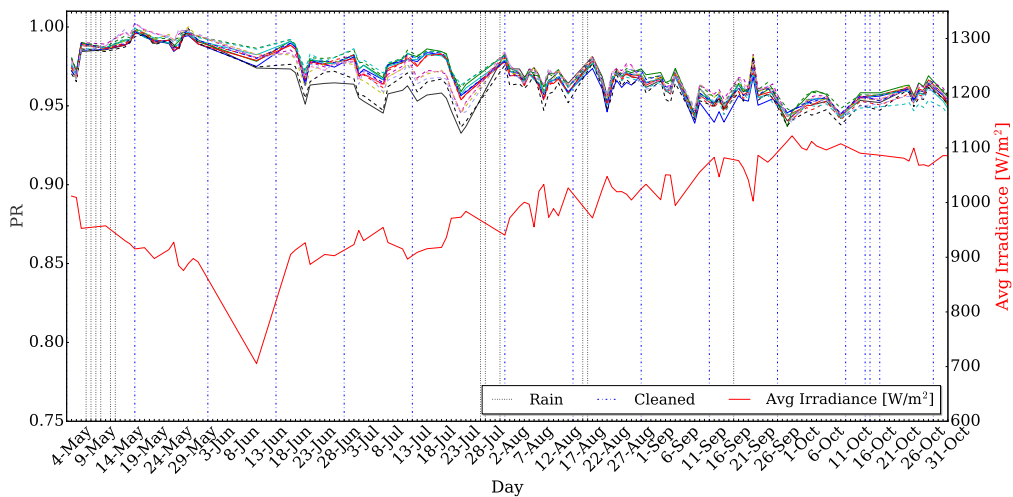


Figure D.8: Average irradiance, compared to stationary PV module performance ratios.

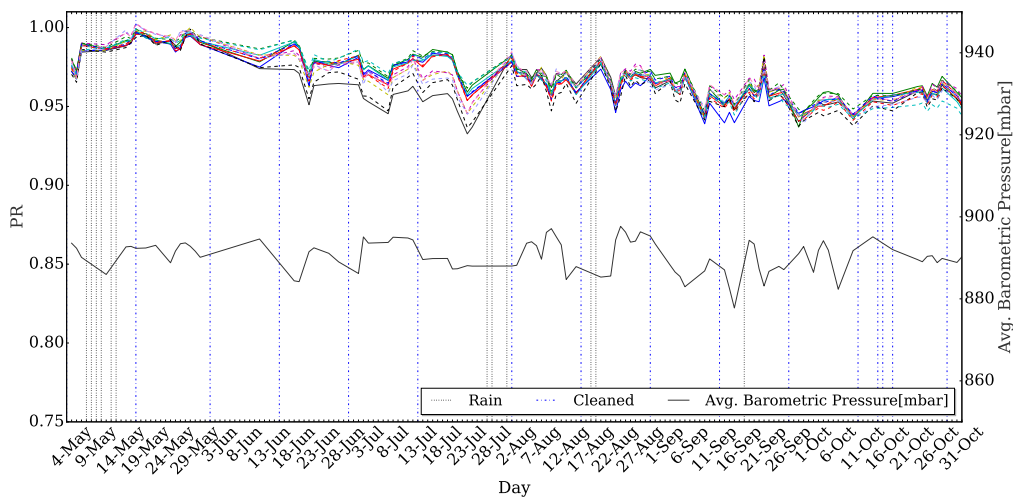


Figure D.9: Average barometric pressure compared to PR.

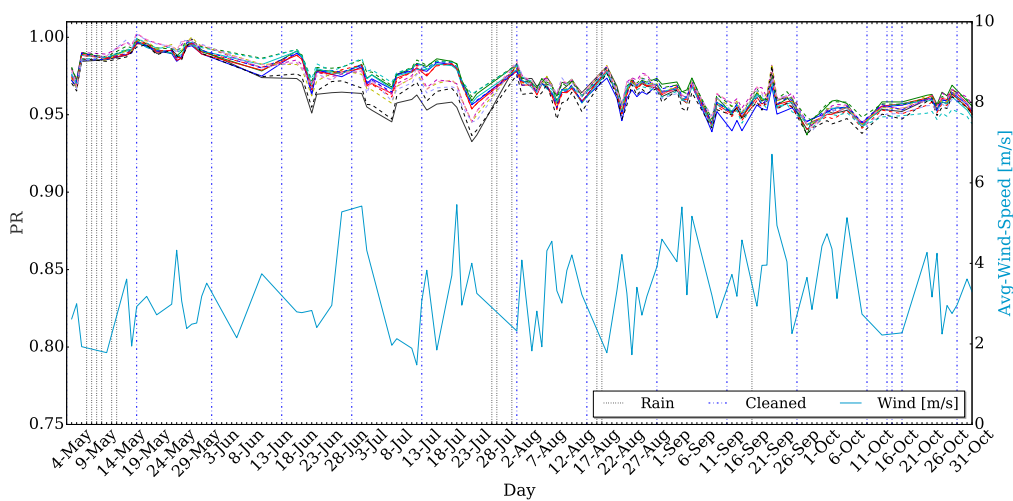


Figure D.10: Average wind speed compared to PR.

# List of References

- [1] T. Randall. (2016, June) The world nears peak fossil fuels for electricity. [Accessed: 27-June-2016]. [Online]. Available: <http://www.bloomberg.com/news/articles/2016-06-13/we-ve-almost-reached-peak-fossil-fuels-for-electricity>
- [2] P. Papapetrou, “Enabling Renewable Energy in South Africa : Assessing the Renewable Energy Independent Power Producer Programme,” Tech. Rep., 2014. [Online]. Available: [http://awsassets.wwf.org.za/downloads/enabling\\_re\\_in\\_sa.pdf](http://awsassets.wwf.org.za/downloads/enabling_re_in_sa.pdf)
- [3] M. G. Tshehla, “Renewable Energy - 2015 - Market Intelligence Report,” Tech. Rep., November 2015. [Online]. Available: <http://greencape.co.za/assets/Uploads/GreenCape-Market-Intelligence-Report-2015-Renewable-Energy.pdf>
- [4] Al Dowsari, J. Riley Caron, R. Bkayrat, and H. AlZain, “Best Practices for Mitigating Soiling Risk Risk on PV Power Plants,” in *Smart Grid Conference (SASG), 2014 Saudi Arabia*. Jeddah: IEEE, 2014, pp. 1–6.
- [5] M. R. Maghami, H. Hizam, C. Gomes, M. A. Radzi, M. I. Rezadad, and S. Hajighorbani, “Power loss due to soiling on solar panel: A review,” *Renewable and Sustainable Energy Reviews*, vol. 59, pp. 1307–1316, 2016. [Online]. Available: <http://linkinghub.elsevier.com/retrieve/pii/S1364032116000745>
- [6] M. Mazumderl, M. Horenstein, J. Stark, P. Girouard, and R. Sumnerl, “Characterization of Electrodynamic Screen Performance for Dust Removal from Solar Panels and Solar Hydrogen Generators,” *Industry Applications Society Annual Meeting (IAS), 2011 IEEE*, pp. 1–8, 2011.
- [7] G. Prinsloo and R. Dobson, *Solar Tracking, Sun Tracking, Sun Tracker, Solar Tracker, Follow Sun, Sun Position*, 2014, no. JUNE 2014.
- [8] H. Qasem, T. R. Betts, H. Müllejans, H. Albusairi, and R. Gottschalg, “Dust-induced shading on photovoltaic modules,” *Progress in Photovoltaics: Research and Applications*, vol. 22, no. 2, pp. 218–226, 2014.
- [9] M. Gostein, B. Littmann, J. R. Caron, and L. Dunn, “Comparing PV power plant soiling measurements extracted from PV module irradiance and power measurements,” in *Conference Record of the IEEE Photovoltaic Specialists Conference*, no. 1, 2013, pp. 3004–3009.
- [10] S. C. S. Costa, A. Sonia, A. C. Diniz, and L. L. Kazmerski, “Dust and soiling issues and impacts relating to solar energy systems : Literature review update for 2012 to 2015,” *Renewable and Sustainable Energy Reviews*, vol. 63, pp. 33–61, 2016. [Online]. Available: <http://dx.doi.org/10.1016/j.rser.2016.04.059>
- [11] Energyblog 95 projects. [Online]. Available: <http://energy.org.za/knowledge-tools/project-database>
- [12] M. R. Maghami, H. Hizam, C. Gomes, M. A. Radzi, M. I. Rezadad, and S. Hajighorbani, “Power loss due to soiling on solar panel: A review,” *Renewable and Sustainable Energy Reviews*, vol. 59, pp. 1307–1316, 2016. [Online]. Available: <http://linkinghub.elsevier.com/retrieve/pii/S1364032116000745>

- [13] S. Mekhilef, R. Saidur, and M. Kamalisarvestani, "Effect of dust , humidity and air velocity on efficiency of photovoltaic cells," *Renewable and Sustainable Energy Reviews*, vol. 16, no. 5, pp. 2920–2925, 2012. [Online]. Available: <http://dx.doi.org/10.1016/j.rser.2012.02.012>
- [14] E. S. Kumar, B. Sarkar, and D. K. Behera, "Soiling and Dust Impact on the Efficiency and the Maximum Power Point in the Photovoltaic Modules," vol. 2, no. 2, pp. 1–8, 2013.
- [15] E. Klugmann-Radziemska, "Degradation of electrical performance of a crystalline photovoltaic module due to dust deposition in northern Poland," *Renewable Energy*, vol. 78, pp. 418–426, 2015. [Online]. Available: <http://dx.doi.org/10.1016/j.renene.2015.01.018>
- [16] J. Mallineni, K. Yedidi, S. Shrestha, B. Knisely, S. Tatapudi, J. Kuitche, and G. TamizhMani, "Soiling Losses of Utility-Scale PV Systems in Hot-Dry Desert Climates : Results from Four 4-16 Years Old Power Plants," New York, 2014, pp. 3197–3200. [Online]. Available: <http://dx.doi.org/10.1109/PVSC.2014.6925615>.
- [17] J. Cano, "Photovoltaic modules: Effect of tilt angle on soiling."
- [18] E. Lorenzo, R. Moretón, and I. Luque, "Dust effects on PV array performance: in-field observations with non-uniform patterns," *Progress in Photovoltaics: Research and Applications*, vol. n/a, no. n/a, 2013.
- [19] M. Maghami, H. Hizam, and C. Gomes, "Impact of Dust on Solar Energy Generation based on Actual Performance," in *International Conference Power & Energy (PECON)*, 2014, pp. 388–393.
- [20] A. J. Carr and T. L. Pryor, "A comparison of the performance of different PV module types in temperate climates," *Solar Energy*, vol. 76, pp. 285–294, 2004. [Online]. Available: <http://www.physics.arizona.edu/~cronin/Solar/References/Degradation/carrPVcomparison2004.pdf>
- [21] C. Cañete, J. Carretero, and M. Sidrach-de Cardona, "Energy performance of different photovoltaic module technologies under outdoor conditions," *Energy*, vol. 65, no. February, pp. 295–302, 2014. [Online]. Available: [https://www.researchgate.net/publication/259996716\\_Energy\\_performance\\_of\\_different\\_photovoltaic\\_module\\_technologies\\_under\\_outdoor\\_conditions](https://www.researchgate.net/publication/259996716_Energy_performance_of_different_photovoltaic_module_technologies_under_outdoor_conditions)
- [22] C. Schill, S. Brachmann, and M. Koehl, "ScienceDirect Impact of soiling on IV -curves and efficiency of PV-modules," *Solar Energy*, vol. 112, pp. 259–262, 2015. [Online]. Available: <http://dx.doi.org/10.1016/j.solener.2014.12.003>
- [23] D. Martinez-plaza, A. Abdallah, B. W. Figgis, and T. Mirza, "Performance improvement techniques for photovoltaic systems in Qatar : Results of first year of outdoor exposure," *Energy Procedia*, vol. 77, pp. 386–396, 2015. [Online]. Available: <http://dx.doi.org/10.1016/j.egypro.2015.07.054>
- [24] J. L. Sawin and et al, "Renewables 2016 Global Status Report," Paris, France, 2016.
- [25] A. Sayyah, M. N. Horenstein, and M. K. Mazumder, "Mitigation of Soiling Losses in Concentrating Solar Collectors," in *2013 IEEE 39th Photovoltaic Specialists Conference (PVSC)*, no. c. Tampa, FL: IEEE, 2013, pp. 480–485.
- [26] A. Verma and S. Singhal, "Solar pv performance parameter and recommendation for optimization of performance in large scale grid connected solar pv plant-case study," *Journal of Energy and Power Sources*, vol. 2, no. 1, pp. 40–53, January 2015.

- [27] K. Midtdal and B. Petter, “Solar Energy Materials & Solar Cells Self-cleaning glazing products : A state-of-the-art review and future research pathways,” *Solar Energy Materials and Solar Cells*, vol. 109, no. 7465, pp. 126–141, 2013. [Online]. Available: <http://dx.doi.org/10.1016/j.solmat.2012.09.034>
- [28] E. Klimm, L. Timo, and K.-A. Weiss, “Can anti-soiling coating on solar glass influence the degree of performance loss over time of PV modules drastically?” in *28th European Energy Solar Conference and Exhibition*, Paris, France, 2013.
- [29] B. Brophy, Z. R. Abrams, P. Gonsalves, and K. Christy, “Field Performance and persistence of anti-soiling coatings on photovoltaic glass,” in *31st European photovoltaics solar energy conference*, 2015, pp. 2598–2602. [Online]. Available: <http://www.eupvsec-proceedings.com/proceedings?paper=34968>
- [30] S. Nishimoto and B. Bhushan, “RSC Advances Bioinspired self-cleaning surfaces with,” *RSC Advances*, pp. 671–690, 2013. [Online]. Available: <http://pubs.rsc.org/en/content/articlehtml/2013/ra/c2ra21260a>
- [31] A. Sayyah, M. N. Horenstein, M. K. Mazumder, and A. E.-p. Sample, “Performance Restoration of Dusty Photovoltaic Modules Using Electrodynamical Screen,” *Photovoltaic Specialist Conference (PVSC), 2015 IEEE 42nd*, pp. 1–3, 2015.
- [32] L. K. Verma, M. Sakhuja, J. Son, A. J. Danner, H. Yang, H. C. Zeng, and C. S. Bhatia, “Self-cleaning and antireflective packaging glass for solar modules,” *Renewable Energy*, vol. 36, no. 9, pp. 2489–2493, 2011. [Online]. Available: <http://dx.doi.org/10.1016/j.renene.2011.02.017>
- [33] J. Son, S. Kundu, L. K. Verma, M. Sakhuja, A. J. Danner, C. S. Bhatia, and H. Yang, “A practical superhydrophilic self cleaning and antireflective surface for outdoor photovoltaic applications,” *Solar Energy Materials and Solar Cells*, vol. 98, pp. 46–51, 2012. [Online]. Available: <http://dx.doi.org/10.1016/j.solmat.2011.10.011>
- [34] M. E. Group. Stain-Resistant Fabric | Exploring the Nanoworld. [Online]. Available: [http://www.education.mrsec.wisc.edu/nanoquest/stain\\_resistant/index.html](http://www.education.mrsec.wisc.edu/nanoquest/stain_resistant/index.html)
- [35] Eccopia. Eccopia Empowering Solar. [Online]. Available: <http://www.ecoppia.com/>
- [36] A. P. Ltd. Aerial Power Ltd. [Online]. Available: <https://www.aerialpower.com/solarbrush/>
- [37] S. O. C. Cañete, R. Moreno, J. Carretero Rubio, M. Piliouguine Rocha, M. Sidrach-de-Cardona, J. Hirose, “Effect of the self-cleaning coating surface in the temperature and soiling losses of photovoltaic modules,” in *27th European Photovoltaic Solar Energy Conference and Exhibition*, 2011, pp. 3432–3435.
- [38] C. Cañete, J. Zorrilla-Casanova, J. Carretero, M. Piliouguine, M. Sidrach de Cardona, J. Hirose, and S. Ogawa, “Performance of Photovoltaic Modules with Self-Cleaning Coating Surface After Two Years of Outdoor Exposure in South Spain,” in *28th European Photovoltaic Solar Energy Conference and Exhibition*, no. September, Paris, France, 2013, pp. 3077–3080.
- [39] J. Hirose, H. Takanohashi, S. Ogawa, M. Piliouguine, J. Zorrilla, J. Carretero, and M. Sidrach-de Cardona, “Evaluation self-cleaning coating for photovoltaic modules,” in *24th European Photovoltaic Solar Energy Conference*, Hamburg, Germany, 2009, pp. 3327 – 3331. [Online]. Available: <http://www.eupvsec-proceedings.com/proceedings?paper=4310>
- [40] M. García, L. Marroyo, E. Lorenzo, and M. Pérez, “Soiling and other optical losses in solar-tracking PV plants in Navarra,” *Progress in Photovoltaics Research and Applications*, vol. 19, no. 2, pp. 211–217, 2011. [Online]. Available: [https://www.researchgate.net/publication/227987524\\_Soiling\\_and\\_other\\_optical\\_losses\\_in\\_solar-tracking\\_PV\\_plants\\_in\\_Navarra](https://www.researchgate.net/publication/227987524_Soiling_and_other_optical_losses_in_solar-tracking_PV_plants_in_Navarra)

- [41] B. Guo, W. Javed, B. W. Figgis, and T. Mirza, "Effect of Dust and Weather Conditions on Photovoltaic Performance in Doha , Qatar," in *Smart Grid and Renewable Energy (SGRE)*. Doha, Qatar: IEEE, 2015, pp. 1–6. [Online]. Available: [http://ieeexplore.ieee.org/xpls/abs\\_all.jsp?arnumber=7208718{\&}tag=1](http://ieeexplore.ieee.org/xpls/abs_all.jsp?arnumber=7208718{\&}tag=1)
- [42] A. Rao, R. Pillai, M. Mani, and P. Ramamurthy, "Influence of dust deposition on photovoltaic panel performance," *Energy Procedia*, vol. 54, pp. 690–700, 2014. [Online]. Available: <http://dx.doi.org/10.1016/j.egypro.2014.07.310>
- [43] R. A. Messenger and J. Ventre, *Photovoltaic Systems Engineering*, 3rd ed. New York, New York: CRC Press Francis and Taylor Group, 2010.
- [44] G. M. Masters, *Renewable And Efficient Electric Power Systems*, 2nd ed. Hoboken, New Jersey: John Wiley & Sons, Inc., 2013.
- [45] S. V. Szokolay, "Solar Geometry," *Design Tools and Techniques*, vol. 53, p. 160, 1989.
- [46] I. Reda and A. Andreas, "Solar Position Algorithm for Solar Radiation Applications," Tech. Rep., 2008. [Online]. Available: <http://www.osti.gov/bridge>
- [47] A. E. Brooks, D. N. Dellagiustina, S. M. Patterson, and A. D. Cronin, "The Consequence of Soiling on PV System Performance in Arizona ; Comparing Three Study Methods," in *Photovoltaic Specialists Conference (PVSC)*. Tampa, Florida: IEEE, 2013, pp. 754–758. [Online]. Available: <http://ieeexplore.ieee.org/document/6744259/>
- [48] D. D. E. E. Geográfica and G. E. Energia, "Assessment of the IEC 60891 norm conversion methods under outdoor test conditions," Ph.D. dissertation, Universidade de Lisboa, 2011.
- [49] GeoSun, "GeoSunAfrica." [Online]. Available: <http://geosun.co.za/solar-maps/>
- [50] "myweather2.com." [Online]. Available: <http://www.myweather2.com/City-Town/South-Africa/De-Aar/climate-profile.aspx>
- [51] FirstSolar, "First Solar Series 4 PV Module," First Solar Datasheet, February 2015. [Online]. Available: [www.firstsolar.com](http://www.firstsolar.com)
- [52] Renesola, "Renesola Virtus II Module 240W, 245W, 250W, 255W, 260W," Datasheet, February 2013. [Online]. Available: [www.ReneSola.com](http://www.ReneSola.com)
- [53] —, "Renesola Virtus II Module 300W,305W,310W," Datasheet, May 2014. [Online]. Available: [www.ReneSola.com](http://www.ReneSola.com)
- [54] OmniPower, "Fully sealed deep cycle rechargable agm+gel vrla solar batteries," OmniPower Datasheet, unknown Accessed: 28 Aug 2016. [Online]. Available: <http://www.sinetech.co.za/assets/img/omnipower-ops/OmniPower%20Battery.pdf>
- [55] V. Energy, "BlueSolar Charge Controller MPPT 100/50," BlueSolar Charge Controller Manual, February 2016. [Online]. Available: [www.victronenergy.com](http://www.victronenergy.com)
- [56] Modbus.org, "MODBUS over Serial Line Specification and Implementation Guide," pp. 1–44, December 2006. [Online]. Available: [http://www.modbus.org/docs/Modbus\\_over\\_serial\\_line\\_V1\\_02.pdf](http://www.modbus.org/docs/Modbus_over_serial_line_V1_02.pdf)
- [57] Tyco-Electronics, "RS485 & Modbus Protocol Guide," 2000. [Online]. Available: <http://energy.tycoelectronics.com>
- [58] M. O. Instruments, "Mso weather sensor," Met One Instruments Datasheet, Revised Oct. 2013. [Online]. Available: [http://www.metone.com/docs/mso\\_datasheet.pdf](http://www.metone.com/docs/mso_datasheet.pdf)



- [59] “International Electrotechnical Commission, Photovoltaic system performance monitoring - Guidelines for measurement, data exchange and analysis, IEC norm No. 61724 1st edition, 1998-04.”
- [60] M. O. Instruments, “370-380 series precipitation gauges,” Met One Instruments Datasheet, Revised Dec. 2010. [Online]. Available: [http://www.metone.com/docs/370\\_380\\_precipitation\\_gauge.pdf](http://www.metone.com/docs/370_380_precipitation_gauge.pdf)
- [61] K. . Zonnen, “Instruction manual smp series smart pyranometer,” User Manual, Jan 2016. [Online]. Available: [http://www.kippzonen.com/Product/281/SMP10-Pyranometer#.V9q6P\\_l95hE](http://www.kippzonen.com/Product/281/SMP10-Pyranometer#.V9q6P_l95hE)
- [62] A. T. Ndapuka and J. M. Strauss, “Design and Development of a Monitoring Station for the Long-Term Investigation of Dust Pollution Effects on the Performance of PV Panels Andreas Tangeni Ndapuka,” Ph.D. dissertation, Stellenbosch University, December 2015. [Online]. Available: <http://scholar.sun.ac.za/handle/10019.1/97823>
- [63] T. C. Ltd., “High power wire wound resistor,” Datasheet, August 2011. [Online]. Available: <http://www.digikey.com/catalog/en/partgroup/te-cgs-series/27488>
- [64] A. D. Inc, “Digital spi temperature sensor adt7310,” Datasheet, year:unknown. [Online]. Available: <http://www.analog.com/en/products/analog-to-digital-converters/integrated-special-purpose-converters/integrated-temperature-sensors/adt7310.html>
- [65] Atmel, “8-bit avr microcontrollers,” Datasheet, Aug 2016. [Online]. Available: [http://www.atmel.com/Images/Atmel-42719-ATmega1284P\\_Datasheet.pdf](http://www.atmel.com/Images/Atmel-42719-ATmega1284P_Datasheet.pdf)
- [66] E. Quartz, “Euro quartz hc49-4h and hc49-4hl crystals,” Datasheet, Accessed: 28 Sep. 2016. [Online]. Available: <http://docs-europe.electrocomponents.com>
- [67] Atmel, “Programmers and debuggers avrisp mkii,” User guide, Jan 2016. [Online]. Available: [http://www.atmel.com/Images/Atmel-42093-AVR-ISP-mkII\\_UserGuide.pdf](http://www.atmel.com/Images/Atmel-42093-AVR-ISP-mkII_UserGuide.pdf)
- [68] Atmel atmega1284p-au, 8bit avr microcontroller. [Online]. Available: <http://uk.rs-online.com/web/p/microcontrollers/6963011/>
- [69] O. Semiconductor, “Mc34063a, mc33063a,sc34063a, sc33063a, ncv33063a 1.5 a, step-up/down/inverting switching regulators,” Datasheet, Aug 2010. [Online]. Available: [http://www.onsemi.com/pub\\_link/Collateral/MC34063A-D.PDF](http://www.onsemi.com/pub_link/Collateral/MC34063A-D.PDF)
- [70] Bourns, “Srr1280 series - shielded smd power inductors,” Datasheet, May 2011. [Online]. Available: <http://docs-europe.electrocomponents.com/webdocs/0ddd/0900766b80ddd400.pdf>
- [71] T. Instruments, “Lm1117 800-ma low-dropout linear regulator,” Datasheet, Jan 2016. [Online]. Available: <http://www.ti.com/lit/ds/symlink/lm1117.pdf>
- [72] E. Corporation, “Enhanced low power half-duplex rs-485 transceivers,” Datasheet, May 2013. [Online]. Available: <https://www.exar.com/content/document.ashx?id=643>
- [73] Vishay, “Surface mount transorb transient voltage suppressors,” Datasheet, Sep 2007. [Online]. Available: <http://docs-europe.electrocomponents.com/webdocs/0dcd/0900766b80dcd12b.pdf>
- [74] A. Technologies, “Single channel, high speed optocouplers,” Datasheet, Jul 2014. [Online]. Available: <http://www.avagotech.com/docs/AV02-0171EN>
- [75] T. Power, “Dc/dc converters tma seres 1 watt,” Datasheet, Feb 2014. [Online]. Available: <http://assets.tracopower.com/20160916155828/TMA/documents/tma-datasheet.pdf>

- [76] Infineon, “Sipmos small signal transistor bss84p,” Datasheet, Jul 2011. [Online]. Available: <http://www.avagotech.com/docs/AV02-0171EN>
- [77] N. Semiconductors, “74lvc86a quad 2-input exclusive-or gate,” Datasheet, Oct 2011. [Online]. Available: [http://www.nxp.com/documents/data\\_sheet/74LVC86A.pdf](http://www.nxp.com/documents/data_sheet/74LVC86A.pdf)
- [78] F. S. Corp., “74lxc08 low voltage quad 2-input and gate with 5v tolerant inputs,” Datasheet, Dec 2013. [Online]. Available: <https://www.fairchildsemi.com/datasheets/74/74LCX08.pdf>
- [79] M. Inc, “Micro sd conn. push/push and normal super-small type,” Datasheet, Apr 2006. [Online]. Available: [http://www.molex.com/pdm\\_docs/sd/5033981892\\_sd.pdf](http://www.molex.com/pdm_docs/sd/5033981892_sd.pdf)
- [80] D. Inc., “Tlv cost effective shunt regulator,” Datasheet, Apr 2011. [Online]. Available: <http://docs-europe.electrocomponents.com/webdocs/0f8c/0900766b80f8c984.pdf>
- [81] Molex surface mount micro sd card connector. [Online]. Available: <http://za.rs-online.com/web/p/memory-sim-card-connectors/8967601/>
- [82] Maxim, “Ds3234 extremely accurate spi bus rtc with integrated crystal and sram,” Datasheet, Jul 2010. [Online]. Available: <http://docs-europe.electrocomponents.com/webdocs/0f6e/0900766b80f6ed2d.pdf>
- [83] K. . Zonnen, “Instruction manual shp1 smart pyr heliometer,” User Manual, Oct 2014. [Online]. Available: [http://www.kippzonen.com/Product/204/SHP1-Pyrheliometer#.V9q8L\\_195hE](http://www.kippzonen.com/Product/204/SHP1-Pyrheliometer#.V9q8L_195hE)
- [84]
- [85] Atmel, “Atmega 164a/164pa/324a/324pa/644a/644pa/1284/1284p 8-bit atmel microcontroller with 16/32/64/128k bytes in-system programmable flash,” Datasheet, Jan 2015. [Online]. Available: [http://www.atmel.com/Images/Atmel-8272-8-bit-AVR-microcontroller-ATmega164A\\_PA-324A\\_PA-644A\\_PA-1284\\_P\\_datasheet.pdf](http://www.atmel.com/Images/Atmel-8272-8-bit-AVR-microcontroller-ATmega164A_PA-324A_PA-644A_PA-1284_P_datasheet.pdf)
- [86] C. Cornwall, A. Horiuchi, and C. Lehman. NOAA Earth System Research Laboratory. Sun Position Calculator. [Online]. Available: <http://www.esrl.noaa.gov/gmd/grad/solcalc/azel.html>
- [87] E. Lorenzo, L. Narvarte, and J. Muñoz, “Tracking and back-tracking,” *Progress in Photovoltaics: Research and Applications*, vol. 19, no. 6, pp. 747–753, 2011.
- [88] T. Power, “Dc/dc converters tme series 1 watt,” Datasheet, Oct 2006. [Online]. Available: <http://assets.tracopower.com/20161125154357/TMA/documents/tma-datasheet.pdf>
- [89] Intersil, “Hip4082,” Datasheet, Jan 2006. [Online]. Available: <http://www.intersil.com/content/dam/Intersil/documents/hip4/hip4082.pdf>
- [90] I. Rectifier, “Irfb4115pbf hexfet power mosfet,” Datasheet, Nov 2011. [Online]. Available: <http://www.infineon.com/dgdl/irfb4115pbf.pdf?fileId=5546d462533600a401535615ba6a1e0f>
- [91] D. A. Neamen, *Microelectronics Circuit Analysis and Design.*, 4th ed. New York, NY: McGraw-Hill, 2010.
- [92] M. H. du T., “Lecture 5. calculation of the losses in switching components.” Lecture Notes, Feb 2014.
- [93] A. Thermalloy, “Aavid thermalloy. the max clip system.” Datasheet, Feb 2004. [Online]. Available: <http://docs-europe.electrocomponents.com/webdocs/0e65/0900766b80e653ff.pdf>

- [94] Microchip, “Mcp601/1r/2/3/4,” Datasheet, May 2007. [Online]. Available: <http://ww1.microchip.com/downloads/en/DeviceDoc/21314g.pdf>
- [95] A. U. Ltd., “Msr bare element resistors,” Datasheet, Nov 2006. [Online]. Available: <http://www.arcolresistors.com/wp-content/uploads/2011/07/MSR-6-11.272.pdf>
- [96] A. D. Inc., “Single supply, low cost instrumentation amplifier,” Datasheet, Dec 2008. [Online]. Available: <http://www.analog.com/media/en/technical-documentation/data-sheets/AD8223.pdf>
- [97] T. I. Inc., “Lm111, lm211, lm311 differential comparators with strobes,” Datasheet, Aug 2003. [Online]. Available: <http://datasheet.octopart.com/LM311P-Texas-Instruments-datasheet-7627217.pdf>
- [98] AMS, “As5048a/as5048b magnetic rotary encoder,” Datasheet, Jun 2014. [Online]. Available: <http://ams.com/eng/Products/Magnetic-Position-Sensors/Angle-Position-On-Axis/AS5048A>
- [99] Bomatec, “Bomatec,” Datasheet, Oct 2015. [Online]. Available: [file:///C:/Users/16082834/Downloads/MD8H-1\\_magnet\\_datasheet%20\(1\).pdf](file:///C:/Users/16082834/Downloads/MD8H-1_magnet_datasheet%20(1).pdf)
- [100] L. T. Corporation, “Ltc6820 isospi isolated communications interface,” Datasheet, Jun 2013. [Online]. Available: <http://www.linear.com/product/LTC6820>
- [101] I. Murata Power Solutions, “786 series general purpose pulse transformers,” Datasheet, NA 2011. [Online]. Available: [http://www.murata-ps.com/data/magnetics/kmp\\_786.pdf?ref=cat-mag](http://www.murata-ps.com/data/magnetics/kmp_786.pdf?ref=cat-mag)
- [102] Rhomberg, “Rhomberg inductive (metal sensing) proximity switches namur (tubular 2 wire) din 19234,” Datasheet, unknown unkown. [Online]. Available: <http://www.rhomberg.com.au/downloads/RI1%20Inductive%20Proximity%20Sensors.pdf>
- [103] N. Semiconductors, “74lvc1g08 single 2-input and gate,” Datasheet, Nov 2016. [Online]. Available: [http://www.nxp.com/documents/data\\_sheet/74LVC1G08.pdf?](http://www.nxp.com/documents/data_sheet/74LVC1G08.pdf?)
- [104] MICROMETALS, “Power conversion and line filter applications,” Datasheet, Feb 2007. [Online]. Available: [http://www.micrometals.com/pcparts/pc\\_1.pdf](http://www.micrometals.com/pcparts/pc_1.pdf)
- [105] S. J. Chapman, *Electric Machinery Fundamentals*, 4th ed. New York, NY: McGraw-Hill, 2005.
- [106] EPCOS, “Film capacitors,” Datasheet, Oct 2011. [Online]. Available: [https://www.arduino.cc/documents/datasheets/cap100nF\\_MKT\\_B32520\\_529.pdf](https://www.arduino.cc/documents/datasheets/cap100nF_MKT_B32520_529.pdf)
- [107] N. C. Corp., “Miniature aluminum electrolytic capacitors,” Datasheet, unknown unkown. [Online]. Available: <http://www.chemi-con.com/upload/files/5/1/74811667552d6c4d41a84c.pdf>
- [108] KEMET, “Kemet part number: R60dn5100aa30j,” Datasheet, Jul. 2016. [Online]. Available: <http://docs-asia.electrocomponents.com/webdocs/1529/0900766b8152900d.pdf>
- [109] K. R. MOTOR, “Dc motor f7147h,” Datasheet, NA NA. [Online]. Available: [http://www.kingright.com.tw/comm/upfile/p\\_140212\\_03600.pdf](http://www.kingright.com.tw/comm/upfile/p_140212_03600.pdf)
- [110] T. P. Ltd, “Worm gear units,” Datasheet, NA NA. [Online]. Available: <http://www.technisales.co.za/skin/images/wormboxes.pdf>

- [111] D. Horvath, "Expert's Opinion. One Surface Energy Doesn't Fit All: Comparing Hydrophobic & Hydrophilic Anti-soiling Coating." [Online]. Available: [http://www.coatingsworld.com/contents/view\\_experts-opinion/2016-04-25/one-surface-energy-doesnt-fit-all-comparing-hydrophobic-hydrophilic-anti-soiling-coating-options](http://www.coatingsworld.com/contents/view_experts-opinion/2016-04-25/one-surface-energy-doesnt-fit-all-comparing-hydrophobic-hydrophilic-anti-soiling-coating-options)
- [112] B. B. Corp., "High speed fet-input instrumentation amplifier," Datasheet, Apr 2015. [Online]. Available: <http://www.ti.com/lit/ds/symlink/ina111.pdf>
- [113] E. Q. B. Macabebe and E. E. V. Dyk, "Parameter extraction from dark current-voltage characteristics of solar cells," *South African Journal of Science*, vol. 104, pp. 401–404, October 2008.
- [114] S. Chowdhury, G. A. Taylor, S. P. Chowdhury, and A. K. Saha, "Modelling , simulation and performance analysis of a PV array in an embedded environment," in *Universities Power Engineering Conference 2007*. IEEE, 2007. [Online]. Available: <http://ieeexplore.ieee.org/document/4469048/?arnumber=4469048{\&}tag=1>
- [115] J. Hyvarinen and J. Karila, "New analysis method for crystalline silicon cells," in *3rd World Conference on Photovoltaic Energy Conversion, 2003*. IEEE, 2003, pp. 18–21.
- [116] M. G. Villalva, J. R. Gazoli, and E. R. Filho, "Comprehensive Approach to Modeling and Simulation of Photovoltaic Arrays," *IEEE Transactions on Power Electronics*, vol. 24, no. 5, pp. 1198–1208, May 2009.
- [117] C. Carrero, J. Amador, and S. Arnaltes, "A single procedure for helping PV designers to select silicon PV modules and evaluate the loss resistances," *Renewable Energy*, vol. 32, no. 15, pp. 2579–2589, December 2007.
- [118] J. Cubas, S. Pindado, and A. Farrahi, "New method for analytical photovoltaic parameter extraction," in *Renewable Energy Research and Applications (ICRERA)*, October 2013. [Online]. Available: <http://ieeexplore.ieee.org/document/6749874/>
- [119] E. Saloux, A. Teyssedou, and M. Sorin, "Explicit model of photovoltaic panels to determine voltages and currents at the maximum power point," *Solar Energy*, vol. 85, no. 5, pp. 713–722, May 2011.
- [120] D. Sera, R. Teodorescu, and P. Rodriguez, "PV panel model based on datasheet values," *Electrical Engineering*, no. 4, pp. 2392–2396, 2007.
- [121] The Scipy Community. `scipy.optimize.minimize`. [Online]. Available: <https://docs.scipy.org/doc/scipy-0.18.1/reference/generated/scipy.optimize.minimize.html>
- [122] J. Stewart, *Calculus: Concepts and Contexts*, 4th ed., J. Campbell, Ed. Belmont, California: Brooks/Cole, 2010.
- [123] M. J. Reno, C. W. Hansen, and J. S. Stein, "Global Horizontal Irradiance Clear Sky Models : Implementation and Analysis," Sandia National Laboratories, Albuquerque, New Mexico, Tech. Rep., March 2012.
- [124] Pv performance modeling collaborative. [Online]. Available: <https://pvpmc.sandia.gov/modeling-steps/>
- [125] A. Awad, A. M. A. M. S. Eldin, A. H. H. Ali, and A. K. Abel-rahman, "Effect of Dust Deposition on Performance of Thin Film Photovoltaic Module In Harsh Humid Climate," in *2nd International Conference on Renewable Energy Research and Applications*. Madrid, Spain: IEEE, October 2013.